Functional and morphological adaptation of the rat musculoskeletal system to electrically induced muscular contraction

Thesis submitted in accordance with the requirements of the University of Liverpool for the degree of Doctor in Philosophy by

Paula Jane Vickerton

October 2014

Abstract

Musculoskeletal tissues exhibit a remarkable extent of plasticity throughout life, with tissues continually able to adapt in line with functional demands. As the skeleton plays a major structural role, its form is profoundly influenced by its mechanical environment, which is largely determined by muscular contraction. Despite the clear functional link between muscle and bone relatively little is known about the biomechanical relationship between these tissues.

This thesis therefore focusses upon the use of implantable neuromuscular stimulators to provide controlled muscular mechanical stimuli. Stimulators were implanted into Wistar rats, inducing muscular contraction every 30 seconds for 28 days. Following stimulation, microCT, histology, and nanoindentation were used to establish changes occurring at the micro and macro-scale in muscle and skeletal architecture. Analysis revealed a localised region of extensive bone growth, with significant increases in cross-sectional area (28.61%, $p<0.05$) and bone volume (30.29%, $p<0.05$) in the stimulated limb. Bone growth was confined to the region which showed peak strain (640μƐ +30.4μƐ). Histology targeted to this region showed clusters of chondrocytes within this new bone growth, possibly indicative of growth via an endochondral process. This region showed a correspondingly low elastic modulus (8.8+2.2 GPa) when compared with established cortical bone (20+1.4 GPa).

To investigate the biomechanical impact of the structural differences in control and stimulated tibiae microCT data were used to construct computational models. Models were used to simulate force propagation throughout the bones in response to muscular contraction. In addition, models were created to investigate the impact of muscle force, bone material properties and bone geometry. The addition of a layer of newly deposited, nascent bone to this region increased effective strain by 8-28% and reduced effective stress by 37-44%. Complete mineralisation of the nascent bone region combined with associated reductions of muscle force production, yielded a significant decrease in both effective strain and stress.

This thesis has demonstrated a rapid and profound skeletal and muscular response to sustained muscle contractions. As such it is a potent reminder of core ideas concerning the significance of interactions amongst tissues in determining overall musculoskeletal form.

Acknowledgements

I would first and foremost like to thank my supervisor Dr Nathan Jeffery for his constant enthusiasm, support and guidance, over the past three years. To put it simply, I couldn't have asked for a better supervisor. I would also like to thank, Michael Fagan, Sue Taft, Riaz Aktar, Hazel Sutherland, Craig Keenan, Jonathan Jarvis, Jim Gallagher, Faye Penrose and Robert Stephenson for their invaluable help with the work presened here, and Rachel Williams for her help and advice over the course of my PhD. Finally I would like to thank my friends and family, especially Racheal Quinn and Ailsa Dermody for their understanding and encouragement, especially during the write up.

List of figures

Chapter 2

Chapter 3

Chapter 4

Chapter 5

Chapter 6

List of tables

List of abbreviations

ADP	Adenosine diphosphate
ATP	Adenosine triphosphate
BMD	Bone mineral density
Botox	Botulinum toxin A
CNS	Central nervous system
CO_2	Carbon dioxide
CT	Computed tomography
DIC	Digital image correlation
DVC	Digital volume correlation
EDL	Extensor digitorum longus
EDTA	Ethylenediaminetetraacetic acid
EMS	Electrical muscular stimulation
eNOS	Endothelial nitric oxide synthase
FE	Finite element
FEA	Finite element analysis
FES	Functional electrical stimulation
FGF-2	Fibroblast growth factor-2
Gly	Glycolytic muscle fibres
GM	Gluteus medius
GMM	Geometric morphometrics
GPa	Gigapascals
H and E	Haematoxylin and Eosin
Hz	Hertz
IFF	Interstitial fluid flow
KPa	Kilo pascals
kV	Kilo vaults

MDA	Multibody dynamic analysis
microCT	Microscopic computed tomography
microMRI	Microscopic magnetic resonance imaging
microPET	Microscopic positron emission tomography
MSC	Mesenchymal stem cell
MHC	Myosin heavy chain
MLC	Myosin light chain
mOsm	Milliosmole
MRI	Magnetic resonance imaging
Myofibrillar ATPase	Myofibrillar adenosine triphosphatase
NADH	Nicotinamide adenine dinucleotide
NMJ	Neuromuscular junctions
NO	Nitric oxide
NOS	Nitric oxide synthases
NS	Not significant
Oxi	Oxidative muscle fibres
Pa	Pascals
PBFS	Phosphate buffered formal saline
PCSA	Physiological cross-sectional area
PET	Positron emission tomography
PGE_2	Prostaglandin E2
PTA	Phosphotungstic acid
PTH	Parathyroid hormone
PTHrP	Parathyroid hormone receptor protein
RF	Rectus femoris
RMA	Reduced major axis

R^2	Coefficient of determination
SD	Standard deviation
TA	Tibialis anterior
TS	Triceps surae
IGF-1	Insulin-like growth factor 1
I_2KI	Iodine potassium iodide
VIP	Vasoactive intestinal peptide
µA	Microampere
µε	Microstrain
µm	Micrometre

Table of Contents

Chapter 1: Introduction to the Rodent Musculoskeletal System and its Response to Loading

Chapter 1

The musculoskeletal system is remarkable in its capacity for adaption, a trait which it maintains throughout life, constantly tuning itself to its shifting demands. The extent of this plasticity is in part determined genetically; however there is a large component which is shaped by environmental factors. The environmental driver for the skeleton appears to be the mechanical forces it experiences. Yet crucial mechanisms linking mechanical input with morphological change are still unknown. Furthermore, the muscular system has close spatial and functional links with the skeletal system, yet muscular contraction is largely overlooked in studies of skeletal mechanoadaptation. Given the increasing burden of musculoskeletal disorders upon society, it is of key importance that the underlying mechanisms controlling musculoskeletal transformation under non-pathological conditions are understood. Here the structure, function, adaptive stimuli and potential of bone and muscle are reviewed.

1.1 Bone function, structure and development

The skeleton is commonly perceived as a static set of levers, setting a rigid framework for the soft tissue and organs of the body to occupy and utilise. This is a gross underestimation of a highly dynamic tissue, as can be demonstrated by the diversity of skeletons seen across vertebrates. The skeleton has many functions, including the protection of internal organs, providing mechanical leverage for muscles, a calcium reservoir for mineral homeostasis, and a site for blood cell production.

Bone is a highly hierarchical tissue which can be described and studied at a number of different levels. At the macroscopic level the skeleton is composed of many bones of differing shapes and sizes, connected to each other via joints. Limbs are typically composed of long bones, with long tubular shafts and expanded ends. The expanded ends (epiphyses) are filled with strut-like trabecular bone (Garner and Anderson 2011). Trabecular bone has a vast surface area, and turnover rate, and is therefore able to provide rapid mineral supplies in times of deficiency (Hadjidakis and Androulakis 2006). The shaft (diaphysis) is composed of dense cortical bone which has a slow turnover rate (Hadjidakis and Androulakis 2006). Within the central cavity of each long bone is bone marrow. At birth this marrow is haematopoietic red bone marrow, and is the site of blood cell maturation. However as the body ages the medullary cavity becomes increasing filled with fat, and there is a corresponding decrease in the haematopoietic capability of the marrow (Naveiras et al. 2009).

Long bones play a major mechanical role within the skeleton, and are required to act as rigid levers throughout foetal and post-natal development whilst they are undergoing rapid growth. Bone deposition is a slow process and so these bones develop via a process of endochondral ossification. Endochondral ossification involves an initial cartilaginous model which is gradually replaced by bone cells (Mackie et al. 2008). In the developing embryo mesenchymal cells from the lateral plate mesoderm, aggregate to form cartilaginous precursors of the skeleton. Peripherally the precursor cells in contact with the periosteum start to differentiate into osteoblasts, and form a bone collar. Centrally mesenchymal cells differentiate into chondrocytes, and secrete cartilagenous extra cellular matrix (Staines et al. 2013). Chondrocytes progressively proliferate, mature, hypertrophy, and die. Hypertropic chondrocytes attract blood vessels (Zelzer et al. 2002). The blood vessels pierce the bone collar, and thus bring with them an invading bone cell population (Karsenty and Wagner 2002) which occupy the matrix left behind after chondrocytes die, this site is the primary ossification centre (Mackie et al. 2008). The replacement of cartilage with bone cells proceeds from this centre and spreads longitudinally along the length of the bone. In long bones this is often followed by invasion at either end of the cartilage precursor by secondary ossification centers (Mackie et al. 2011). As bone develops centrally and from either end of the cartilaginous template a thin band of cartilage towards either end of the bone is retained, as a growth plate (Fig.1.1). The presence of a growth plate allows for continued longitudinal growth of the bone, mainly achieved via rapid hypertrophy of chondrocytes (Kobayashi and Kronenberg 2014). At skeletal maturity longitudinal bone growth ceases and the cartilaginous growth plates close (Mackie et al. 2011).

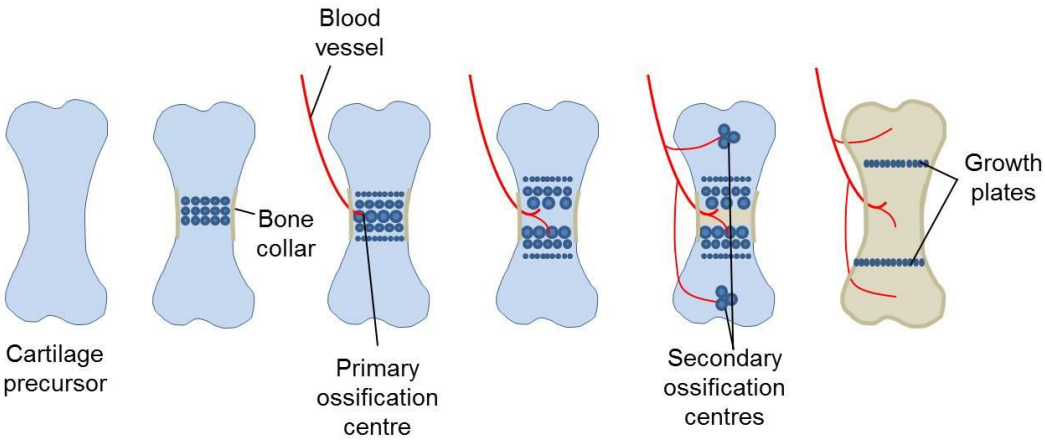

Figure 1.1 Diagrammatic sequence of stages of endochondral ossification. Endochondral ossification begins with a cartilage precursor, which forms a bone collar, and becomes invaded by blood vessels forming the primary ossification centre. From this centre cartilage cells begin to proliferate, mature, hypertrophy, and die. The matrix left behind is invaded by osteoblasts, which form bone. In many long bones secondary ossification centers develop at either extremity, forming thin bands of cartilage towards either end of the bone, the growth plates. Figure modified from Mackie et al (2011).

Not all bones within the skeleton form by endochondral ossification. For instance, the bones of the cranial vault primarily form instead by intramembranous ossification (Hall 2005). During intramembranous ossification embryonic mesenchymal cells condense and differentiate into osteoprogenitor cells, which in turn differentiate into osteoblasts (Kronenberg 2003). The cells which are innermost secrete osteoid and become bone, whilst the cells on the periphery differentiate into the periosteum (Hall 2005). The periosteum forms a continuous double layered envelope around bones with an outer fibrous layer, and an inner cambial layer. The cambial layer retains mesenchymal stem cells (MSCs) throughout life, allowing for continued appositional growth via intramembranous ossification (Wang et al. 2014).

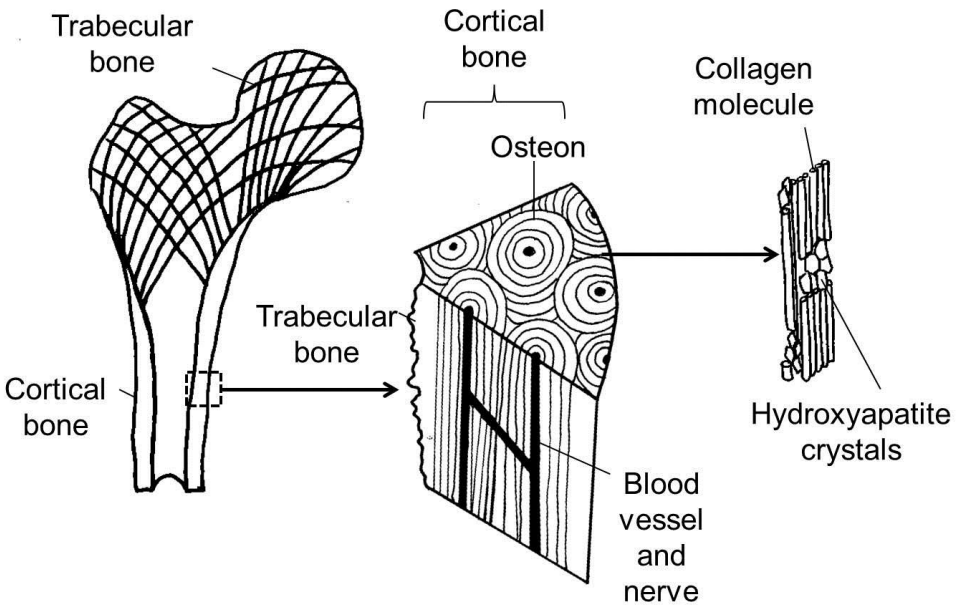

Figure 1.2 Diagrammatic representation of the hierarchical structure of bone. Long bones contain trabecular and cortical bone. Mature cortical bone is composed of sub units of osteons. Each osteon has a central canal containing a blood vessel and a nerve, surrounded by concentric circles of collagen. At the sub-microscopic level collagen molecules are interspersed with hydroxyapatite mineral crystals. Figure modified from Rho et al (1998).

During development, bone is often initially formed in a chaotic manner (Currey 2003), and subsequently undergoes a process of remodelling (see section 1.4) to obtain its mature structure. Microscopically mature cortical bone consists of a series of canals containing a blood vessel and nerve and surrounded by concentric circles of densely packed collagen fibrils (Fig.1.2). Mature bone cells (osteocytes) are located between the concentric lamellae of collagen. Each osteocyte sits within a space (lacunae) and has many cell processes, connecting it to other osteocytes in a dense three dimensional network. The cell processes lie in fluid-filled channels (cannaliculi) which are continuous with the lacunae and allow for the exchange of nutrients, waste products and interstitial fluid (Rauner et al. 2012). This network of interstitial fluid is thought to play a major role in mechanotransduction (see section 1.6.2). At the sub-microscopic level bone is composed of a collagen matrix, water and mineral hydroxyapatite (Currey 2002). The water is thought to combine with the collagen element of bone, and their porportion is inversley proportional to mineral content of a bone (Zioupos et al. 2000).

1.2 Biomechanical performance of bone

1.2.1 Material properties

The skeleton plays a major structural role. For this, bone is required to support loads and withstand fracture whilst remaining light enough for efficient locomotion. The skeleton has therefore evolved as a compromise of its often conflicting requirements.

The ability of a bone to resist fracture and deformation is a result of the mechanical performance of its material and its structural arrangement. The mechanical performance of a material can be summarised by a stress-strain curve (Fig.1.3). Stress is the amount of force per unit area. Strain is a measurement of the deformation in an object caused by an applied force, length divided by original length. Strain is a ratio and so is unit-less. One microstrain (με) is equal to 0.0001% strain (De Souza and Saxon 2012). As stress upon a material is increased the material will deform. Initially this deformation is elastic, that is, the material will revert back to its original form once the force is removed. The gradient of the elastic region of a stress-strain curve represents the materials elastic modulus, or how much a bone will deform under load. A high elastic modulus represents a material which deforms very little under load and is therefore, rigid. Bone is required to be rigid to act as a mechanical lever for muscles to pull against, and to bear body weight without buckling. The rigidity of bone is derived from its mineral component (Currey 1988), with higher mineral densities resulting in more rigid bones. The elastic modulus of bone shows remarkable diversity across different species and bones (Currey 1988). The antlers of deer have incredibly low elastic moduli (2.23GPa) and whale bulla bones showing very high moduli (33.65GPa) (Currey 1988).

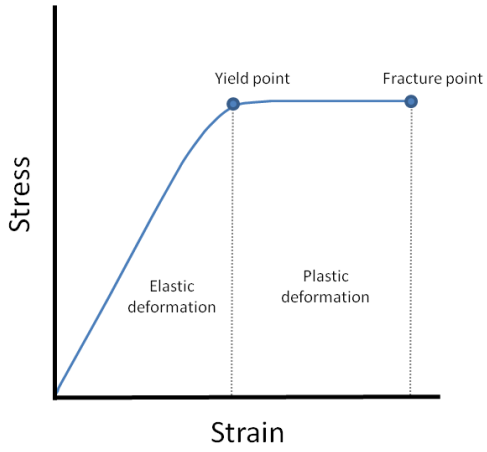

Figure 1.3 A example of a stress-strain curve. A stress-strain curve summarises a materials mechanical performance. As a load is applied a material will deform, initially this deformation is reversible with removal of the load, elastic deformation. As the yield point is surpassed deformation becomes permanent, plastic deformation. Figure modified from Turner (2006).

Bone will not continue to deform elastically under an ever increasing load. At a certain point irreversible damage occurs within the bone and it reaches a yield point. Beyond this point bone deforms plastically, that is it will not revert to its original form upon removal of the load (Fig.1.3).

Not all materials deform plastically, a rigid material, by its very definition, will not deform to a great extent, and so if stress becomes too great, energy is dissipated instead by fracture. A material which fractures without deforming significantly is brittle. Hence, the extent of plastic deformation is inversely proportional to brittleness. The high elastic modulus of the bulla bone would therefore not provide a mechanical advantage to a long bone, but plays an important acoustic role. As the bulla is encased within the skull it is unlikely to become fractured as a result of mechanical loading. Long bones are not only required to be rigid, but also tough, which is the ability to absorb energy without fracture. Bone toughness is a result of its collagen component. This can be demonstrated by decalcifying a bone; it retains its shape, yet can be easily manipulated, unable to resist compressive forces, but very difficult to break.

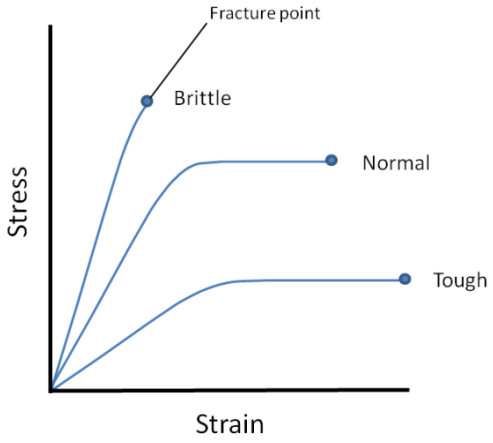

Figure 1.4 How variation in stress-strain curves reflects material properties. Non-pathological bone usually exhibits both elastic and plastic deformation before reaching its fracture point. A brittle bone has a steep elastic region, and very little plastic region. Conversely a tough bone shows a large about of deformation for very little force. Figure modified from Turner (2006).

A material's toughness or, work to failure is represented by the region under the stress-strain curve (Fig.1.4). A homogenous material can only ever be tough or rigid. The combination of collagen and hydroxyapatite found within bone result in a material which is both rigid and tough (Albright and Skinner 1987). Variation of the proportion of these components over an evolutionary time scale, as seen with the whale bulla and deer antler can have remarkable effects upon the mechanical performance.

1.2.2 Structural properties

It is not only the proportion of collagen and mineral which affect the mechanical performance of a bone, but also their arrangement at microscopic and macroscopic scales. Within mature osteonal bone, collagen fibrils are arranged in concentric circles aligned in the direction of principal loading (Riggs, Lanyon, et al. 1993). The orientation of fibrils can influence both the elastic modulus and ultimate tensile stress of bone at the microscopic level (Riggs, Vaughan, et al. 1993). Bone as a material is almost always anisotropic, that is, the mechanical behavior is not the same in all dimensions. Such patterns of anisotropy can persist at the macroscopic level too, though these can often be generalised because the net directionality is already represented by the geometry of the bone. For example, bones are most

resistant to fracture along their principal geometrical axes over which they are most routinely loaded during life (Wolfram et al, 2010a).

Loads experienced by bones can be divided into; compression, tension and shear stress (Einhorn, 1992) resulting in compressive, tensile and shear strain. Compressive forces are applied in opposing directions towards each other. Tensile forces are applied in opposing directions away from each other. Shear loads are applied opposite directions, in parallel to each other but not along the same line (Fig.1.5) (Einhorn, 1992). The stress and strain experienced within a structure often exists as a combination of different forms, and the distribution is rarely unidirectional. The stress and strain acting within an object can be divided into vectors. There are three vectors normal to the object (x, y, z) and each of these vectors has two shear vectors. The three normal vectors are known as the principal stress and strains (Frankel and Nordin 2001). The 1st principal stress has the largest magnitude, and 3rd has the lowest. As tension is represented by positive values, and compressive forces as a negative values the 1st principal stress often represents the tensile stress, and the 3rd often represents compressive stress.

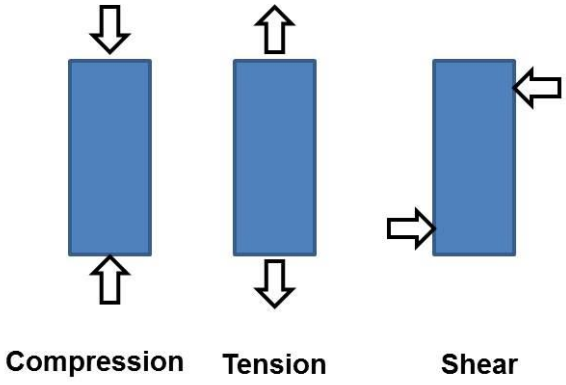

Figure 1.5 A diagram of compressive, tensile and shear stress. Compressive forces are applied in opposite directions towards each other. Tensile forces are applied in opposite directions away from each other. Shear stresses are applied in opposite directions but along different lines. Figure modified from Einhorn (1992).

The vast majority of long bones take the form of a hollow tube. This reduces weight over a solid tube, with very little loss of weight bearing potential. The circumferences of long bones are rarely perfectly circular. Mice heterozygous for the mutation muscular dysgenesis (mdg mouse) have skeletal muscles that lack contractile activity. Mdg mice have been used to demonstrate that the particular cross-

sectional shape of a long bone is determined by muscle contractile activity. The long bones in the mdg mouse had circular circumferences, which provided inferior biomechanical performance compared with long bones in wildtype control mice (Sharir et al. 2011).

The cross-sectional diameter of a bone plays an important role in determining the stress within the bone. A bone with a thicker cortex has more material for load to be spread over, and so stress is lower when loaded in tension or compression than in a bone with a smaller diameter (Frankel and Nordin 2001). However, long bones usually exhibit a curvature along their length. A curved bone loaded axially experiences both compressive and tensile stresses along its length, resulting in a transition from compression to tension across its diameter (Fig.1.6). The strain environment is further complicated as loads are not simply applied axially. Muscles contract and impose bending forces in a multitude of directions. When a bone is loaded in bending it is not only the quantity of a bone material, but its distribution which affects mechanical performance. The distribution of bone from the axis of loading is the moment of inertia (Frankel and Nordin 2001). Placing the same amount of material further away from the axis of loading does not alter the magnitude of stress, but does alter its distribution. A wider cylinder has a more gradual transition from compression into tension across its diameter, and thus lower shear forces, and fracture risk. The addition of bone to the periosteal surface of a bone therefore has a higher structural benefit than endosteal growth to a bone exposed to bending forces (Turner 2002).

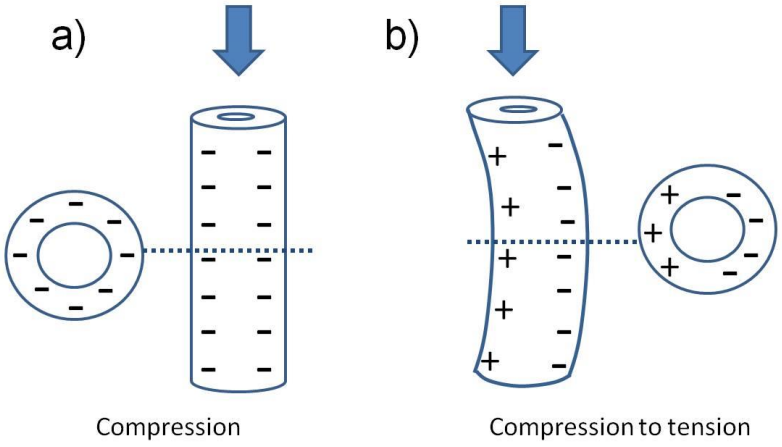

Figure 1.6 A diagram of a straight and curved bone in axial loading. a) When a straight bone is loaded axially, the stresses are compressive. b) a curved bone loaded axially experiences both compressive and tensile stresses along its length, resulting in a transition from compression to tension across its diameter.

Not all of the skeletons structural parameters act to directly minimise fracture risk. The curvature exhibited by long bones results in higher strains relative to a straight bone, thus long bones are enhancing their susceptibility to fracture by not being straight (Bertram and Biewener 1988). The advantage of a curved bone is not in strain magnitude, but the predictability of strain distribution. A straight tube compressed axially may fail in any direction, and a bone can only accommodate to this by growing in all dimensions, which is inefficient in terms of materials, and will result in a heavier skeleton. A bent tube will always fail in the same place, and so localised bone growth can occur in response to high stresses, reducing the chance of failure for a minimum of material (Lanyon 1987).

1.2.3 Bone fracture

The ability of a bone to absorb and dissipate energy can be demonstrated by the ability of bone to form micro-cracks. Micro-crack propagation degrades the elastic modulus of bone, and so reduces stiffness (Burr et al. 1998), but increases the ultimate strength (as defined by the amount of energy required to result in fracture of the bone). The accumulation of small, fractures throughout a bone allows a certain amount of “give”, which can be repaired directly without a loss of mobility (Frost 1960; Bentolila et al. 1998; Wu et al. 2013). Without this capability bones would be far more susceptible to fracture. The manner in which micro-cracks heal is dependent upon the type of micro-crack. Linear micro-cracks, cause osteocyte death, and initiate remodelling, and are repaired as bone is turned over (Frost 1960). Diffuse micro-cracks on the other hand, do not cause osteocyte death, or bone remodelling (Herman et al. 2010), and heal by an unknown mechanism (Seref-Ferlengez et al. 2014).

A fracture occurs when the stress within the bone exceeds the limit of the material in its given distribution. Bone is one of the only tissues capable of repairing itself without the formation of scar tissue. Fracture healing requires more extensive mechanisms than micro-crack repair and usually involves intramembranous and endochondral ossification (Marsell and Einhorn 2011), the two mechanisms through which all bones are formed (see section 1.1). A discrete skeletal fracture initiates a rapid process of MSC recruitment. Where the MSCs come from is not clear but the bone marrow and surrounding soft tissues are likely candidates (Marsell and Einhorn 2011). MSCs aggregate between the fractured bone and form a soft cartilage callus. Within the callus endochondral ossification occurs, and the callus

becomes progressively mineralized and replaced by bone cells (Martinez et al. 2010). At the same time the periosteal portion of the callus forms bone directly from mesenchymal stem cells via intramembranous ossification, creating a hard callus (Schindeler et al. 2008). The region of bone spanning across the fracture site creates a semi-rigid structure which allows some degree of weight bearing (Marsell and Einhorn 2011).

1.3 Wolff's law

For the skeleton to avoid fracture and retain mechanical competence across the varying loading conditions imposed throughout life, an ongoing process of structural optimization is required. As the skeleton grows it is subject to gradually evolving mechanical demands, as limbs lengthen they experience greater torque, and the adjacent growth of skeletal muscle leads to greater contractile and bending forces. Conversely in ageing, skeletal muscle mass typically decreases and mechanical forces upon the skeleton decline. Even during adulthood, the mechanical demands to which the skeleton is accustomed vary substantially between individuals of different sizes and mass. Additionally there is substantial diversity in the mechanical demands resulting from lifestyle with elite athletes imposing substantially larger loads than the population in general. A skeletons mechanical environment is clearly not a fixed state and varies substantially between individuals and across a lifetime.

The idea that bone adapts its structure to its functional demands is most famously associated with Julius Wolff and his landmark publication "Das Gesetz der Transformation der Knochen". Wolff's law dictates that a bones internal architecture and external form are defined by mathematical rules, which arise as a consequence of mechanical forces (Ruff et al. 2006). The general concept that a bone’s structure is heavily influenced by its mechanical environment is widely accepted. For example tennis players have markedly thicker bone’s in their playing arm than their throwing arm, and astronauts can lose up to 1.6% bone mineral density in the lower appendicular skeleton per month when in space (LeBlanc et al. 1998). Wolff's law was not however a general principle, but a mathematical treatment of a biological principle which contained both biological and engineering misconceptions (Ruff et al. 2006).

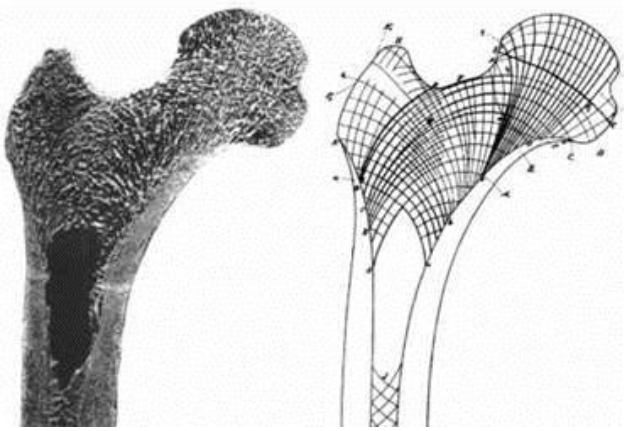

Figure 1.7 A comparison of trabecular architecture and principal loads within the human femoral head. The basis of Wolff's trajectorial theory is demonstrated by the remarkable similarity between the trabecular orientation in the femoral head (left) and Meyer's schematic representations of principal loads (right)(Meyer 1867). Figure modified from Huiskes (2000).

Much of Wolff's theories centered on his trajectorial theory, informed by Meyer (an anatomist) and Culmann (an engineer) who correlated the anatomical arrangement of trabeculae in the femoral head with the principal stress trajectories (Fig.1.7) (Skerry 2006). Wolff believed that such a remarkable similarity could not be coincidental. He proposed that the structure of bone transformed with the altered loading pattern (Bertram and Swartz 1991). It is now known that the healing of femoral head fracture is a particularly complex process, often involving partial occlusion of the blood supply, which results in substantial bone loss. Therefore the trabeculae "adaptation" that Wolff studied was actually trabeculae being resorbed and then as the bone healed new trabeculae formed. This process is not technically the trabecular shift Wolff envisioned (Bertram and Swartz 1991). Despite this, there is a large body of work supporting Wolff's theory that trabeculae dynamically adapt to new loading conditions with a high degree of sensitivity (van der Meulen et al. 2009; Barak et al. 2011).

It is not only bone's macroscopic structure which appears to be influenced by mechanical stimuli. Within bone lies a 3D network of bone cells, osteocytes. The structure of this network becomes increasingly organised and aligned during development (Hirose et al. 2007), with the mature morphology of the network and osteocytes differing across anatomical location (Vatsa et al. 2008; Himeno-Ando et al. 2012). The mouse fibula is loaded principally in one direction and shows

elongated cells, aligned parallel to the main axis of loading. In the calvaria, osteoblasts show no particular directionality, and loads are imposed radially and tangentially by intracranial pressure and mastication (Vatsa et al. 2008). Furthermore neurectomised mice showed osteocyte networks that were less developed than wild-type age matched mice (Sugawara et al. 2013). Suggesting that, mechanical loading plays a defining role in both the macro and microscopic structure of bone.

1.4 The mechanostat theory of bone modelling and remodelling

Mechanical stress within a bone results in strain. Peak strains in long bones were found to be remarkably consistent across a number of species (Rubin and Lanyon 1982). Sites of peak strain correspond with sites of bone formation (Rubin and Lanyon, 1984). These key observations paved the way for Harold Frost's "mechanostat" theory (Frost 1987). This hypothesis likens the skeleton to a thermostat, governed by mechanical, not thermal influences (Fig.1.8). The skeleton is accustomed to habitual strains; if strains fall within this threshold then the skeleton mass is maintained. If strains exceed or fall below this threshold then bone modelling will be activated. Bone modelling is the process of bone formation and resorption on separate bone surfaces (Gerhard et al. 2009) and can be either resorption modelling which results in a net bone loss or formation modelling which results in a net bone gain (Hughes and Petit 2010). When strains exceed the habitual level, formation modelling is activated, increasing bone mass and reducing strain. Conversely if strains fall below habitual levels resorption modelling is activated, bone mass decreases and strains increase, returning to their habitual level (Frost 1987). Modelling can be considered distinct from the process of remodelling in which bone is turned over, that is, bone resorption is followed by formation on the same region of bone and there is no net change in bone mass.

The extent to which modelling and remodelling are linked is not clear. The remodelling process begins with bone resorption. Osteocyte apoptosis associated with micro-cracking (Herman et al. 2010), and hindlimb unloading (Aguirre et al. 2006) initiate bone resorption. The difference which then arises may be a result of the bone’s mechanical environment. Micro-cracks form in bone which is being loaded. Osteocytes are damaged, and resorption is provoked. However, there is an ongoing mechanical stimulus within this region and bone formation is then provoked, resulting in the remodelling sequence observed. This can be contrasted with the

unloading model where a lack of loading reduces strain and initiates osteocyte apoptosis. Following bone resorption there is no increase in strain, as the limb is still unloaded, and so there is no subsequent bone formation. Furthermore bone formation modelling can occur without any prior resorption (Boyde 2003). The processes of modelling and remodelling could therefore be regarded as part of the same continuum of bone responses which could be divided instead into bone formation or resorption.

The simplicity of the mechanostat theory has led to its widespread use. However, the relationship between bone's structure and applied mechanical loads is not as simple as initially suggested. The original mechanostat theory relates bone activity with strain magnitude, there is a clear functional logic to this, as a structure will only fail under loads at the edge of its mechanical competence. Therefore bone growth is driven by large strains. However strain magnitude is only one element to which bone is responsive, strain rate (Mosley and Lanyon 1998), how frequently the load is applied (Qin et al. 1998) and rest periods between loads (Robling et al. 2000) all contribute to the total strain environment which determines the skeletal response.

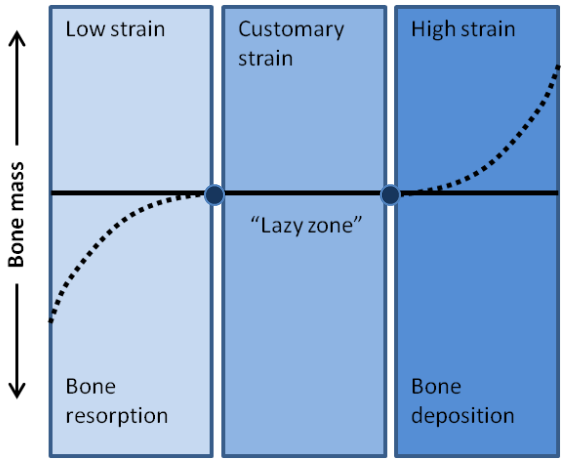

Figure 1.8 A Diagrammatic representation of Frost's mechanostat theory. Bones are accustomed to a specific range of strain, whilst strains are within this range no net bone resorption or formation will take place. As strain increases above a specific strain threshold bone formation is activated. Conversely as strains fall below a threshold then bone resorption is activated. Figure modified from Frost (2003).

Frost's original theory gave specific strain values which governed bone formation (1500 με) and resorption (300 με), between these values there was a threshold of

strain in which there was no net formation or resorption (between 300 and 1500με), this became known as the "lazy zone" (Fig.1.7). The concept of a lazy zone has recently been challenged by experiments showing that the skeleton responds to applied strains in an essentially linear manner (Sugiyama et al. 2012; Ellman et al. 2013) or to strain energy density in a exponential fashion (Schulte et al. 2013). It is possible that the lazy zone was a by-product of bones being loaded naturally through ambulation as well as experimentally. If the loads applied experimentally do not exceed those arising from normal ambulation then no additional bone formation will be seen in relation to the experimental condition. This does not mean that bone is not responding.

It may be more suitable to replace the "lazy zone" with a continuous scale of bone activity in the middle of which is a single minimum effective strain value, acting as a pivot point. Strains exceeding this value will result in bone deposition, and values below the value will result in bone resorption, in a continuous fashion (Fig.1.9).

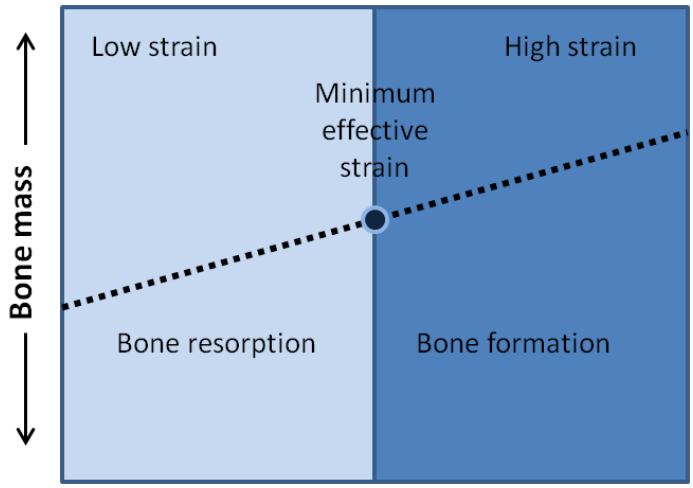

Figure 1.9 A Diagrammatic representation of Sugiyama's theory of bone mechanoadaptation. Loading increases mass in a linear manner, disuse returns bone towards the minimum mass. The precise minimum effective strain is a derivative of strain magnitude, rate, frequency and site specific. Figure modified from Sugiyama et al (2012).

The strain values to which bone responds are not global across all bones. Habitual strains in the skull are far lower than those experienced by the tibia (Skerry 2006). If the tibia was exposed to strains experienced across the skull it would undergo severe resorption modelling. Bones of the calvarium and long bones fulfil ultimately

different functions, and so have been shaped by different evolutionary pressures. The skull fulfils a protective function, and its fracture would be far more detrimental to the survival of the individual than the fracture of a long bone, and so the conservation of skull mass is of great importance regardless of the mechanical demands imposed upon it. In contrast, long bones play a mechanical function, and their reshaping by mechanical forces allows for the reduction of weight. The failure penalty of a long bone is far lower than the skull, and so its mass does not need to be as tightly regulated. Furthermore bone is often cited as responsive to dynamic and not static loads (Turner 1998). However, static loads imposed upon growing long bones actually result in restricted growth (Robling et al. 2001a), and so shorter bones. A shorter bone is more stable for bearing large loads.

The mechanostat theory is further complicated by systemic factors, such as the differing hormonal environments in males and females, which is thought to be responsible for the difference in mechanical sensitivity (Martin 2002). Males are more responsive than females to both increased (Martin 2002) and decreased loading (Bertram and Biewener 1988)

1.5 Frequency of loading vs Magnitude of load

Over the course of daily activity the skeleton is exposed to an almost constant barrage of very low strain signals caused by muscular contraction, and the number of high-strain events are only very few (Ozcivici et al. 2010). In 1998 Qin et al studied the interrelationship between the number of loading cycles and bone growth in the turkey ulna, and found a non-linear relationship (Fig.1.9) dictating that bone could be maintained by either few large loads or many smaller loads (Qin et al. 1998). This can be seen in its extreme by a single bout of loading resulting in bone formation (Forwood et al. 1996) as does the application of low-magnitude high-frequency vibrations (Rubin et al. 2001).

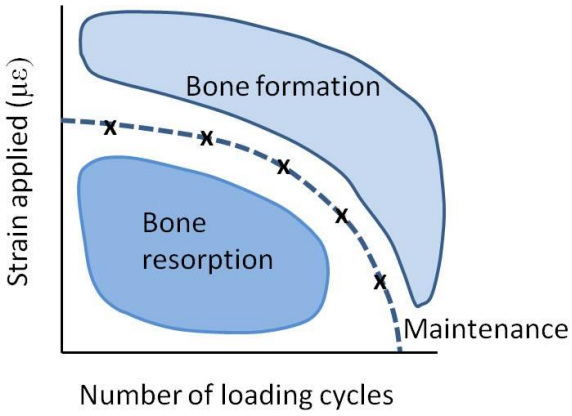

Figure 1.10 Graph representing the relationship of loading magnitude against how frequently a load is applied upon bone mass. A large infrequent load can have the same osteogenic potential as a smaller more frequent load. The region above the dashed line represents loads which will result in bone formation. Loads which fall below the line represent loads which will result in bone resorption. Figure modified from Ozcivici et al (2010).

The frequency-magnitude relationship is complicated as bones rapidly de-sensitise to applied loads, with continued cycles of loading showing diminishing returns in terms of an osteogenic response (Rubin and Lanyon 1984). This has been tested extensively in the rat tibia. The same total load (360 loading cycles, of 54N) can be broken down into multiple loading sessions (4 sessions, of 90 loading cycles, of 54N) and the osteogenic response is enhanced compared with the load being applied in a single session (Robling et al. 2000). This shows that the bone is not forever sensitised to that stimulus, but regains sensitivity. In fact in the rat tibia the insertion of a rest period of just 14 seconds was found to be sufficient to recover some sensitivity, and significantly increase bone formation, though a recovery period of 8 hours is required for sensitivity to be fully recovered (Robling et al. 2001b). The insertion of rest periods during vibratory loading does not enhance the osteogenic response (Xie et al. 2006).The magnitude of a load and how frequently it is applied have a complex relationship, but both appear to play crucial roes in determining the mechanical environment of the skeleton.

1.6 Mechanotransduction

In order for a bone to be able to adapt its morphology to the mechanical demands it must be able to sense the mechanical environment, and transduce this into a biochemical signal, initiating bone activity. The exact biological mechanisms for this are not fully understood.

The tight spatial coordination between bone activity and strain magnitude implies that a sensory network would need to be extensively distributed throughout the skeleton. Bone tissue contains a number of different cell types which could act as sensory cells. Osteoblasts are derived from mesenchymal stem cells, they function to form bone by secreting collagen and directing its mineralisation (Dillon et al. 2012). During this process many osteoblasts become entombed within the bone matrix. These cells change their phenotype, extend their cell processes and become osteocytes. The osteoblasts which do not become entombed remain on the bone surface taking on a flattened morphology and are known as bone-lining cells. Osteocytes make up 90-95% of the cell population within adult bone. Osteocytes have extensive cell process, connecting them to each other, surface-bound bone lining cells, and to the MSC population of the marrow cavity (Kamioka et al. 2001) in a dense three-dimensional network (Garner and Anderson 2011). A third cell type, osteoclasts are large multinucleated cells which act to break down bone, and have a distinct lineage from other bone cells, originating instead from a hematopoietic cell lineage (Bar-Shavit 2007). Osteocytes, with their extensive distribution would provide an ideal strain-gauge network allowing for highly regionalised bone mechaoadaptation. Additionally the network is connected to both bone forming and bone resorption cell populations. The importance of osteocytes for mechanoadaptation has been clearly demonstrated in mice with ablated osteocytes, in unloading experiments these mice showed no bone resorption (Tatsumi et al. 2006).

In vitro studies have shown that not only osteocytes, but also osteoblasts and bone lining cells all show cellular responses to mechanical input (Haj et al. 1990; Pitsillides et al. 1995). However osteocytes showed far greater sensitivity than either osteoblasts or periosteal fibroblasts (Klein-Nulend et al. 1995). Direct application of mechanical loads to osteocytes results in cellular activity, but the strain must exceed 5000με (You et al. 2000). This far exceeds strain magnitudes typically generated during strenuous exercise, which in human tibias rarely exceeds 1000με (Lanyon et al. 1975). Therefore strains may be amplifed before reaching the osteocyte.

Cells in vitro do not accurately represent osteocytes in situ. When grown in flasks osteocytes can only develop into a two-dimensional network as opposed to their natural three-dimensional network (Bakker and Klein-Nulend 2010). This reduction in dimensionality will restrict the cells potential for sensing applied mechanical stimuli. It has also been demonstrated that inhomogeneity in the bone matrix may be able to amplify a mechanical signal by as much as three times its original strength (Rath Bonivtch et al. 2007). It is therefore possible that strains around osteocytes in situ far exceed those measured on the bone surface, and that the osteocytes themselves are far more sensitive than those grown in vitro and so can sense matrix strains directly.

An alternative explanation for the apparent mis-match in strain sensitivity is that strains are amplified by fluid flow. In vitro osteocytes are responsive to fluid flow (You et al. 2000), and in situ osteocytes exist surrounded by interstitial fluid (Klein-Nulend et al. 2012). The application of a load on a bone causes deformation of the bone matrix, applying pressure on the fluid within the lacuna-canliculi system in which osteocytes exist. Interstitial fluid therefore flows away from areas of high pressure towards areas of lower pressure, and presents a mechanism for highly regionalised bone growth in response to mechanical input (Fig.1.11). Furthermore, fluid flow across osteocytes and their cell processes leads to an influx of Ca^{2+} into the cells (Hung et al. 1996). The rise in intra-cellular Ca^{2+} activates a number of signaling pathways, with osteocytes releasing signaling molecules; prostaglandins (Klein-Nulend et al. 1997), nitric oxide (Klein-Nulend et al. 1995a), ATP (Bowler et al. 1998) along with decreased levels of sclerostin expression (Robling et al. 2008). These cellular signals act upon osteoclasts and osteoblasts to bring about appropriate responses (Klein-Nulend et al. 2012).

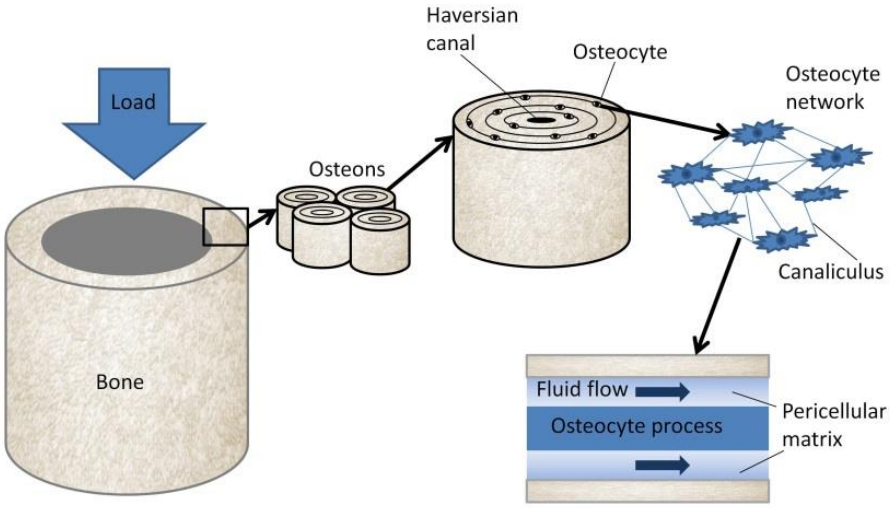

Figure 1.11 A diagram of the interstitial fluid flow theory. Loading a bone creates a current of interstitial fluid flow within the lacuno-canallicular system containing the osteocytes and their cell processes. This initiates cellular signalling processes, which result in bone formation via osteoblasts. Figure modified from Chen et al (2010).

Possibly the most convincing evidence supporting the role of interstitial fluid-flow (IFF) in mechanotransduction was presented by Kwon et al, who essentially decoupled IFF from matrix deformation. IFF in the absence of matrix deformation protected against bone loss caused by skeletal unloading (2010).

Despite the overwhelming evidence that osteocytes and IFF play a crucial role in mechanotransduction it is interesting to note that many species of teleost fish have bone which is entirely devoid of osteocytes, yet is capable of modelling in response to mechanical loads (Shahar and Dean 2013). Furthermore experimental ablation of osteocytes in mice, followed by loading revealed that bone formation can still occur. Bone formation was here attributed to the activity of surface residing cells (Kwon et al. 2012). Therefore osteocytes may work in synergy with bone-lining cells to sense bone strain.

1.7 Neural distribution and function within bone

Entering long bones with blood vessels are large nerves (Gros 1846) the distribution of these nerves remained unclear for a long time, as they were encased in mineralised matrix. However advances in visualisation has lead to a clearer picture of neural distribution. Within the marrow space are a large amount of sensory fibers (Mach et al. 2002) and sympathetic vasomotor fibers which wrap around blood vessels (Duncan and Shim 1977). The periosteum has the most dense neural innervation, consisting of a network of sensory fibers, sensitive to both mechanical stimulation (Mahns et al. 2006) and pain (Mach et al. 2002).

The way in which this network of neural fibers control bone modelling and remodelling is not well understood. It has been shown that the extensive sympathetic innervation can modulate bone mass though a number of pathways, including vasoactive intestinal peptide (Hohmann et al. 1986) and Leptin (Elefteriou et al. 2005a). Furthermore, bone cells express receptors for neurotransmitters and neuropeptides, which can modulate bone formation and resorption activity (Lerner 2002). Despite this, it is well established that bone remodelling can occur entirely independent of any input from the CNS (Hert et al. 1971) and in the absence of input from the sympathetic nervous system (De Souza et al. 2005a). This view has been challenged by Sample et al who demonstrated that an extreme loading regime resulted in contra-lateral bone formation, and that this was not the case with neuronal blocking agents (Sample et al. 2008). Subsequent studies have found that in less extreme loading regimes there is no contra-lateral effect upon bone (Sugiyama et al. 2010), suggesting that very high levels of loading, possibly associated with blood vessel trauma, induce systemic effects via the nervous system. Alternatively, the extreme loading resulted in pain within the loaded side, and the animals loaded their contra-lateral limbs more heavily as a result. The application of nerve block in the form of anesthesia removed the pain stimulus and animals ambulated normally, and bone formation was only seen on the loaded bone. The role of the nervous system in regulating bone mass is clearly a highly complex process, yet it appears that mechanical loads create the key stimuli, which can then be modulated by neuronal input.

1.8 Musculoskeletal loads

Stress within the skeletal system arises from three main sources; muscular contraction, kinematics and gravitational forces. Muscular contraction creates compressive and tensile forces within bones, generating motion, leading to kinematic loading, created by accelerations, decelerations and changes in direction. Gravitational forces are reactive loads resulting from contact with surrounding substrates. Muscular, kinematic and gravitational loading are all thought to profoundly shape the skeletal system, however as loads are usually a combination of all three their relative influence is a matter of debate.

1.8.1 Muscular loading

The skeleton is spatially and functionally linked to the muscular system, with the skeleton providing a set of rigid levers for skeletal muscles to pull on and generate movement. Skeletal muscle therefore provides the most immediate source of mechanical loading, and is often cited as having the most pronounced effect upon bone (Frost 1997; Judex and Carlson 2009).

Indeed bone and muscle mass appear closely correlated throughout life. Cross-sectional studies have shown bone mineral content (BMC) and cortical bone mass closely correlate with muscle mass (Schoenau 2005; Kohrt et al. 2009). However, trabecular density does not (Schoenau 2005). Numerous studies show strong links between long term exercise regimes and high bone mass and density (Huddleston et al. 1980; Lee et al. 2012; Lee et al. 2013). Causal studies highlight relationships but cannot account for other influences in loading, for example if an individual took up running, their skeletons would experience an increase in muscular, kinematic and gravitational loading.

During embryonic development the skeleton develops in a weightless environment, lending itself to the study of muscular contraction and kinematic loads over gravitational loads. It appears muscular loading plays a profound role in determining many aspects of skeletal morphology including proper joint formation (Pitsillides 2006), limb proportion (Drachman and Sokoloff 1966) and the morphology of muscular attachment sites (Blitz et al. 2009). Furthermore intrauterine onset neuromuscular paralysis results in extremely thin cortical bone, often associated with fractures despite the weightless environment (Rodríguez et al. 1988). Implying that loading as a result of muscular forces plays a defining role in the development of skeletal mass and geometry.

In the post-natal skeleton botulinum toxin A (botox) provides a useful experimental agent as a rapidly acting paralytic agent with fully reversible effects, so both the induction of the paralysed muscle and the recovery period can both be studied (Manske et al. 2010; Poliachik et al. 2010). Botox is often injected into a functional group of muscles, to reduce muscular loading, and impairing gait, so altering gravitational loads (Warner et al. 2006). Both muscle and bone showed marked changes, post-paralysis with muscle volume reduced after 2-4 weeks. The same lag time as observed for maximal reduction of tibial trabecular bone volume fraction and tibial cortical area. By the end of the study there was partial recovery of muscular volume and of trabecular bone volume fraction, and full recovery of cortical bone volume. These studies demonstrate that bone recovery precedes muscular recovery, an interesting caveat suggesting that this cortical recovery is independent of the muscle recovery. Alternatively this may reflect that as muscle regains contractile ability there is an increase in gravitational loads imposed by gait.

A further complication with models of neurectomy or botox induced paralysis is that they destroy innervation to the bone as well as the muscle, which may further impact upon the bone response (see section 1.7). Indeed these methods result in bone catabolism which is far more extensive than that seen by disuse alone (Warner et al. 2006; Ellman et al. 2014).

1.8.2 Kinematic loading

Variations in kinematics are difficult to alter without also altering the muscular activity of an animal. Kinematic variation has been brought about by altered exercise regimes in mice which were limited to climbing or running and compared with unexercised controls. The climbers showed a significantly altered morphology in the scapula (Green et al. 2012). However it is not possible to conclude that this is purely a result of kinematic forces as muscular and reaction forces presumably also varied across the regimes.

The most convincing work demonstrating the influence of kinematic loading utilised oscillatory movements applied in the absence of weight bearing, and muscular tone (via anaesthesia). This resulted in significant bone formation (Judex and Rubin 2010) implying that neither muscular input, nor gravitational loads are required for mechanoadaptation.

1.8.3 Gravitational loading

The influence of reactive forces, as a result of gravity appears to have a profound influence on the skeleton. This can be clearly demonstrated by the skeletons of astronauts who, despite daily in-flight training regimes, suffer bone losses of 1.6% bone mineral density per month in weight-bearing regions of the skeleton (LeBlanc et al. 2000). To simulate space-flight tail-suspension models have been used. A period of tail-suspension results in a decrease in cortical and trabecular volume, and bone mineral density. This is a result of an increase in osteocyte apoptosis and bone resorption (Aguirre et al., 2006).

Both ground reaction forces and skeletal kinematics are inherently linked to muscular activity. Therefore it can be argued that all three forms of loading are simply variations in muscular loading. Skeletal muscle activity is therefore of paramount importance when discussing mechanoadaptation of the skeleton.

1.9 Skeletal muscle structure and function

1.9.1 Functions of muscle

Muscle tissue is unique in its ability to generate tensile forces. There are three types of muscle found within the body: smooth muscle, which is found as part of many organs including blood vessels, functioning to constrict vessels and so regulate blood flow. Cardiac muscle forms the bulk of the heart, and its powerful contractions are responsible for the movement of blood around the hearts chambers, and the circulatory system. Finally, skeletal muscle is attached to the skeleton via connective tissues, and utilises its tensile forces to pull against bones to provide the body with strength, and movement.

1.9.2 Gross anatomy of skeletal muscle

At the gross anatomical level skeletal muscles have a fibrous appearance, and can take on a variety of different shapes and sizes. As muscle tissue generates contractile force, it is intuitive that a larger muscle produces more force. Size is not the only determinant of a muscle's force, in fact fibre orientation, or muscle architecture, is the primary indicator of a muscle's functional capacity (Lieber and Ward 2011). The contractile units of skeletal muscle are arranged in series along the length of muscle fibres. Thus the orientation of a fibre determines the axis of force generated (Lieber and Fride´n, 2000).

Across skeletal muscles the range in fibre architecture is almost as varied as the number of muscles themselves, but broad terms can be used to describe common arrangements (Fig.1.12). Concentric rings of muscle fibres can provide a sphincter function, as seen in orbicularis oculi and orbicularis oris, guarding the eye and mouth respectively, this arrangement is known as a circular muscle. In some muscles the fibres are arranged parallel to each other and the axis of force generation, these are termed parallel or strap muscles as seen in sartorius and pronator quadratus. Fibres can be arranged at a single angle relative to the axis of force generation, these are unipennate muscles. Many skeletal muscles have fibres orientated at two or more angles relative to the axis of force generation and these are termed bipennate and multipennate muscles respectively (Lieber and Fride´n, 2000).

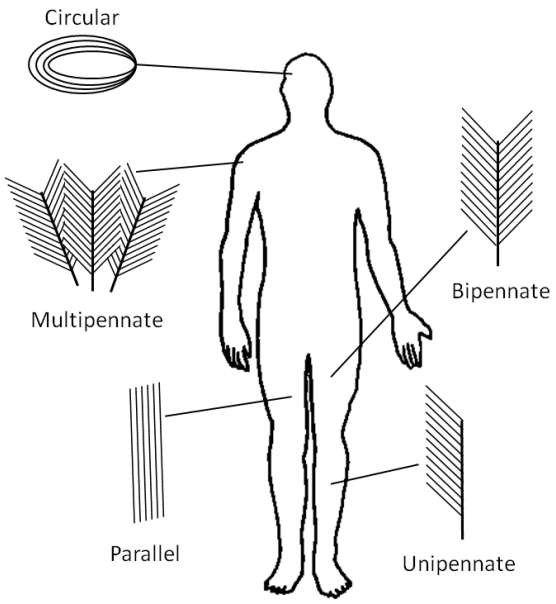

Figure 1.12 Examples of different muscular architectures. Skeletal muscles have large variations in the arrangements of their muscle fibres, some common arrangements being parallel, circular, as found in orbicularis oris, multipennate, as found in deltoid, parallel as found in sartorius, bipennate as found in rectus femoris and unipennate and found in extensor digitorum longus. Figure modified from Marieb and Hoehn (2007).

The pennation angle of a fibre is the angle at which it is orientated with respect to the axis of force generation. Often an increase in pennation angle reflects a decrease in contractile force as a smaller proportion of tensile force is transmitted along the tendon (Lieber and Fride´n, 2000). Despite this, many muscles exhibit highly pennate architectures, as a shift in pennation angle will also influence the length of muscle fibres (Lieber and Ward 2011) and so the excursion and velocity of a muscle (Bodine et al. 1982). A muscle with a highly pennate architecture will have shorter fibres than one of equal size without pennation. Shorter fibres consume proportionally less energy than longer fibres (Biewener and Roberts 2000) and so a greater pennation angle reflects an energy saving. Consequently, the magnitude of force a skeletal muscle can generate is determined by the number, length and arrangement of fibres it is composed of. These parameters can be summarised by the physiological cross-sectional area (PCSA) of a muscle (Powell et al. 1984). PCSA is the cross-sectional area of the muscle fibres in a muscle and has been found to correspond proportionally to the maximum force generation potential of a muscle (Lieber and Fride´n, 2000). The formulation of PCSA is often derived with the formula (Alexander and Vernon 1975);

$$\text{PCSA } (\text{mm}^2) = \frac{\text{muscle mass (g)}}{\text{muscle density (g/mm}^3) \cdot \text{fibre length (mm)}}$$

1.9.3 Microscopic anatomy of skeletal muscle

As with bone, skeletal muscle is a hierarchical tissue (Fig.1.13). At the macroscopic level skeletal muscle appears striated. Each striation is a muscle fascicle, which is a bundle of muscle fibres and is surrounded by a layer of connective tissue, the endomysium (Purslow 2010). Skeletal muscle fibres are among the largest and most complex cells found in vertebrates (Resnicow et al. 2010) and are themselves composed of smaller units termed myofibrils. Myofibrils are long cylindrical multinucleate structures composed of an arrangement of end-to-end contractile units called sarcomeres. Sarcomeres are composed of thin actin filaments and thicker myosin filaments. Thick and thin filaments are arranged in inter-digitating rows, which interact with each other to generate force. The number of sarcomeres present in a myofibril is dependent upon the length and thickness of the fibre, which is why these parameters play such a crucial role in force production (Lieber 2002). Functionally skeletal muscle is composed of motor units. Each motor unit consists of

a motor nerve, and a number of muscle fibres. Nerves communicate with fibres via motor end-plates, or neuromuscular junctions (NMJ) (Schiaffino and Reggiani 2011). This functional grouping of fibres allows for selective recruitment of motor units, allowing a muscle a wide range of contractile states, not simply on or off.

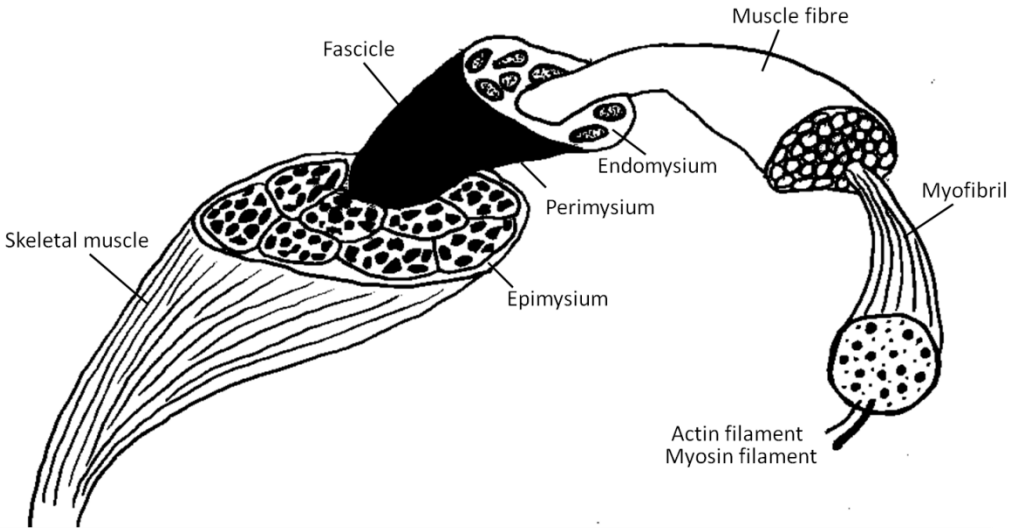

Figure 1.13 Diagrammatic representation of the hierarchical structure of skeletal muscle. Skeletal muscle is composed of a vast number of muscle fascicles bounded by connective tissue. Each fascicle is made up of a number of muscle fibres, which themselves are composed of myofibrils. Each myofibril is composed of the proteins actin and myosin. Figure modified from Whiting and Rugg (2006).

1.10 Force production and transmission

1.10.1 Skeletal muscle force production

The fundamental molecules that are responsible for skeletal contraction are actin and myosin. Myosin is the most abundant molecule in striated muscle (Baldwin and Haddad 2001) and exists as a complex molecule, composed of two myosin heavy chains (MHC) and four myosin light chains (MLC). Each MHC has distinct tail and globular head regions (Fig.1.14). The globular head contains the binding site for interaction with actin as well as the ATP binding and cleavage site. Actin molecules form long helical strands, which myosin binds to (Spudich et al. 1972).

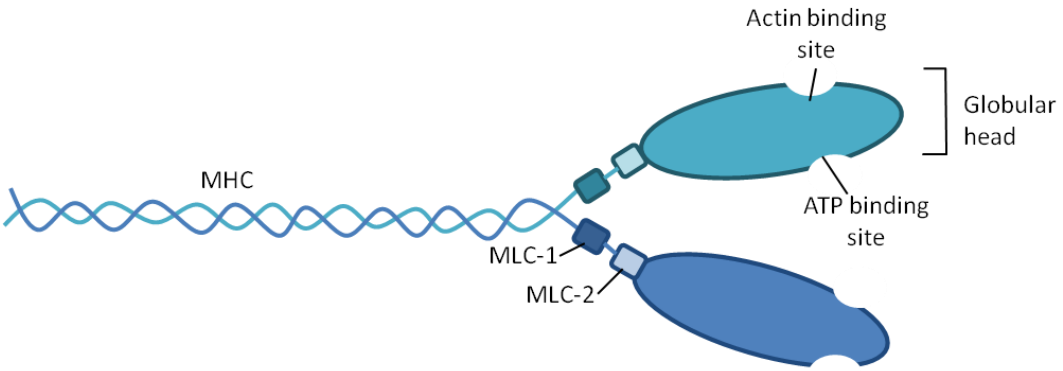

Figure 1.14 Schematic representation of a myosin molecule. Myosin molecules are composed of coiled Myosin heavy chains (MHC), the Myosin light chains (MLC) 1 and 2, attached to the globular head which contains Actin and ATP binding sites. Figure modified from Vicente-Manzanares et al (2009).

At the microscopic level muscular contraction begins with the generation of an action potential at the neuromuscular junction, resulting in a release of Ca^{2+} from the sarcoplasmic reticulum to act upon the actin and myosin filaments (Westerblad et al. 2010). The increase in calcium results in activation of the actomyosin cross-bridge cycle. The cross-bridge cycle involes actin and myosin interactions which result in myosin being propelled along the actin filament. This interaction requires ATP fro energy (Cooke 1997). With this happening in a co-ordinated manner across the sarcomeres in series, there is a resultant shortening of the muscle.

Force production is dependent upon the length of the muscle. At the optimal length actin-myosin interactions are at their maximal, producing the largest force possible. As sarcomere length increases there is a decreasing number of myosin-actin interactions and so the force generated will decrease. At shorter than optimum sarcomere lengths actin begins to interdigitate with myosin and other actin filaments from the opposite side of the sarcomere and force decreases (Lieber and Ward 2011).

1.10.2 Connective tissue force transduction

For effective force transmission individual muscle fibres cannot act alone, but require a material to integrate and coordinate their actions. This is achieved by the presence of a three-dimensional network of connective tissue surrounding the

muscles and extending beyond the muscle to attach to the skeleton. Generally speaking these layers of connective tissue are composed of collagen fibres in a proteoglycan matrix composed of heparin sulfate proteoglycans, including decorin (Brandan and Inestrosa, 1987; Velleman, 1999).

Every muscle fibre is surrounded by a layer of endomysium. Groups of muscle fibres are grouped together in to fascicles which are surrounded by a layer of endomysium (Fig.1.12). The endomysium is an effective mechanism for the transmission of contractile forces between fibres and within fascicles. Each muscle fascicle is surrounded by connective tissue termed perimysium (Sharafi and Blemker 2010). Muscle fascicles span the length of the muscle and along with their perimysium are surrounded by a final layer of connective tissue, the epimysium. Muscle fibres interdigitate with tendon to form the myotendinous junction. Not all fibres within a muscle will be involved in this joint, and so the extracellular matrix plays an important role in force transmission (Trotter and Purslow, 1992).

As with other tissues in the musculoskeletal system, connective tissue is continually remodelled so it is mechanically adapted for its function (Kjaer and Magnusson 2008). In general, mechanical loading results in an increase in collagen production and degradation, resulting in an increase in turnover (Kjaer and Magnusson 2008). Exactly how connective tissue senses mechanical stimuli is not clear. In developing muscle there is a close coupling of myogenesis and inter-muscular extra cellular matrix development, but to what extent this continues in mature muscle is not known. It seems likely, given their functional relationship that a coordinated response is maintained (Kjaer and Magnusson 2008).

The connective tissue providing the crucial mechanical link of the contractile skeletal muscle to the rigid skeleton is tendon. Tendon is composed of water and collagen fibrils. The collagen fibrils are arranged parallel to each other and arranged into bundles, this arrangement increases functionality during damage, as damage can be confined to a small number of bundles, without affecting the other bundles (Kjaer 2004). The tensile material properties of a tendon are non-linear, with a stress-strain curve best described as sigmoidal (Evans and Barbenel 1975). The material properties of tendon play a defining role in the extent of muscular force which is transmitted, or absorbed. For example, a stiff tendon will transmit a large proportion of force, absorbing very little. Conversely, a compliant tendon will absorb a large proportion of the force, and transmit very little. As with bone, tendon is able to adapt both its material properties, and its structure in response to loading.

The material properties of tendons can be altered microscopically by variation in the number of cross-links between collagen fibrils, with more cross-links resulting in a stiffer tendon (Reddy 2004). The number of cross-links has been found to increase following treadmill exercise in rats despite no significant increases in collagen content (Carroll et al. 2012). Whilst a tendon with increased stiffness enhances the rate of force transmission to bone, tendons do not simply act to transmit force. Their elastic nature enables them to store elastic energy, and act as springs. The incorporation of a spring into a muscle can reduce energetic demands during locomotion (Alexander 2003). The detrimental effects of connective tissue stiffening can be demonstrated in ageing in which increased cross-linking of collagen fibrils results in stiffer tendons (Kjaer 2004). This stiffening of tendons is likely to enhance the tendons susceptibility to rupture (Plate et al. 2013). The connective tissues of skeletal muscle also increase in thickness in ageing muscle, which disrupts force transmission through a muscle, reducing the force transmitted to the skeleton (Zhang and Gao 2014).

At the macroscopic level long-term loading of tendons appears to increase cross-sectional area, as tendons in athletes have been found to show significantly larger cross-sectional area than non-athletes (Rosager et al. 2002). Short-term exercise regimes (in the order of magnitude of months) on the other hand, rarely show significant changes in cross-sectional area (Arampatzis et al. 2010; Hansen et al. 2003; Urlando and Hawkins 2007). This may be in part due to the fact that tendons, as with bones, show regional responses to loading (Magnusson and Kjaer 2003). If all other parameters remain constant, an increase in cross-sectional area of a tendon increases its stiffness. This structural adaptation enhances the transmission of higher muscular forces by increasing the rate of force transmission, and the control over the insertion site (Biewener and Roberts 2000) for the same amount of energy. In animal studies it has been possible to examine not just the gross anatomical cross-sectional area of tendons, but the area of individual fibrils within the tendon. In one study it was found that fibrils initially increased in size in response to loading, with a subsequent decrease in size, followed by a second increase in fibril size. The sudden drop in fibril cross-sectional area was attributed to large fibrils splitting to produce smaller fibrils (Michna 1984).

1.11 Muscular Plasticity

1.11.1 Classification of muscle fibre types

Not all skeletal muscle is equal in its functional capacity. An endurance athlete's muscles are less susceptible to fatigue than those of an untrained individual. This is achieved largely by training of the muscle, suggesting at a transformative potential. The first functional classifications of muscle was made based on colour differences, with muscles grouped into pale and fast or dark and slow (Ranvier 1873). These differences in colouration arise from physiological differences within the fibres. Darker muscles have denser capillary networks and higher myoglobin content than pale muscles (Salmons 2009). The functional consequence of this is a richer blood supply, allowing for oxidative metabolism. Dark fibres can therefore sustain contraction. The speed at which a muscle contracts is linked with the force it can generate;

Power = force x shortening velocity (Ranvier 1874)

Assuming the force generation is the same, slowly contracting fibres generate less power than rapidly contracting fibres. Dark muscles are largely composed of slow-twitch, oxidative fibres. Slow-twitch fibres are found in abundance within lower-limb muscles used for postural activity (Schiaffino and Reggiani 2011). Conversely pale muscle does not have the blood supply or mitochondria to sustain contraction, and generates fast, forceful contractions that are short lived (Salmons 2009). Fast-twitch fibres are found in abundance in muscles of the upper limb (Schiaffino and Reggiani 2011).

The differences in contractile and metabolic properties between fast and slow fibre types are summarised in Table 1.1, and arise as a consequence of the isoform of myosin heavy chain (MHC) present within the fibre. Adult mammalian skeletal muscle has four distinct MHC classifications; type 1, type 2a, type 2x and type 2b (Bottinelli et al. 1994). Type 1 is the slowest MHC isoform, with the highest oxidative capacity, this specialises it for prolonged low-intensity activity. Type 2x or 2b are the fastest isoforms specialised for short-burst activity (Westerblad et al. 2010). Type 2a fibres are an intermediate fibre type which are fast-contracting (but not as fast as 2b or 2x), but are also fatigue-resistant (Salmons 2009).

Table 1.1 Differences between fast and slow twitch muscle fibres, as stated in Salmons (2009).

	Fast-twitch	Slow-twitch
Mitochondria	Few	Many
Myoglobin	Low	High
Capillary network	Sparse	Well developed
Major energy source	Anerobic glycolysis	Oxidative pathways

1.11.2 Neural component of muscular plasticity

Mammalian skeletal muscles are rarely homogenous for fibre type, with a mixture of fibre types co-existing within a muscle. The relative proportions of fibres vary dependent upon the muscles functional requirements. This heterogeneity allows for diversity in contraction, with a single muscle able to function for a whole range of activities, from precision movements to forceful contractions (Schiaffino and Reggiani 2011). Diversity in fibre type and selective recruitment of muscle fibres act as a safeguard against muscle fatigue. Each motor unit is associated with fibres of one type only. Small motor units are associated with slow muscle fibres, and large motor units with fast fibres. As a muscle begins to contract, the smallest, slow motor units are activated. As contraction continues sequentially larger motor units are recruited, which innervate faster fibres. The largest motor units, innervating the fastest, most powerful glycolytic fibres are recruited only when a muscle is contracting at very high forces, for example in sprinting (Henneman et al. 1965). This organisation allows muscles to engage in a wide array of contractions whilst limiting the likelihood of failure due to muscle fatigue.

The proportion of differing fibre types varies substantially between species and anatomical site (Schiaffino and Reggiani 2011). However, even in the same site of the same animal these proportions can be completely transformed with targeted training or disuse. Endurance training induces a significant increase in the mitochondrial content (Seppet et al. 2013), and capillary density within skeletal muscle (Andersen and Henriksson 1977). This improves the aerobic capacity of the muscle, allowing for sustained periods of work (Seppet et al. 2013). Conversely when a muscle is subject to a period of disuse (Booth and Kelso 1973) or denervation (Wicks and Hood 1991) the muscle responds by decreasing the mitochondrial content of its fibres. The benefits of endurance training can also be

undone by overtraining of muscle, resulting in muscle damage and suppression of oxidative energy metabolism (Seppet et al. 2013). Resistance training increases muscle mass, but as this requires fast, high power contraction the fibres are predominantly type 2b or 2x, so there is often not a net increase in mitochondrial content (LeBrasseur et al. 2010).

Muscular activity is controlled by neural innervation, and the rate and frequency of motor nerves fire is a major governing force behind fibre characteristics (Buller et al. 1960; Salmons and Sreter 1976). Slow fibres are innervated by low frequency impulses which are active for long periods of time, whilst fast fibres receive brief periods of high-frequency impulses (Hennig and Lomo 1985). Transformation of the impulses a muscle receives can therefore transform the muscle fibre type (Jarvis et al, 1996). Motor nerves interact with the muscle fibre via the neuromuscular junction (NMJ). The NMJ is not a rigid structure, but shows considerable plasticity, the extent of which varies across muscles (Wigston 1989). In ageing muscle there is a change in NMJ morphology and neurotransmitter release which results in a selective denervation of fast fibres, and reinnervation of slow fibres. Leading to death of the fast fibre population, and substantially reducing muscle force (Jang and Van Remmen 2011). Furthermore, age-related NMJ degeneration can be prevented with exercise (Nishimune et al. 2012). Taken together this suggests that NMJ competency, as well as neurotransmitter release as a result of activation play a pivotal role in the determination of fibre type population.

1.11.3 Mechanical component of muscular plasticity

As well as neural influences, skeletal muscle has been found to respond to decreased and increased mechanical stimuli. In 1978 Williams and Goldspink conducted a series of immobilization experiments in mice. The mice had their ankles immobilized in series of positions for 3 weeks. This resulted in soleus adapting its force-tension properties, via the number of sarcomeres present, so that maximal isometric tension was achieved at the angle of immobilization (Williams and Goldspink 1978). This sensation has also been observed in women who frequently wear high-heels. The habitual high-heel wearers had significantly shorter fascicles within gastrocnemius and stiffer Achilles tendons than those that did not (Csapo et al. 2010).

Increased mechanical stimuli can also affect muscles with passive stretching resulting in muscle growth (Goldspink et al. 1995). This mechanism is presumably utilised during growth, as muscles are gradually stretched as a result of skeletal

growth. Unlike the mystery which surrounds mechanotransduction in bones skeletal muscle contains a vast sensory network of muscle spindle cells which are embedded within sarcomeres (Bewick and Banks 2014). In addition many mechanically regulated transcriptional links are characterised within skeletal muscle, with the differentiated sarcomere acting as a complex feedback device for active muscle remodelling (Braun and Gautel 2011).

1.12 Animal models for skeletal mechanoadaptation

The study of the relationship which exists between bone and its mechanical environment can be conducted using cellular in vitro models, but this does not always accurately represent the cells in situ environment, and limits investigation to the cellular level. It is therefore important to have experimental models, in which loading can be carefully controlled, and the resultant bone response measured. Much of the early work into bone mechanoadaptation was carried out by surgical methods in sheep and turkeys (Rubin and Lanyon 1984; Lanyon and Rubin 1984). Clearly surgical interventions are more straightforward on larger animals. However the cost of housing large animals is far larger than for rodents. Increasingly rats and mice are becoming the animals of choice for skeletal research, largely due to their low cost to acquire and maintain, rapid growth and reproduction rates, and the extensive genetic knockouts available. One genetic knock-out which has been used in bone-muscle relationships is the myostatin deficient mouse, myostatin is a negative regulator of muscle development, and the myostatin (GDF-8) deficient mouse has double the muscle mass of wild type mice. The skeletons of myostain-deficient mice show increased bone mineral density, and trabecular area (Elkasrawy and Hamrick 2010).

Despite the established relationship between muscle and bone (see section 1.8) previous work investigating mechanoadaptation of the skeleton has largely avoided the use of muscular contraction. The earliest investigations into bone adaptation often utilised drastic surgical methods such as, the removal of one in a set of paired bones, to increase loads upon the other (Lanyon et al. 1982). This was found to result in substantial bone growth. However surgical interference with the periosteum has been found to cause osteogenesis, and without the ability to perform a sham osteotomy it is not possible to conclude that bone growth arises exclusively from mechanical loads (Churches et al. 1980). The alternative technique of pin-loading has also been used extensively (Lanyon and Rubin 1984). In this model metal pins

are surgically inserted in to long bones. Under anaesthesia the pins could then be pulled together statically or dynamically by engaging the pins in a loading apparatus which pulled the pins together creating a compressive load. This technique also showed dramatic bone growth under dynamic loading conditions (Lanyon and Rubin 1984), with the advantage of being able to be run in conjunction with sham experiments, in which pins are inserted but not loaded.

Whilst sham experiments provide a level of certainty in results, using non-surgical techniques is often preferential in terms of animal welfare, and can create a more easily reproducible loading condition. A number of such methods have been developed. The main loading models can be broadly divided into bending, axial compression and oscillation. Bending methods include, three-point bending (Fig.1.15a) (Sakai et al. 2011), four-point bending (Turner et al. 1994), and cantilever bending (Gross et al. 2002). Axial compression comprises of the distal and proximal ends of a bone constrained in cups, whilst a compressive force is transmitted between the two (Fig.1.15b) (Poulet et al. 2011; Torrance et al. 1994). Axial compression is often regarded as the gold-standard for studying mechanoadaptation in rodents, as it mimics physiological loading through the joints (McBride and Silva 2012). Furthermore mechanical loads can be easily controlled and manipulated, and the contra-lateral limb can be used as a control. All of these models require anesthesia and do not allow the investigation of muscular forces upon bone. Placing rodents upon low-magnitude, high-frequency oscillating platforms has been found to provide robust osteogenic responses (Rubin et al. 2001) however the forces being applied in this model are not clear, and are substantially complicated by muscular interaction (Judex and Rubin 2010).

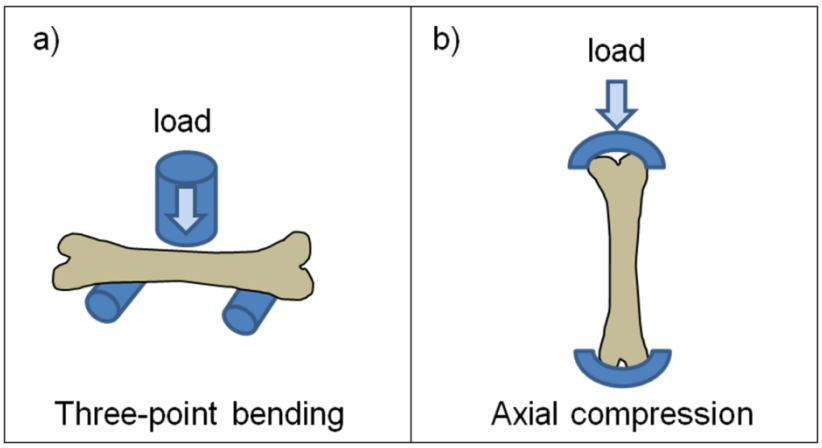

Figure 1.15 Diagrammatic representations of established bone loading techniques, a) diagram of 3-point bending, in which a long bone of an anesthetised animal is secured longitudinally between three points. Loads are applied by the superior point, figure modified from Sakai et al (2011). b) a diagram of axial compression, in which the an anesthetised animal has their long bone secured between an upper and lower cup, and forces are applied axially, figure modified from Poulet et al (2011).

Mechanoadaptation occurs in response to decreased as well as increased loading. Two contrasting forms of unloading frequently investigated are, loss of muscular contraction, as seen in spinal cord injury, and removal of reaction forces, as seen in space flight and bed rest. Spinal cord injury is very simple to bring about in an experimental animal, by dennervation of muscles (Tuukkanen et al. 1991). Alternatively paralysis can be induced by the injection of botulinum toxin A (botox) (Manske et al. 2010; Poliachik et al. 2010) (see section 1.8.1). Tail or hindlimb suspension is a widely used technique to study the effect of unloading upon the rodent skeleton (Morey-Holton et al. 2005). In this model a rodent has its tail suspended to the top of its cage, so its hindlimbs do not touch the floor of its cage, removing ground reaction forces. The forelimbs remain fully weight bearing and support locomotion. More recently a partial weight suspension model has been developed (Wagner et al. 2010). This model allows quadrupedal suspension of the mouse, and so preserves normal gait characteristics, achieving a model closer to spaceflight conditions than hindlimb suspension. So whilst methods exist for studying the removal of muscular forces there is still little work looking at the controlled application of muscular forces upon the skeletal system.

The most popular animals used for both loading and unloading experiments are rats and mice. Therefore experimental outcomes in rats and mice can be reviewed in the context of a vast body of previous work.

1.13 Anatomical Overview of the Rodent Hindlimb

1.13.1 Hindlimb Skeleton

The rat is an animal commonly used for bone research (Lelovas et al. 2008) whilst there is very limited literature on the anatomy of the rodent hindlimb, it is clear that it differs from human anatomy in various fundamental ways. Anatomically, the skeleton of the rat hindlimb is comprised of the same major bones as those found in the human; the femur, patella, tibia, fibula, tarsal bones, metatarsals and phalanges. The arrangement of these bones is remarkably different with the hindlimb being held in complete flexion at both the hip and knee joints (Fig.1.16). Another distinction between the skeleton of the rat and the human is that in the human the tibia and the fibula are distinct bones, lying alongside each other and articulating at the proximal and distal tibiofibular joints. In the rat the fibula articulates proximally with the tibia and distally the bones fuse for a short distance (Fig.1.17). Distally the fibular and tibia are distinct bones again (Greene 1963). Rats also show a large number of sesamoid bones found consistently around these joints, in particular the knee, which in additon to the patella, has the lateral and medial fabellae, which are associated with the heads of triceps surae (Fig.1.17) (Greene 1963).

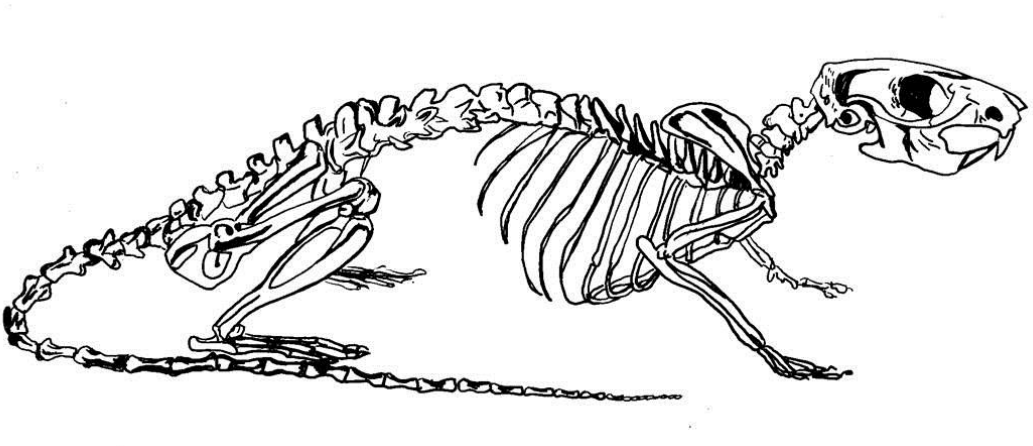

Figure 1.16 A diagram of a rat skeleton. Rat's hindlimb's differ from humans biomechanically as the hindlimb is held in complete flexion at the hip and knee joints. Figure modified from Greene (1963).

Figure 1.17 A 3D reconstruction of a mouse hindlimb skeleton. Showing the gross anatomy of the skeleton of the mouse leg, including the knee and ankle joints. The tibia and fibula are fused distally.

Anterior to the knee joint are two small bones (Fig.1.17). These structures are ossified menisci, or ossicles, which are fibrocartilage structures in the human knee joint. Ossicles in the rat knee joint were first described by Pederson as a disc with a core of bone and marrow, which is surrounded by calcified cartilage (Pedersen 1949). These structures are consistently in adult rodents, developing at around 6 weeks of age from a cartilage precursor (Pedersen 1949). It has been suggested that they form in menisci where the angle between the articulating surfaces exceeds 45° in order to reduce pressure (Barnett 1954).

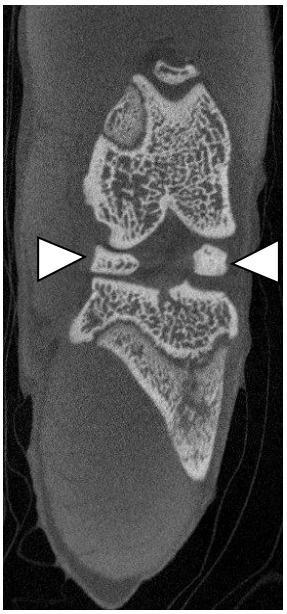

Figure 1.18 A microCT image of a murine knee joint. Many rodents, including rats and mice have ossified menisci in their knee joints, these are highlighted with white arrowheads.

Rat and human bones differ not only morphologically, but also biologically. Most mammals experience closure of growth plates and subsequent cessation of growth around sexual maturity. Sexually mature animals are therefore assumed to have reached their peak in longitudinal length of long bones; this is not the case in the rat. Rats reach sexual maturity at 7-8 weeks of age (Lee et al. 1975). However, growth plates of the tibia and fibula were found to be open and actively growing long past this age (Trudel et al. 2001).

Despite the anatomical distinction of an open growth plate bony bridges have been found to form across the plate, leading to a functional closure of the plate at 8 months in males, and 10 months in females Despite cartilage still being present, the distinct zones of cartilage were not present after 6 months (Martin et al. 2003). The failure of growth plate closure distinguishes the rat from most studied animals, including mice, which display tibia and femur growth plate closure after around 5 months (Kilborn et al. 2002).

The lack of epiphyseal growth plate closure has been linked to the lack of secondary bone turnover, with the theory that as a growth plate closes, and longitudinal growth ceases then secondary osteons develop to maintain bone turnover. Therefore as

rats growth plates do not close, they have little need for secondary osteons (Jowsey 1966).

1.13.2 Muscular system

The rat and mouse hindlimb is held in a dramatically different position to that of the human. Consequently the musculature of the thigh differs from that of the human across a number of muscles. The most striking example being that of Biceps Femoris, in humans this is one of the hamstring muscles found on the posterior aspect of the thigh. In rats and mice it is a very large muscle which originates at the sciatic tuberosity, and insert into the distal end of the femur, and along the proximal 2/3rds of the tibia (Greene 1963). Also the gluteus maximus which is enlarged in humans due to bipedalism is far smaller and referred to instead as gluteus superficialis in rodents (Fig, 1.19, 1.20). The muscles of the leg are fairly similar in the rat and the human, with their tendons taking similar paths (Fig. 1.21).

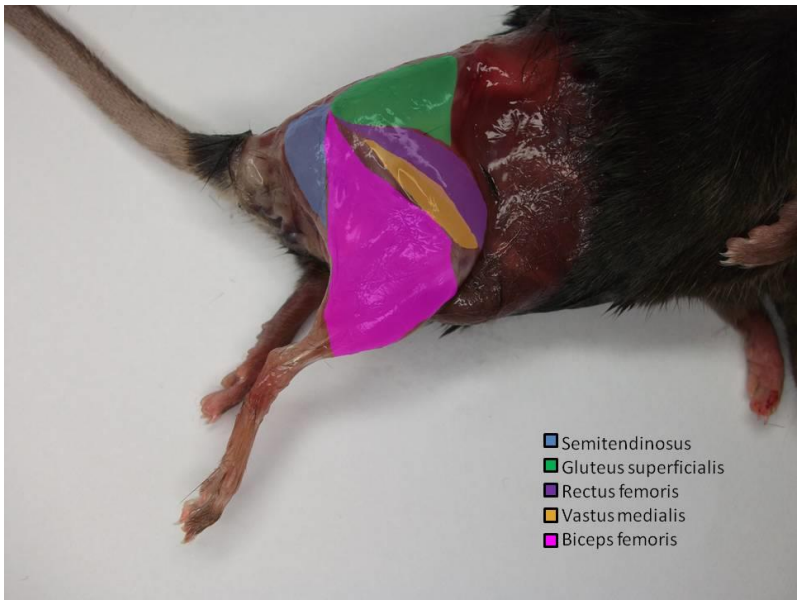

Figure 1.19 A dissection of a murine hindlimb showing superficial musculature. The anatomy of hindlimb musculature is markedly different in rodents and humans, with the biceps femoris being a far larger muscle in rodents, with an extensive attachment along the tibia.

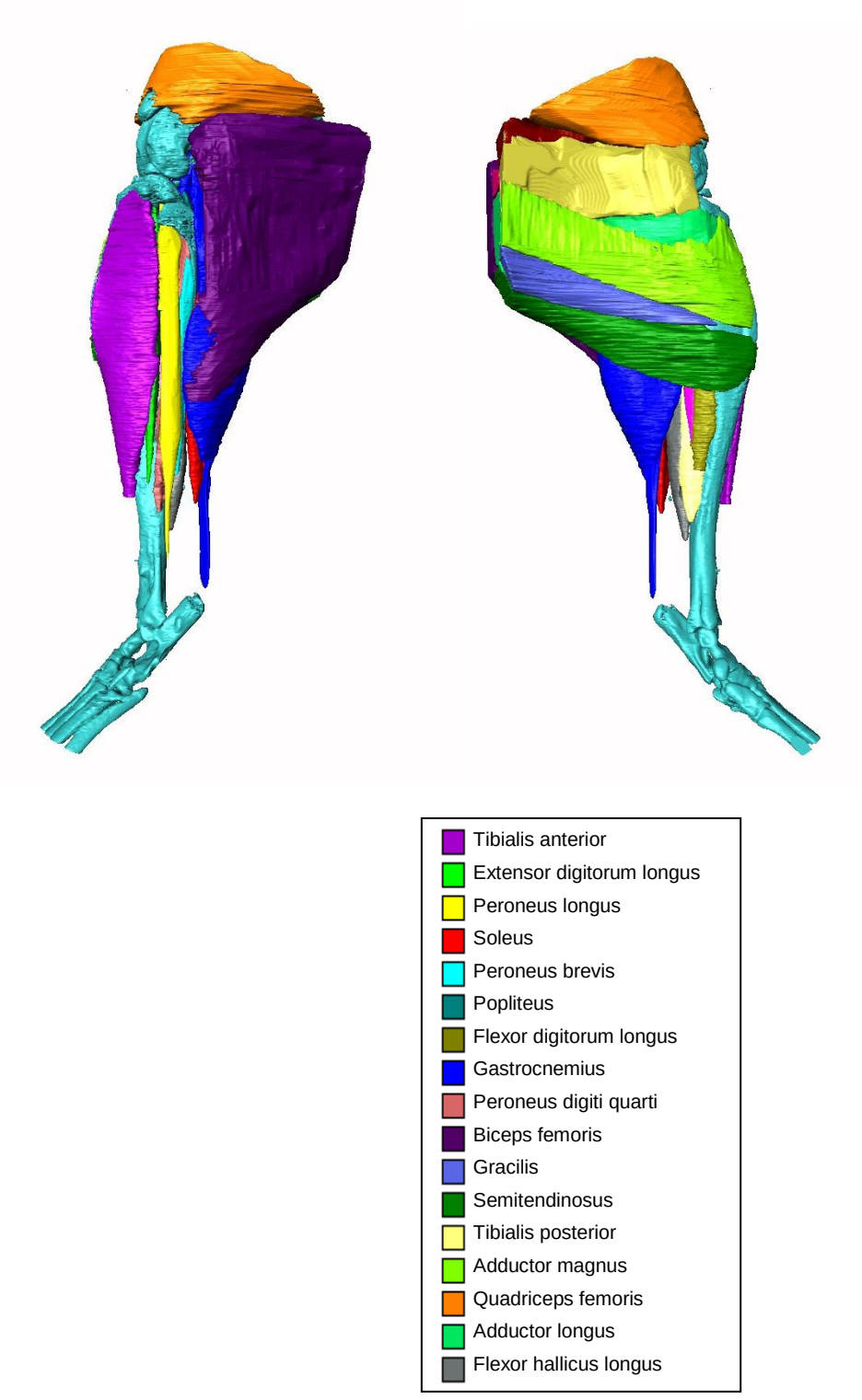

Figure 1.20 A 3D reconstruction of the muscles of a mouse hindlimb. Iodine-enhanced microCT data were used to identify and segment the muscles of a mouse hindlimb in situ with the skeleton of the hindlimb.

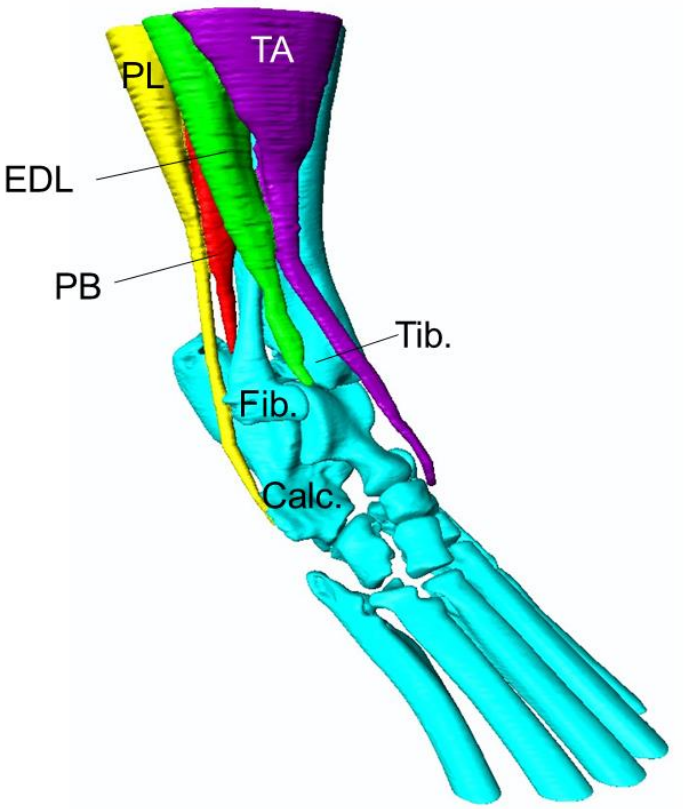

Figure 1.21 A 3D reconstruction of the muscles and tendons transversing the rat ankle joint. a) a dissection of the rat hindlimb, the skin and superficial fascia has been removed to reveal the tendons transversing the ankle joint. b) Iodine-enhanced microCT data were used to create a 3D reconstruction of the muscles and tendons transversing the rat ankle joint. TA indicates tibilis anterior, EDL, extensor digitorum longus, PL, Peroneous longus, PB, Peroneous brevis, Tib., tibia, Fib., fibular, Calc., calcaneous.

Small rodent skeletal muscles are largely composed of fast-twitch glycolytic fibres (Armstrong and Phelps 1984) with high motor unit firing frequencies (Hennig and Lomo 1985). Rat muscles also have a different isoform of myosin which is rarely found in human tissue, type 2b (Schiaffino and Reggiani 2011). So it should be borne in mind that muscle physiology results are not necessarily directly transferrable between rodents and humans.

1.14 Summary

The skeleton is a highly dynamic structure, which adapts its geometry to suit its mechanical environment. Despite a long continued history of research into skeletal

mechanoadaptation the exact stimulus, its mechanism of sensation and transduction into a biological response remain unknown. However, the tight correlation of bone activity with strain parameters have led to the consensus that strain is the driving force behind bone adaptation**.** The skeleton experiences a complex strain environment and so most previous work has simplified this load by using external devices. The morphological response of bones to differing mechanical environments, and subsequent strain distribution and magnitude can therefore provide considerable insight into the biomechanical influences which are integral to skeletal mechanoadaptation.

Muscular contraction applies the largest and most frequent forces upon the skeleton. Muscle also displays a large amount of plasticity throughout life to optimise its structure and contractile properties to its functional demands. In vivo, skeletal responses to increased loading are therefore likely to be part of an integrated musculoskeletal response. Despite the importance of muscular contraction in defining a bone's mechanical environment, it is largely avoided as a means of increasing mechanical loads experimentally. The complex nature of the forces arising from increased muscular activity, and lack of experimental control has led instead to the widespread use of external loading devices. This thesis will therefore utilise controlled muscular contraction to impose a mechanical stimulus which is therefore closer to physiological loading than current methods. To impose muscular contraction, by its definition requires that the stimulus will be supra-physiological in terms of the pattern of loading, but physiological in the magnitude of forces it applies. Given the importance of muscular loading in determining bone mass and distribution, it is expected that a prolonged period of controlled muscular contraction will provoke a significant bone response.

In order to address this hypothesis this thesis will take the form of a methodological review followed by a series of papers. The first paper addresses a methodological limitation to inform the following work. The second paper exploits the latest advances in imaging and computational modelling technology to correlate muscular and skeletal transformation at macro and microscopic scales. Finally the biomechanical performance and distribution of strain within the adapted and control skeletons are assessed to shed light upon the relationship between musculoskeletal form and function.

The overarching aims of this thesis are to:

- Implement a controlled muscular loading regime upon a rodent limb.

- Devise a methodology to measure and quantify the macroscopic and microscopic adaption within the muscle producing the load.
- Pinpoint the regions of bone which are responding to the muscle contraction.
- Devise a methodology to measure and quantify the macroscopic and microscopic adaption within the bone most directly exposed to the increased loading.
- Asses the biomechanical performance of control and loaded bones to the controlled muscular loading.

Chapter 2: Review of methodology

Chapter 2

To investigate the relationship of skeletal form and function many different methods have been developed (see section 1.12). However these do not address the large role which muscular forces play in defining skeletal morphology. To address this, controlled muscular contraction can be used for skeletal loading. The manner in which musculoskeletal form adapts to varying functional demands may be evaluated by a multitude of different criteria. Here methods for increasing muscular contraction as well as analysing and quantifying morphological and biomechanical differences in bone and muscle are reviewed.

2.1 Controlled muscle contraction

The simplest way to increase muscular activity is with an exercise regime. The osteogenic potential of running (Hamann et al. 2012), jumping (Umemura et al. 1997), and swimming (Buie and Boyd 2010) have been tested under controlled conditions. These regimes often result in mild osteogenic responses which are highly variable between individuals. This is further complicated as exercise induces systemic effects (Radak et al. 2008; Stewart et al. 2007) which extend beyond the imposition of mechanical forces. The mechanical forces created as a result of exercise are complex, and subsequently it is difficult to draw clear conclusions upon the form-function relationship.

Targeted contraction of a single muscle, or group of muscles would substantially clarify the forces being applied to a bone. During voluntary muscular contraction, the motor cortex initiates neural impulses which pass along a series of motor nerves to innervate the target muscle, resulting in contraction. Neural tissue can be artificially activated in a number of ways. Recently, optogenetics has emerged as a promising new method for the in vivo control of motor activity (Llewellyn et al. 2010). Optogenetics involves the insertion of a photo-sensitive ion channels and pumps into a target neuron, either by genetic modification of the animal before birth (Liske et al. 2013) or post-natally by the insertion of a genetically modified virus (Towne et al. 2013). The photosensitive proteins are then expressed in neurons, and neuronal activity can be controlled with flashes of light. All neurons show similar levels of photosensitive protein expression. Smaller neuronal axons have lower threshold activation than larger axons and so are activated at lower levels of light, mimicking the natural recruitment of motor units in muscle (Llewellyn et al. 2010).

A graded muscle response is useful clinically, as it reduces possible muscle damage. However the forces generated by a graded contraction are not maximal, and so the magnitude of the generated force cannot be simply estimated by calculation of the PCSA (section 1.10.2). Furthermore, as this is an emerging technique, a lengthy process of optimisation would be required to set up a model suitable for the purposes of this study. Therefore, whilst optogenetics present an exciting future development, it is not currently developed to the stage where it can provide a simple method of loading bone by muscular contraction.

Muscular contraction can also be controlled by the application of a localised electrical current across the muscle belly or its motor nerve. This has been utilised extensively in basic neuromuscular research as well as for enhancing athletic ability (Babault et al. 2007) and therapeutically in paralysed muscles (Gerrits et al. 2002).

Stimulation of the motor nerve at a low frequency results in the flow of ions through the neuronal membrane. If the resultant change in electrical potential across the neuronal membrane is sufficient, an action potential is induced which propagates along the nerve (Tsui et al. 2007). Electrical stimulation applied across a motor nerve acts across all neurons within the nerve, overriding the natural sequence of motor unit recruitment. Therefore all neuromuscular junctions release neurotransmitter, resulting in maximal muscle contraction (Fig.2.1). If the frequency of stimulation increases (above 200Hz) then action potential propagation is instead blocked, which can be used in sensory neurons, as pain treatment (Tsui et al. 2007).

The application of an electrical current across a muscle belly can be applied transcutaneously and so is less invasive than stimulating a motor nerve. Transcutaneous stimulation results in depolarisation of motor end plates with which the current comes into contact. This results in contraction of peripheral parts of the muscle (Bergquist et al. 2011) resulting in a partial muscle contraction (Fig.2.1). Stimulation of the motor nerve is clearly an invasive procedure, but can result in maximal muscular contraction, allowing force to be estimated by PCSA calculation.

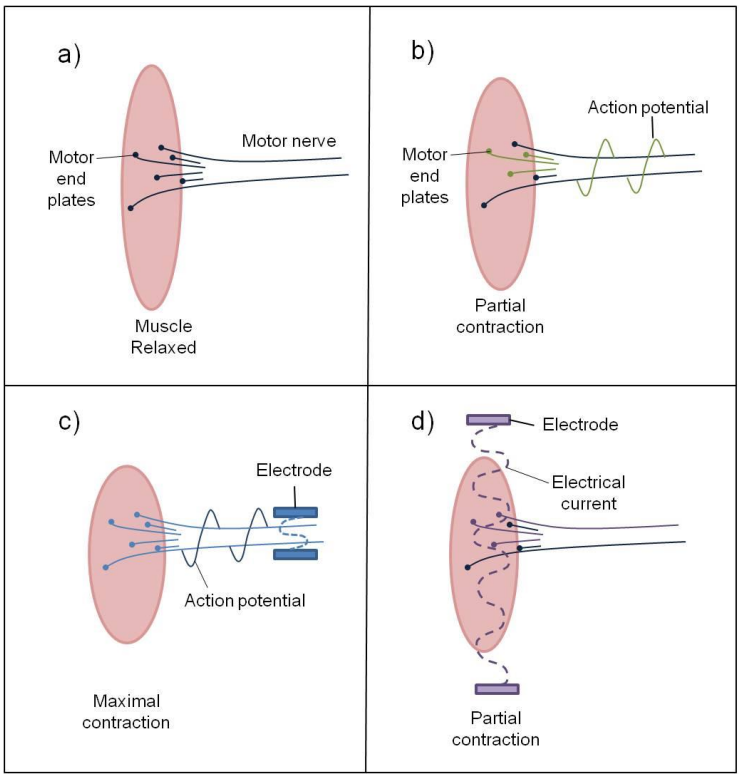

Figure 2.1. Diagram of different methods of electrical muscle stimulation. a) Skeletal muscle is innervated by motor nerves, which interact with the muscle via motor end plates. b) During natural contraction action potentials are initiated in the fibres of the motor nerve according to the recruitment principle (see section 1.11.2), resulting in muscle contraction. c) The application of an electrical current to the motor nerve results in depolarisation of the entire nerve and all motor units are recruited, resulting in maximal contraction. d) The application of a current across a muscle belly stimulates the motor end plates to release neurotransmitters, and result in recruitment of only the motor end plates which come into contact with the current.

The development of a fully implantable battery powered miniature electrical stimulators (Salmons, 1967) allowed for a continued application of electrical stimuli for weeks or months following surgery, with no further procedures required. Therefore, for a lengthy loading period implantable stimulators present a less invasive loading method than the repeated anesthetising and loading of bones by an external loading device (section 1.12). Implantable stimulators have been used extensively for studying muscular plasticity (Jarvis et al., 1996, Jarvis, 1993, Eisenberg et al., 1984, Brown et al., 1989). Implants consist of a power source, controlling device and electrodes to apply the current. Many investigators have attached the electrodes to a cuff, which is then wrapped around the nerve. The

electrical impulses can then be transmitted across it. This procedure has been associated with mechanical damage to the nerve (Kim et al. 1983), and may complicate explant surgery. Alternatively electrodes can be sutured either side of a motor nerve, and the electrical current is passed between them.

The possibility that the application of an electrical current may cause damage is a key issue with stimulator technology. As selective recruitment of motor fibres is overridden, some fibres are working under conditions which they are unaccustomed, leading to fatigue. This has raised the question of whether the reported transformation of fibres is a result of muscle damage (Maier et al. 1986)? However, studies have shown that it is possible to transform a muscle composed almost entirely of fast-twitch fibres into slow-twitch fibres (Sutherland et al. 1998). If this were due to fast-fibre degeneration over 90% of the muscle fibres would be lost, this would be clearly apparent at both the macroscopic and microscopic levels, which it is not. A study focussed on quantifying damage found a peak of 3.5% degenerating fibres, and even lower levels for intermittent stimulation (Lexell et al. 1992). Therefore, fibre degeneration is not sufficient to explain the extensive shift in fibre type observed. Furthermore, studies have demonstrated that fibres switch their myosin expression in response to muscle simulation (Rubinstein 1978). Cessation of stimulation results in muscle restoring their original characteristics (Eisenberg et al. 1984; Brown et al. 1989) which would require extensive neuronal repair if the shift in fibre type was a result of damage.

The frequency at which stimulation is delivered determines the muscular phenotype. Low-frequency continuous stimulation has been found to result in decreased muscle volume, maximum isometric tension and power, along with a significant increase in the proportion of slow-twitch muscle fibres (Sutherland et al. 1998). Interestingly skeletal muscle appears to respond to aggregate levels of stimulation, with a 10-month period of continuous stimulation at 2.5Hz showing similarities to shorter periods of continuous stimulation at 10Hz (Sutherland et al. 1998). Furthermore, intermittent high force and continuous low force stimulation, with a similar aggregate amount of pulses result in similar fibre type transformation. However, intermittent stimulation preserves muscle mass and force to a greater extent than continuous stimulation (Ferguson et al. 1989). This aggregate response resembles the relationship between magnitude of load and the frequency it is applied in determining a bone response (see section 1.5).

Given that an implanted device can stimulate a muscle for an extended period of time the muscle being innervated should be causing a minimal disturbance to the animal's behavioural pattern. This is of less importance in human studies, involving consenting participants who are receiving stimulation in sessions and it is therefore not interfering with normal activity. In an experimental animal however the selection of muscles is critical, as the stimulation of many muscles would severely compromise the animal's locomotion. Many studies have stimulated the dorsiflexors of the hindlimb (McNeal and Bowman 1985; Reichmann et al. 1985; Qin et al. 2013; Agnew et al. 1989). This group of muscles cause foot flexion, and as experimental animals tend to ambulate on 4 limbs this does not significantly impede locomotion, minimising behavioural disturbance.

A further consideration for minimising disturbance to locomotion is the size of the implanted device, which therefore should not exceed 2% of an animal's body weight. This presents a challenge when designing stimulators for laboratory animals such as rats and mice. The reduction in implant size is limited by the energy supply, which usually occupies 70% of an implant's volume (Jarvis and Salmons 2001). The volume of battery defines the aggregate amount of stimulation an implant can deliver. Given the size constraints of a device, a longer stimulation experiment may necessitate using a larger animal. Rabbits have been stimulated at low frequencies (10Hz) for as long as 10-months (Sutherland et al. 1998). Implants in mice therefore typically run for considerably shorter periods, with a 40Hz stimulation pattern only being able to be supported for 4 weeks (Russold and Jarvis 2007). Developments in microelectronics has led to miniature neuromuscular stimulators which at only $1cm^3$ are small enough to be implanted into the abdominal cavity of mice or rats, with adjustable stimulation amplitude, and a life-time of 4 weeks (Russold and Jarvis 2007). Implantation of a stimulator into rats would make work comparable with a great number of mechanoadaption studies (Forwood and Turner, 1995; Kotha et al 2004; Tuukkanen et al 1991; Mosley and Lanyon, 1998). Furthermore, stimulation of the common peroneal nerve focuses the mechanical stimuli upon the tibia, which is often the bone within a rat's skeleton which is experimentally loaded (Turner et al. 1994; Robling et al. 2001b; Torcasio et al. 2012; Akhter et al. 1992; Forwood and Turner 1995).

Implantable electrical stimulators have been utilised extensively for testing muscular plasticity, and so provide an establish technique, which requires considerably less development than an optogenetic regime. Surprisingly, given their long history of use in muscle research, stimulators have been used very little to investigate skeletal

responses to mechanical forces. For example, Qin et al used muscular stimulation to investigate the influence of muscular contraction upon the molecular signalling within cellular populations within bone (Qin et al. 2013). A clear advantage to muscular stimulation is that it can be applied continuously, or for bursts over 24 hours a day, which far exceeds even the most extreme exercise or loading regime. The result being fibres are stimulated at frequencies and over time courses that they are not accustomed to, and transformation in muscular phenotype can be far more dramatic than achieved by exercise (Salmons 2009).

Electrical muscle stimulation therefore presents an interesting method for investigating the musculoskeletal relationship. To assess the influence of electrical muscle stimulation upon the morphology of rodent bone and muscle requires a highly sensitive technique. As an intermittent stimulation preserves muscle mass, and force, it provides a better loading mechanism than continuous stimulation. The implantation of a neuromuscular stimulator allows for far more frequent loads to be applied than with external loading devices, as anaesthesia is not required to apply each load. Electrical muscle stimulation would therefore be especially interesting in light of the relationship between loading magnitude and frequency in determining an osteogenic response in bone.

2.2 Visualising and Quantifying Tissues of the Musculoskeletal system

A period of increased muscular activity will impose mechanical forces upon both bone and muscle, and given the plastic nature of both tissues they may both undergo a process of fine-tuning. The hierarchical nature of muscle and bone means adaptation at both the microscopic and macroscopic scales should be considered.

2.2.1 Histology

Histology has been employed by anatomists for centuries to aid in the visualisation of the fine detail of biological structures. This long history of histological techniques has led to widespread use and familiarity in the methods involved, and it continues to be used for the study of a vast number of tissues and organs in isolation, or combination, including the kidney (Taylor et al. 2012), bones (Shipov et al. 2013), muscle (Jarvis et al., 1996), cartilage (Taylor et al. 2012).

Structures are visualised and magnified by light microscopy, which requires that tissues are thin enough for light to pass through. Whilst this presents little problem for muscular tissues, finely slicing mineralised tissue requires that bones are first demineralised, by emersion in an acidic solution, resulting in a reduction in compressive strength. For fine slicing, samples ideally should be soft enough for a blade to pass through, but rigid enough to hold their form during sectioning. To achieve this level of rigidity samples are either frozen or embedded in paraffin. For freezing, tissues are immersed in liquid nitrogen immediately following harvest, to prevent necrosis. This requirement limits its use for the study of mineralised structures, as demineralisation can take weeks. Freezing is a far faster process than paraffin embedding, but doesn't allow sections to be cut as finely (Ham, 1974), and so provides a lower resolution data set. Paraffin is hydrophobic, and embedding a specimen in paraffin requires that tissues are first dehydrated through a series of ethanol to remove water, a process which requires a tissue processor, and takes considerably more time than freezing with liquid nitrogen.

The fixation and dehydration of biological samples causes tissue deformation (Boyde and Maconnachie, 1980) which results in an overall distortion of the three-dimensional structure (Adriaens 2012). Histology is therefore not an ideal quantitative technique, despite being extensively used as one (Zhou et al. 2007; Dalle Carbonare et al. 2005; Dempster et al. 2013). Although it is possible to control for distortion to some extent by standardising solutions and protocols across specimens within studies, it is not possible to have this standardisation between different studies, as variation in protocols will inevitably arise.

Tissue sectioned to a thickness of 10µm allows light to pass through it. In light microscopy white light is used, and so transparent sections need to be stained to be visualised. A wide variety of stains are used, the commonest combination being hematoxylin and eosin (H and E). Haematoxylin stains nuclei blue/purple. Eosin is a counterstain and stains the remaining material pink (Schmitz et al, 2010) (see Fig.2.2a). The way in which staining solutions affect tissue is not exactly known (Ham, 1974), however H and E is a very useful none-specific stain, which can be used to visualise morphology across different tissue types. There are many different stains and techniques which are used across the field of histology; here histological methods particularly useful for the study of musculoskeletal tissues are discussed.

White light waves can travel in any direction. Polarisation of light waves ensures they travel in a single plane only. If this light then passes through a fibrous structure

it is split into two orthogonal rays, a second filter then combines the split wave. As the human eye cannot register different light waves this is only registered in intensity, so fibrous structures are visualised as far brighter than surrounding material. Bone contains a large proportion of collagen fibrils, and so polarised light microscopy allows for the visualisation of collagen orientation within bone (Fig.2.2b). The manner in which the light is split depends upon the orientation of the fibrils (Changoor et al., 2011) which in turn impact upon the biomechanical properties of the bone, and so histology can provide information upon the microstructure of the bone tissue.

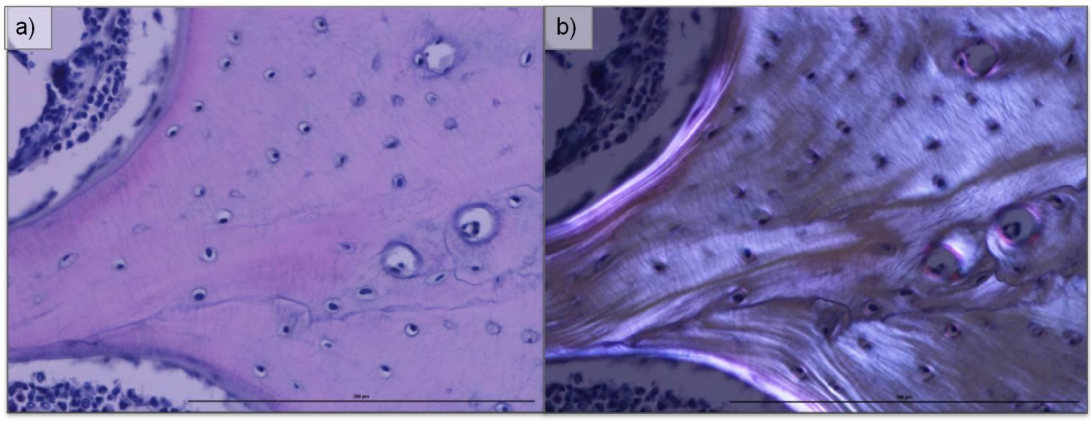

Figure 2.2 Bone visualised microscopically using hematoxylin and eosin staining and polarised microscopy. A histological section of a rat trabecular projection stained with hematoxylin and eosin and visualised using a) light microscopy, b) polarised microscopy. Scale bar is 200 microns.

It is often useful to be able to distinguish cartilage, from bone, for example, in the study of growth plates (Cancel et al., 2009), and identifying cartilage zones within bony structures (Zaslansky et al., 2013). For this there are two commonly used staining pairs, Safranin O with fast green (Shipov et al. 2013) and Alizarin Red S with Toluidine Blue (Panagiotopoulou 1976). Safranin O and Touidine blue stain proteoglycans, which are a major component of the extracellular matrix of cartilage, yet exist in small quantities in bone (Knudson and Knudson 2001). Both staining pairs distinguish cartilage from bone with distinctly different colours. There does not appear to be any great advantage to either stain in particular, and the stain of choice is largely determined by availability of the stains.

The microscopic structure of muscle can also be visualised using H and E staining; this provides information upon the fibre's cross-sectional area, and blood vessel distribution. Further information on muscular function can be visualised by utilising the differing biochemical properties of different fibre types (see section 1.12.1). Skeletal muscle fibres can be divided into glycolytic (easily fatigued) or oxidative, dependent upon the amount of mitochondria present within the fibre. Oxidative fibres possess a larger number of mitochondria than glycolytic fibres. Therefore to visualise if a fibre is oxidative of glycolytic a marker for mitochondrial activity can be stained. Mitochondria release ATP for oxidative muscle contraction as a result of the electron transport chain. Nicotinamide adenine dinucleotide (NADH) dehydrogenases are a group of enzymes that play an important role in the electron transport chain. For this stain NADH and a terazolium salt are applied to histological sections. At sites of dehydrogenase activity the added NADH is reduced, and hydrogen is released, which binds to the terazolium salt, producing a blue dye. This stain therefore represents the mitochondrial content of the muscle fibre. More mitochondria create a more oxidative muscle fibre, and stain darker blue. The lower the oxidative capacity of the muscle fibre the lighter it is (Fig.2.3).

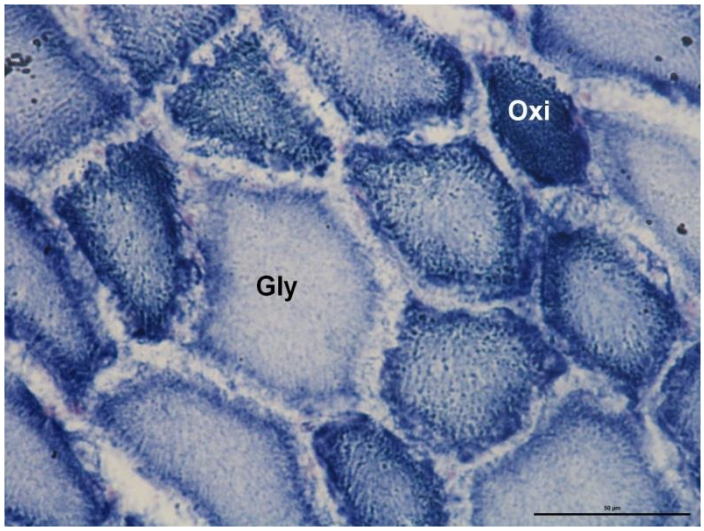

Figure 2.3 Rat muscle stained using NADH. NADH stains for mitochondria, and so fibres which stain darkly represent glycolitic fibres (Gly) and fibres which stain lightly represent oxidative fibres (Oxi).

For the histochemical discrimination of fibre types 1 and 2 their differing sensitivity to formaldehyde can be used. Brooke and Kaiser expanded on this technique to further discriminate type 2 fibres into a and b subclasses based upon their pH sensitivity

(Brooke and Kaiser 1970). Similar methods have been created by Guth and Samaha (1970) and Tunnel and Hart (1977). Tunell and Hart claimed that previous techniques showed overlap in pH sensitivities of fibres. In their method staining was more distinct. Tunnel and Hart staining differentiates type 1, type 2a, and 2b fibres of human, rat, rabbit, or porcine muscle in a single incubation (Tunell and Hart, 1977). Myofibrillar adenosine triphosphatase (ATPase) is an enzyme, which provides the basis of converting chemical energy in to mechanical energy. Myofibrillar ATPase is present at different levels of activity across the different MHC fibre types, and shows sensitivity of acidic conditions. During the staining process of all three techniques the pH is manipulated to produce differential staining of fibre types. as a result of Tunnel and Hart staining type 1 fibres do not show any staining, type 2a fibres show dark staining, and type 2b fibres show intermediate staining (Fig.2.4). All three methods require a certain degree of optimisation with regards to incubation times and pH levels, for the species under investigation, therefore preference for a particular stain is often based on previous experience.

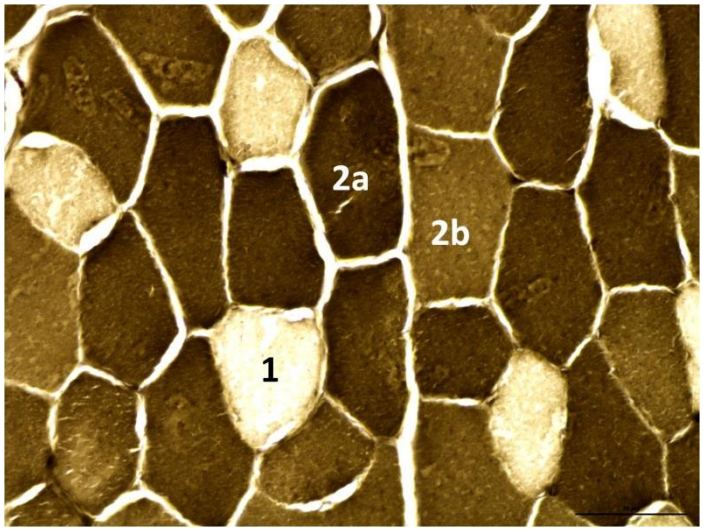

Figure 2.4 Rat muscle stained using the Tunell and Hart method. Tunell and Hart staining of muscle fibres differentiate MHC fibre types 1, 2a, and 2b. Type 1 fibres are unstained, type 2a fibres stain dark brown and type 2b stain an intermediate brown, representative fibres are labelled.

In summary, histology provides a powerful, cheap method for the descriptive assessment of internal structure across tissues and at high resolution. Possibly the largest limitation of histology is that it provides two-dimensional data of three-dimensional structures. Techniques have been developed for the reconstruction a

three-dimensional from histological sections, but this remains a laborious and destructive process (Weninger et al. 2006). The destruction of a sample limits any further analysis, such as materials testing. Therefore a technique which allows for three-dimensional analysis of musculoskeletal arrangement in a none-destructive manner could be utilised in complement with, or instead of histological techniques.

2.2.2 Imaging

Imaging can provide information of a specimen's morphology in a non-destructive manner. Computed tomography (CT) utilises x-rays acquired at multiple projection angles to collect three-dimensional data sets (Hsieh, 2009). Despite the invaluable clinical advantages of CT, its spatial resolution has limited its use for basic research, which is largely carried out in small animals. The introduction of microscopic computed tomography (microCT) (Elliott and Dover 1982), which provides far higher resolution than clinical CT enabled this technology to become an established technique for skeletal research.

The basic principle of microCT is the interaction of ionising radiation (x-rays) with matter (Fig.2.5). The x-ray attenuation of a material is dependent upon the material in question and the energy of the x-ray source. In microCT x-rays are emitted over a range, in a polychromatic beam (Stauber and Müller, 2008). X-rays are accelerated towards the specimen being imaged (Hsieh, 2009). As an x-ray beam hits a material it is exponentially attenuated according to the material it encounters. The projection of x-rays is picked up by a detector, which is usually based on a charge-coupled device camera with a phospholayer. The detector converts x-ray into visible light (Stauber and Müller, 2008). For a three dimensional image to be created the specimen can be rotated (Fig.2.5) or the x-ray source and detector can be rotating around the specimen (Holdsworth and Thornton, 2002). Both methods of rotation provide a 3-dimensional array of x-ray attenuations.

MicroCT has become an established tool for the field of bone biology, and its fundamental principles have been extensively reviewed elsewhere (Seeram, 1996, Hsieh, 2009). The majority of previous reviews for biologists address the technical considerations for the application of microCT, without addressing the physical principles underlying the techniques (Bouxsein et al. 2010). This chapter therefore aims to review the physical principles most salient to the quality of data collection for musculoskeletal studies, chiefly the manner in which x-rays interact with biological tissues.

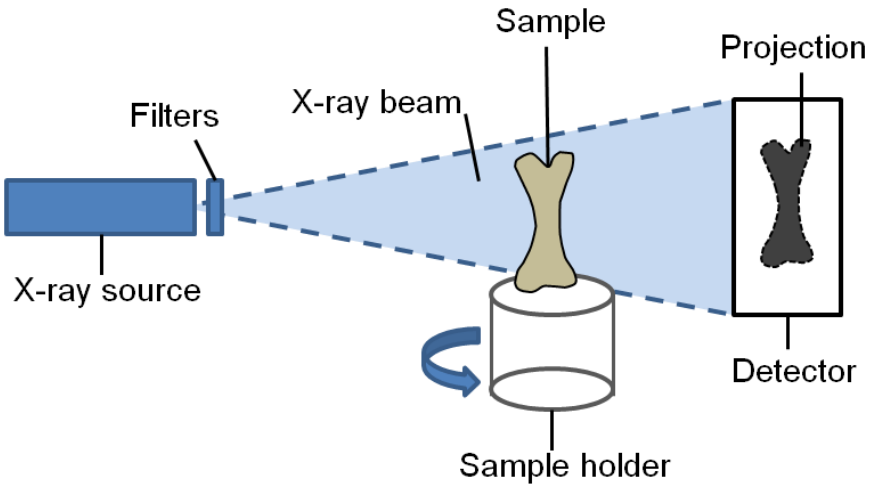

Figure 2.5 A diagram of the major components of a microCT scanner. MicroCT imaging requires X-ray information acquired at multiple projection angles. X-rays are projected from a source, and can be filtered before reaching the sample. X-rays are differentially attenuated by the sample, and so the x-rays reaching the detector give information on the spatial arrangement of material. The sample is rotated so that data is collected from multiple angles, to produce a three-dimensional data set. Figure modified from Stauber and Müller (2008).

X-rays are electromagnetic waves. They can be produced by electrons giving up kinetic energy. For the generation of x-rays in microCT electrons are fired at a target element. The interaction of the electrons with the target can generate x-rays in two ways. A high-speed electron can interact with an electron in the target element, and bind with sufficient energy to propel the target electron from its shell (Hay and Hughes 1983). Electrons have a negative charge, and orbit the positively charged nucleus in shells. Electrons which exist in outer shells are orbiting the nucleus at a higher speed than those in the inner shells, and so have a higher energy state. Thus, if a space in an inner shell becomes available an electron from an outer shell will jump up to fill this and energy is released. The energy is released as an x-ray (Fig.2.6a). The second way in which x-rays are produced is by Bremsstrahlung production, a high-speed electron passes close to the nucleus of the target material, and is decelerated by its positive charge. The kinetic energy that the electron gives up is converted into electromagnetic radiation and emitted (Fig.2.6b) (Hay and Hughes 1983).

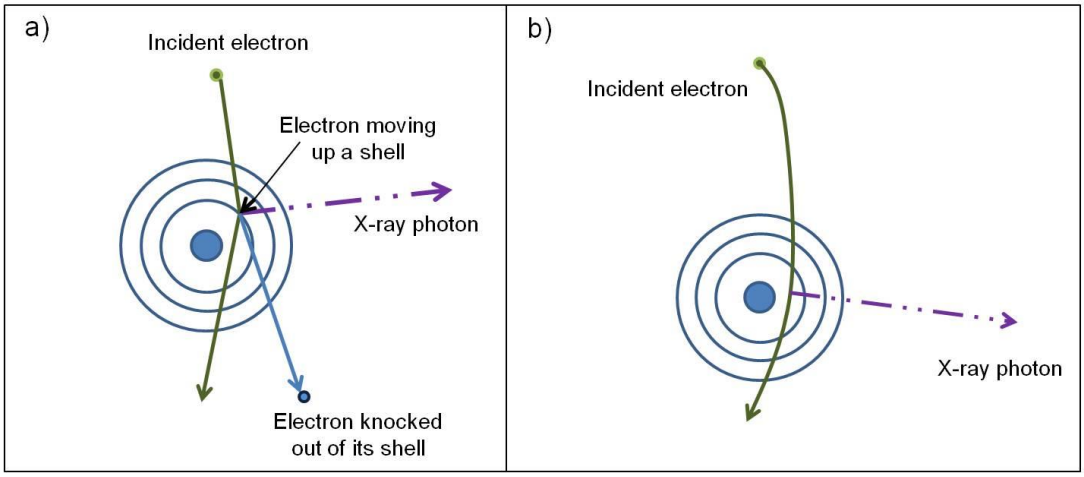

Figure 2.6 A diagram of different ways x-rays can be produced. X-rays are produced in two ways, a) the incident electron binds to an electron of the target with sufficient energy to knock the electron out of its shell, leaving an empty space. An electron from a further out shell moves up a level and releases energy, as an x-ray. b) The incident electron passes close to the nucleus of the target, and is decelerated, its kinetic energy is converted into electromagnetic radiation and emitted. Figure modified from Hay and Hughes (1983).

A large proportion of x-rays produced by the target element have the same energy, known as the characteristic radiation. The characteristic radiation is the amount of energy released as electrons move between shells, and is specific for the element, and the shells involved. In Bremsstrahlung production the energy of the x-ray produced is dependent upon the deceleration of the electron, and so x-rays are produced over a range of energies (Hay and Hughes 1983). A target material with a higher atomic number has a larger number of protons in its nucleus, and so has a greater positive charge relative to the high-speed electrons fired at it, and so creates a greater deceleration, and higher energy x-rays. For this reason, Tungsten is often used as a target material (atomic number, 74), however other targets, such as Silver and Molybdenum can be used to create different x-ray spectra.

The energy of an x-ray is determined not only by the target material but also by the voltage (kV) and the current (μA) used to propel electrons into it. The voltage determines the energy with which the electrons interact with the target. If propelled electrons do not have sufficient energy to bind the electrons of the target material, then no characteristic radiation will be produced, but x-rays produced by Bremsstrahlung interactions can still be created. Increasing the voltage will increase

the energy of the emitted x-rays, enhancing electron binding and the penetration of the beam (Hay and Hughes 1983). The current applied to produce the electrons fired at the target material to create x-rays, affects the number of x-rays which are produced, but not their energy. The number of x-rays interacting with the matter does not affect the penetration of the x-rays, but the intensity of x-rays reaching the detector, which in turn affects the intensity of the image.

All digital images are composed of discrete two-dimensional sub-units known as pixels. MicroCT imaging creates three-dimensional data composed of three-dimensional sub-units known as voxels. A single voxel can only represent a single value, and any changes across its volume are averaged (Spoor et al., 2000). Therefore for a given scan volume, smaller voxels provide more data. A greater amount of data results in higher spatial resolution (the ability to resolve image details from each other). MicroCT often produces data in voxels with equal dimensions, known as isometric voxels. Ideally to achieve the highest image quality, with the smallest voxels, every specimen would be imaged at the highest resolution possible (Bouxsein et al., 2010). In microCT scan resolution can theoretically reach 1µm (Spoor et al., 2000). The achievable resolution is limited by the size of a specimen, which is directly negatively proportional to resolution.

Each voxel contains a grey-scale value, which represents the total attenuation of the x-ray. Black represents the lowest x-ray attenuation, and white the highest attenuation (Spoor et al., 2000). In figure 2.7 the bone attenuates the most x-ray and is white, soft tissue and medullary cavity appear grey as they attenuate less x-ray. The surrounding air is black, demonstrating it attenuates little, if any, of the x-rays between the source and detector.

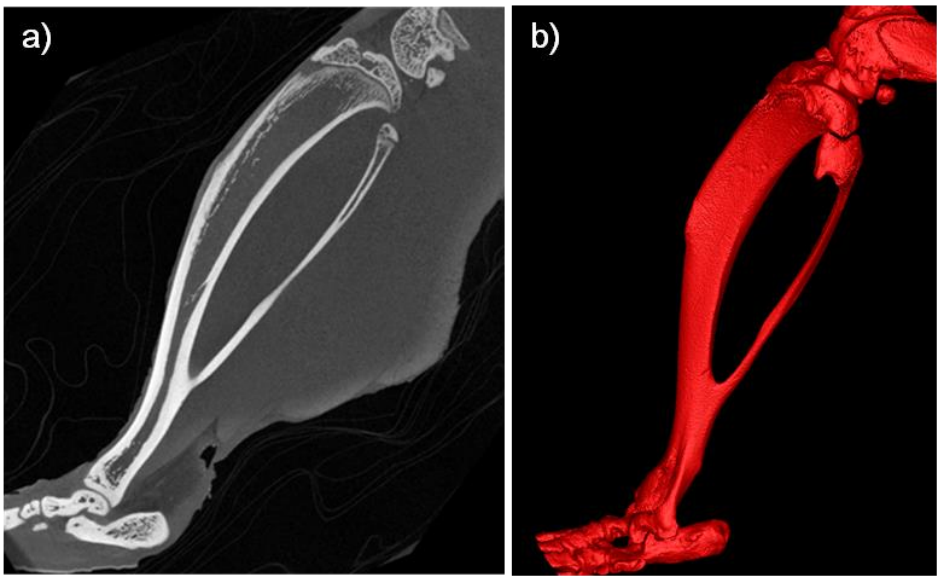

Figure 2.7 A mouse hindlimb visualised using microCT. MicroCT uses x-ray attenuation acquired at multiple projection angles to create a three-dimensional data set which can be viewed as a) a longitudinal slice of data or, b) reconstructed into a volume. Both images are the same mouse hindlimb.

The attenuation of an x-ray refers to the reduction in its intensity due to the wave being scattered or absorbed by the material encountered. The extent to which x-rays are attenuated is dependent upon the size, material density, and atomic number of the material it encounters. X-rays can be scattered and absorbed in a number of different ways, but the most important to consider for biological specimens are photoelectric absorption and Compton scattering. Photoelectric absorption is similar to the creation of x-rays. The incident x-ray binds an electron with sufficient energy to knock it out of its shell, leaving a vacancy. An electron from another shell moves up into to empty shell, releasing energy (Fig.2.8a). This is absorption, not scatter, as energy is absorbed, and then a different wave of energy emitted. Compton scatter occurs when an x-ray interacts with an electron with sufficient energy for the electron to behave as if it was free, the electron re-coils and the x-ray is scattered with a loss of energy (Fig.2.8b) (Hay and Hughes 1983).

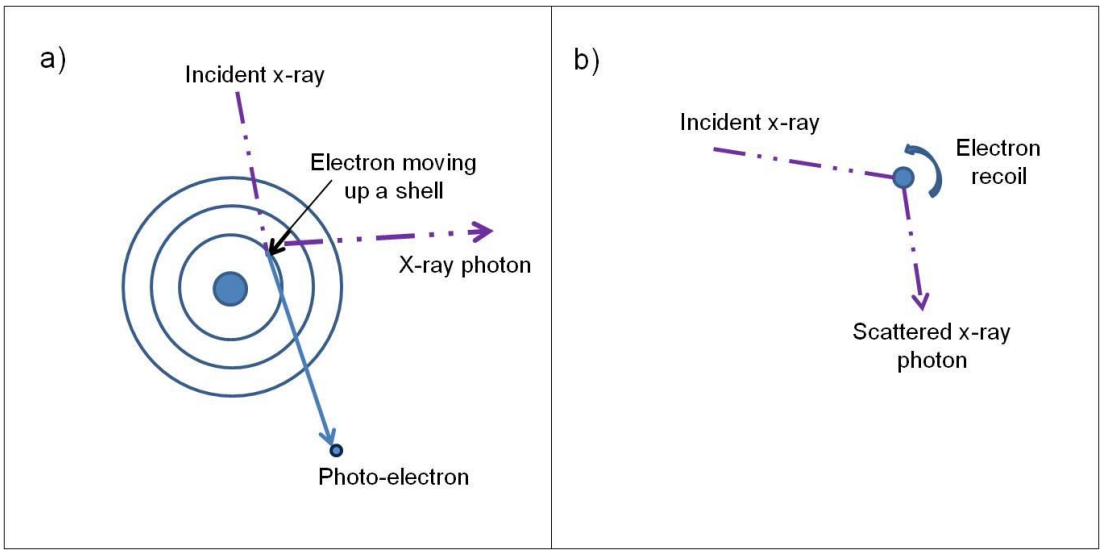

Figure 2.8 A diagram of ways in which x-rays can be attenuated. X-rays can be attenuation by absorption or attenuation such as a) photoelectric absorption, in which the incident x-ray binds with an electron with sufficient energy to knock it out of its shell, creating a photo-electron. An electron from an outer shell then moves up to fill the empty shell and emits an x-ray photon. b) Compton scatter, the incident x-ray binds electrons with sufficient energy for them to behave as a free electrons, and re-coil, scattering the x-ray photon. Figure modified from Hay and Hughes (1983).

The proportions of scatter and absorption are dependent in part upon the energy of the incident x-ray photons, with photoelectric absorption dominating at lower energies, and Compton scatter being more influential at higher energies. The proportion of x-ray attenuated is dependent upon the density, size and atomic number of the tissues it encounters. A tissue with a high density has a larger amount of electrons to collide with, and thus a greater proportion of x-ray energy will be attenuated whilst passing through it. Similarly a tissue of a larger size has a greater number of electrons to pass through before the detector is reached, and thus there is more chance of x-rays interacting with electrons. Finally a material of a higher atomic number has a greater number of protons in its nucleus, and so its electrons are bound with a higher energy, and more energy is required to knock them from their shells, so photoelectric absorption is proportional to atomic number (Hay and Hughes 1983). Compton scatter results in the detector picking up x-rays which have been deflected, and so results in a less crisp image than absorption, therefore lower energy x-rays produce better contrast of materials, but lower penetration of the

tissue (Fig.2.9). Consequently, selecting an x-ray energy is a trade-off between penetration and contrast (Stauber and Müller, 2008).

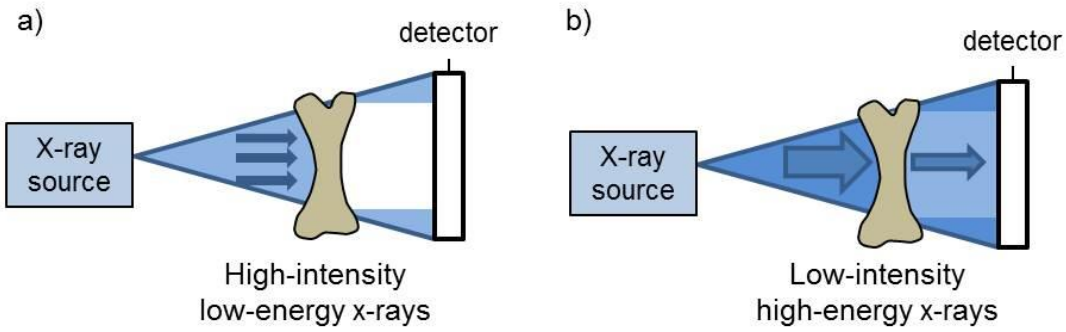

Figure 2.9 A diagram of the effect of current and energy upon the contrast and intensity of x-rays. The energy of the x-rays affects the image quality, a) high current, low energy x-rays has limited penetration, and high contrast. b) High energy, low current x-rays has good penetration, and lower contrast.

X-rays used in microCT are emitted over a range of energies, in a polychromatic beam. During interaction with matter x-rays are differentially attenuated, with lower-energy x-rays being attenuated to a greater extent than high-energy x-rays. This results in an upwards shift in the effective energy of the x-ray spectra, resulting in a harder, more penetrating beam. Beam-hardening can lead to imaging artefacts such as streaks and differential greyscale values across an object of homogenous density. Imaging artefacts can be reduced by the use of filters, such as metals that absorb the lower energy x-rays before they reach the specimen, so reducing the range of energies (Stauber and Müller, 2008). The effects of beam-hardening and image noise can also be reduced to a certain degree with post-acquisition mathematical filters (Bouxsein et al. 2010).

Bone contains elements such as calcium and phosphate with far higher atomic numbers (20 and 15 respectively) than those found in soft tissue (carbon, 6, and hydrogen, 1) (Descamps et al. 2014). The differential attenuation of bone and soft tissue has led to microCT being very useful for studying skeletal form (Badea et al., 2008), but limited in studies of soft tissue. CT does provide some information upon the mass of soft tissue (Fig.2.7) but this is limited, at most, to a gross muscular mass volume. The volumes of individual muscles, and architectural parameters

cannot be distinguished (Rittweger and Ferretti 2014). Therefore, to investigate the inter-related morphological relationship between bone and muscle, previous studies have dissected the muscle, whilst deriving skeletal parameters from microCT (Warner et al. 2006). Dissection of the muscle is a destructive method, and destroys the in situ relationship of the muscle and the bone, and in small animals, the intricate nature of muscle dissection, can easily lead to muscular fibres not being fully dissected.

Skeletal muscle can be imaged in high-resolution with the use of magnetic resonance imaging (MRI). MRI produces three-dimensional data sets of soft tissue using pulses of radiofrequency. Imaging involves placing a sample within a strong magnetic field. This magnetic field results in the atoms within the sample becoming aligned, and rotating about their axes. A pulse of radiofrequency is then transmitted, which excites the nuclei flipping them into a higher energy state. The atoms then relax, releasing characteristic radio waves (Berquist 2012). The signal is received by a coil, and is dependent in part upon the concentration of atoms within the sample (Spoor et al. 2000).

Diffusion tensor imaging of MRI data, has allowed architectural parameters of skeletal muscle to be determined (Adriaens 2012) allowing a complete three-dimensional data set of muscle in situ. Whilst MRI provides excellent three-dimensional data on soft-tissue structures it offers only a negative signal of bone, as bone is proton deficient (Spoor et al. 2000). MRI and CT can therefore be co-registered to provide high-resolution three-dimensional data of muscle and bone, whilst maintaining their in-situ relationship. This approach necessitates time and money to acquire two separate data sets. A more practical approach would be a method which combines both muscle and bone visualisation together, as MRI has longer acquisition times, higher cost and lower signal to noise ratio (Jeffery et al., 2011) so enhancing soft-tissue detail in microCT is a practical approach.

Soft tissue is not distinguishable on CT due to the poor attenuation of x-rays by this tissue. As the size and density of soft-tissue cannot be easily altered to enhance their attenuation, their atomic number is the obvious target. The introduction of a heavy element (high atomic number) to a tissue greatly enhances its x-ray attenuation. This has been extensively utilised clinically with the use of barium (atomic number 56) and iodine (atomic number 53) (Hay and Hughes 1983). This concept was applied to small-animal imaging by Metscher, who introduced a series of contrast enhancing agents for the study of embryonic soft tissues (Metscher,

2009b, Metscher, 2009a). These solutions have been used for differentiation of muscular, neural, and epithelial tissues within embryos. The solutions used were osmium tetroxide, phosphotungstic acid (PTA), and inorganic iodine. These all contain heavy elements, osmium (76), tungsten (74), and iodine (53), and so their selective diffusion into embryonic soft-tissues can increase the x-ray attenuation, and so enable visualisation. Of these solutions osmium tetroxide is toxic, volatile and expensive (Metscher 2009). PTA is acidic, and so not ideal for studying muscles in tandem with mineralised structures as it will demineralise bones. Demineralisation will degrade the imaging quality of bones, and prevent any further analysis of their material properties. Furthermore in a comprehensive study of 28 contrast-enhancing soft tissue stains I_2KI has emerged as the stain which most readily diffuses into tissues (Pauwels et al. 2013), and thus is the most suited for larger samples, such as rodent limbs. Indeed Iodine Potassium Iodide (I_2KI) has found the most wide-spread use (Jeffery et al., 2011), in post-natal specimens, the extent of which is demonstrated by Gignac and Klay who used I_2KI to gain detailed anatomical data of alligator and emu heads (Gignac and Kley 2014). and cardiac muscle (Aslanidi et al., 2012) via microCT imaging

The way in which Iodine interacts with the soft tissues is not fully understood. Some authors report iodine as staining tissues in a uniform manner (Mizutani and Suzuki 2012), however iodine shows especially strong staining in liver, muscle and adipose tissue (Jeffery et al. 2011; Gignac and Kley 2014). This has led to the theory that iodine is binding the storage molecule glycogen, which is found within all of these tissues, this is further supported by intense staining in red blood cells (Sengle et al. 2013), which also carry glycogen. Furthermore iodine is known to be able to bind glycogen (Lecker et al. 1997). This possibility is especially interesting in light of the work of Gignac and Kley, who found more intense staining in glycolytic fibres, than in oxidative fibres (Gignac and Kley 2014). Implying that iodine-enhancement could even be extended to the use of fibre type discrimination, in a none destructive manner.

MicroCT can provide a powerful tool for the assessment of the morphology of the musculoskeletal system, by providing high resolution, three-dimensional data upon both muscle and bone, whilst maintaining their in-situ relationship. Three-dimensional data can provide a wealth of information upon the geometry of the bone. The parameters measured are determined by the question under investigation. Morphometric analyses such as cortical thickness, medullary area, moment of inertia, trabecular volume, connectivity and anisotropy are all commonly

reported parameters which can be easily calculated from microCT data (Bouxsein et al. 2010). However, bones have complex shapes, which often cannot be adequately described by conventional measurements. For example, describing a bone by cortical thickness measurements simplifies a three-dimensional shape into a one-dimensional measurement. Shape can be defined as all the geometric information about a configuration, bar the position and size. Changes across complex three-dimensional shapes can be quantified using geometric morphometrics (GMM). GMM usually involves plotting a series of homologous landmarks across multiple geometries. The differences in these landmarks can then be calculated to provide data on which landmarks are shifting across samples. This technique has found particular use in assessing the functional significance of skeletal changes across evolution, for a detailed handing see Zelditch (2004). GMM presents the advantage of providing a clear visualisation and quantification of differences between complex shapes. This provides powerful data across a single study, but is a far less transferable across studies than a more simple geometrical measurement such as cortical thickness.

Morphological parameters can provide insight into the biomechanical performance of a bone, for example microCT data can be used to calculate a bones moment of inertia. Furthermore some detail on the mineral content of a structure can be obtained by comparison of greyscale values with hydroxyapatite phantoms. This only describes the volume of mineral within a region of bone, which does not necessarily reflect the density, for example a bone could be highly mineralised, but very porous, and the BMD measured by microCT would be equivalent to a bone with a lower mineral density, which was less porous (Fajardo et al, 2009). Therefore for more detailed information upon how the bone is performing biomechanically further techniques are required.

2.3 Materials testing and strain measurement

2.3.1 Material properties

Whilst morphological data can provide some information upon the biomechanical performance of the bone in terms of collagen orientation, the moment of inertia, and the volumetric bone mineral density, it sheds little light on the overall mechanical performance of the bone. The mechanical performance of a bone is in part determined by the bones material properties (see section 1.2.1).

As discussed previously (see section 1.2.1) a materials elastic modulus represents the extent to which a material deforms under load. The elastic modulus of bone has been estimated from bone mineral density measurement from microCT imaging (Zannoni et al. 1999). This method only accounts for the mineralised component of bone, and completely disregards the involvement of collagen in defining a bone's mechanical behaviour. The elastic modulus of a bone can also be derived by ultrasonic acoustic measurements (Turner et al. 1999). This involves an ultrasonic wave being created by a transducer, and aimed at the specimen. The wave on the other side of the specimen is picked up by another transducer. The time taken for the wave to transverse the specimen, along with specimen volume can be used to derive the waves velocity, and from this the elastic modulus can be calculated (Ashman et al. 1984). The results obtained are dependent not only upon a materials elastic modulus, but also the local material density (Hengsberger et al. 2002) therefore errors can accrue.

The elastic modulus of an object can be established directly by testing the extent to which a bone deforms under a given load. Microindentation or microhardness techniques involve the indentation of a flat surface of bone using a rigid indenter, and a given load. The extent to which bone deforms can be measured optically, and the materials hardness can be calculated (Donnelly 2011). Hardness is a complex property, and here refers to the average pressure a material can support (Li and Bhushan 2002). The measured hardness of a material cannot be easily converted into continuum-level properties such as elastic modulus (Hengsberger et al. 2002).

Nanoindentation, derived from microhardness measurement has gained popularity as a method for deriving a material's elastic modulus. Nanoindentation involves the controlled application of load and unloading into a material. The indenter is a depth-sensing tip, which measures the displacement of the material during loading. Load-displacement curves can then be created for both loading and unloading of the material. From this a material's elastic modulus and hardness can be calculated. Indentation at the nano-scale ensures that measurement is unaffected by the macroscopic arrangement of bone (Lewis and Nyman, 2008). The sensitivity of nanoindentation is incredibly high, with loads as low as 1 nanonewton, and displacements of 0.1 nm accurately measured (Li and Bhushan 2002) and a higher resolution than ultrasonic measurement (Turner et al. 1999). However, nano-indentation assumes a material is isotropic, which bone is not, however studies comparing moduli obtained with nanoindentation and ultrasonic techniques (which account for anisotrophy) showed comparable results (Turner et al. 1999). Therefore

nanoindentation is a valuable technique for the measurement of bone material properties in rodent bones.

There are a number of factors both intrinsic and extrinsic to a material which can affect the hardness and elastic moduli values measured. Intrinsic factors affect the properties of the material itself, whilst extrinsic factors affect the measurement of the values. An important intrinsic factor to consider for indentation of biological materials is the hydration state of the tissue. In bone water plays an important mechanical role within the tissue, and elastic moduli, as determined by nanoindentation, was drastically lower in hydrated bone than dehydrated bone (Hengsberger et al. 2002; Guidoni et al. 2010; Wolfram et al. 2010). Whilst short term preservation of bones in formalin solutions shows no significant difference in elastic modulus (Nazarian et al. 2009), long term preservation has been shown to result in a loss of elastic modulus (Ohman et al. 2008).

Extrinsic factors which can influence nanoindentation data include numerical methods used, indenter tip and indentation temperature. There are numerous numerical methods used for establishing the elastic modulus and hardness from the loading and unloading curves see Li and Bhushan for a thorough review (2002). The oldest and most widely used method is the Oliver-Pharr method (Lewis and Nyman, 2008). This method has been found to have a number of limitations which can result in significant underestimates of elastic moduli (Bolshakov, 1996). Alternatively the continuous stiffness method can be used. As the name suggests this method allows for the measurement of material stiffness at any point of the loading curve, not only at the point of unloading (Li and Bhushan 2002), this is of particular benefit for bone indentation (Lewis and Nyman, 2008) as mechanical properties can vary with indentation depth.

Indenters are usually diamond, due to its high elastic modulus and hardness, its use minimises the effect of indenter deformation upon the measured displacement. The indenting tip can be shaped into a number of different ways. A three-sided pyramidal shape known as a Berkovich indenter, is commonly used. Three-sided tips are preferred as they are more readily ground into a sharp point than an indenter tip with four-sides (Li and Bhushan 2002). It is also possible to use a spherical point for indentation, which provides information of yield properties, however it is practically very difficult to obtain a spherical indenter out of diamond (Pharr 1998). The temperature at which indentation is performed needs to be tightly controlled as

increased temperature has been shown to result in a reduced elastic modulus and hardness measurements (Fang et al. 2003).

Nanoindentation allows materials to be tested to a high degree of accuracy, however care must be taken that the correct parameters are being used for the experimental outcomes. For more detailed reviews of nanoindentation of bone see Ebenstein and Pruitt (2006) and Lewis and Nyman (2008).

2.3.2 Strain measurement

Using a combination of structural information alongside material properties it is possible to build up a clearer picture of the biomechanical performance of a bone. However the response of a bone to a biomechanical input is in the physical manifestation of strain. Strain is the parameter most commonly linked to bone mechanoadaptation.

One of the most established, widely used and reliable methods for measuring bone strain directly is strain gauges (Lanyon and Rubin 1984; Burr et al. 1996; Lanyon and Smith 1969). Strain gauges are composed of a thin foil element on a backing. The gauge physically deforms with the underlying structure, and changes electrical resistance produced during surface deformation and measured using a Wheatstone bridge (Humphrey and Delange, 2004) into a strain value (Rayfield 2007). Strain gauges measure changes in resistance along the axis they are oriented (Humphrey and Delange, 2004). This simplifies the complex three-dimensional strain event into a single strain value. This can be overcome to a certain degree with the use of a rosette strain gauge, which consists of two or more (commonly three) gauges arranged in different orientations, to measure strains along different axis. Three measurements are required to determine the principal strains (refer to section 1.2.1). A further limitation of strain gauges is that they are only capable of measuring strain across the part of the bone to which they are adhered. Bones have inhomogenous material properties, complex geometries and loading patterns, all of which will produce a non-uniform strain environment. This is reflected in the observation that strains recorded are highly variable dependent upon the gauge location (Torcasio et al., 2012). Furthermore the size of the gauge limits their use in small bones such as rodent long bones, as the gauges require a flat surface for adherence, of which are very few of sufficient size in the mouse or rat limbs.

To assess the strain distribution across a bone's geometry digital image correlation (DIC) and speckle interferometry have been utilised. DIC involves covering a

structure in a speckle pattern, and imaging it using a charge-coupled device whilst it is loaded. During loading the speckle pattern physically deforms with the underlying structure, and the degree to which the pattern is distorted reflects the strain that the tissue is under (Sztefek et al. 2010). The use of DIC for investigating subtle changes in strain environments is limited by its sensitivity of 300με in mice tibiae (Sztefek et al. 2010). Also the coating of a bone with a speckle pattern may in fact alter the mechanical properties of the bone, and hence the strain magnitude. Speckle interferometry is a similar process to DIC, but the speckle pattern is generated by a laser, the deformation of the laser pattern during loading can be measured, and strains calculated. With a reported repeatability of 200με, this technique is limited in its ability to measure subtle strain variations (Yang et al. 2007). Both DIC and speckle interferometry can only measure strains occurring across the bone surface, and therefore tell little about the strain distribution within a bone.

For the measurement of strain across an entire bone geometry a technique which can measure internal deformation is required. Recently digital volume correlation (DVC), has been used to do just this (Gillard et al. 2014). DVC utilises microCT imaging for volumetric data across a bones geometry. The bones geometry is broken down into sub-units and loaded, the variation in greyscale values is used to calculate deformation across each sub-unit. As microCT imaging requires that a sample is static for the duration of the scan. This means that the bone is imaged, then a static load is applied, and the bone re-imaged, this is repeated for a number of loads. DVC therefore cannot measure dynamic strains. Furthermore the sensitivity of the technique was found in trabecular bone to be between 70 and 800με. Though subsequent studies have found DVC in cortical bone to be more precise, with an error of 200με (Dall'Ara et al. 2014). This sensitivity means it is a valid method for testing material failure, but not for subtle strain distribution. However future developments within this area present a promising technique for direct strain measurement across entire geometries.

2.3.3 Computational simulation of strain distribution

Whilst it is not possible to directly measure strain across an entire three-dimensional geometry to a high sensitivity, it is possible to estimate them. Mechanical principles can be applied to a computational model to estimate the stress and strain environment throughout the entire structure in response to applied loads through a method know as finite element analysis (FEA). Despite its initial formulation in 1943 (Courant 1943) FEA only gained widespread use with increased accessibility of

computers, and processing power. Subsequently, the use of FEA in engineering and biomechanics has dramatically increased. A PubMed search of the words "finite element analysis bone" returned over four times the citations in 2013 than in 2003 (Fig.2.10) demonstrating the growing popularity of this method for aiding in biological analyses.

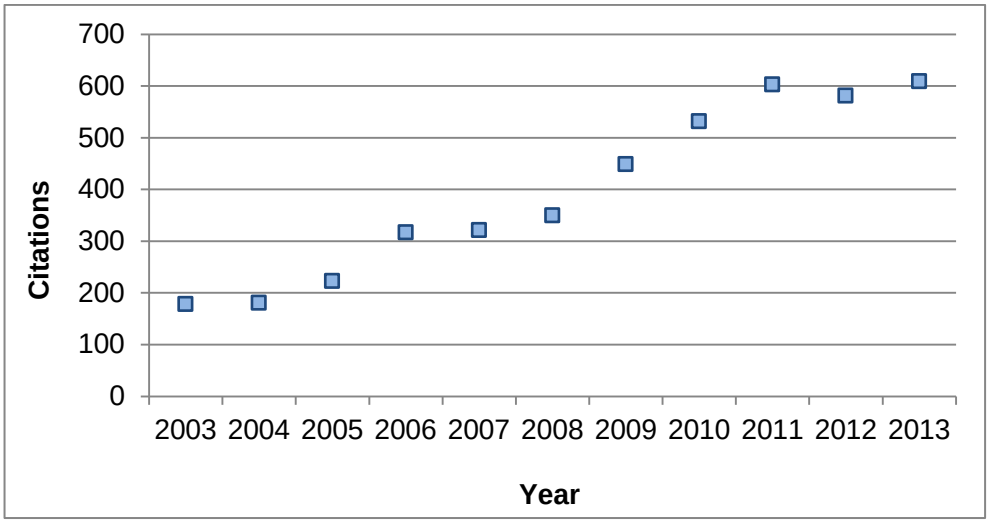

Figure 2.10 The growth of popularity in FEA as a technique for the field of biomechanics. The words “finite element analysis bone” were searched for on each individual year between 2003 and 2013, and the number of returned results plotted.

The process of FEA consists of creating a three-dimensional model of the structure, breaking it down into a large number of elements, joined together to form a mesh. The mesh is given material properties, constraints and forces to mimic its biological situation (Fig.2.11). Then finite elements analysis, which is based on solving partial differential equations, is run. The complex mathematical basis of FEA requires high computational power, and is not as widely understood, as experimental measurement of strain by strain gauges. However the benefit to quantifying the mechanical environment of a bone through FEA is that it is a simulation, and so any number of different parameters can be tested. FEA can therefore be used to simulate biomechanical situations which would not be experimentally possible, such as simulating a bone being loaded, and then lengthening the bone, and repeating the simulation to test the biomechanical impact of bone proportionality. However a model can only produce solutions based upon the information supplied, so the accuracy and reliability of the model should be ensured. This review deals instead with the main stages of model creation, and analytical considerations relevant to

simulation of biological situations, the mathematical principles of FEA are beyond the scope of this chapter, and are presented elsewhere, see Logan and Richmond et al (2011; 2005).

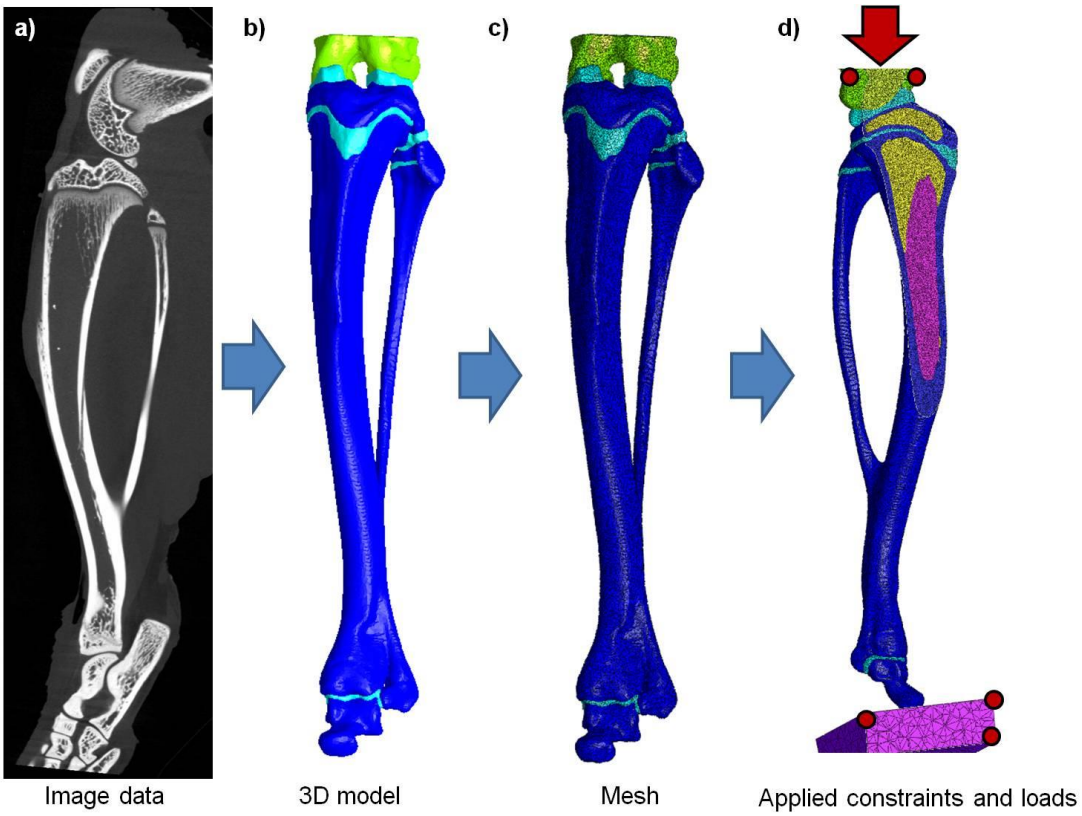

Figure 2.11 Stages of finite element model creation. In order to run a finite element analysis first the geometry must be defined which may come from a) image data, this is used to create b) a 3D model, the model is then divided into a finite number of elements in a c) mesh, finally d) elements are assigned material properties, boundary constraints and forces.

The process of FEA begins with the creation of a virtual model of the structure under investigation. A simple geometry can be created in autoCAD software (Richmond et al., 2005). For more complex geometries the data is best obtained from three-dimensional imaging data such as that produced by laser scanning, computed tomography or MRI imaging (Panagiotopoulou, 2009). This model is then broken down into elements. An element is a discrete volume of model, for three-dimensional analyses usually tetrahedral or hexahedral, each vertex of the element constitutes a node (Moazen et al., 2009) (Fig.2.12). The network of elements and nodes constitutes the mesh (Fig.2.11). How accurately the solution reflects the

actual biological response is in part determined by the quality of the mesh (Burkhart et al. 2013). Bones have smooth, curved surfaces. For their geometry to be accurately represented by tetrahedral or hexahedral components the components must be sufficiently small. A very simple mesh can often result in a distorted geometry and result. However, computational time and demand increases with model complexity, so it is practical to use a model which most accurately represents the geometry for a minimum number of elements.

The quality of a mesh is also determined by the geometry of the element. Tetrahedral elements have been found to produce more accurate solutions than hexahedral elements (Ramos and Simões 2006). Perhaps due to the fact that they replicate can provide a better replication of bone geometry (Ulrich et al. 1998). However tetrahedra are less stable (Ramos and Simões 2006). Element's quality is also determined by its aspect ratio, that is, the ratio of the longest side to the shortest side, which is ideally as close to 1 as possible. The modelling of complex biological structures which often contain highly curved surfaces means that an aspect ratio of 1 across all elements is unlikely, but as low as possible is aimed for. In the same way an internal angle of the element should be as close to idealisation as possible (90° for hexahedral, 60° for tetrahedral) (Burkhart et al. 2013). The degree to which elements differ from the idealised geometry can be summarised by a Jacobian value (Knupp 2001), negative Jacobian values represents an elements which are inverted, this prevents analysis.

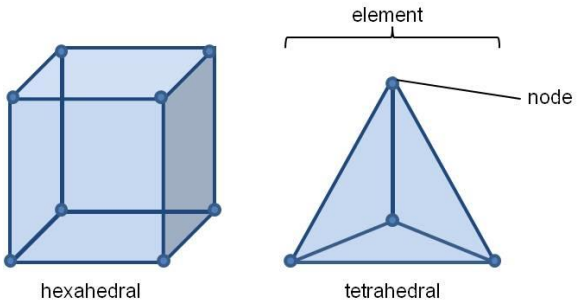

Figure 2.12 Diagram of hexahedral and tetrahedral elements and nodes. A mesh is composed of a large number of hexahedral or tetrahedral elements. The vertex of each element, or node, is connected to a number of other elements. Adapted from (Burkhart et al. 2013)

A mesh defines the geometry of the structure to be analysed. The mechanical behaviour of the structure as a whole is dependent upon the mechanical behaviour

of the materials which constitute the structure. Materials may behave linearly or non-linearly. In a linear material stress and strain are linked linearly, as can be seen in the elastic portion of a stress strain curve (Maas and Weiss, 2007). Usually during biomechanical simulations of physiological loading bone deforms within its elastic range. That is, upon removal of the load the bone reverts back to its original shape. To model an elastic material the elastic (or Young's) modulus and Poisson's ratio are required. The elastic modulus as defined previously (see section 2.4.1) represents the extent to which a material deforms under load. The Poisson's ratio describes how a material behaves under tension or compression to maintain its volume. For linear, elastic, isotropic materials only the elastic modulus and Poisson's ratio are required. An isotropic material performs equally under loads applied in any dimension. Bone is not an isotropic material (see section 1.2.2) yet is often modelled as such (Kotha et al. 2004; Torcasio et al. 2012; Moazen et al. 2009; O'Hare et al. 2012), however models with isotropic bone material calculate strain results comparable to experimentally measured strains (Kupczik et al., 2007). This implies that the net directionality of bone geometry is sufficiently influential to define bones anisotropic behaviour.

Biological materials often exhibit mechanical behaviour in which stress and strain are not linked linearly. In a hyperelastic material, stresses generated during deformation are dependent upon the initial state, and the resultant configuration (Maas and Weiss, 2007). Materials which show no change in their volume during deformation are incompressible (Maas and Weiss, 2007). To model incompressible materials the deviatoric (distortional) and volumetric components of the strain tensor are de-coupled (Maas and Weiss, 2007). This has been used to model muscle (Blemker et al. 2005).

To further add to the challenge of modelling biological materials, the material properties are inhomogeneous across structures. To establish the most accurate model possible every element would be assigned its own material properties, based on experimentally derived values. With models typically composed of hundreds of thousands, if not millions of elements this is highly impractical. However it has been shown that regional mapping of material properties provides a greater degree of accuracy in strain magnitude measured (Strait et al., 2005). The degree to which modelling accuracy is required depends upon the biological question being addressed. The extent to which material properties affect the results of the simulation can be addressed with a sensitivity analysis (see section 2.5.2).

For the simulation of a mechanical event a structure must be loaded in some way. For biomechanical simulations this load may be a body weight (O'Hare et al., 2012), bite forces (Cox et al., 2011), or muscular loading (Gröning et al. 2012). The force of a muscle can be measured experimentally (Jarvis, 1993), estimated by multibody dynamics analysis (MDA)(Curtis et al., 2010) or physiological cross- sectional area. Most usually maximum contractile muscle force is estimated based on physiological cross-sectional area calculations, which takes into account muscle volume and pennation angle (see section 1.10.2).
Before simulation it is necessary to constrain the model in some way, as it exists suspended in space, and the application of any load will result in a mathematical problem which cannot be solved. In life all biological structures are constrained in some way, and boundary constraints should reflect this as accurately as possible. Ideally the model should not be constrained over a very small number of nodes as this can lead to an unrealistic concentration of stress/strain at this point. It is therefore often useful for boundary constraints to be distant from the structure of interest (Richmond et al., 2005).

In brief, finite element analysis arrives at its solution, using partial differential equations to calculate deformation across each node. The manner in which the nodes are displaced is dependent upon their material properties, boundary conditions and loads applied. The displacement field is then interpolated from the displacements of individual nodes. The strain distribution is derived from this, and the stress derived from the strain (with regard to the elastic modulus) (Richmond et al., 2005). In a three-dimensional problem each node has stress acting upon it in three-dimensions. The entire stress state can be summarised by a tensor. In biomechanical problems a Cauchy stress tensor is often used, as it is useful for materials undergoing small deformations. This is a linear map with 9 components defining the state of stress within a material (Fig.2.13)

.

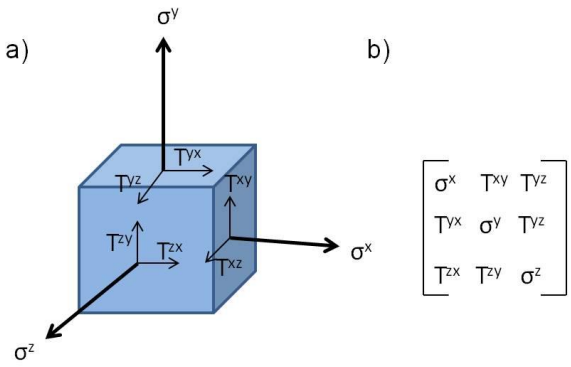

Figure 2.13 Diagram of the Cauchy stress tensor. At each point in an object the stress environment can be described by 3 normal (σ) stresses and 6 shear stresses (T). The Cauchy stress tensor summarises these stress values.

The analysis performed can be, quasi-static or dynamic, implicit or explicit. These terms, and their implications are covered in brief here, for a more thorough analysis see Maas and Weiss (2007). A quasi-static analysis ignores inertial effects. Dynamic analysis includes inertial properties and solves problems in a time-dependent analysis (Maas and Weiss, 2007). Dynamic analysis is therefore very useful for studies focussing upon impact events, such as car crashes, where the effects of inertia play a large role in the resultant forces. However, in small animal simulations the effects of inertia upon the biomechanical environment of a bone will be negligible, and a quasi-static analysis is usually used. An implicit analysis solves equations at every stage of the analysis, ensuring equilibrium of energy is reached, and not continuing the analysis until it is, this results in a more reliable result. However implicit analysis requires longer solving times, and greater computational power than the alternative. Explicit analysis does not re-form the mesh at every stage, to ensure equilibrium but continues, thus it is useful for non-linear dynamic problems, such as impact loading caused by a car crash (Ruan et al. 1994). However, as the energy is not all accounted for at each stage of calculation, error can accumulate. So for simulation were inertia is unlikely to play a large role in determining the mechanical response the implicit method with quasi-static analysis provides more robust solutions (Doweidar et al. 2010).

The sheer quantity of data produced by FEA means that there is no standard result reported. Results are instead interpreted in light of the biological question being addressed. For example the distribution of stress across the structure may be of interest, in which case stress values can be colour coded and mapped across the

structure. Alternatively the magnitude of shear strain within a particular region of the structure may be the focus, in which case nodes across this region can be sampled, and data extracted.

As FEA is a model, and not a real-life experiment it is therefore important to establish to what extent these simulations reflect real loading conditions. To ensure that the combination of geometry, forces and material properties are producing an accurate result, with regards to values produced experimentally a validation study is required (Erdemir et al., 2012). Validation can be indirect, with values compared against already published data, or direct, comparison against experimental data. The validation in general should match the purpose of the computer model (Erdemir et al., 2012). However, FEA is a particularly valuable tool for the investigation of the biomechanics of a location, or situation which is not feasible to measure directly. In this situation is it clearly not possible to directly validate the model, this is the case with models of trabecular bone, which often have no validation (Zhu et al. 2013). In these cases the workflow can still be validated (Stern-Perry et al. 2011; Macho et al. 2005).

Across geometries and within materials there is a range of natural variation across individuals. To establish to what extent natural variation will affect the results generated a sensitivity analysis should be conducted, in which the factors are varied systematically, and the results assessed with respect to the original model (Cox et al. 2011; Stern-Perry et al. 2011; Gröning et al. 2012). Following sensitivity analysis it is possible to define to what extent natural variation in each parameter has on the mechanical performance of the object.

The precision of the model, that is, the degree to which the values produced by the model fit the biomechanical solution can be calculated with a convergence test. A mesh which is too coarse will provide different values to a mesh which is sufficiently dense to reflect the biomechanical situation. Therefore the FE model can be meshed at a relatively coarse density, and run. The model can then be meshed at a higher density and run under identical conditions, and results compared. This process continues until the results between models are not significantly different (Richmond et al. 2005).

2.4 Summary

Electrical muscle stimulation provides many advantages over other methods of increasing skeletal load, including the frequency at which loads can be applied. Possibly the greatest advantage is the fact that loads are applied by muscular contraction making it an interesting method for investigating musculoskeletal responses to increased loading. To measure and quantify adaptation in bone and muscle phenotype microCT used in conjunction with iodine-enhanced microCT and histology can provide morphological data at macro and microscopic scales. To shed light upon the biomechanical performance of the bone nanoindentation can provide data on the material properties. To characterise the stress and strain experienced across three dimensional structure of the tibia finite element analysis provides a method to simulate muscular loading. An advantage of using a model is that hypothetical adaptations of bone can also be explored. This may shed light upon the biomechanical cues bone responds to, and what effect bone adaptation then has upon its own mechanical environment.

Chapter 3: Concentration-dependent specimen shrinkage in iodine enhanced micro-CT

Chapter 3

Iodine Potassium Iodide (I_2KI) solution can be employed as a contrast agent for the visualisation of soft tissue structures in micro-computed tomography studies (see section 2.2.2). Initial studies suggest that the staining solution can cause substantial specimen shrinkage. As outlined in the introduction, this chapter aims to establish the extent of specimen shrinkage associated with I_2KI staining, for use in musculoskeletal studies.

3.1 Introduction to iodine-enhanced staining

Micro-Computed Tomography (microCT) is an established modality for the non-destructive analysis of mineralised tissue in a co-registered space (section 2.2.2). MicroCT has been used extensively to obtain 3D data on bone density, structure and micro-architecture, often used in conjunction with, or replacing laborious histological sectioning. As reviewed in section 2.2.2 standard microCT does not lend itself well to soft tissue investigation, as soft tissues attenuate very little X-ray energy (see section 2.2.2), resulting in amorphous silhouettes containing little internal detail (Fig.3.1).

Recently, Iodine Potassium Iodide (I_2KI) solution has been used as a contrast agent to improve the imaging of soft tissues via microCT (Fig.3.1). The preferential binding of iodine to skeletal muscles over connective tissue allows the visualisation of bone and muscle, in detail comparable to histology (Fig.3.2). Iodine-stained microCT has proved itself particularly useful for the characterisation of complex musculoskeletal arrangements, such as skulls. A three-dimensional data set of bone and muscle morphology allows for digital reconstruction of the tissues, which provides a data set which can be accessed at need, which is far more convenient than traditional dissection methods. Digital dissection has been successfully utilised in studies of a number of species including buzzard (Lautenschlager et al. 2014), naked mole-rat (Cox and Faulkes 2014), mouse (Baverstock et al. 2013), squirrel, rat, guinea-pig (Cox and Jeffery 2011), alligator (Holliday et al. 2013) and sea turtles (Jones et al. 2012). The fine detail obtained from I_2KI-enhanced microCT is sufficient to study incredibly fine detail, which would present quite a challenge for manual dissection, such as the syringeal muscles of zebra finch (During et al. 2013).

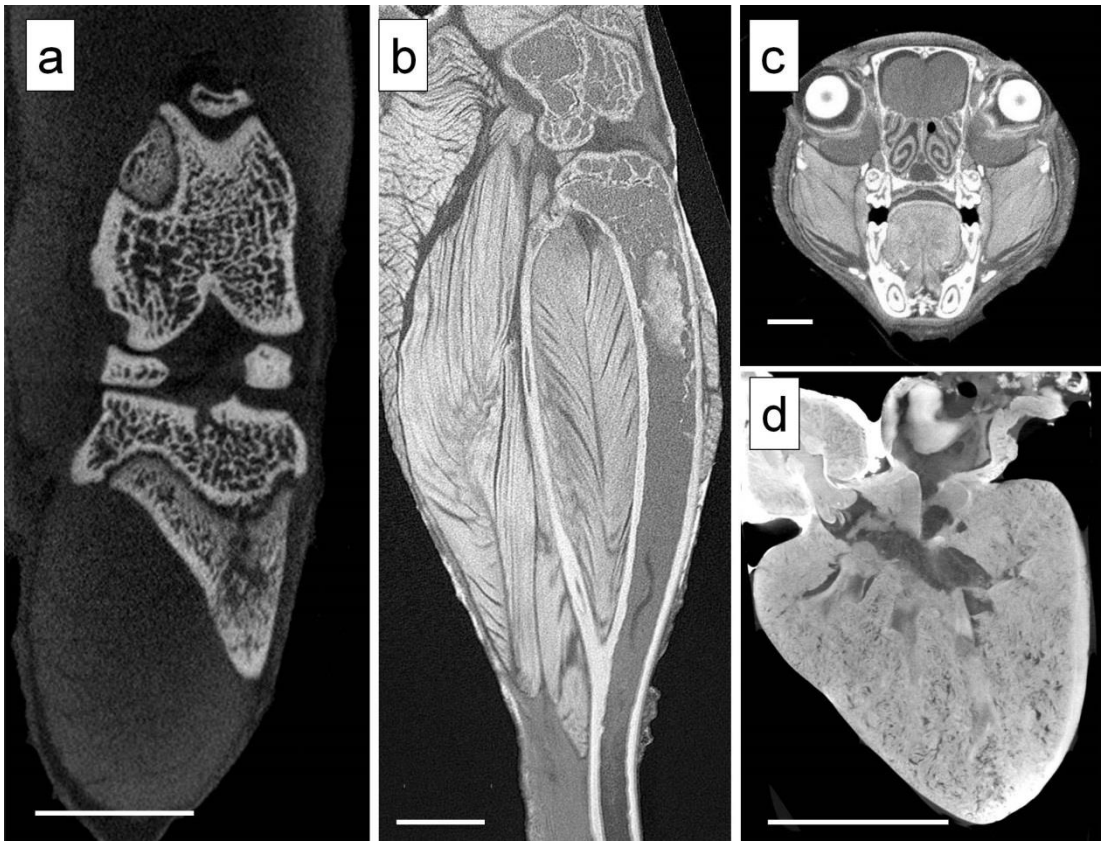

Figure 3.1 Conventional microCT compared with iodine-enhanced microCT. MicroCT scans of a) a mouse knee joint, and I_2KI enhanced scans of b) a mouse head, c) a bream (*Abramis brama*) heart, d) a mouse hindlimb. Scale bars are 2mm.

The simple iodine stain has also been used to characterise the arrangement of cardiac muscle in three-dimensions (Aslanidi et al. 2012) and provided stunning high-resolution visualisation myofibre orientation (Jarvis and Stephenson 2013). Furthermore, the differential attenuation between the muscle tissue and its embedded neural tissue has allowed detailed, three-dimensional characterisation of the cardiac conduction system (Stephenson et al. 2012).

Three-dimensional data of bone and muscle is particularly useful for the creation of computational models. Cardiac myofibre data has been used for simulations of electrical propagation through the tissue (Haibo et al. 2013). Whilst skeletal muscle data is particularly useful for biomechanical simulations of muscle forces and activity patterns (Aslanidi et al. 2012; Cox et al. 2012).

Remarkably, despite the long history of I_2KI staining for starch in histology (Wick 2012), the exact mechanism of I_2KI staining remains unknown. Iodine's use as a

colour changing starch indicator test (Ameen and Abedin 1975) implies that the iodine is trapped in the structure of complex carbohydrate molecules such as those found in glycogen (see Jeffery et al 2011 and section 2.2.2). Recent work to investigate I_2KI distribution using backscattered electron scanning microscopy is likely to provide more definitive answers in the future (Boyde 2012).

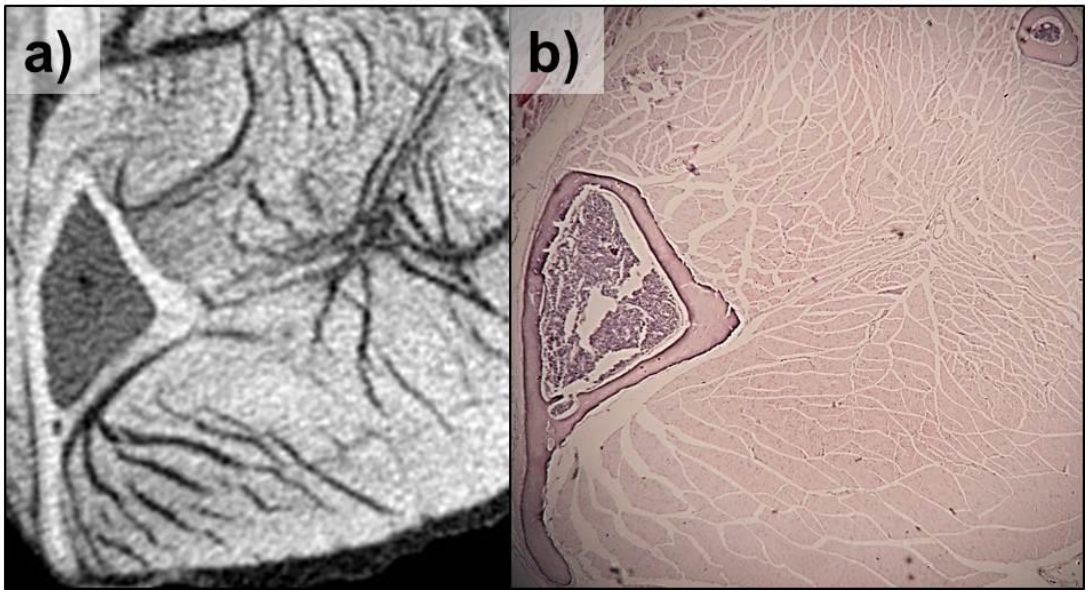

Figure 3.2 MicroCT and histological visualisation of the murine hindlimb. The use of iodine as a contrast agent for microCT allows for the visualisation of muscle and bone, providing detail comparable to that achieved by histological preparation of bone and muscle tissue. Here the same mouse hindlimb has a) been imaged using iodine-enhanced microCT and b) sectioned, stained and visualised with light microscopy.

A potentially major limitation of I_2KI enhanced microCT is soft-tissue shrinkage. Initial studies have suggested that this staining process is associated with shrinkage beyond that normally found with, for example, tissue fixation. As discussed in section 2.2.1, specimen deformation during preparation is a problem common to many tissues and techniques such as histology and scanning electron microscopy (Boyde and Franc 1981; Boyde and Maconnachie 1981; Boyde and Maconnachie 1980; Boyde and Maconnachie 1983). Understanding the degree of shrinkage and factors that may introduce variability in the shrinkage is key to the application of the technique to quantify soft-tissues.

The aim of this chapter is to quantify the degree of shrinkage in dissected mouse skeletal muscle, cardiac muscle, and cerebellum, over a range of I_2KI concentrations and incubation periods. Alternative formulations of iodine and fixatives used for imaging, for example, embryos (Metscher 2009) have yet to be proven effective for imaging the comparatively larger samples described in the aforementioned papers. Hence, the current chapter will focus only on solutions of I_2KI and formalin and compare findings against generally accepted levels of shrinkage associated with conventional forms of preservation (i.e. freezing, formalin, ethanol and glutaraldehyde).

3.2 Materials and Methods

3.2.1 Specimens

Tissue samples were harvested from post-mortem BL6 mice, selected because it represents the most commonly used strain of the most commonly used mammalian model species. The soft tissues investigated were skeletal muscle, cardiac muscle, and brain. These represent a broad range of tissues that have been the focus of recent I_2KI studies. The skeletal muscle samples consisted of whole tibialis anterior, triceps surae, gluteus medius and rectus femoris muscles. These were dissected from 5 previously frozen (-10°C, for in excess of 6 months), and 7 non-frozen mice. Cardiac muscle samples consisted of 7 dissected and then bisected hearts. These were washed to remove any residual blood. Brain tissue was represented by 7 dissected cerebelli. A total of 58 samples from 12 mice were investigated for tissue shrinkage.

3.2.2 Volume measurements

Volumes were measured using a microvolumeter (Fig.3.3) based on the apparatus described by Douglass and Wcislo (Douglass and Wcislo 2010) but with the addition of a laser level to improve the precision of our measurements of fluid displacement. The samples were first immersed in water, and then blotted dry. They were then placed in a water-filled specimen cylinder, which was attached via a water-filled polypropylene tube to a 1ml measurement syringe. The level of the water in the specimen cylinder was measured with a laser beam, which was reflected off the surface of the water on to a wall. As specimens were placed in the receptacle cylinder, the reflected laser point was deflected. The measurement syringe was then withdrawn until the laser point was back to its original position, giving the volume of

the sample. Each sample was immersed in water for less than a minute whilst it was measured to reduce the effect of osmotic gradients upon accuracy. To ensure movement of water molecules during measuring was not significantly altering the measurements, unstained and stained tissues (20% I_2KI for 14 days) were measured repeatedly using the microvolumeter filled firstly with water (hypotonic relative to the samples), then with formaldehyde dissolved in phosphate buffered saline (PBFS, hypertonic) and finally with 20% I_2KI (to represent the most extreme hypertonic solution).

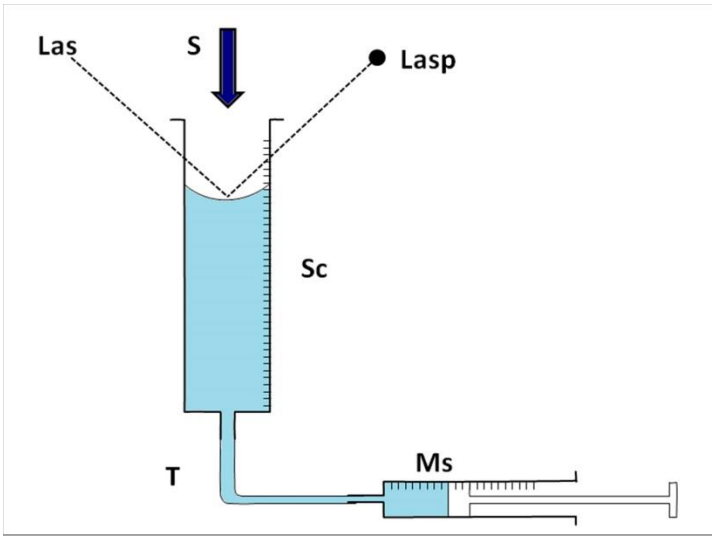

Figure 3.3. Schematic representation of the microvolumeter apparatus. The equipment used to measure the volume of the specimens. Las, Laser source; Lasp, Reflected Laser point; T, tubing; Ms, measurement syringe; Rc, receptor cylinder; S, specimen. Apparatus and figure modified from Douglass and Wcislo (2010).

The apparatus was validated with reference to standard samples (steel bearings) of known diameter from which the volumes were calculated [$v = (4/3)\ \pi\ (d/2)^3$]. Five repeated volume measurements were taken for each bearing. To validate the microvolumeter apparatus at lower volumes, 2 muscles which had been previously stained using I_2KI and scanned via microCT were measured using computational stereological methods, and were then measured using the microvolumeter. Findings were compared on the basis of least-squared regression analysis.

Baseline volumes for all samples were measured immediately post dissection. Each measurement was taken as the average of 5 repeats with the specimen being

blotted between each repeat to remove excess fluid. Samples representing each tissue type were then immersed in 10% formaldehyde dissolved in phosphate buffered saline (PBFS), 3% glutaraldehyde in phosphate buffered saline, 70% ethanol or solutions of 2%, 6%, 10%, and 20% Iodine Potassium Iodide (I_2KI) dissolved in 10% PBFS. Samples were then measured at intervals of 1, 2, 7, 14, and 28 days following the procedure outlined above. The measurement variables are outlined in table 3.1.

3.2.3 Statistical analysis

All statistical analyses were conducted in Excel Office 2007 and PAST v2.15 (Hammer et al, 2001). For all microvolumeter measurements, the volumes were recorded 5 times and an average volume calculated. Differences between variables were tested for using a two-tailed unequal varience t-test, with p values>0.05 considered significant. The accuracy of the microvolumeter equipment was tested for by regression analysis, with average measured volumes plotted against calculated volumes.

Average volume measurements were taken over a series of time points. This data were then used to calculate the percentage of initial sample volume, for comparison between different sized samples (sample volume/intial sample volume x 100). Percentages of initial volumes were plotted against the incubation period to demonstrate the progressive shrinkage of samples.

The original volume of samples was plotted against the volume of the same samples at 14 days to test for a size related relationship of the extent of shrinkage. Least-square regression was used to establish slopes and euations of each iodine-concentration.

Least-squared multiple regressions were calculated in order to capture the interdependency of shrinkage on the three principal variables of, initial sample size, I_2KI concentration and incubation time. This allowed the creation of formulae to predict the extent a sample will shrink.

Table 3.1 Summary of experimental conditions for shrinkage experiments. TA, tibialis anterior, TS, triceps surae, GM, gluteus medius, RF, rectus femoris

Tissue type	Previous treatment	Solution	Sample	Measurement (days post dissection)
Skeletal Muscle	Frozen, -10°C for an excess of 6 months	PBFS, I_2KI 2%, 6%, 10%, 20%	Muscles, TA, TS, GM, RF for each conc.	0, 1, 2, 7, 14, 21, 28
Skeletal Muscle	none	PBFS, Glutaraldehyde, 70% ethanol, I_2KI 2%, 6%, 10%, 20%	Muscles, TA, TS, GM, RF for each conc	0, 1, 2, 7, 14, 21, 28
Cardiac Muscle	none	PBFS, Glutaraldehyde, 70% ethanol, I_2KI 2%, 6%, 10%, 20%	A bisected heart, for each conc.	0, 1, 2, 7, 14, 21, 28
Cerebellum	none	PBFS, Glutaraldehyde, 70% ethanol, I_2KI 2%, 6%, 10%, 20%	A cerebellum sample at each conc.	0, 1, 2, 7, 14, 21, 28

3.3 Results

Repeated measurements in different volumeter reservoir solutions showed no significant difference ($p>0.05$, t-test of means) for either stained or unstained samples. This demonstrates that the hypotonic water reservoir has no significant effect on the measurements.

Findings for the standard volumes showed that the mean repeated microvolumeter readings were not significantly different from the microCT estimates of muscle

volume or the calculated steel bearing volumes (Fig.3.4). Regression analysis for the combined data gave a slope though the origin of 0.998 (R^2=0.9997), and an average error of only +/- 0.00262ml (ranging from +0.005 to -0.007ml). This level of error (+/- 1.36% average, +/-0.21 to 2.8% range) is low relative to the changes of tissue volume under investigation (see below).

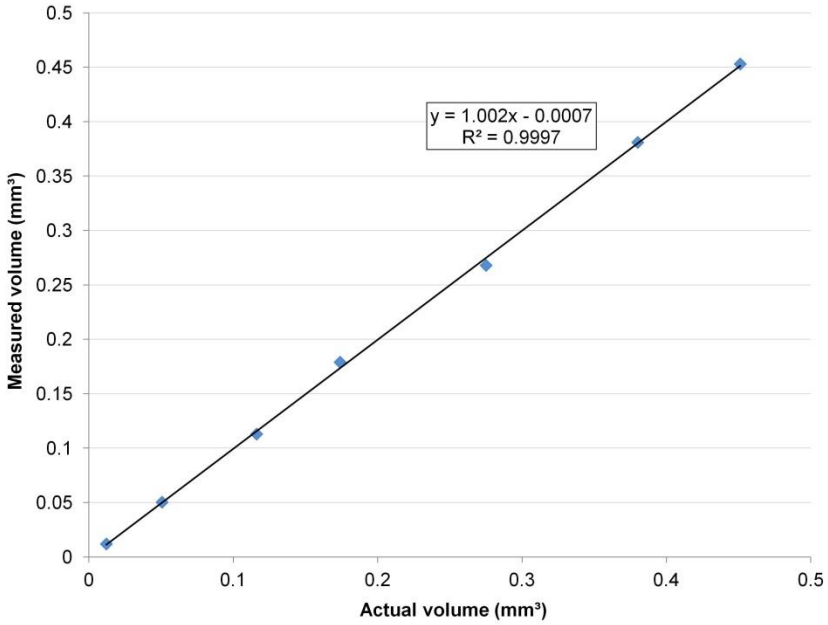

Figure 3.4 Regression analysis of measured ball-bearing volume against actual volume. The accuracy of the microvolumeter apparatus was tested by measuring the volume of ball-bearings of a known volume. The measured volumes of ball-bearings are plotted against their actual volumes.

Tissues immersed in the 3 different fixatives showed markedly different changes in volume. After immersion in PBFS all of the samples underwent an initial rapid increase in volume, and a subsequent, far more gradual decrease in volume. Immersion in 70% ethanol resulted in a gradual decrease in tissue volume. The tissue samples immersed in glutaraldehyde initially swelled and then began to shrink, but on average remained a little larger than their initial volume (Fig.3.5).

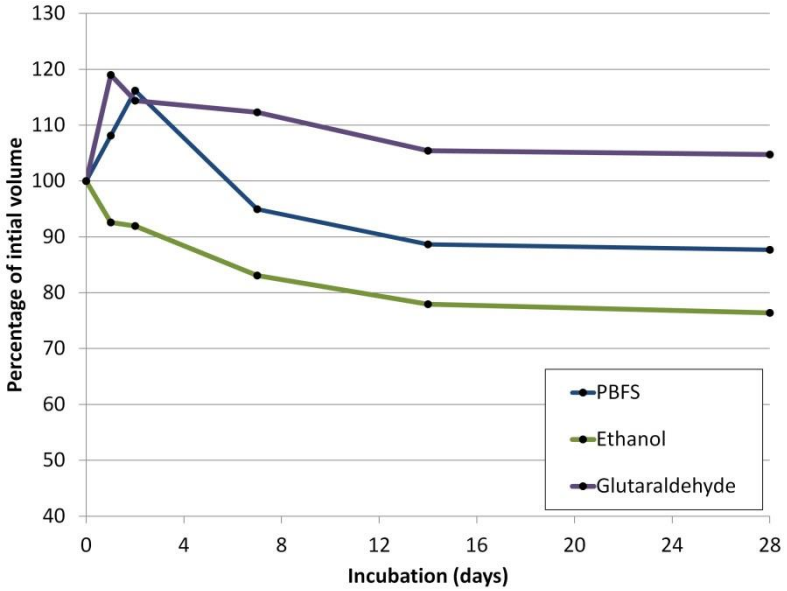

Figure 3.5 Average tissue shrinkage caused by commonly used fixatives. A graph showing the average percentage of the initial volume of skeletal muscle, cardiac muscle and cerebellum samples immersed in 10% PBFS, 70% ethanol or 3% glutaraldehyde (GlutA) for a period of 28 days, (n=6 for each fixative).

Immersing specimens in I_2KI solution (dissolved in PBFS), results in a rapid decrease in volume in both freshly dissected and previously frozen specimens of skeletal muscle. There was no significant difference ($p>0.05$) between the volume of samples previously frozen and non-frozen (Fig.3.6). Subsequent analysis therefore used both frozen and un-frozen skeletal muscle data in order to maximise the data set.

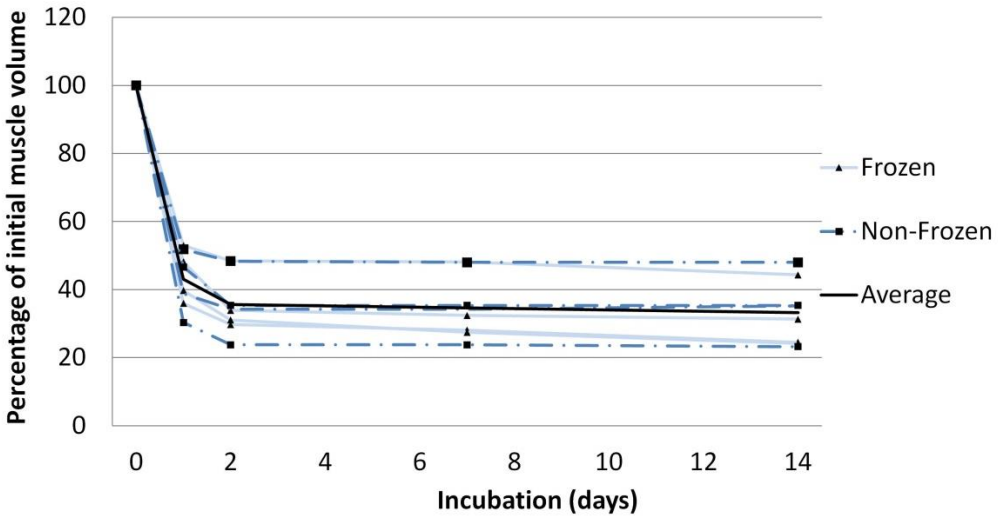

Figure 3.6 The difference in tissue shrinkage caused by I_2KI staining between previously frozen and unfrozen skeletal muscle. A graph showing the proportional decrease in skeletal muscle volume over 14 days in 20% I_2KI in both previously frozen (solid light blue line, n=4) and un-frozen (dashed dark blue line, n=4) specimens. The average of the frozen and un-frozen specimens is displayed in black.

All three tissue types showed a concentration dependent shrinkage after immersion in I_2KI solution (Fig.3.7) which was more extensive than that brought about by immersion in PBFS alone. A higher I_2KI concentration resulted in a greater level of shrinkage. The cerebellar samples showed least shrinkage, and the skeletal and cardiac samples showed similar levels of shrinkage (Fig. 3.8). The muscle samples undergo an initial rapid phase of specimen shrinkage over the first 2 days of staining, with the rate beginning to reach a plateau at around 7 days. The higher I_2KI concentrations brought about a more rapid and extensive shrinkage than the lower concentrations.

Table 3.2 The average percentage volume of skeletal muscle volume remaining after 14 days immersion in PBFS or I_2KI. Standard deviation values are in brackets.

Fixative	Average/ Percentage of original volume after 14 days (±SD)
PBFS	81 (±15.35)
Glutaraldehyde	105 (±8.18)
70% Ethanol	78 (±7.24)
2% I_2KI	74 (±7.08)
6% I_2KI	58 (±11.40)
10% I_2KI	53 (±9.52)
20% I_2KI	33 (±9.34)

Figure 3.7 Bisected mouse hearts stained in different iodine concentrations, in a similar orientation on day 4 of immersion in: a) 10% PBFS, b) 2% I_2KI, c) 6% I_2KI, d) 10% I_2KI, e) 20% I_2KI. On day 0 all 5 samples were measured as being between 0.07-0.09ml. Image obtained by photography, and to scale, scale bar 5mm.

There is a linear relationship between the original volume of the tissue sample and the volume after 14 days of immersion (Fig. 3.10) with the gradients dependent upon the concentration of I_2KI used. Figure 3.10 illustrates that there was no correlation between the original tissue volume and the percentage remaining of the original volume after 14 days of immersion in each solution. Therefore smaller samples did not show more extensive shrinkage than larger samples. Some concentrations in figure 3.10b appear to show weak correlations between original muscle size and the degree of shrinkage experienced (see 2% I_2KI) but none were found to be statistically significant. For all microvolumeter data see Appendix 1.

Figure 3.8 Graph of tissue volume across a 28 day incubation period. Graphs show the percentage of the initial tissue volume after immersion in differing concentrations of I_2KI solution, or PBFS over a 28 day incubation period for: a) skeletal muscle, b) cardiac muscle, c) cerebellum.

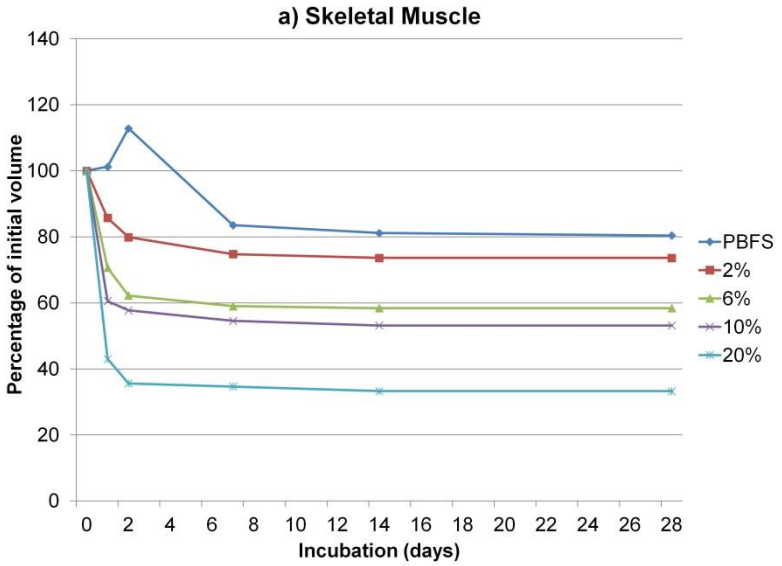
a) Skeletal Muscle
Percentage of initial volume
Incubation (days)
PBFS
2%
6%
10%
20%

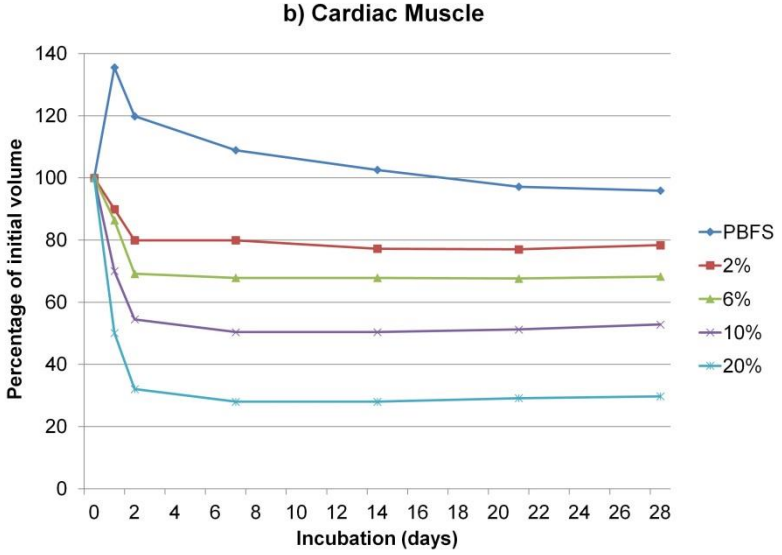
b) Cardiac Muscle
Percentage of initial volume
Incubation (days)
PBFS
2%
6%
10%
20%

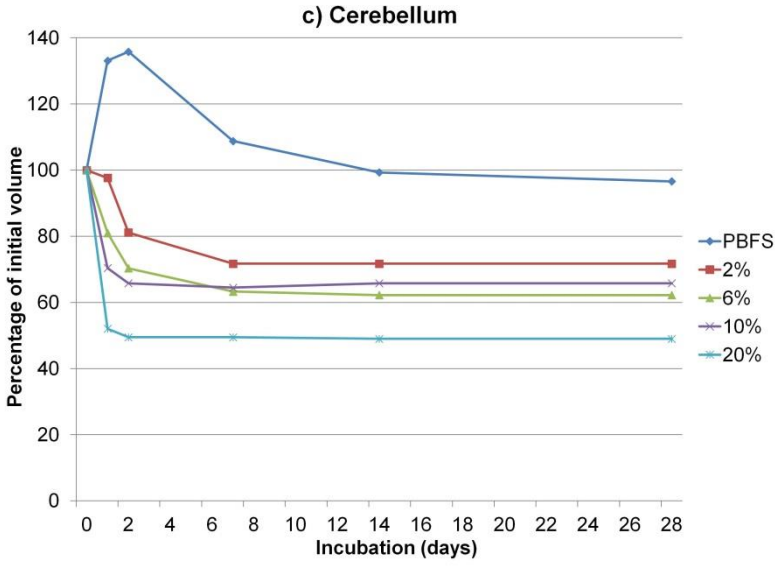
c) Cerebellum
Percentage of initial volume
Incubation (days)
PBFS
2%
6%
10%
20%

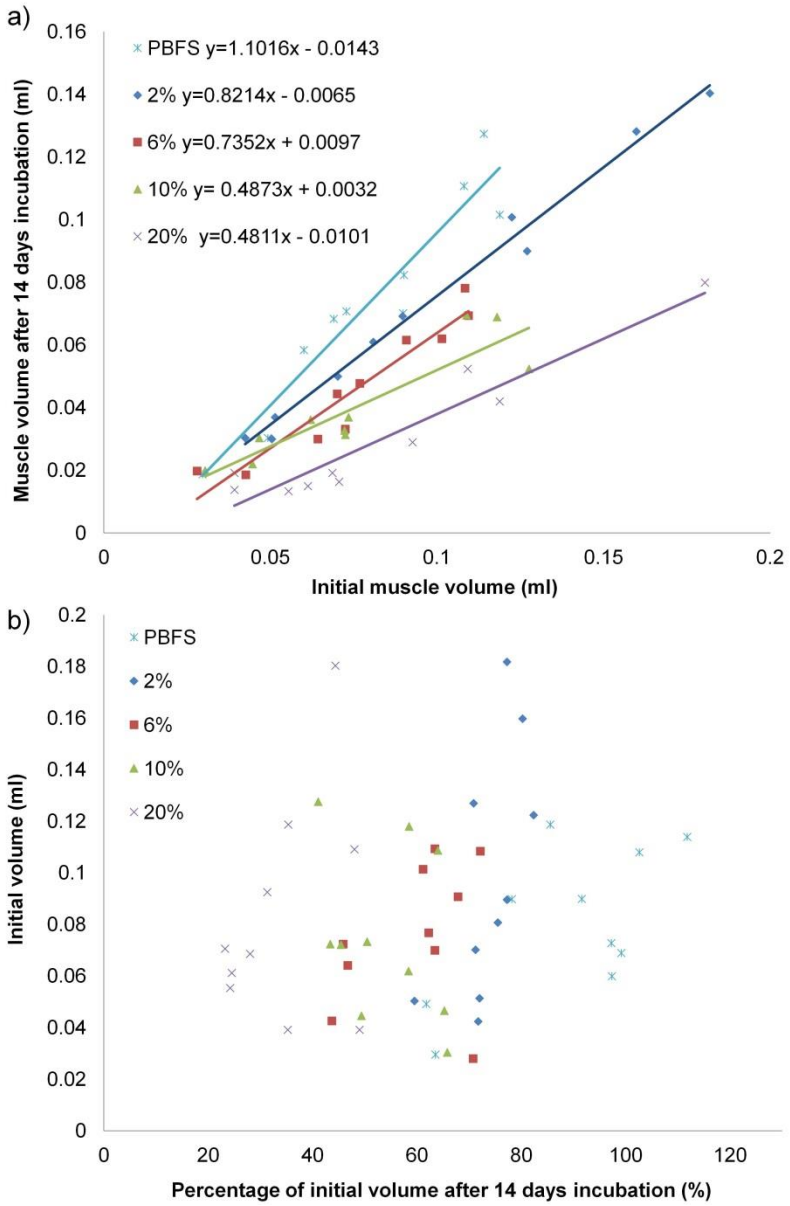

Figure 3.9 Graphs demonstrating the influence of initial sample volume on the extent of shrinkage. a) Plot of skeletal muscle volume after 14 days incubation, against initial tissue volume. Least square regression slopes and equations are shown. b) Comparison of initial skeletal muscle sample volume versus the percentage of sample volume remaining after 14 days incubation. Both previously frozen and unfrozen material was used to maximise the data set. Spearman rank correlation coefficients were 0.48 ns for PBFS, 0.55 ns at 2%, 0.35 ns at 6%, 0.41ns at 10%, 0.19 at 20%.

Least-squared multiple regressions were calculated in order to capture the interdependency of shrinkage on the three principal variables of, initial sample size, I_2KI concentration and incubation time. The R^2 values (coefficient of determination) are given in Table 3.3, and demonstrate that in all three tissues the percentage reduction in volume is most closely related to I_2KI concentration. Only in cardiac samples was there a secondary relationship, with initial sample size, however the range of sample sizes had very little influence beyond 14 days as the shrinkage plateaus between 3 and 7 days (Fig. 3.8). The multiple regressions can be used to create a formula to predict the percentage volume of the original sample following staining:

Skeletal muscle E.vol. = 90.66 (o.vol) - 2.18 (conc.) - 0.66(t) + 75.39;

Cardiac muscle E.vol. = 463.77 (o.vol) - 2.06 (conc.) - 0.97 (t) + 49.32;

Cerebellar E.vol. = -102.51 (o.vol) - 1.70 (conc.) - 0.79 (t) + 92.28

(o.vol = original volume in ml, conc. = I_2KI concentration in %, and t = incubation time in days, E.vol.= end volume, as a percentage of original volume).

Table 3.3 Multiple regression statistics for shrinkage experiments. R^2 values indicate the strength of the relationship between each variable and the overall percentage shrinkage of the tissue. Individual R^2 values for each determinant are given in [ ]. N reflects the number of samples, each of which is recorded for each variable.

Tissue type	N	Multiple R^2	Original Volume (ml) [R^2]	I_2KI Concentration (%)[R^2]	Incubation (days) [R^2]	Intercept
Skeletal	128	0.77	90.66 [0.06]	-2.18 [0.70]	-0.66 [0.04]	75.39
Cardiac	16	0.91	463.77 [0.73]	-2.06 [0.83]	-0.97 [0.07]	49.32
Cerebellar	16	0.83	--102.51 [0.02]	-1.70 [0.71]	-0.79 [0.10]	92.28

Table 3.4 Linear regression statistics for shrinkage experiments. Spearman's rank correlation coefficient and p-value statistics indicating the relationship between the overall percentage shrinkage of the tissue and each of the variables independent of the other variables investigated. R-rank gives the strength of correlation between the variables (±1 reflects a strong correlation, 0 reflects a weak correlation). P-values indicate the significance of this correlation ($p < 0.05$ is significant).

Regression series	R rank	p-value	RMA slope (a)	95% confidence interval	b
% skeletal muscle vol. vs. original vol.	0.21	*	444.55	520.2 to 387.4	19.634
% skeletal muscle vol. vs. I_2KI conc.	-0.82	***	-2.6412	-2.434 to -2.864	83.763
% skeletal muscle vol. vs. time	-0.23	**	-3.4322	-2.974 to -3.892	79.265
% cardiac muscle vol. vs. original vol.	0.74	***	1980.5	2377 to 1443	-98.57
% cardiac muscle vol. vs. I_2KI conc.	-0.90	***	-2.9187	-2.32 to -3.568	89.087
% cardiac muscle vol. vs. time	-0.36	ns	-3.7929	4.306 to -5.738	84.116
% cerebellum vol. vs. original vol.	0.28	ns	713.94	1413 to -936.4	33.034
% cerebellum vol. vs. I_2KI conc.	-0.84	***	-1.9077	-1.32 to -2.624	84.712
% cerebellum vol. vs. time	-0.38	ns	-2.479	2.175 to -4.033	81.463

3.4 Discussion

The technique of visualising complex soft-tissue, three-dimensional shapes by microCT with contrast agents was originally employed by Metscher (2009). As discussed in section 2.2.2, of these contrast agents, only one (I_2KI) has been used extensively to examine skeletal muscle of post-natal specimens (Jeffery et al. 2011; Cox and Jeffery 2011; Hautier et al. 2012). With interest increasing in this contrast technique it is likely to find many more applications, particularly in anatomical and biomechanical studies. It is therefore important to determine the alteration to the normal morphology resulting from its use.

Fixation of tissues aims to prevent cellular breakdown whilst preserving the tissue's shape, volume and components as close to their living state as possible. No fixative is currently available which is capable of fixation without some degree of distortion, the mechanism of which is not fully understood (Hopwood 1982). For this reason 3 commonly used fixatives (ethanol, glutaraldehyde and formalin) at commonly used concentrations were investigated for subsequent volume changes.

Of the three fixatives, glutaraldehyde produced a fixed sample closest to the specimen's original volume. It has been reported that 3% formaldehyde solution has a far higher osmolarity (approx. 1000 mOsm) that that of a 3% solution of glutaraldehyde (approx. 300 mOsm), (Bacallao et al. 2006) and so a far larger degree of shrinkage would be expected from tissue immersed in PBFS than glutaraldehyde. However, it is important to note that earlier studies have suggested that aldehydes exert no effective osmotic pressure (Young 1935). In a number of studies cells immersed in glutaraldehyde have been noted to swell (Arborgh et al. 1976) as figure 3.5 shows. However most studies show that glutaraldehyde fixation causes tissue shrinkage (Gusnard and Kirschner 1977). The difference between results shown here and those in the literature may be due to difference in the buffer (PBS instead of sodium cacodylate), or a difference in the timescale over which the volume changes were recorded. Ethanol immersion resulted in a prolonged shrinkage of the tissue. Fixation by ethanol rapidly changes the hydration state of tissues, removing water and hence reducing their volume. Figure 3.5 shows a similar (though not quite as extensive) degree of shrinkage as that recorded by Boyde and Maconnachie (1980), who also measured the relationship between the concentration of ethanol and degree of tissue shrinkage. Of the 3 solutions, formalin is by far the most prevalent in the preservation of whole bodies and organs, and so the most suitable fixative in which to dissolve an Iodine staining solution.

The next challenge was to determine whether there was any shrinkage over and above that observed by formalin fixation with the addition of I_2KI to the PBFS solution. Addition of I_2KI to the specimen's fixing solution resulted in a pronounced period of specimen shrinkage. The magnitude of shrinkage varied with tissue type, probably due to differences of cellular organisation and composition, altering the diffusion in to and out of the tissue. For example, Weisbecker (2012) found that the cerebellum shows less shrinkage than other brain tissue as a result of formalin fixation. This discrepancy was attributed to smaller cell size, and higher neuron density within the cerebellum. In the present study, shrinkage also varied in relation to incubation time, with the greatest change occurring in the first few days. By far the greatest influence on shrinkage, however, was I_2KI concentration. Samples in solutions of PBFS containing 20% I_2KI shrank by as much as 70% (cardiac muscle) compared with a 20% reduction at 2% I_2KI. The effects of concentration are clearly shown in Figure 3.7. In comparison, the influence of initial sample size on percentage shrinkage experienced was negligible. Although the I_2KI solution probably diffuses more rapidly into the smaller samples, due to greater surface area to volumes ratios, the resulting shrinkage as a proportion of original sample size is not statistically different from that experienced by larger specimens after 14 days (Figure 3.10). The volume range used in this study was limited, and it may be that with a larger discrepancy in initial volume a relationship between initial volume and percentage shrinkage would become apparent. Indeed, the largest specimen currently to utilise this method, an alligator head, notes considerably less than 50% shrinkage (Gignac and Kley 2014).

Since it is not always practical to fix all specimens as soon as they are obtained, storage of specimens by freezing and then defrosting is a common and convenient alternative. We therefore wanted to establish if freezing specimens further exacerbated tissue shrinkage. Our findings suggest that freezing and subsequent thawing of specimens before treatment with fixative and I_2KI does not alter the overall magnitude at which the skeletal muscle specimens shrank after immersion with I_2KI (Fig.3.6).

The microCT data in figure 3.1 and in Jeffery et al (2011) show large dark bands within the skeletal muscle (Fig.3.1d). These bands are not seen in cardiac tissue and so may indicate connective tissue. Alternatively, as the specimens were scanned in air, the bands may signify air-filled gaps as a result of tissue cleavage. The possibility of tissue cleavage was commented on by Degenhardt et al (2010), in

which stained embryos showed a large black region between the diaphragm and the heart. This region was larger in embryos stained at higher concentrations of I_2KI. This would imply that these bands represent air or retained rinsing buffer (samples are routinely rinsed and blotted before scanning to remove surface coat of I_2KI solution). Given the degree of shrinkage reported here it seems likely that some degree of tissue cleavage may occur.

Metscher's paper (2009) demonstrated that a range of solutions were capable of increasing soft-tissue contrast in small specimens a few millimetres in size: 1% iodine in ethanol, Phosphotungstic acid, as well as established stain osmium tetroxide. No doubt these other compounds together with appropriate fixatives also result in tissue deformation (see for example Schmidt et al. 2010 embryo work). However, shrinkage associated with the above stains has not been investigated here or elsewhere, as they have not been used successfully for contrast enhanced imaging of musculoskeletal anatomy in larger specimens. In particular, osmium tetroxide has been found to offer inferior bone-muscle contrast (Aoyagi et al. 2013).

The tissue samples measured in the present study were isolated tissues; it is not clear if the same degree of shrinkage would occur in, for example, a whole head, limb, or indeed a whole animal. It is possible that there would be the same volume reduction, but that the bony restraints would create tissue cleavage in the soft tissues saturated with I_2KI. It also seems likely that shrinkage would be less in-situ than reported here as the tissues, particularly muscles, are attached, enclosed or otherwise supported by surrounding structures like bone. As part of an investigation using 10% I_2KI as a contrast agent, shrinkage measurements of whole skulls reported only a 5% decrease in volume (Tahara and Larsson 2013). This is almost certainly due to the fact that they were measuring a fully ossified skull which could not shrink to the same degree as the soft tissues investigated here.

As the exact chemistry of fixation and staining are not fully understood it is not possible to give a definitive biochemical explanation for the tissue shrinkage documented here. A possible explanation for the concentration-dependent pattern is that increasing the iodine content in the solution is creating an increasingly hypertonic solution so that water moves along the osmotic gradient, out of the tissue causing shrinkage. This is supported by

found that tissue distortion was reduced, but not prevented by using isotonic solutions of I_2KI.

The concentration-dependent nature of tissue shrinkage reported here is an important consideration for experimental design. If an iodine solution is too low then samples will not be fully stained and only the most superficial muscles will be stained (Jeffery et al. 2011). As I_2KI has the potential to be highly important in musculoskeletal and biomechanical analyses the volume changes it produces are of the upmost importance.

In conclusion, the evidence presented here suggests that I_2KI enhanced microCT cannot be used for obtaining absolute quantitative data. However, given the many advantages this technique provides over the alternatives for studying musculoskeletal form (see section 2.2.2) it should not be disregarded. Comparative data may be obtained provided iodine concentration and incubation times are standardised across specimens. If these conditions cannot be met then some adjustment of the results may be necessary with reference to the values reported in this chapter.

Chapter 4: Morphological and histological adaptation of muscle and bone to repetitive electrical muscle stimulation

Chapter 4

As outlined in the introduction, the muscular and skeletal systems are functionally and spatially interlinked, acting mechanically as a unit. Therefore the fact that muscle is rarely used as an experimental method to load bone is surprising. In Chapter 2, different methods for applying controlled muscular contraction were reviewed and electrical muscular stimulation emerged as the best option currently available. As, both muscle and bone are highly plastic in response to mechanical forces, they are likely to undergo an interlinked response to increased muscular contraction. Therefore, to characterise the morphological musculoskeletal response both tissues require assessment. As established in Chapter 2, a method which presents a real advantage for musculoskeletal visualisation is I_2KI-enhanced microCT. This technique, as the previous chapter established, is associated with a considerable degree of shrinkage to soft tissues. Using recommendations from the previous chapter I_2KI-enhanced microCT will be used alongside standard CT, histology, material testing and biomechanical simulation. This powerful combination of techniques allows the quantification of morphological and material transformation.

4.1 Introduction

In 1892 Julius Wolff famously proposed a set of laws concerning bone adaptation to mechanical stimuli (1892). His broad principle, that bone is able functionally to adapt to its mechanical environment, is widely accepted (Bertram and Swartz, 1991; Ruff et al., 2006). The skeletal environment is heavily influenced by contractile and kinematic forces generated by skeletal muscle during movement. Despite this, as outlined in section 1.12, muscular contraction is rarely used experimentally to load bones under closely controlled conditions (Lanyon et al., 1982; Turner et al., 1994; Akhter et al., 1998; Gross et al., 2002; Poulet et al., 2011). Typically, animals are either anaesthetised and the bones are loaded in daily sessions using an external mechanical device or they are subjected to exercise regimes (Umemura et al., 1997; Buie and Boyd, 2010; Hamann et al., 2012). These exercise regimes have reported mild osteogenic responses that are highly variable between individuals, probably reflecting intraspecific variations of morphology, physiology and aptitude. Of the methods of controlling muscular contraction review in section 2.1, electrical muscular stimulation (EMS) via the motor nerve offers several potential advantages over the above paradigms. Perhaps its greatest advantage is experimental control; neuromuscular stimulation can generate contractions of the whole muscle for a pre-

set time period at a pre-set frequency. The stimulation can also be delivered continuously over days or weeks without the need for anaesthesia, supervised exercise sessions or mechanical loading protocols, offering a greater potential to resolve the integrated changes of muscular and skeletal phenotype.

Here, recent advances in implantable microelectronics are used to determine the effect of electrical neuromuscular stimulation on the global and local morphology of bone. A period of EMS increases mechanical forces in both the muscle and bone and thus provides a stimulus for an adaptive shift in the musculoskeletal phenotype. Based on the principles of the mechanostat theory (see section 1.4) morphological changes are likely to occur within regions of greatest strain. In order to assess the extent to which the musculoskeletal phenotype is transformed, a combination of microCT and iodine-enhanced microCT (see section 2.2.2) imaging techniques are used. Three-dimensional data sets allow computational simulations of loading, allowing histological analysis and nanoindentation to be targeted to regions of biomechanical interest.

4.2 Methods and Materials

4.2.1 Animal model

Preliminary work was conducted in mice. Stimulators were implanted into 6 BL6 mice, however, 3 of the stimulators failed within 2 days of implantation. The experiments were therefore moved to rats, in which a larger implantable stimulator, which has been used more extensively, could be used. This allowed options in the stimulation patterns. As continuous stimulation results in high muscular atrophy (Ferguson et al. 1989), a burst pattern was selected. Bone deposition is not a fast process with a maximal response to an established loading protocol using high forces being achieved 4-8 days after the initial load (Forwood et al. 1996). Therefore, as this protocol used a smaller load, a period of 28 days was selected, as this would allow both muscle and bone ample time to show a response.

Nine male, eight week-old Wistar rats (weights 228-282g) underwent surgical implantation of miniature neuromuscular stimulators (Russold and Jarvis, 2007). It was not possible to conduct a power analysis as this was the first experiment to look at bone morphology in response to electrical stimulation, and therefore it was not possible to estimate the effect. Given the ethical implications of animal work it was decided that 9 was the largest sample size justifiable. Under general isoflurane

anaesthesia (Isoflurane 2%, O_2 49%, NO_2 49%) rats were injected with analgesia (intramuscular Buprenorphine, 0.3mg/ml) and antibiotic (subcutaneous Baytril, 25mg/ml). Incisions were made in the left flank for stimulators to be implanted in to the peritoneal cavity, and sutured in place. The electrodes were passed subcutaneously into the hindlimb and sutured either side of the left common peroneal nerve. The incision was sutured closed; a further intramuscular injection of Buprenorphine was delivered along with subcutaneous saline to replace fluid. Rats were kept warm at all times with a heat pad. Stimulators were switched on by passing a magnet over the implant. Stimulators delivered 0.2ms pulses at 100 Hz for a total of 200ms every 30s, resulting in a total of 9.6 minutes of stimulation per day. Each 200ms burst of stimulation at 100Hz caused a very brief but fused (tetanic, near maximum force) contraction of the muscles in the antero-lateral compartment of the leg (Fig.4.1). The right hand side was left as a contra-lateral control. Animals were free to ambulate throughout the stimulation period and were checked daily for any behavioural disturbance, weight loss and to ensure stimulators were working. Over this time period all animals were considered to be showing normal behaviour. After 28 days of stimulation the animals were euthanized by CO_2 asphyxiation. All experiments received ethical approval and were carried out in strict accordance with the Animals (Scientific Procedures) Act of 1986. To evaluate any possible systemic or surgical effects on the contra-lateral control limb, three additional age, sex and strain matched rats were analysed as controls (no surgery or specific loading regimes).

4.2.2 Imaging

Hindlimbs from 6 experimental and the 3 control animals were removed, and stored in 10% phosphate-buffered formal saline (PBFS). Hindlimbs were imaged along with a hydroxyapatite phantom using the Metris X-tek custom 320kV bay system (University of Manchester). Data were reconstructed at 40µm resolution (isometric voxels). For standard microCT, x-ray tube parameters of 75kV and 200µA were used. As conventional microCT imaging does not provide muscular detail (see section 2.2.2 and Fig.4.2) limbs were stained with I_2KI. To control for concentration-dependent specimen shrinkage (see Chapter 3) all samples were immersed in the same concentration solution (9% I_2KI, dissolved in PBFS) for the same time period (9 days). Specimens were then imaged with microCT for a second time (90Kv; 130uA; 40µm). Hindlimbs from the remaining three experimental animals were subjected to muscle histology (see below).

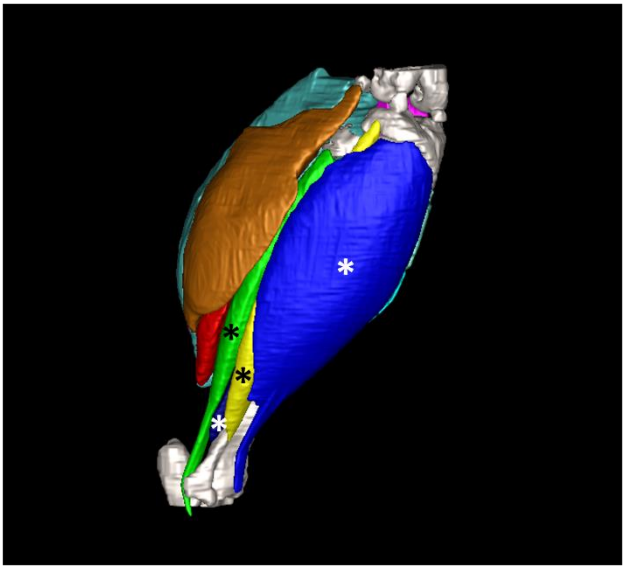

Figure 4.1 A three-dimensional reconstruction demonstrating the muscles which were stimulated by the miniature implantable stimulator. Stimulation of the common peroneal nerve resulted in contraction of tibialis anterior, extensor digitorm longus, peroneus longus and peroneus brevis, all marked with a *.

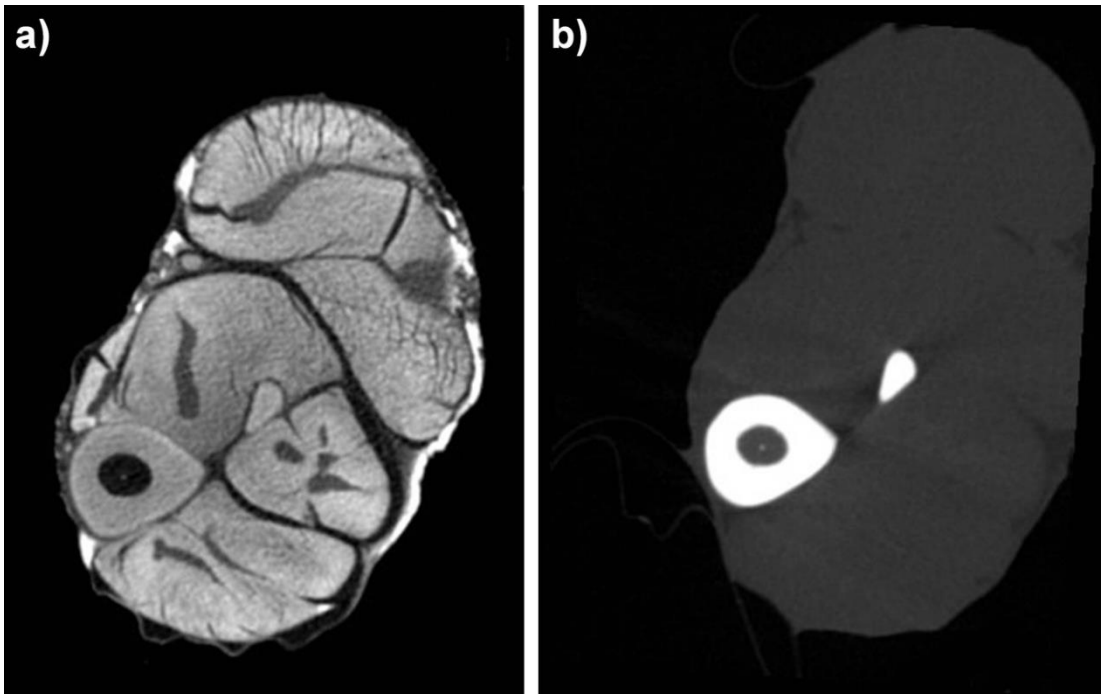

Figure 4.2 Iodine-enhanced microCT compared with standard microCT. Transverse cross-sections of the same mouse hindlimb imaged using a) iodine-enhanced micro-CT, and b) standard micro-CT.

4.2.3 Macroscopic analysis

Relative volumes of stimulated muscles tibialis anterior (TA) and extensor digitorum longus (EDL) were calculated from contrast enhanced microCT images using the stereological method of Volume Est plugin for ImageJ (Merzin, 2008; Schneider et al., 2012).

The maximum force production capability of TA was estimated using I_2KI microCT data. Average fascicle lengths were calculated from 20 fascicles throughout TA. Physiological cross-sectional area was calculated by dividing average muscle fascicle lengths by muscle volume (Alexander and Vernon 1975). Muscle force estimates were then calculated by multiplying PCSA with muscle stress value of 0.3 N mm^{-2} (Strait et al., 2005). Force estimates correspond well with measured values for male Wistar rat TA (Maas et al. 2001).

MicroCT data provides a wealth of different factors which could be measured (see section 2.2.2). Initially, regional measurements were made along the length of the bone to allow targeted further analysis. BMD and cortical thickness measurements in particular were selected as they address the two main ways in which a bone can adapt; through its structure or composition. Regional cortical thickness and bone mineral density (BMD) data were obtained from microCT data using the BoneJ plugin for ImageJ (Doube et al., 2010; Schneider et al., 2012). To capture regional differences, 10 evenly distributed sites were sampled along the posterior and anterior surfaces of the tibia. For BMD measurements, greyscale values from the rat data were compared with greyscale values of a hydroxyapatite phantom by regression analysis. The greyscale values in the rat tibia were then calibrated for hydroxyapatite concentration.

4.2.4 Geometric morphometrics

To establish the control and experimental tibiae with geometries closest to the mean form, geometric morphometrics (GMM) was used. Twelve homologous landmarks and four curves were identified on each tibia (n=6 control, n=6 stimulated, Table 4.1) using Landmark (Wiley et al. 2005). Landmark data were then analysed using Procrustes superimposition and principal components analysis in MorphoJ (Klingenberg, 2011).

Table 4.1 Tibial landmarks used for geometric morphometrics

Number	Landmark description
Point 1	Lowest most anterior point on proximal epiphysis
Point 2	Lowest point on fibular hook
Point 3	Most posterior point on fibular head
Point 4	Point between tibial condyles
Point 5	Highest, most medial point on lateral condyle
Point 6	Highest, most medial point on medial condyle
Point 7	Most anterior point of lateral malleolus
Point 8	Most anterior point on medial malleolus
Point 9	Most lateral point of lateral malleolus
Point 10	Point between tibia and fibula fusion anteriorly
Point 11	Point between tibia and fibula fusion posteriorly
Point 12	Most lateral point of medial malleolus
Curve 1	Tibial ridge (proximal diaphysis to distal extent of tubersity)
Curve 2	Fibular curve (From tibia-fibular fusion distally to the posterior point of proximal fibular diaphysis)
Curve 3	Lateral curve of proximal growth plate
Curve 4	Medial curve of proximal growth plate

4.2.5 Finite element analysis (FEA)

FEA was used to simulate the strains experienced by the tibia-fibula complex during TA muscular contraction. The simulation was based on the control limb geometry closest to the mean form in the experimental sample (see section 4.2.4). Bones for

the selected individual were reconstructed in 3D from the standard microCT data in Amira v 5.4.0 (Visage Imaging, Pro Medicus Limited Melbourne, Australia). The model included the tibia-fibula complex, the talus and the condyles of the femur as well as cartilaginous growth plates, articular cartilages and medullary fat. The talus was set on a rigid body platform. The reconstruction was converted to a tetrahedral mesh in Amira, consisting of 284,766 elements and was parameterised as well as analysed using FEBio version 1.8 (Maas et al., 2012). Constraints were applied to the femoral head and at the rigid body. Bone and fat were modelled as isotropic elastic materials with reference to published values (Turner and Burr, 1993; Rho et al., 1997; Jämsä et al., 2002; Gefen and Dilmoney, 2007; Akhtar et al., 2008). Cartilaginous structures were modelled as near incompressible Mooney-Rivlin materials with reference to published values (Erdemir A, 2010; Sibole, 2010). Loads of 8.7N were applied across TA's attachment site to represent the estimated contractile muscle force (see macroscopic analysis). A force was also applied at the femoral condyles of 0.89N approximating the influence of body mass during stance. Force vectors were based on the attachment sites of the muscle and the typical orientation of the limb. To validate the use of isotropic materials to simulate rat tibiae, a version of the model was validated against previously published strain data for a comparable rat tibia, loaded under ex vivo external compression (Torcasio et al., 2012). For strain calculations 50 nodes were selected across the region of the tibia experiencing peak strains. The average effective strain, 1st principal, 3rd principal and shear strains were calculated.

4.2.6 Focussed bone analysis

Guided by the FEA and cortical thickness measurements, a distal segment of the tibia was selected for further analysis. Measures of bone area and volume for this region were taken with Amira from both hindlimbs of four experimental rats.

4.2.7 Histology

For histological analysis of muscle, fresh TA samples were dissected from the widest part of the muscle in three experimental animals. Samples were transferred to cork discs and snap frozen in isopentane and stored in -80°C for subsequent cryostat processing. Serial frozen sections of 10 µm were cut in a cryostat at -20°C. Sections were stained for myofibrillar ATPase (Tunell and Hart, 1977) which allows identification of type 1, type 2a and type 2b/d fibres in one incubation. Further sections were stained with NADH dehydrogenase, to indicate the mitochondrial

content of the muscle fibres and to cross-check fibre identification (see section 2.2.1).

For bone histology the individual that was closest to the mean shape was selected. Guided by the FEA, the distal portion of the tibia was targeted for histological analysis. A distal portion of the tibia was cut from the rest of the bone using a slow speed diamond saw, and samples were immersed in 12% ethylenediaminetetraacetic acid (EDTA) diluted in 10% formalin, pH 7.4. Following fixation and decalcification, tissues were processed for histology and embedded in paraffin wax. Paraffin blocks were sectioned at 5µm intervals using a semiautomatic microtome, mounted, and stained with haematoxylin and eosin (H and E). Further sections were stained using safranin O and fast green for indication of chondrocytes (see Section 2.2.1). For all solutions used in histological staining protocols see Appendix 2. Images were obtained using a Nikon, eclipse Ci-L light microscope and a Nikon DS-Fi2 camera (Nikon, Tokyo, Japan).

Muscle fibre data were obtained from the histological sections using 1200x900µm light microscopy images. In order to select an unbiased sample of fibres a random number generator was used to select 200 sets of coordinates for each image of muscle taken. The coordinates were used to identify a sample population of fibres which were manually categorised into type 1, 2a, or 2b.

4.2.8 Nanoindentation

Slices of tibia were cut with the diamond saw from the control and experimental tibias. To ensure that sections of bone were fixed in place, in a way which would not affect the indentation modulus bone slices were cold-mounted in a non-infiltrating epoxy resin (Eposet, MetPrep Ltd, Coventry, UK). Samples were then polished using P4000 silicon carbide paper to achieve a surface finish of 5µm, followed by polishing with an Opus colloidal silica suspension polishing compound, to ensure a smooth bone surface for contact with the indentation tip (MetPrep Ltd, Coventry, UK).

Nanoindentation was carried out using an Agilent Nanoindenter G200 (Agilent Technologies Inc., Chandler, AZ, United States) instrument with an ultra-low load Dynamic Contact Module indentation head. Indentations were carried out using a Berkovich tip with a 20nm radius. The Continuous Stiffness Measurement option (Li and Bhushan, 2002), which presents the preferred method for bone testing (see section 2.3.1) was utilised at a frequency of 75Hz for the testing. Each indent was

made in the bone up to a maximum depth of 500nm with surface detection limited to 100N/m. A Poisson's ratio of 0.3 was assumed (Rho et al., 1997; Akhtar et al., 2008). Three distinct bone regions were identified for indentation (Fig.4.3). Thirty indents across regions A and C were made in an array, 20 indents across region B were manually selected to avoid indentation of any blood vessels or fibrous tissue. The nanoindenter was calibrated using fused silica with known mechanical properties before and after testing the specimen.

4.2.9 Statistical analysis

All statistical analyses were conducted in Excel Office 2007 and PAST v2.15 (Hammer et al, 2001).

Cortical thickness and BMD measurements were taken for 10 sites. At each site a measurement was made across 5 slices and an average value taken. Differences between the stimulated and contra-lateral control tibiae in cortical thickness and BMD were tested for using un-equal variance, two-tailed student's t-tests, with p-values<0.05 considered significant. The measurements for the cortical thickness of stimulated tibiae were averaged, as were the measurements for the contra-lateral control tibiae. The results were plotted against each other for each sample site.

In order to validate the FEA model a version of the model was validated against previously published strain data for a comparable rat tibia, loaded under ex vivo external compression (Torcasio et al., 2012). A region of 50 nodes was selected on the model, in the region that strain gauges were placed in the published study. An average strain value was calculated and compared against published strain values.

Differences in bone volume and cross-sectional area were compared using two-tailed, un-equal variance t-tests, with $p<0.05$ considered significant.

For measurement of muscle fibre differences the cross-sectional area of each fibre was measured. For each slide a proportional cross-sectional area of each fibre type was calculated. Differences in fibre populations were tested for using a two-tailed un-equal variance student's t-test, with $p<0.05$ considered significant. Average proportional cross-sectional areas were calculated for each fibre type, along with their standard deviation, and plotted for stimulated and contra-lateral control.

For nanoindentation thirty indents across regions A and C were made in an array, 20 indents across region B. For each indent the elastic modulus was calculated and averaged across the population. The average elastic modulus was plotted against

the displacement into the surface, with standard deviations plotted alongside, to demonstrate the variation across the indents.

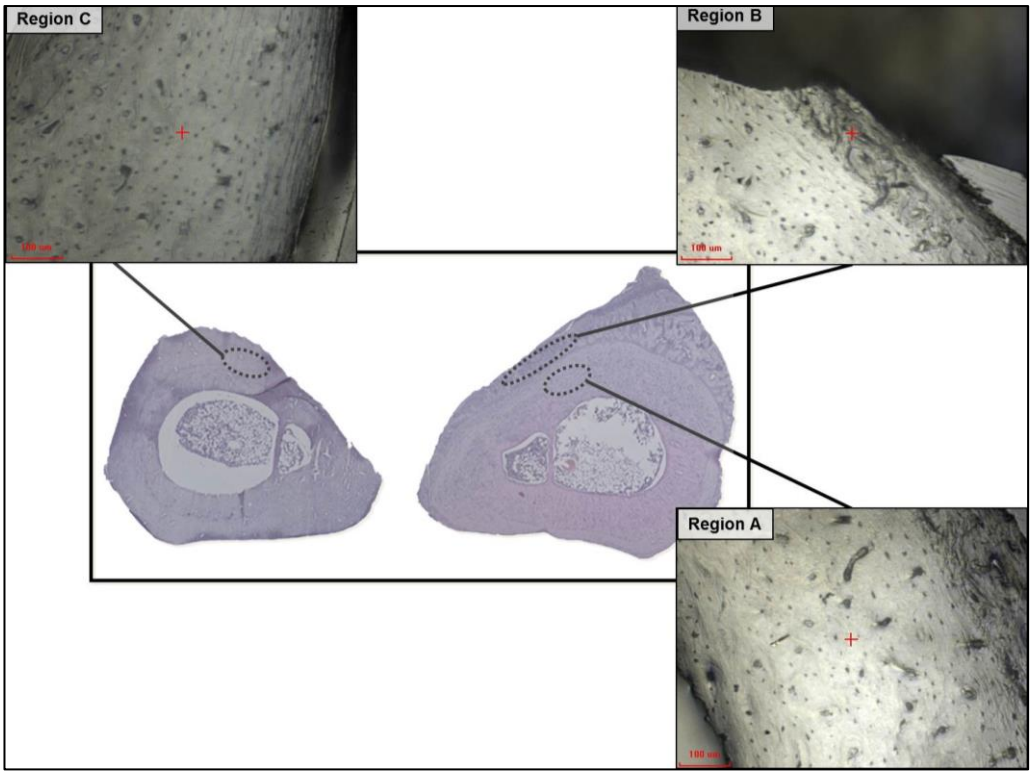

Figure 4.3 The approximate regions of nanoindentation analysis. For targeted analysis of regional bone material properties nanoindentation was localised in three regions of bone. Region A, which was deemed to be the region of established cortical bone within the experimental tibia. Region B represents the region of newly formed bone within the experimental tibia, and region C, cortical bone within the contra-lateral control tibia. Approximate regions of indentation are outlined with dashed lines, and representative regions of indentation represented in images obtained by light microscopy. Scale bars represent 100µm.

4.3 Results

4.3.1 Muscular transformation

The estimated volume of the stimulated muscles, TA and EDL, had a significantly smaller volume of, on average 19%, 16% ($p<0.05$) respectively when compared with the contra-lateral control muscles (Fig.4.4).

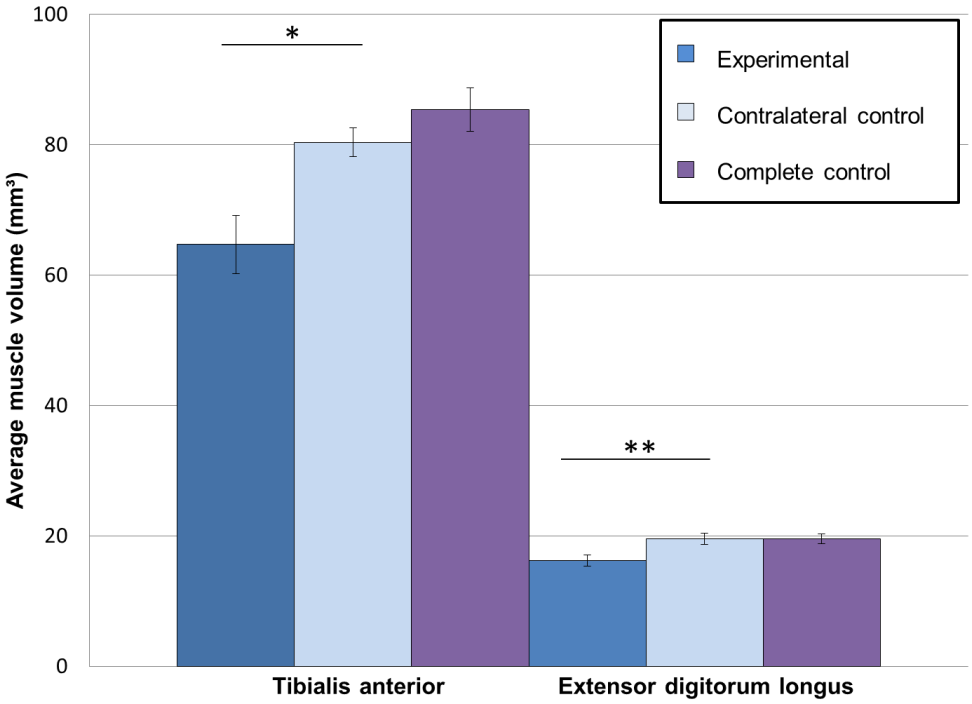

Figure 4.4 The average volumes of tibialis anterior and extensor digitorum longus muscles in experimental, contra-lateral control and complete control limbs. Both tibialis anterior and extensor digitorum longus were significantly smaller in the experimental relative to the control limbs (* $p<0.05$, ** $p<0.01$, $n=6$). There were no significant differences between the either muscle in the contra-lateral control and complete control limbs. Error bars represent standard error.

Histological analysis of fibre types within TA showed that both contra-lateral control and stimulated muscles contained a mix of type 1, 2a and 2b fibre types. Stimulated muscles showed a significant decrease in the proportion of total cross-sectional area of type 2b fibres (20%, $p<0.01$, figs 4.5-4.7). There were no significant differences amongst other fibre types.

NADH staining represents mitochondrial content in muscle fibres. In the contra-lateral control muscle NADH staining revealed fibres that were either un-stained or densely stained (Fig.4.8). In the stimulated muscle all fibres showed some NADH staining (Fig.4.9).

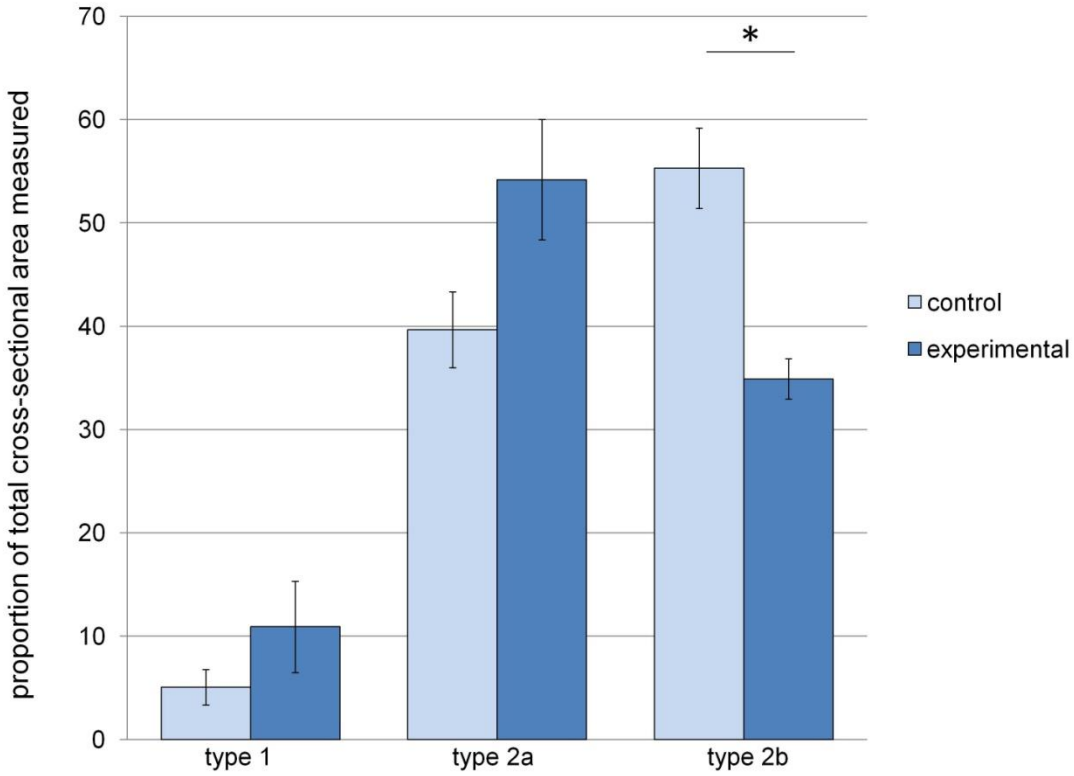

Figure 4.5 Proportional (%) of cross-sectional area of fibre types within experimental and control tibialis anterior muscle. Fibre types 1, 2a and 2b were measured within a sample area of tibialis anterior. There was a significant decrease in type 2d cross-sectional area ($p<0.05$).

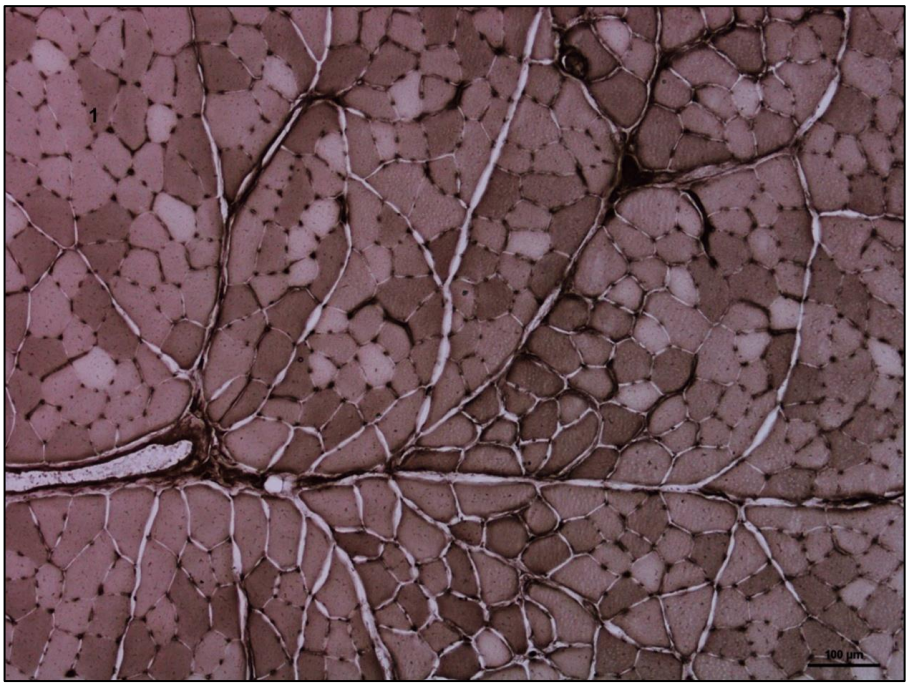

Figure 4.6 Tunell and Hart staining in control tibialis anterior muscle. A histological section taken from a control tibialis anterior muscle**.** Staining distinguishes muscle fibre types 1 (pale), 2a (dark staining) and 2b (intermediate staining). Scale bar represents 100µm.

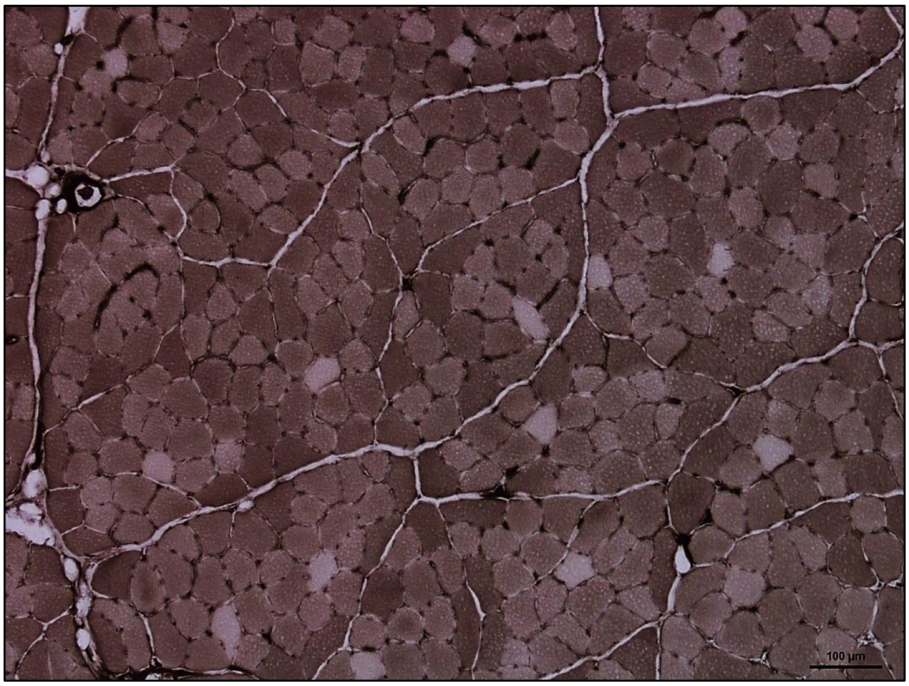

Figure 4.7 Tunell and Hart staining in stimulated tibialis anterior muscle. A histological section taken from a stimulated tibialis anterior muscle**.** Staining distinguishes muscle fibre types 1 (pale), 2a (dark staining) and 2b (intermediate staining). Scale bar represents 100µm.

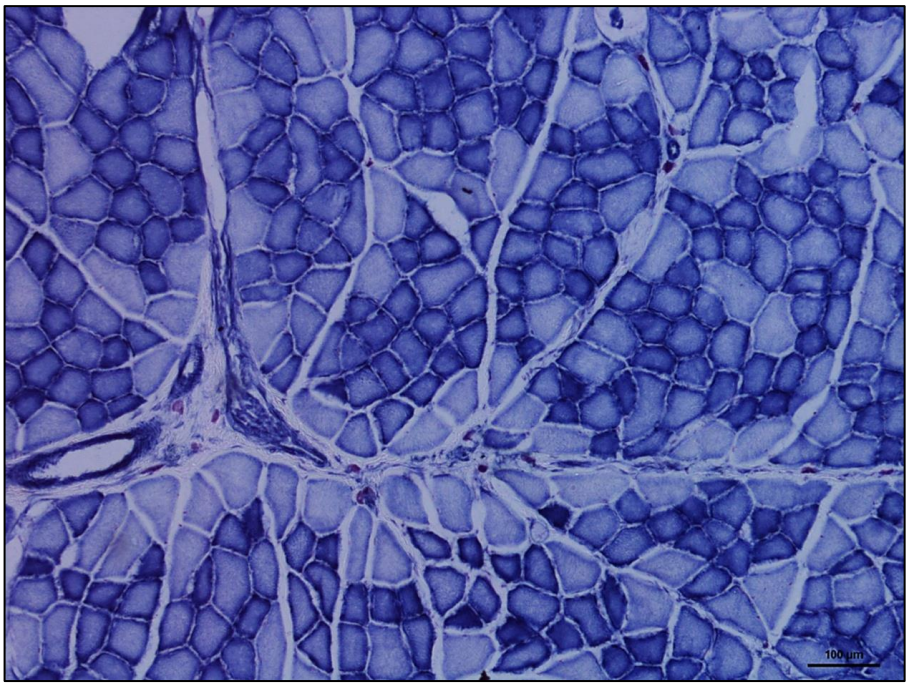

Figure 4.8 NADH staining in control tibialis anterior muscle. Histological section of control tibialis anterior muscle stained with NADH for oxidative capacity. A darker stain represents a higher mitochondrial content within the fibre. Scale bar represents 100µm.

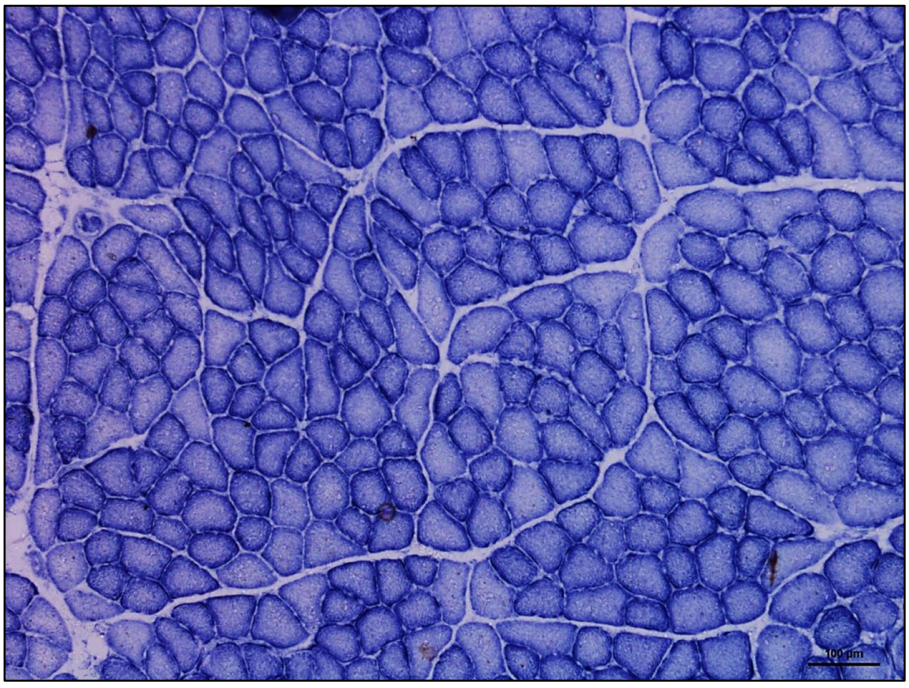

Figure 4.9 NADH staining in experimental tibialis anterior muscle. Histological section of stimulated tibialis anterior muscle stained with NADH for oxidative capacity. A darker stain represents a higher mitochondrial content within the fibre. Scale bar represents 100µm.

4.3.2 Macroscopic bone analysis

Regional sampling of the cortical thickness along the anterior and posterior aspects of the tibias showed that there were no significant differences between regional cortical thickness along the posterior aspect of the tibia (Fig.4.10). Along the anterior aspect of the experimental tibia the cortical bone was highly significantly thicker (300µm, $p<0.001$) than in the control tibia within the distal region (Fig.4.11). There were no significant differences in any parameter measured by microCT between the contra-lateral control legs and the control animals.

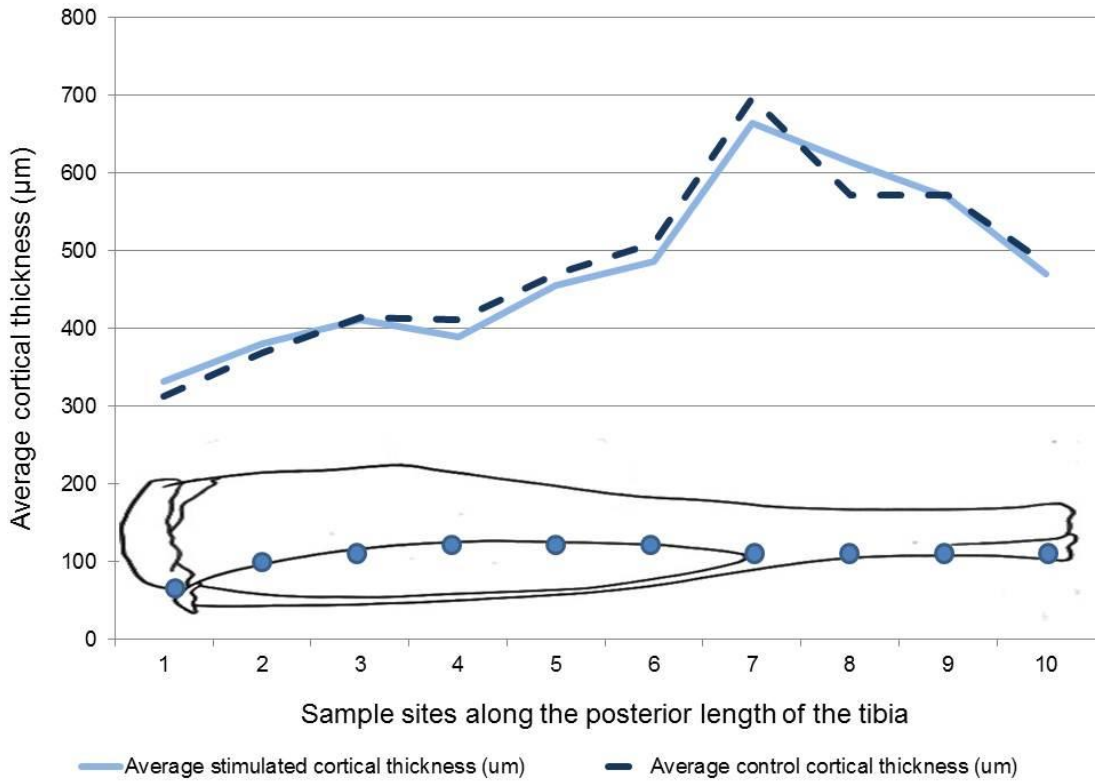

Figure 4.10 Average cortical thickness of the posterior aspect of the tibia. Regional measurements of the cortical thickness along the anterior aspect of the experimental (solid line) and contra-lateral control (broken line) tibiae (n=6). The diagrammatic outline of the tibia represents the approximate location of sites along the tibia.

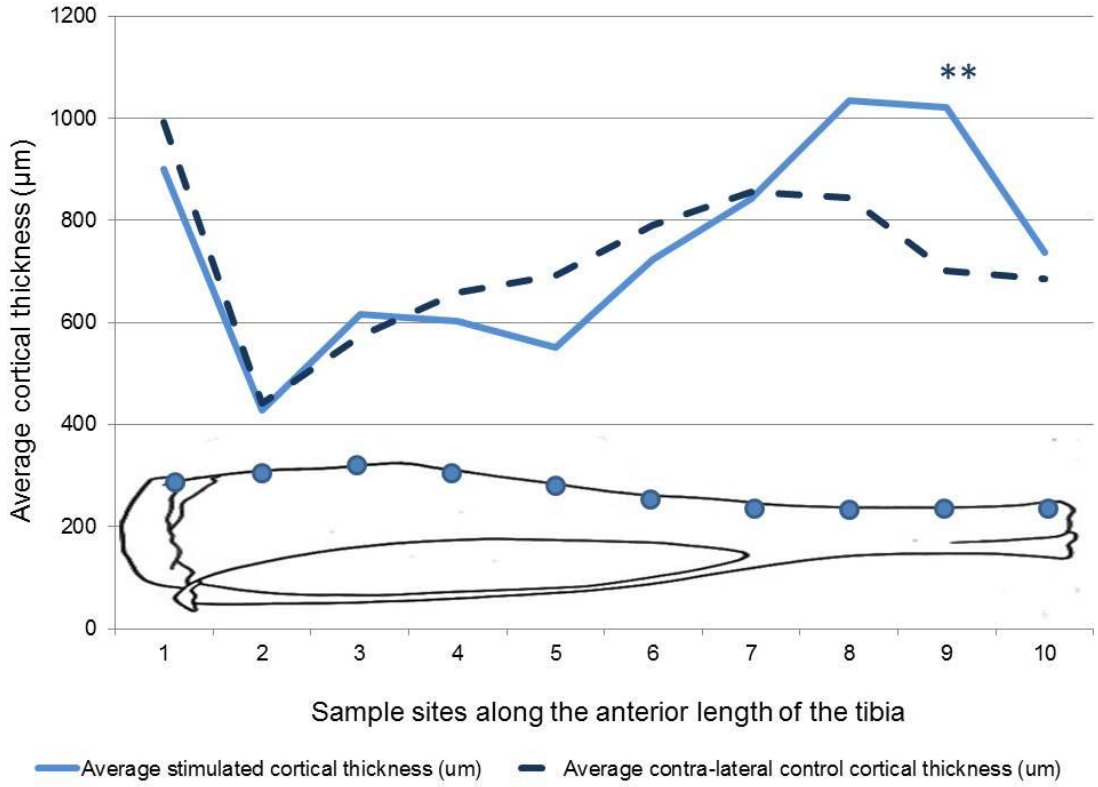

Figure 4.11 Average cortical thickness of the anterior aspect of the tibia. Regional measurements of the cortical thickness along the anterior aspect of the experimental (solid line) and contra-lateral control (broken line) tibiae (n=6). Asterisks represent a highly significant difference ($p<0.01$). The diagrammatic outline of the tibia represents the approximate location of sites along the tibia.

Regional sampling of the bone mineral density along the anterior and posterior aspects of the tibias showed that there were no significant differences between control and experimental tibia (Table 4.2). Within the region which showed a significant increase in cortical thickness (sample site 9) there was a decrease (though non-significant) in bone mineral density. For all bone and muscle volumetric data see Appendix 3.

Table 4.2 Average regional bone mineral density measurements of the anterior aspect of the tibiae. Standard deviations are given in brackets, n=6.

Sample site along the tibia	Average control tibia BMD (Hpa concentration)	Average experimental tibia BMD (Hpa concentration)	p-value
1	403 (±59)	353 (±22)	0.09
2	747 (±171)	845 (±38)	0.22
3	907 (±75)	924 (±102)	0.74
4	848 (±99)	841 (±81)	0.90
5	1020 (±74)	1086 (±42)	0.09
6	1133 (±27)	1140 (±19)	0.63
7	1142 (±53)	1169 (±21)	0.29
8	1099 (±114)	1187 (±19)	0.12
9	1006 (±179)	1147 (±15)	0.11
10	1036 (±40)	1060 (±45)	0.35

Principal components analysis was used to identify the control and experimental bones closest to the mean shape for further analysis. Of the control tibiae 3 bones were close to the mean control geometry (Fig.4.12). In the experimental tibiae there was one tibia that was clearly the closest to the mean shape. As the experimental tibia which was closest to the mean shape corresponded with one of the 3 control tibia this animal was selected for further analysis (control 4, experimental 4, Fig.4.12).

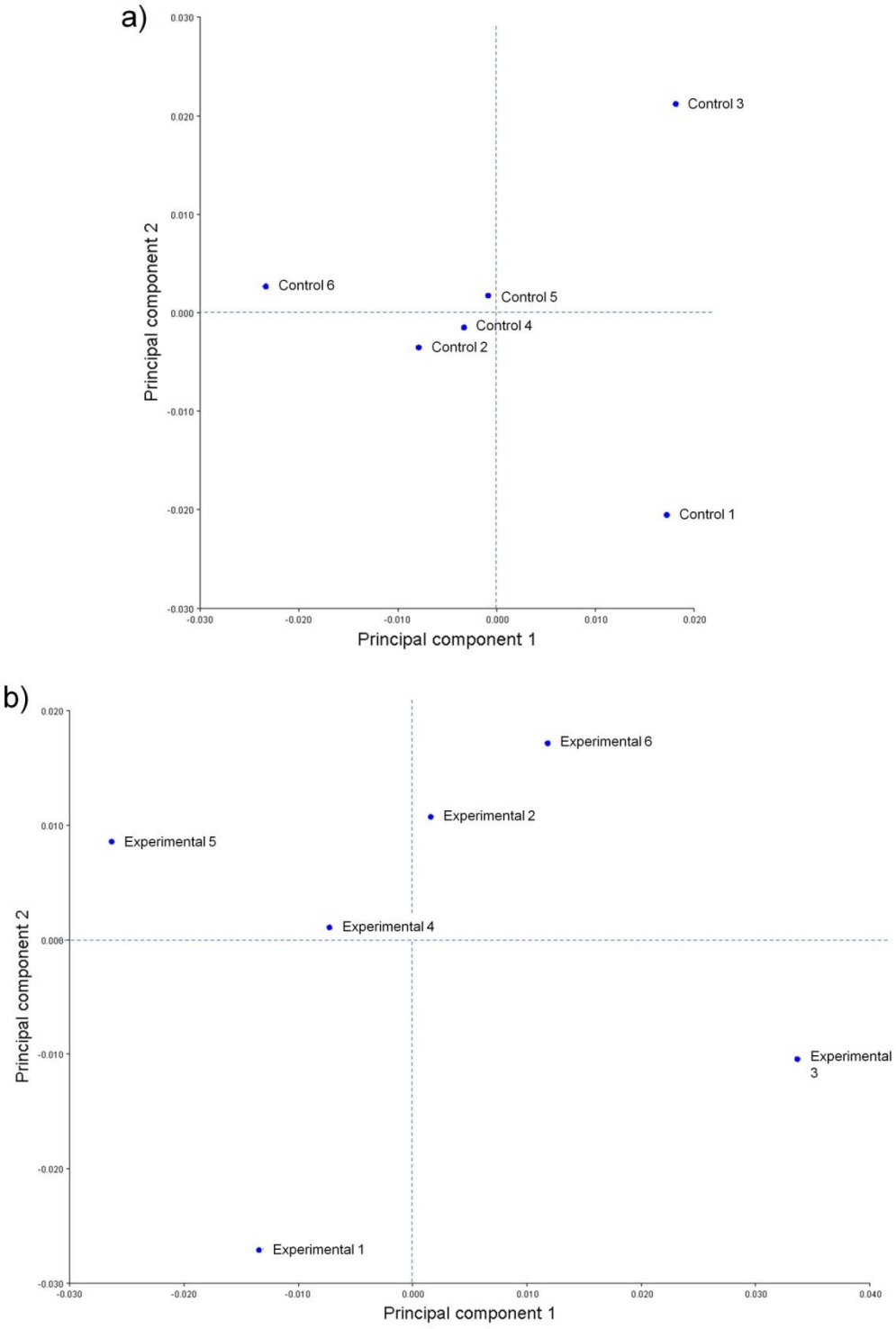

Figure 4.12 Principal components analysis of the control and experimental tibiae. Homologous landmarks were used across a) the control tibiae, and b) the experimental tibiae. The bones closest to the mean shape are represented by the points closest to 0 in both principal component 1 and principal component 2.

FEA revealed a region of high predicted strain in the antero-distal region of the tibia (Fig.4.13). The antero-distal area experienced averages of 640με effective, 158με 1st principal, 497με 3rd principal and 328με maximum shear strains.

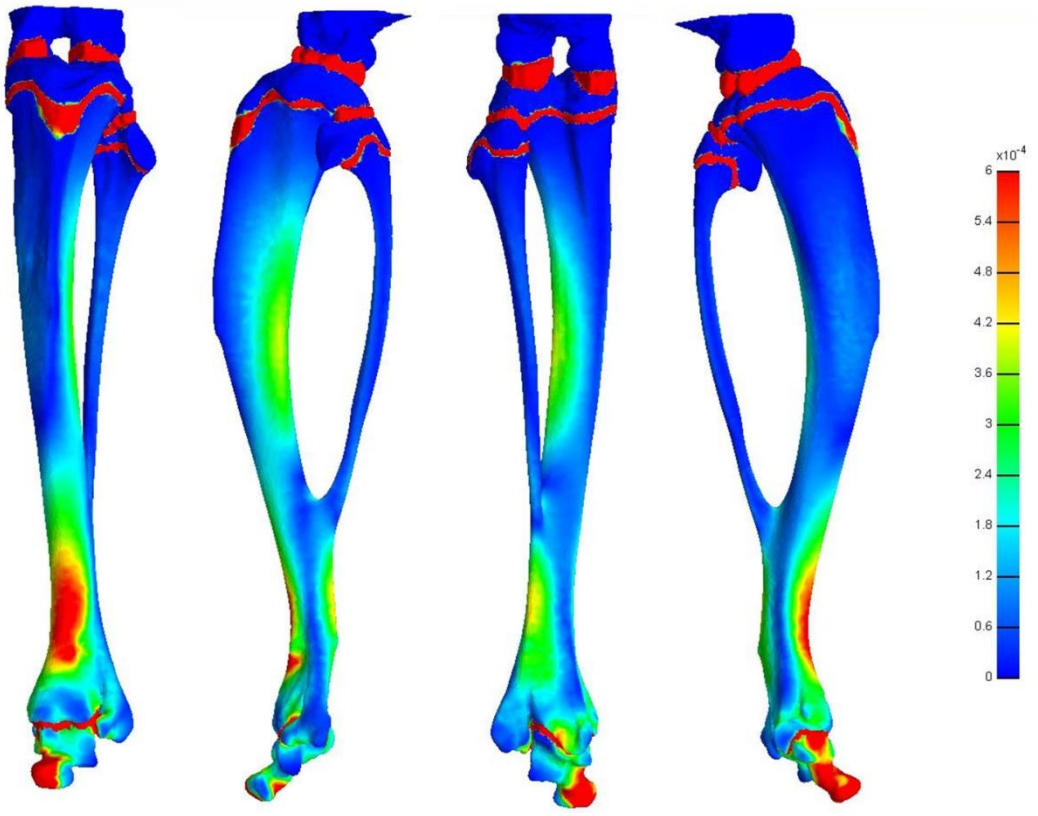

Figure 4.13 Finite element simulation of effective strains across the tibia as a result of the loading regime. The distribution of effective strain across the tibia on the anterior, lateral, posterior and medial surfaces respectively. The highest strain values are represented by red, and the lowest by blue.

4.3.3 Targeted bone analysis

Guided by the regional cortical thickness measurements and the FEA results, the distal region of the tibia was targeted for subsequent analysis. Within this region there was a significant increase in average cross-sectional area of 1.41mm² ($p<0.05$), and an increase in total volume of 4.98 mm^3 ($p<0.05$) in the stimulated limb compared with the contra-lateral control (Fig.4.14, Table 4.3).

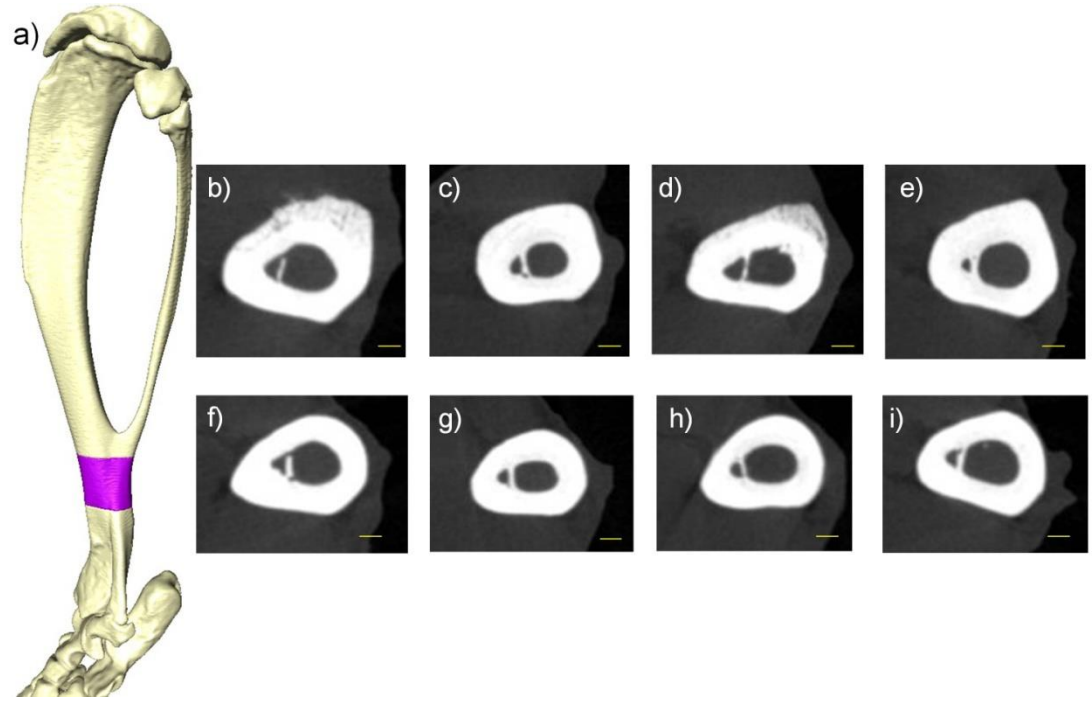

Figure 4.14 Cross-sectional data of experimental and corresponding control tibiae within the region of principal change. a) the purple region on the volume reconstruction of the tibia represents the volume used for targeted analysis (table 4.3). b-i) Cross sections taken from the microCT data within this region for (b-e) experimental limb, (f-i) corresponding control limb. Scale bars represent 400µm.

Table 4.3 Average targeted bone volume and cross-sectional area values

	Stimulated	**Control**	**P-value**	**Difference**	**Difference as a percentage of control**
Bone volume (mm^3)	21.44	16.45	0.010	4.98	30.29
Average cross-sectional area (mm^2)	6.36	4.94	0.027	1.41	28.61

Histological sectioning targeted to this distal region in both the control and experimental tibiae revealed that the cross-sectional geometries were markedly different (Fig. 4.15). The control tibia showed histological features consistent of a rat long bone (Shipov et al. 2013). The experimental bone showed a large region of primary osteon formation. This was characterised by the invasion blood vessels, from which osteoid is spreading (Fig.4.16). The region of primary osteon formation shows very little organisation in collagen orientation (Fig.4.17). The periosteum of the experimental tibia also appears to be expanding (Fig. 4.16). There are regions where the periosteum appears to be contributing to the region of new bone (Fig. 4.16).

Within the region of new bone were rounded cells which appeared to be dividing, indicating the possibility that they were chondrocytes (Fig.4.19). Safranin O staining revealed the presence of clusters of chondrocytes within the region of primary osteon formation (Fig. 4.21-4.22).

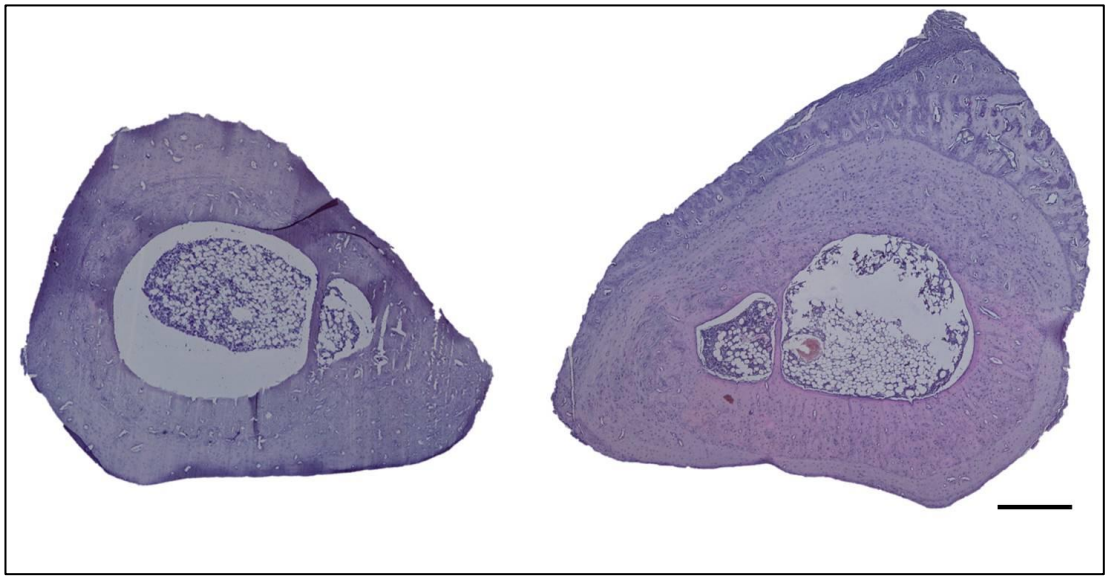

Figure 4.15 Histological cross-sections of control and experimental tibiae. Histological cross-sections of the targeted region in the tibias with closest to mean shape, stained with haematoxylin and eosin. The scale bar represents 400µm.

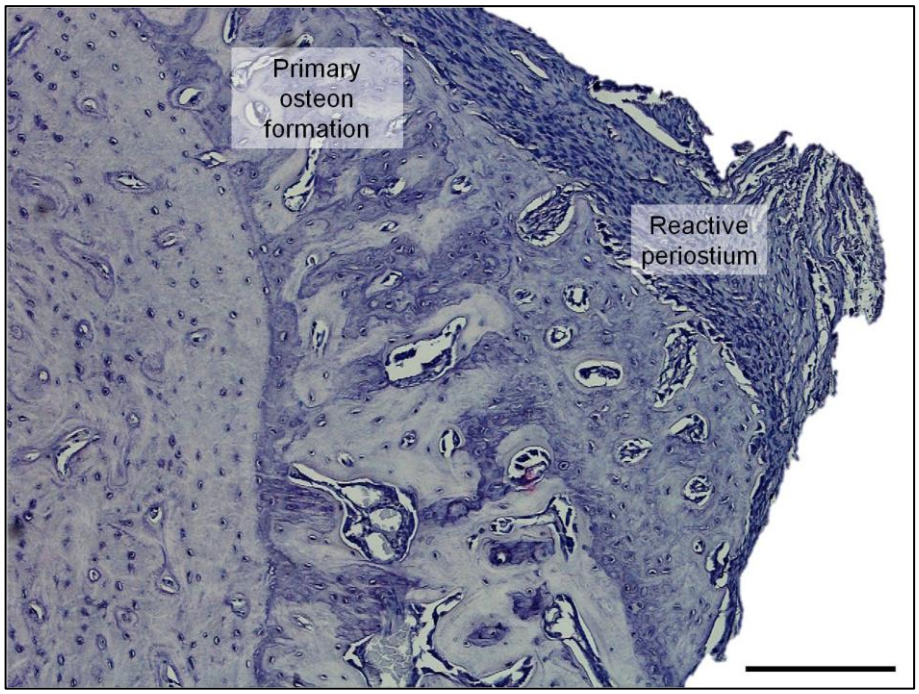

Figure 4.16 Region of new bone in the stimulated tibia. The region of new bone in the stimulated tibia visualised with light microscopy. Section stained with haematoxylin and eosin. Scale bar represents 200µm.

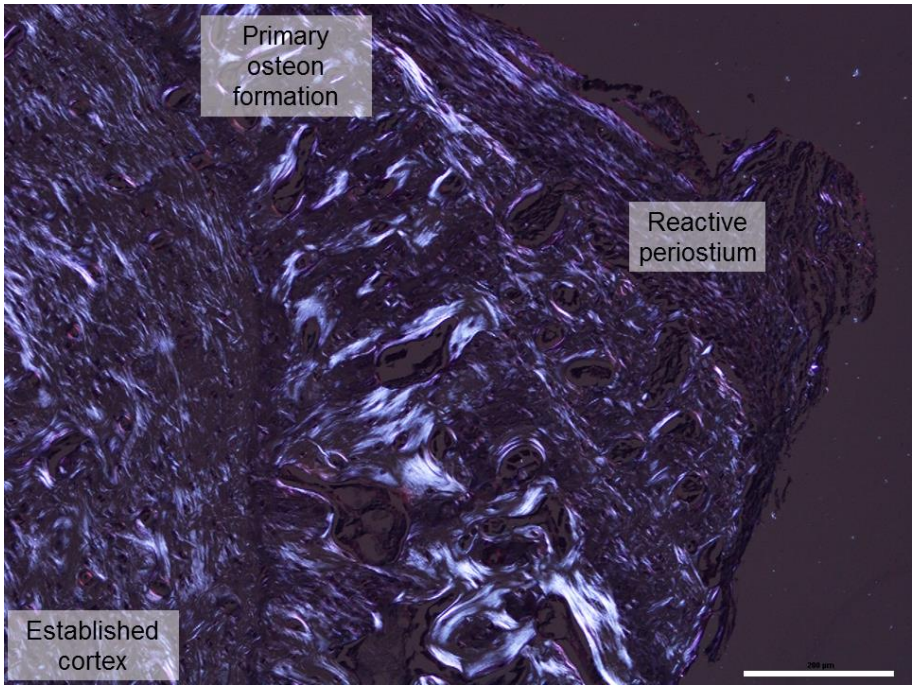

Figure 4.17 Region of new bone in the stimulated tibia, visualised by polarised microscopy. The region of new bone in the stimulated tibia visualised with polarised light microscopy. Scale bar represents 200µm.

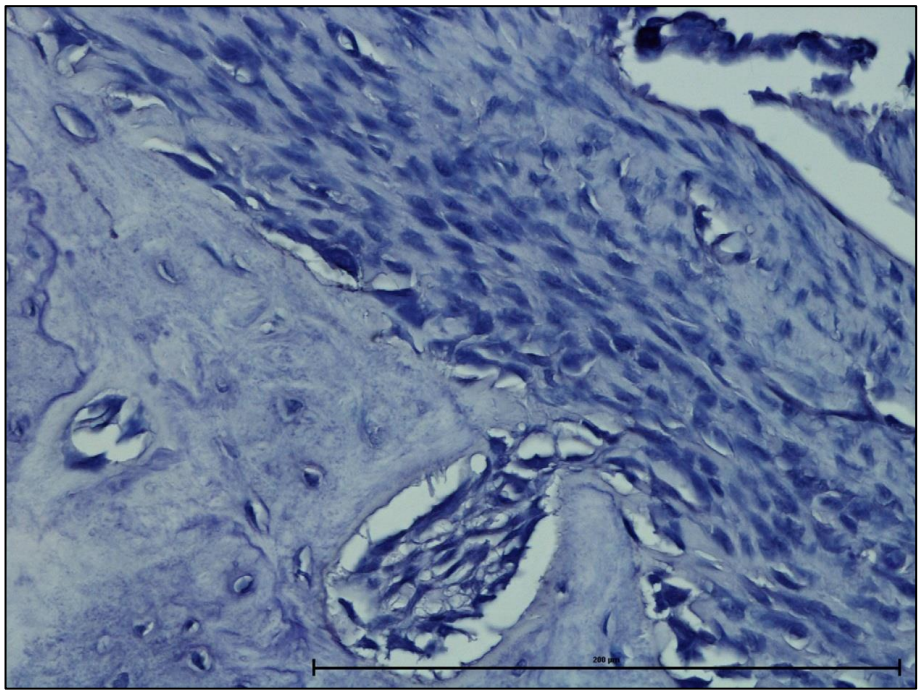

Figure 4.18 Histological section showing a reactive periosteum. A histological section of the experimental bone, which has a very thick periosteum, which at points appears to be contributing to bone formation. Scale bar represents 200µm.

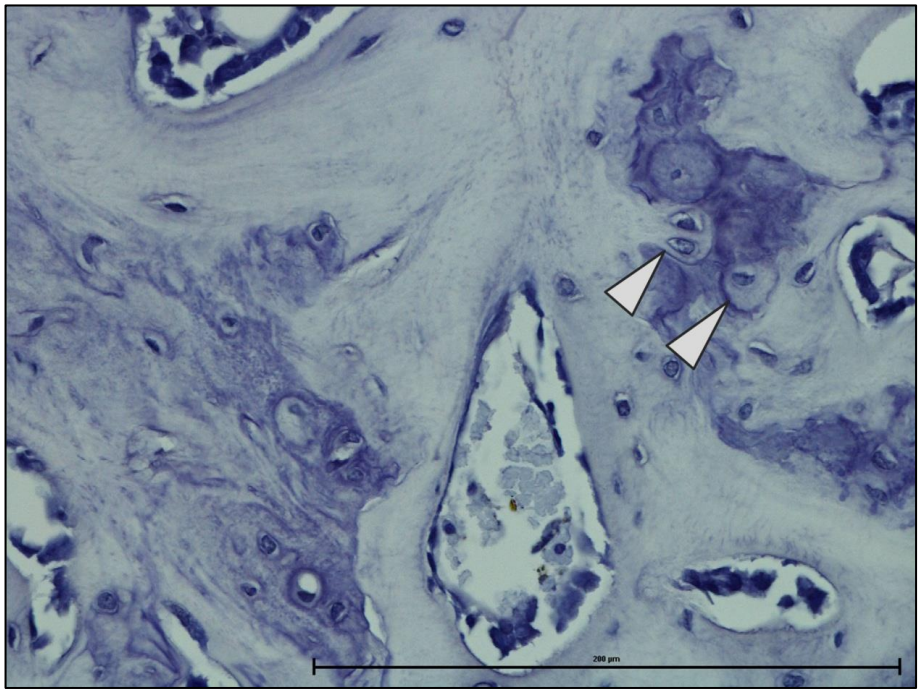

Figure 4.19 Histological section showing chondrocytes within new bone region. Histological section of the region of new bone within the experimental bone. Within the new bone were many rounded cells, some of which appear to be dividing, indicating they may be chondrocytes (arrowheads). Scale bar represents 200µm.

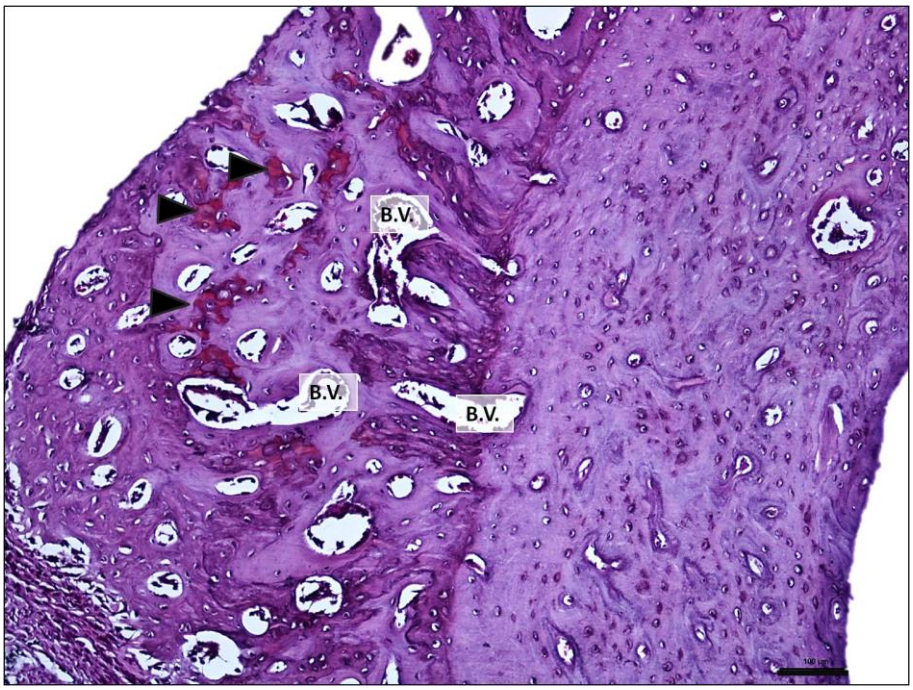

Figure 4.20 Histological section of Safranin O stain in the experimental tibia. Regions of cartilage stain red (highlighted with arrowheads). B.V. represents a number of invading blood vessels. Scale bar represents 100µm.

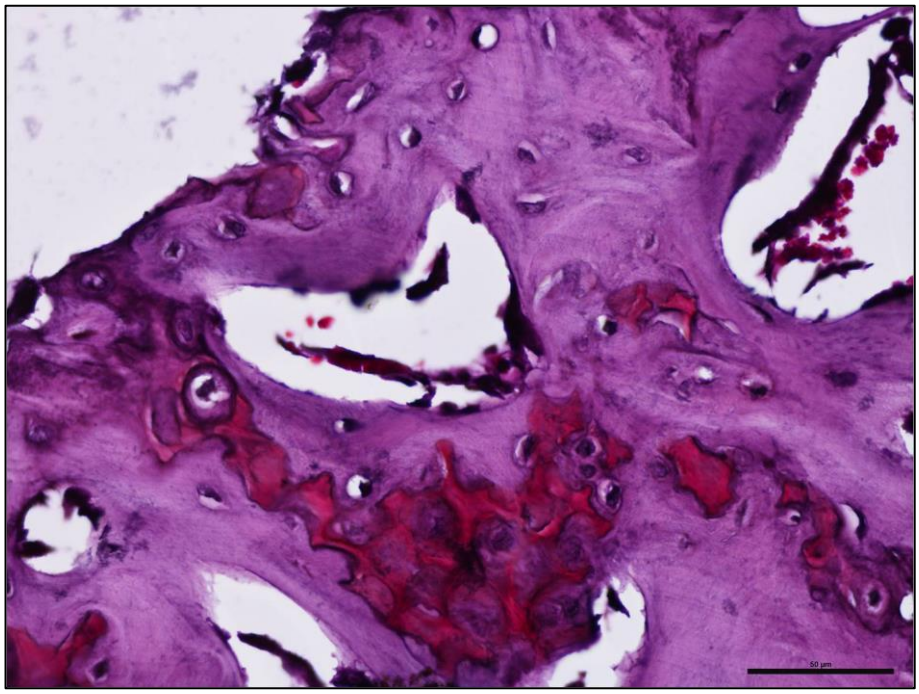

Figure 4.21 Histological section of a proteoglycan stained cartilage island. A region of high safranin O staining within the region of new bone, representing an island of cartilage. Scale bar represents 50µm.

Nanoindentation measurements on the distal regions within the contra-lateral control and experimental bones showed that the average elastic modulus of region A, which represents the established bone, was 20±1.4GPa. Region B, representing the region of new bone was 8.8±2.2GPa and region C, which was the contra-lateral control tibia was 15±1.5GPa (Fig.4.22).

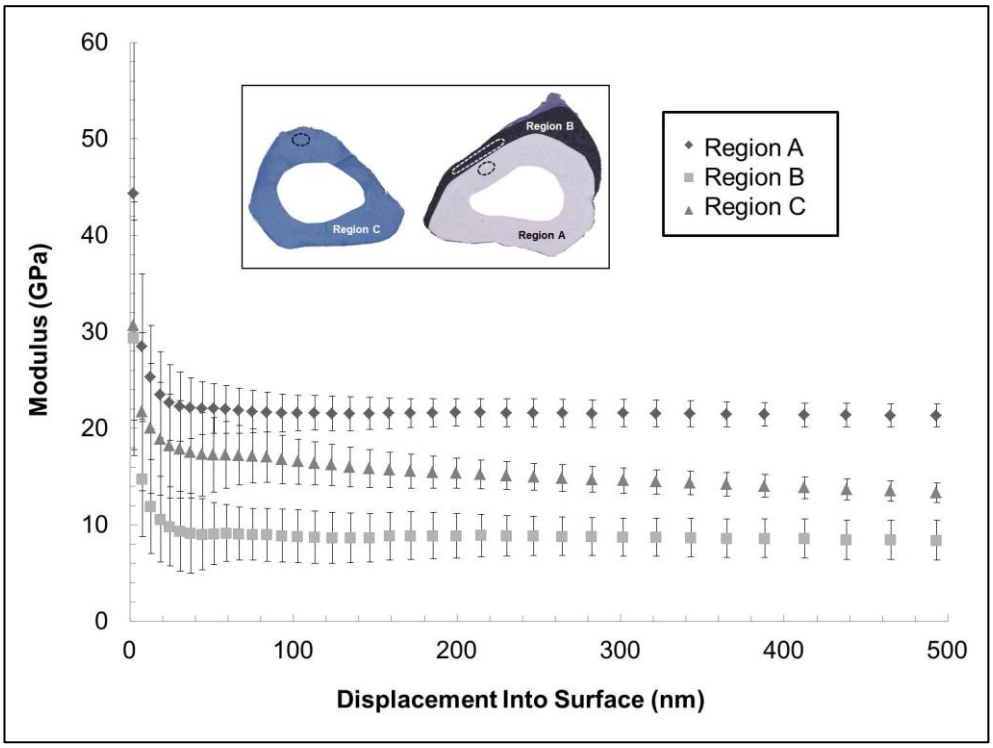

Figure 4.22 Modulus vs displacement of cortical bone as determined by nanoindentation. Three regions of bone were selected to represent the established bone (Region A, white), the new bone (Region B, black) and the contra-lateral control bone (Region C, blue) for nanoindentation. The approximate regions of indentation are outlined by dashed lines. The graph represents the measured modulus of each region against its displacement into the bone surface.

4.4 Discussion

As outlined in the methods chapter, electrical muscle stimulation (EMS) has been used extensively for examining the plastic potential of skeletal muscle (Salmons and Sreter, 1976; Jarvis, 1993; Jarvis et al., 1996; Salmons, 2009) and only recently used for studying bone. For instance, Qin Y-X. et al (2009) and Qin W. et al (2013) both used EMS to study the response of bone cell populations and select regions of trabecular architecture to electrical muscle stimulation. Hence, the present study is the first to use EMS to assess the effect of controlled muscular contraction upon the macro and micro-anatomy of the supporting skeleton.

EMS resulted in transformation of TA towards a less-fatigable phenotype. Three major fibre types found in rat muscle are: type 1 (slow, oxidative), type 2b (fast, glycoytic) and the intermediate type 2a (fast twitch, and oxidative) (see section 1.11). These results demonstrate that a pattern of 100 Hz burst stimulation every 30 seconds for 28 days resulted in a significant decrease in type 2b fibres (Fig.4.5) and an increase in mitochondria within the fibres (Fig.4.8-4.9). As mentioned in the introduction, fast-twitch fibres require more ATP per unit of force generated than slow-twitch fibres (Biewener and Roberts 2000). Taken together, these data suggest an optimisation towards high-force repetitive contractions by a decrease in susceptibly to fatigue, and energy requirements. The relative reduction in muscle volume of the stimulated muscles is unlikely to be an artefact caused by I_2KI staining (see previous chapter) as all muscles were stained under the same conditions. Furthermore, volume reduction is commonly reported in EMS studies (Salmons 2009). The volume reduction (Fig.4.4) is likely to represent the net effect of muscle fibre type transformation away from fatigable type 2b fibres. Fibre types 2a and 1 have a smaller cross-sectional area than type 2b fibres (Pullen, 1977). These changes are consistent with transformation of muscle in endurance training (Gollnick and King, 1969; Green et al., 1984), and is clearly distinct from muscle atrophy caused by disuse, in which there is a shift towards glycolytic-fibres, and therefore a decrease in mitochondria (Braun and Gautel 2011).

As established in the introduction, muscle fibre architecture is highly influential in determining a muscles functional capacity (Lieber and Ward 2011) and this is, to some extent, plastic (Williams and Goldspink 1978). It would have therefore been interesting to use I_2KI-enhanced microCT data to explore the extent to which muscular architecture can be transformed by a period of increased contractile forces. However, as spatial resolution and specimen size are inherently linked in

microCT (see section 2.2.2) it was not possible to obtain a scan of high enough resolution, whilst maintaining the region of interest. Exploratory studies demonstrated it was possible to establish the major orientation of connective tissue tracts running through the muscle (Fig.4.23). However, there was not sufficient data to conduct analyses to quantify the extent to which connective tissue tracts, fascicles, of fibres have transformed, though it does appear that there is more connective tissue in the stimulated muscle than in the contra-lateral control muscle. Therefore this represents an interesting future application of the technique.

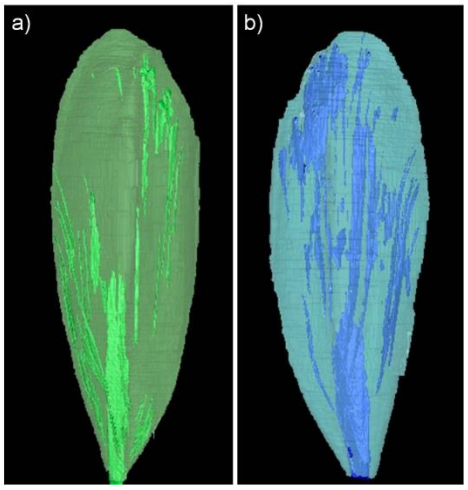

Figure 4.23 Visualisation of three-dimensional reconstructions of connective tissue tracts in contra-lateral control and stimulated tibialis anterior muscles. Iodine-enhanced microCT allows visualisation of muscular tissue, which is clearly differentiated from connective tissue. This allows for the three-dimensional tracking of connective tissue fibre tracts throughout the a) contra-lateral control and b) stimulated tibialis anterior muscles.

In addition to muscular transformation, which has already extensively been demonstrated by EMS (see section 2.1), these results show that EMS can be an effective technique for loading bone. A relatively short period of loading resulted in a dramatic increase in bone volume, which surpassed that seen by, for example, radical surgical methods (Lanyon et al., 1982). The speed of bone deposition required for such a large increase in bone cross-sectional area (Fig.4.15) over 28 days would require a minimum of 10μm in transverse bone growth a day. Bone has a highly ordered structure, and mature bone cells are highly differentiated, so the

deposition of bone is an iterative surface bound, and often time consuming, process. In rats, the surface deposition of bone by osteoblastic apposition has a maximal rate in the region of 3.5µm a day (McBride and Silva, 2012). By contrast, cartilage is able to dramatically increase its volume, as its cells are capable of division and hypertrophy across its volume. This capability can be seen in the growth plates where in rats the growth rate can be up to 125µm per day (Kember, 1960). The chondrocytes then undergo cell death, and are replaced by bone cells (see section 1.1 for more detail). This mechanism provides a mechanically sound structure capable of faster growth than direct growth of bone. The presence of chondrocytes within the region of new bone reported here implies that the adaptive response of the tibia to muscular contraction was initially a result of a rapid phase of cartilage proliferation followed by endochondral ossification. Unfortunately the I_2KI staining which was used to image the bone and muscle in situ causes extensive soft tissue shrinkage (see previous chapter) and also has caused shrinkage of cells. The bones were also particularly brittle during sectioning for histology. It may therefore be recommended that separate specimens are used for I_2KI stained microCT and histological analysis.

The elastic modulus of bone is indicative of the overall mechanical performance of bone as a material, reflecting microstructural changes. Nanoindentation analysis showed that the region of new bone (region B, Fig.4.22) has a far lower elastic modulus than the established bone (region A, Fig.4.22). Newly deposited bone is less stiff as compared to established bone (Gourion-Arsiquaud et al., 2009; Donnelly et al., 2010) largely due to a lower mineral content. This discrepancy in moduli quickly diminishes as new bone mineralises, with bone reaching a similar indentation modulus to established bone within 4 days of lamellar deposition in rats (Donnelly et al., 2010). The region of the experimental tibia which had significantly thicker cortical bone than the control tibia also showed a tendency towards a decrease (though not significant) in BMD. The high standard deviation in BMD results within this region reflects the variety of mineralisation within this region (Table 4.2). Therefore it seems likely that this region of bone represents a nascent form, which in some specimens is fully mineralised, and others it is undergoing mineralisation. The mineralisation process is not the only factor influencing the mechanical properties of bone. Increased porosity decreases bone stiffness (Currey, 1988) and the presence of chondrocytes is also likely to decrease stiffness as cartilage has a far lower modulus than bone (Radhakrishnan et al., 2004). The lower elastic modulus of the region B is likely to be a combination of the relative immaturity

of the bone, a lack of mineral, inclusion of chondrocytes and a higher porosity than region A (Fig.4.16).

The elastic moduli of all regions of bone measured are at the lower end of reported values for rat cortical bone (Donnelly et al. 2010; Busa et al. 2005). This is likely due to their prior treatment which had involved fixation, staining with iodine, and a period of storage in PBFS. Long periods of storage in formalin have previously been shown to reduce bones elastic modulus (Ohman et al. 2008). Despite this, all regions of bone were treated in the same way, so whilst the absolute values may not be physiologically accurate, the relative differences between them are still valid.

The skeleton is shaped by the effects of the forces it experiences. With an increase in strain resulting in bone deposition, and a decrease in strain resulting in bone absorption (Ozcivici et al., 2010). This was originally thought to be governed by specific strain thresholds, with strains above 1500με resulting in bone growth (Frost, 1987). Later work in rats has shown that no bone response was shown below strains of 1050με (Turner et al., 1994). This is still higher than the strains recorded in our FE model (640με), albeit limited to a quasi-static simulation of just one contraction. As such these results underline the importance of frequency as well as magnitude of load, both in terms of the force applied and the strains produced, in determining an osteogenic response (Qin et al., 1998, see section 1.5). This is especially interesting in light of the work of Turner et al (Turner et al., 1994). Here, we used approximately 2880 cycles per day, resulting in a total of 9.6 minutes of 10N loading per day and provoking a large region of bone growth. In Turner et al's experiments it was found that the lower limit for bone formation was 40N; however the loading protocol involved only 36 cycles per day, totalling 10.8 minutes of 40N of loading per day. So whilst the overall loading time is fairly similar, applying loads more frequently appears to have a greater effect than simply increasing the magnitude of the load, assuming the nature of the adaptive response was similar to the apparent endochondral process reported for the first time here.

The exact mechanism for the response reported here is not fully understood (and is further commented upon in Chapter 6) but it seems likely that the mechanical stimulus initiates the recruitment of precursor cells, possibly mesenchymal stem cells (MSCs). The MSCs may be from the cambial layer of the periosteum (Wang et al. 2014) which appears to be expanding (Fig.4.16). The differentiation and eventual fate of mesenchymal cells are controlled by biomechanical factors (Roux, 1912), with compressive forces resulting in cartilage. If continuous compression is applied

then cartilage will remain, but if it is intermittent then chondrocytes undergo endochondral ossification to become bone (Shapiro, 2008). Our FEA model shows that this region is intermittently exposed to compressive forces, which could explain the clusters of cartilage.

This study shows the value of EMS for skeletal biology. With a relatively short experimental period resulting in dramatic bone growth, both in terms of the volume generated and the timescale over which it was achieved. The large volume of new bone appears to be a product of endochondral processes, though further work is needed to establish the timescale over which this occurs. The results presented here tend to suggest that a carefully designed muscle stimulation protocol could offer targeted bone growth to ‘at risk’ regions of bone. This is a significant finding in light of the growing ageing population and the burden of bone disease for healthcare providers.

Chapter 5: Do things get worse before they get better?: simulating the effects of musculoskeletal mechanoadaption on the local mechanical performance of the rat tibia

Chapter 5

The previous chapter documents profound adaptations of rat muscle and bone to a period of electrical stimulation of tibialis anterior. As established in the introductory chapter, the structure of a bone plays a defining role in determining its mechanical performance. This chapter utilises the computational simulation techniques reviewed in Chapter 2, to replicate biomechanical forces experienced by the tibia during electrical muscle stimulation. The models can then be used to predict the relative magnitude and distribution of stresses and strains in the rat tibia under various conditions. This chapter therefore addresses the fundamental question, to what extent is form influencing function?

5.1 Introduction

Throughout life the skeleton is exposed to a multitude of forces, arising from movement driven by muscular contraction and gravitational loads, and these forces dissipate through bones creating stress and local strain. As reviewed in the introduction, the tight spatial coordination between changes of bone geometry and strain have led to the widespread acceptance that strain is the controlling stimulus behind this relationship (Frost 2003), ensuring that at any one time the form of a bone represents a compromise between strength and efficiency of materials. It had been suggested (Frost 1987) that if strains rise above a habitual level then bone deposition is activated, thereby reducing strain within the bone and preventing further bone deposition. Conversely, as strains fall below habitual levels, bone resorption is activated, and strains are increased. More recently, there is increasing evidence that such absolute strain values and thresholds are not as informative as previously imagined and that bone adapts in a more fluent, continuous fashion (Sugiyama et al. 2012; Ellman et al. 2013; Schulte et al. 2013).

The mechanoadaptive response of a bone is governed not only by the magnitude of strains, but also by how frequently they are applied (Forwood et al. 1996; Qin et al. 1998), their rate (Mosley and Lanyon 1998) and the insertion of rest periods during loading (Robling et al. 2001). The influence of strain magnitude, rate and the interval between loading events as well as the frequency of loading episodes are often inter-related and so are difficult to alter independently. A consensus is now emerging that all these qualities of a mechanical stimulus, and possible others, contribute to the regulation of bone. Unfortunately, we still know relatively little about how these qualities are perceived by bone cells in-vivo (see section 1.6). Of all the different cell types found within bone, the osteocytes, which exist in a highly connected three-

dimensional network surrounded by interstitial fluid, appear the most likely candidates for mechanosensation (Klein-Nulend et al. 2012). In vitro work has established that osteocytes are responsive to mechanical deformation applied via fluid flow (You et al. 2000). It is therefore postulated that increased bone strain increases fluid flow over osteocytes which in turn respond by orchestrating the activity of osteoclasts and osteoblasts accordingly (Nakashima et al. 2011). Despite this, both mice with ablated osteocytes (Kwon et al. 2012) and teleost fish with bone that naturally lacks osteocytes (Shahar and Dean 2013), both demonstrate mechanically regulated bone adaptation. This suggests that other cell types and mechanisms may also be involved.

As reviewed in section 1.12, in the past skeletal mechanoadaptive responses have been investigated following supra-physiological loading by an external devices (Sztefek et al. 2010; Turner et al. 1994; Nagira et al. 2013; Sugiyama et al. 2012). This has the benefit of being easily reproducible and repeatable, but makes it difficult to approximate the habitual mechanical environment of the skeleton which is largely governed by muscular contraction rather than externally imposed loads (Judex and Carlson 2009). Recent advances of electrical stimulator technology now allow for the controlled loading of bone by muscle contraction. Indeed, the previous chapter demonstrated that a 28 day period of tibialis anterior stimulation in rats resulted in an integrated musculoskeletal response. The response included a decrease in muscle mass and force, and a highly regionalised increase in bone volume within the antero-distal region of the tibia. As discussed in section 4.4, it is though that this region of bone represents a lowly mineralised nascent stage of bone development. The present chapter aims to investigate how these adaptive changes could have altered the local mechanical performance of the bone. In particular, the widely accepted theory that mechanoadaption occurs primarily to diffuse regions of high strain (Frost 2003; Qin et al. 1998; Mosley and Lanyon 1998; Klein-Nulend et al. 2012; You et al. 2000) is tested.

5.2 Materials and Methods

5.2.1 Input Data

Micro CT data was used from the six stimulated Wistar rats from the previous chapter (8 weeks old, weights 228-282g). In brief the animals were stimulated with 0.2ms pulses at 100 Hz for 200ms every 30s, resulting in a total of 9.6 minutes of

stimulation per day. Following the stimulation period, hindlimbs were removed, stored and then imaged with standard microCT and contrast-enhanced microCT, see section 4.2.2 for imaging details.

5.2.2 Reconstruction and meshing

As described in the previous chapter, the individual with the geometry closest to the mean form was selected using homologous landmarks and morphoJ (Klingenberg 2011). MicroCT data for this individual was imported into Amira 5.4.1 (Visage Imaging, Pro Medicus Limited, Melbourne, Australia) and used to recreate and mesh (tetrahedral) FE models of the control and adapted tibia-fibular complex. Each model included cortical bone, trabecular bone, cartilage, medullary fat, femoral condyles, and a rigid body platform constraining the distal portion of the talus. Multiple models were created to test the influence of geometry, nascent bone and muscle force upon the local biomechanical performance of the tibia. Some models also included an additional component representing the nascent region of bone formation (Fig.5.1). To ensure that the meshes created were complex enough to represent the biomechanical situation, a convergence test was performed (see section 2.3.3 for more detail). The mesh representing the control condition was generated at four mesh densities ranging from 55,000 to 600,000 tetrahedra. Initial tests in FEBio 1.5 (Maas et al. 2012) showed that numerical solutions had converged by around 430,000 tetrahedra. Models of this density or above were used in subsequent analyses.

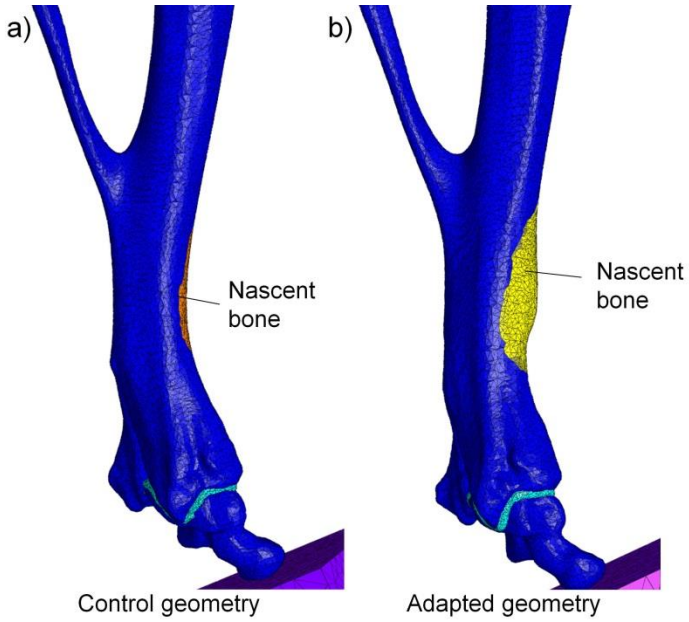

Figure 5.1 Regions of nascent bone within the control and adapted geometries. Tetrahedral meshes for the distal portion of the (a) control and (b) adapted geometries in models C, D, G and H, (see table 5.1). The models differ in the relative size of the nascent bone region (orange and yellow respectively) which is surrounded by regions of established cortical bone (blue).

5.2.3 Models, constraints and loading conditions

A total of eight models were created in Preview 1.12 (Maas et al. 2012), four models presenting the control geometry and four representing the adapted geometry. Models are summarised in Table 5.1. Nascent bone on the control geometries represented a smaller, initial response (models C and D) and the nascent bone on the adapted geometries represented a much larger, later phase (models G and H; see Fig.1). Both were located with reference to the microCT images and histology (see section 4.3). Versions of the adapted model also include a geometry in which the nascent bone is presumed to have completed mineralisation and has the same properties as the surrounding cortical bone (models E and F). Each model was constrained at the femoral condyles in all dimensions except Z. The loading platform was constrained in all dimensions. The talus was attached to the platform by a group of approximately 20 nodes. The muscle forces for control and adapted muscles, 8.7 and 6.9N respectively, were calculated based on microCT data (see section 4.3.1). The femoral condyles were loaded with 0.89N, which was calculated

using average body weight/4 limbs multiplied by the gravitational constant. All models were run in FEBio 1.5 (Maas et al. 2012). The models here differ from that of the previous chapter in that they use a dynamic approach. Inertial properties are not deemed to be particularly important in the rat hindlimb, however a dynamic analysis allows time to be derived within each simulation, enabling approximation of relative changes of strain rate between conditions. These timings are dictated primarily by the transfer of force from the muscle to the bone. The time taken for rat muscle to reach maximum contractile force is approximately 20ms for a stimulated muscle with 20% type 1 fibres (see section 4.3.1 and Jarvis et al. 1996). Additionally, the time taken for the rat foot to dorsi-flex following peak contraction is about 13ms (Gruner et al. 1980). So the total time over which the muscle force was increased from 0 to 100% was 33ms. Femoral loads increased over a 1 second timeframe to replicate the transfer of body weight. Strain rates could have been estimated by dividing effective strain values by 33ms, but this does not take into account the longer timescale of the femoral load which in this instance consistently reduced loads by 11%.

Table 5.1 The different conditions of each FE model

Model	Geometry	Muscle force (N)	Nascent bone region
a	Control	8.7	no
b	Control	6.9	no
c	Control	8.7	yes
d	Control	6.9	yes
e	Adapted	8.7	no
f	Adapted	6.9	no
g	Adapted	8.7	yes
h	Adapted	6.9	yes

5.2.4 Material Properties

Medullary fat was modelled as an isotropic elastic material with a Young's modulus of 500 Pa and a Poisson's ratio of 0.4 (Gefen and Dilmoney 2007). Cartilage was modelled as a hyper-elastic material (Maas et al. 2012). The supporting platform and femoral heads were modelled as rigid bodies. Structural densities were required for the dynamic (inertial) analyses (see above). For all materials, these were

calculated from published data for a range of bones and species as averages weighted by the number of samples in each study (see Appendix 4): cortical bone was 1946kg/m^3 (Rajaram and Ramanathan 1982; Peterson and Dechow 2003; Dechow and Hylander 2000; Phelps et al. 2000; Currey 1979; Somerville et al. 2004; Clifton et al. 2008); trabecular bone was 569kg/m^3 (Ashman and Rho 1988); bone marrow was 921kg/m^3 (Hosokawa and Otani 1997; Mendez et al. 1960); cartilage was 1107kg/m^3 (Jaremko et al. 2007; Lohmander and Hjerpe 1975; Zhou et al. 2004; Joseph et al 1999).

The elastic moduli of bone can vary substantially between individuals and according to hydration state. In order to capture an appropriate range of values to use in our simulations of an 8-12 week old rat tibia under physiological 'wet' conditions, properties were therefore derived from a review of a range of relevant nanoindentation studies (see Appendix 4). Mean values for dry adult (8 weeks or older) rat bone were calculated by multiplying each reported modulus by the sample size and then dividing the sum by the total number of individuals investigated. This minimises the bias of many studies with small sample sizes. The review yielded an estimation of 29.9GPa for dry cortical bone from the rat hindlimb (Busa et al. 2005; Bach-Gansmo et al. 2013; Jaramillo Isaza et al. 2014; Zaslansky et al. 2013; Donnelly et al. 2010; Vickerton et al. 2014, Brüel et al. 2011). Due to the paucity of published trabecular data specific to the rat hindlimb bones, the equivalent weighted value for dry trabecular bone of 18.4GPa was estimated with reference to data on rat vertebral as well as femoral trabecular struts (Ammann et al. 2007; Guo and Goldstein 2000; Sun et al. 2009; Sheng et al. 2006). A broader review of differences of moduli between hydrated and dry bone was also conducted, revealing that hydrated bone has on average a modulus approximately 33.6% lower than dry bone (Hengsberger et al. 2002; Bushby et al. 2004; Guidoni et al. 2010; Lee et al. 2013; Rho and Pharr 1999; Wolfram et al. 2010b; Akhtar et al. 2008; Ammann et al. 2007). This yields estimates of wet trabecular struts and cortical bone of 12.2GPa and 19.9GPa, respectively. Trabecular bone was modelled as a volume (not individual struts) and so the modulus was further scaled with respect to the measured fraction of bone volume to total volume, which was measured as 0.32 from the microCT data using BoneJ (Doube et al. 2010). This fraction was consistent with published values (Laib et al. 2000; Yang et al. 2014) and yielded a final elastic modulus value for the trabecular volume of 3.9GPa. The nascent bone had a dry modulus of 8.8GPa (Vickerton et al. 2014), and was modelled with a modulus of 5.8GPa to reflect wet conditions. For bone a Poisson's ratio of 0.3 was assumed (Rho et al. 1997).

Given the normal variation and uncertainty regarding the elastic modulus, a sensitivity analyses was also performed. Models A and F had the elastic modulus of cortical and trabecular bone varied by the standard deviations seen among values reported in the literature (see Table 5.3). This yielded ranges of 15.5 to 24.7GPa for wet cortical bone and 2.6 to 4.7GPa for the trabecular volume. No range for hyper-elastic values of cartilage could be established, so values were varied by ±30% which broadly reflects the ranges seen for bone.

5.2.5 Model validation

The control model (A) was evaluated implicitly by comparing the predicted location of bone adaptation with that reported Chapter 4. As outlined in section 2.3.3 it is not always possible to reliably replicate the conditions which are being simulated by FEA. Indeed replicating the in-vivo conditions represented by the FE models presented here in an engineering rig whilst gathering sufficiently accurate strain data would not be possible. Instead the work-flow was validated, from microCT imaging through to FE simulation. A rat tibia-fibular complex was stripped of soft tissue, fixed in 70% ethanol and then dried. Both ends of the bone were mounted in epoxy resin (Bondloc, B2001, Worcestershire, UK) to provide even surfaces for loading (see also (Amin Yavari et al. 2013)). Despite the limitations of strain gauges discussed in section 2.3.2, they provide a relatively simple method for the direct measurement of regional surface strains to a high sensitivity. A miniature single element strain gauge with an active grid of 0.6mm (model no EA-06-03IDE-350 Omega Engineering Ltd) was adhered to the medioproximal surface with the axis parallel to the longitudinal axis of the bone. The gauge was placed approximately 33% of tibial length (Fig.5). Strains were measured using a D4 Acquisition system (Vishay, Malvern, PA, USA). The tibia-fibular complex was subjected to axial compression using a Lloyd LRX materials testing machine (AMETEK Inc, Berwyn, PA, USA). Load was applied at 0.1 mm/s up to 10N, then released and repeated a further 3 times. The mounted tibia-fibular complex was then imaged using microCT (100 kV, 30 uA, 0.1mm copper filter, 1466 projections averaging 2 frames per projection). Data were reconstructed at 27µm. An FE model composed of 606,880 tetra was created and parameterised (Fig.5.2b). Material properties of bone were taken from the dry values calculated from the literature. The dried cartilage growth plate was modelled as an isotropic elastic material with values from the literature (Athanasiou et al. 1991). Epoxy resin blocks were modelled as rigid bodies, and constrained in XY dimensions proximally and in all dimensions distally. Loads of 10N were applied axially along the Z axis, to

represent a load in the same range as the loads applied in the FE model. FE analysis was quasi-static. Simulated first principal strain vectors were found to correspond with the longitudinal axis of the bone and the gauge (Fig.5.2c). Twenty-five nodes across the region of gauge application on the tibial surface were selected. First principal strains were averaged across these nodes, and compared with experimental values.

5.2.6 Statistical analysis

All statistical analyses were conducted in Excel Office 2007 and PAST v2.15 (Hammer et al, 2001).

To ensure that the meshes created were complex enough to represent the biomechanical situation, a convergence test was performed. Mesh densities of 55,000, 100,000, 200,000 and 600,000 tetrahedra were created and loaded. 40 nodes were selected within the region of interest. Effective strain values were recorded across these nodes. Differences were tested for using un-equal variance, two-tailed student's t-tests, with p-values<0.05 considered significant.

FE models were compared by selecting 40 homologous surface nodes across the same region presenting the antero-distal portion of the tibia (node IDs were the same for comparable geometries). Mean values of effective strain and effective stress were compared using standard student t-tests, with p-values less than 0.05 deemed significant.

For the validation study twenty-five nodes across the region of gauge application on the tibial surface were selected. First principal strains were averaged across these nodes, and compared with experimental values using standard student t-tests, with p-values less than 0.05 deemed significant.

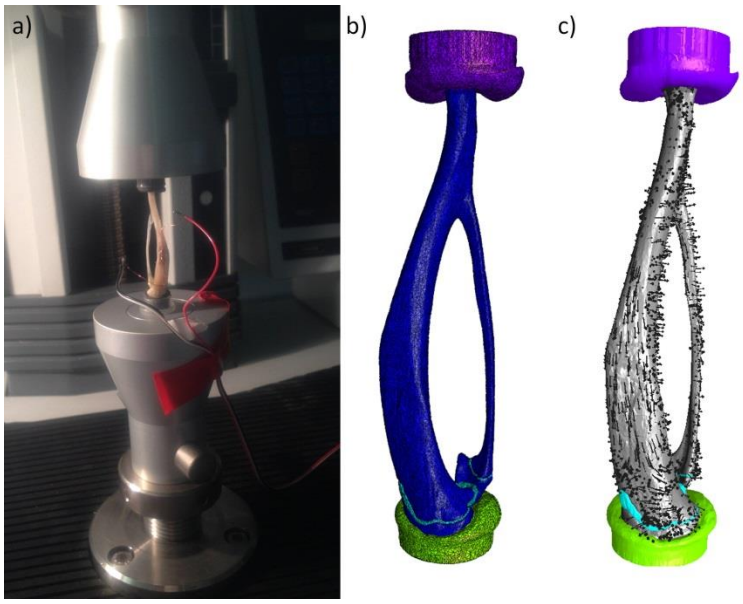

Figure 5.2 The experimental set up for FEA validation. In order to validate the work-flow a) a rat tibia was loading in a materials testing machine whist the strains were measured with a strain gauge. These strains were compared with those found in b) the finite element model replicating the strain gauge experiment. c) First principal strains were found to be aligned to the direction of the stain gauge, and so these were the strains compared in the analysis.

5.3 Results

5.3.1 Validation

Strains recorded by the strain gauge were found to be repeatable, with an average strain of 120.5 με ±4.04 over 4 loading cycles. The comparable FE model showed average 1st principal strains of 128.6με, at a load of 10N across the region of the strain gauge application. Strains measured by FE and strain gauge therefore differed by 6.3%. The strains in the control FE model (A) also predicted the location of bone adaptation described in Chapter 4.

5.3.2 Finite Element Analyses

The distribution of effective stress and strain across the control tibia-fibular complex showed a region of peak values within the antero-distal aspect of the tibia (Figs. 5.3-5.4). The average effective stress, strain and strain rate across the antero-distal region of the tibia in each model are summarised in Figures 5.5-5.6 and Table 5.2. Average stress and strain are also shown on Figure 5.7. For all nodal data see Appendix 5.

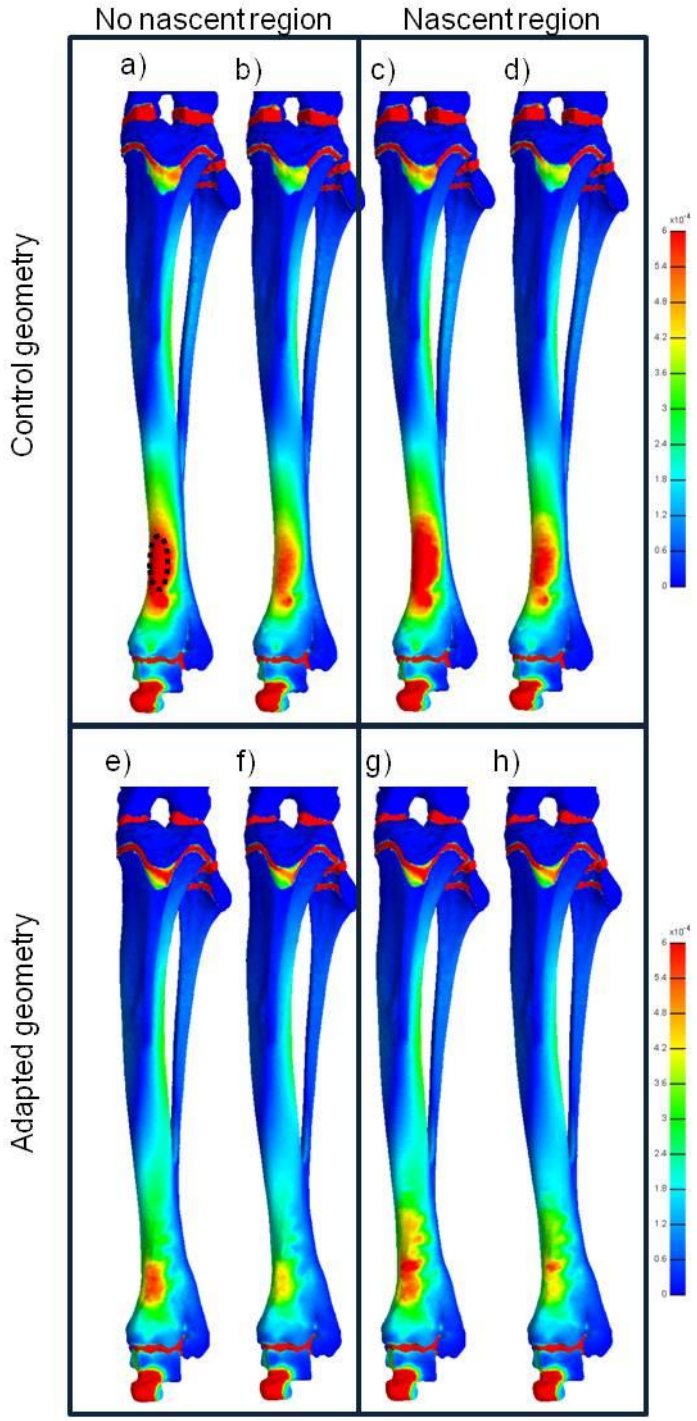

Figure 5.3 Distribution of effective strain across the 8 FEA models. Distribution of effective strain across the anterior aspect of the tibia-fibular complex in the FE models (refer to Table 5.1 for model details). Pseudocolour scale is in strains with blue representing low strain (0με) and red high strain (>600με). Broken line indicates the location of the surface nodes sampled in each model (see Table 5.2).

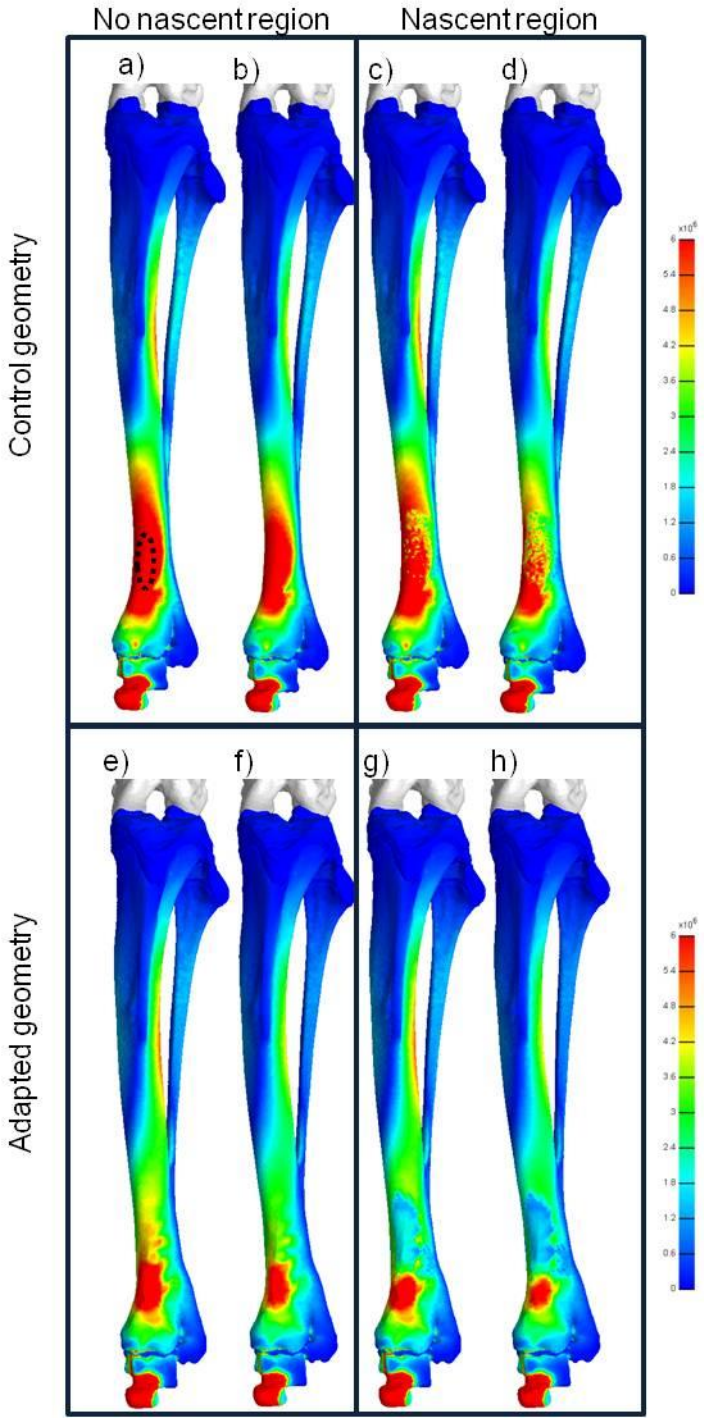

Figure 5.4 Distribution of effective stress across the 8 FEA models. Distribution of effective stress across the anterior aspect of the tibia-fibular complex in the FE models (refer to Table 5.1 for details). Pseudocolour scale is in MPa with blue representing low stress (0MPa) and red high stress (>6MPa). Broken line indicates the location of the surface nodes sampled in each model (see Table 5.2).

Table 5.2. Summary of models and simulated average effective strains (± SD), average effective stresses (± SD) and effective strain rates for the antero-distal region of the tibia in each model.

Model	Average effective strain (με)	Strain rate (με/s)	Average effective stress (MPa)
A	695 (±24)	20800	10.6 (±0.36)
B	552 (±19)	16500	8.4 (±0.29)
C	751 (±48)	22500	6.7 (±1.67)
D	596 (±38)	17800	5.3 (±1.33)
E	356 (±89)	10600	5.4 (±1.36)
F	282 (±70)	8400	4.3 (±1.08)
G	456 (±79)	13700	3.0 (±1.35)
H	362 (±63)	10800	2.4 (±1.07)

Model C (control geometry, control muscle force, and small region of nascent bone) showed the highest strain rate (22500με/s) and effective strain (751με, Fig.5.5), which was 8% ($p<0.001$) higher than in the control model A. The addition of a larger region of nascent bone to the adapted geometry (compare models E and G) resulted in a 28% increase of effective strain ($p<0.001$). Model F, with adapted geometry and adapted muscle, showed the lowest strain rate (8400 με/s) and effective strain (282με), which was 60% lower ($p<0.001$) than in the control model A.

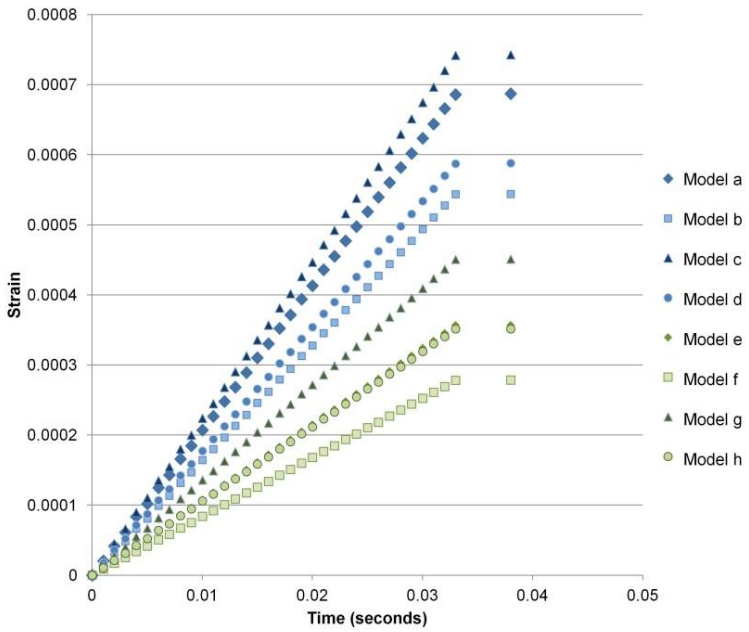

Figure 5.5 A graph of average effective strain rate within the antero-distal region of the tibia. Model parameters are summarised in table 5.1. Following 0.04 seconds the average effective strain remained constant, and so data was not included here.

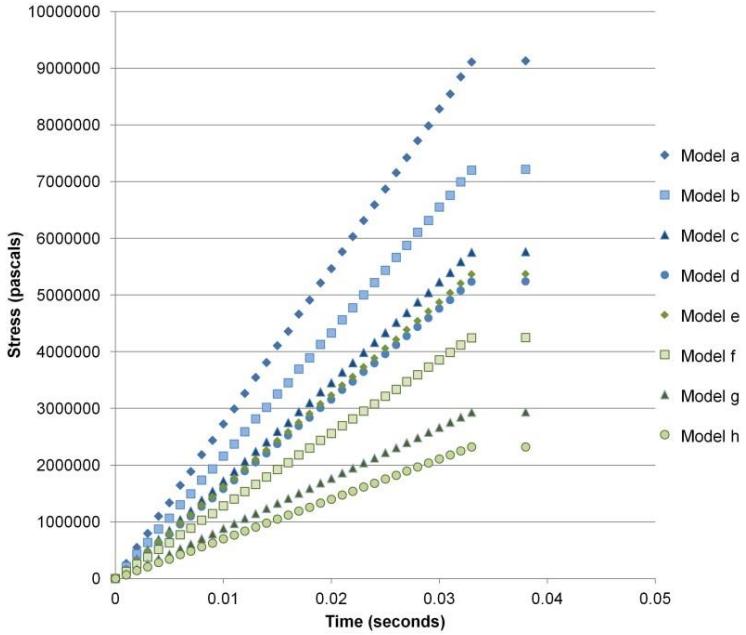

Figure 5.6 A graph of average effective stress rate within the antero-distal region of the tibia. Model parameters are summarised in table 5.1. Following 0.04 seconds the average effective stress remained constant, and so data was not included here.

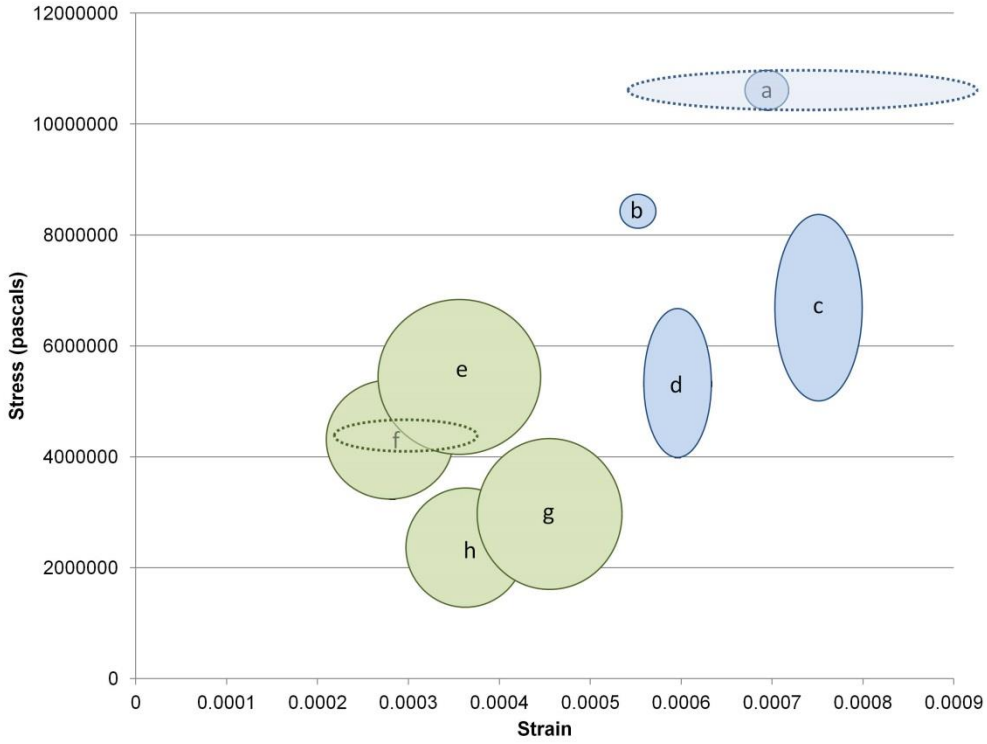

Figure 5.7 A graph of average effective stress plotted against average effective strain. Solid lines represent the standard deviation for each model average (A to H). Dashed lines represent the average effective stress and average effective strain due to variation of elastic modulus of cortical bone within models A and F.

The largest reduction in effective stress was seen in relation to the control geometry with the control muscle (model A). The addition of even a small region of nascent bone (model C) significantly reduced stress by 37%, from 10.6 to 6.7MPa ($p<0.001$). The addition of a larger nascent region to the adapted geometry gave a 44% reduction ($p<0.001$). The reduction of muscle force seen by the 28th day of stimulation (model D) appears to decrease effective stress by a further 21% whilst the adaption of geometry (model H) reduced effective stress by another 54%. These different trends are illustrated by the relative position of datum points shown on Figure 5.7.

To summarise, significant reductions of effective strain were achieved with changes of bone geometry (models A and E) and decreased muscle force (models A and B) whilst significant reductions of stress were achieved by changes of bone geometry (models A and E), reductions of muscle force (e.g. models A and B), and the

presence of more compliant nascent bone (e.g. models A and C). Conversely, nascent bone significantly increased effective strains (e.g. models E and G).

5.3.3 Sensitivity analysis

Changing the material properties of trabecular bone between 2.6 and 4.7GPa had a negligible effect on the magnitude of simulated effective strain and stress (± ~1με and ± ~4KPa, respectively). Altering the material properties of the cartilage by ±30% resulted in a small change in the magnitude of effective strain (between +31 and -22με) and effective stress (+350 and -467KPa). The largest variation in strain was seen by shifting the elastic modulus of the cortical bone (see Table 5.3). This resulted in effective strain values ranging by as much as +226 and -153με, and effective stress values varying by +364 and -309KPa. Sensitivity ranges are also shown by dashed lines around models A and F on Figure 5.7. These results demonstrate that variations in the elastic modulus of cortical bone shift the absolute strain values by up to 33% but if applied consistently the relative differences between models were preserved (refer to Table 5.3).

Table 5.3. The effect of varying the estimated elastic modulus of cortical bone upon the average effective stress (MPa) and average effective strain (με) within the antero-distal region of the tibia. Standard deviations for each average value are represented in brackets.

	Strain (με)			**Stress (MPa)**		
	19.9GPa	**15.5GPa**	**24.7GPa**	**19.9GPa**	**15.5GPa**	**24.7GPa**
Model A	695 (±24)	921(±31)	542(±18)	10.6(±0.36)	11.0(±0.37)	10.3(±0.35)
Model F	282 (±70)	376(±93)	219(±55)	4.3(±1.08)	4.5(±1.11)	4.2(±1.05)

5.4 Discussion

Previous studies have suggested that strain magnitude, strain rate, as well as the frequency of each stimulus episode, and the timing of rest periods between episodes all effect the nature and scale of the resulting osteogenic response (see

section 1.4 and 1.5). Our control model indicates that a response can be elicited at an effective strain of about 695με, which is lower than the reported threshold of 1050με required to induce an osteogenic response in the rat tibia (Turner et al. 1994). Similarly, simulated strain rates values are within the low to medium ranges of strain rate reported by Mosely and Lanyon (1998) for normal rat activity in the laboratory. These findings might therefore suggest that low magnitude strain episodes delivered at a low rate can also have a potent osteogenic effect if endured at regular intervals over an extended period of time (approximately 2880 cycles/day for 28 days, see Chapter 4). However, because we are simulating not replicating the physiological conditions, some degree of uncertainty is inevitable regarding the absolute values produced by our models. For instance, in-vivo strain rates could have been significantly higher than documented here in-silico if foot flexion occurred more rapidly than reported (Gruner et al. 1980). Furthermore as the stimulation did not impede the animals locomotion, muscular loads could coincide with high-impact forces arising from the animals ambulation. The emphasis is therefore primarily on the relative changes reported here, and the absolute values are indicative of the prevailing conditions (see sections 5.3.1 and 5.3.3).

Irrespective of trade-offs between strain attributes, the same general principle applies - deformation provides a localised stimulus to guide bone increase in regions of mechanical need, and removes regions which are structurally superfluous, therefore reducing the chance of skeletal fracture for a minimum amount of material (Frost 2003). Skeletal optimisation can occur within the material or the geometry. The behaviour of bone as a material is largely determined by its constituent materials, collagen and hydroxyapatite mineral (see section 1.2.1). Mineral provides rigidity which bone requires to act as a lever and to bear loads without buckling. During muscular contraction long bones are exposed to a large amount of bending, and so must also be tough in order to absorb energy without fracture, a characteristic achieved by its collagen component (Currey 1979). As bone is formed it is progressively mineralised, and so becomes increasingly rigid. In rats, mineralisation is a very rapid process, with new bone reaching a mature elastic modulus just 5 days post deposition (Donnelly et al. 2010). Despite the speed of mineralisation there remains a period of time in which even a small region of newly deposited (nascent) bone acts paradoxically to increase, not decrease, effective strain (model C). It remains to be determined whether the reduction of muscle force mirrors the nascent bone formation closely enough to negate these strain increases.

A bone experiencing bending forces is required to be both rigid and tough (Currey 1979). It is therefore interesting to note that in the adapted bone, the nascent region of bone, as discussed in section 4.4, was sufficiently large to suggest that it is more than 5 days old, yet still displayed a substantially lower elastic modulus than the established cortical bone (see section 4.3). If this region had undergone more rapid mineralisation, our models (models E and G) indicate the effective strains would be marginally reduced by 22% (456με to 356με) at a cost of an 80% increase in effective stress (3.0 to 5.4MPa). This suggests that the region of nascent bone remains to act as a shock absorbing bandage (Figs.3g-h).

Utilising FEA has enabled detailed investigation of the biomechanical environment of the skeleton, both in control and adapted bones. A similar experiment used DIC (see section 2.3.2) to investigate how bone adaptation to axial compression changes the strain across a bones geometry (Sztefek et al. 2010). DIC investigation revealed that following loading there is a smoothing of strain across the lateral and medial surfaces of a mouse tibia. However, the sensitivity of DIC (300με) means that no significant differences in strain are reported (Sztefek et al. 2010). Therefore here FEA has allowed investigation of a more subtle loading regime, and changes to it caused by skeletal adaptation.

In summary, the models presented here indicate that the region of new bone reported in section 4.3 could, in the short term, exacerbate strain magnitude by preferentially decreasing stress to minimise the risk of fracture. Continued bone growth, subsequent mineralisation, and a decrease of muscle force, result in a decrease in strain as well as stress. Thus these results indicate that the combined response of the musculoskeletal system may achieve the end goal of the mechanostat hypothesis in a less straightforward manner than originally postulated.

Chapter 6: The musculoskeletal system is vital for movement, and movement is vital for the musculoskeletal system

Chapter 6

6.1 Summary of results

In the introductory chapter it was hypothesised that a prolonged period of controlled muscular contraction will provoke a significant bone response. This was addressed by three major experimental components. The first major component consisted of quantifying the extent of shrinkage which I_2KI staining causes to soft tissues. Quantification of shrinkage allowed for an evaluation of the use of the technique for subsequent studies. The extent of shrinkage in tissues stained at low I_2KI concentrations (2%) was comparable with that resulting from traditional fixation techniques, such as 70% ethanol and phosphate buffered formal saline (PBFS, approximately 25% volume reduction). Higher I_2KI concentrations, which are often used in morphological studies of post-embryonic samples, caused more substantial shrinkage. The extent of shrinkage varied across cardiac muscle, skeletal muscle and cerebellar tissues, and incubation periods. The largest determinant upon shrinkage, by far, was the concentration of iodine used to stain the tissues (see section 3.3).

The advantage of being able to image soft tissue at high resolution has led to I_2KI being especially useful for morphological studies. The use of this technique is largely for staining small specimens, with the largest specimen being a juvenile alligator head (approximately 500g) (Gignac and Kley, 2014). In order to achieve sufficient contrast and penetration of the iodine into the tissues the authors recommend high iodine concentrations and extended incubation periods. Interestingly, despite using 11.25% I_2KI for several weeks the soft tissues did not appear to undergo the extensive shrinkage documented in Chapter 3. The apparent difference in shrinkage levels may be a result of larger specimens shrinking to a lesser degree than smaller samples. Assuming that the shrinkage observed is a result of osmotic gradients, a larger block of soft tissue would lose proportionally less of its water than a smaller volume content to equalise the osmotic potential between tissue and solution. The results in Chapter 3 show no correlation between the initial sample size and the extent of the shrinkage, however only mouse material was used, and as tissues were standardised, only a small range of sample sizes was possible. Therefore to investigate the effect of initial sample size upon shrinkage it may be useful to include a greater number of larger species which have been used in iodine-enhanced microCT such as rabbit (Stephenson et al. 2012).

Alternatively the intact alligator skull may undergo less shrinkage as the tissues are stained in situ. The tissues studied here were stained in isolation in order to test the differences in shrinkage which may exist between tissue types. This makes the results directly applicable to cardiac tissue which is often scanned as an isolated organ (Stephenson et al. 2012). Skeletal muscle however, is often stained and imaged in situ, where shrinkage may be limited by bony constraints. Indeed, Tahara and Larsson found that an intact ossified skull with muscles attached and stained with I_2KI showed only 5% shrinkage (2013). In this respect, the results in this thesis present a worst case scenario in terms of the extent of shrinkage which may occur, and document for the first time the extent of soft tissue shrinkage resulting from emersion in I_2KI.

Despite the extensive shrinkage that can be caused by I_2KI staining, this method presents a convenient technique for imaging bone and muscle within a co-registered space at high resolution. The benefit of co-registered imaging of muscle and bone for this investigation outweighed the disadvantage of the tissue shrinkage. The effects of shrinkage are likely to be less than reposted in Chapter 3 as the muscles were stained in situ, and so were unlikely to exhibit the worst-case shrinkage documented in Chapter 3. In Chapter 4 iodine-enhanced microCT was utilised to document relative changes in muscle volume.

Of the different methods of applying controlled muscular contraction to bone, electrical muscular stimulation (EMS) presented the most benefits (see section 2.1), and yet has been used surprisingly little to investigate bone's mechanoadaptive responses. Therefore, in line with the aims of this thesis, the second major component of this thesis utilised EMS to experimentally load muscle and bone. Following stimulation the morphological responses at both the macro and microscopic levels were documented by the use of microCT. Stimulated muscles were 20% smaller relative to their contra-lateral control muscles. The difference in muscle volumes is unlikely to be an artefact of the shrinkage caused by iodine staining, documented in Chapter 3. In Chapter 4 the muscles measured were stained in situ, using the same concentration of I_2KI solution, whilst some variation exists in the extent of tissue shrinkage it is not sufficient to explain a statistically significant decrease of 20% in muscle volume. Furthermore, previous studies have found similar periods of muscle stimulation result in reduced muscle volume (Salmons 2009).

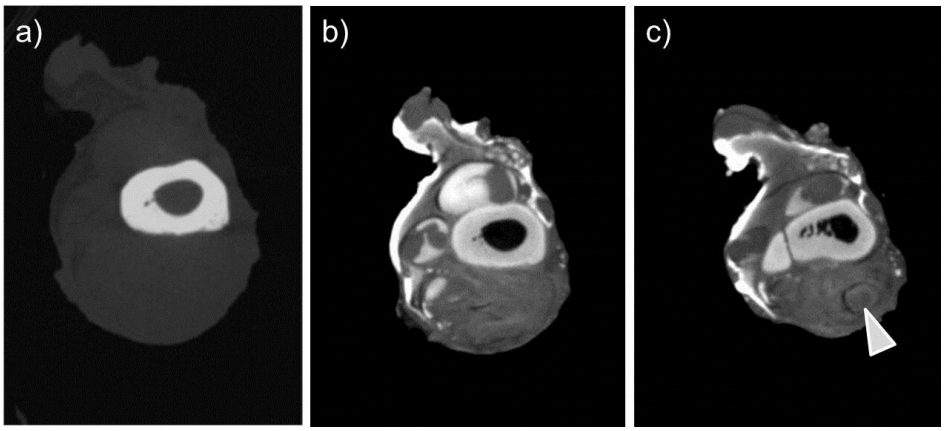

Figure 6.1 Iodine-enhanced microCT for visualising bone, muscle and tendon. MicroCT imaging of the same rat hindlimb a) without a contrast agent provides detail of mineralised structures but no detail of soft tissue. b) Iodine-contrast enhancement provides some soft tissue detail, such as muscle outlines, however here tendons are not visible c) more distally some tendons, such as the tibialis anterior (arrowhead) can be visualised. Images are to scale.

Regional cortical thickness and bone mineral density measurements along the anterior and posterior aspects of the tibia revealed no global changes across the tibia. There was instead a highly regionalised, significant increase in bone volume (Fig.6.2) of 30% within the antero-distal region of the tibia compared with contra-lateral control tibia. A biomechanical model further highlighted the importance of this region, by indicating that it was the region of peak strain as a result of contraction of tibialis anterior. This region was therefore focussed upon for histological investigation. Histological sectioning revealed a large region of newly deposited bone, apparently containing regions of chondrocytes. Given the short space of time over which this large bone growth was achieved, and the presence of chondrocytes, it is possible that this growth was achieved by endochondral ossification. This is an unusual response to loading, and endochondral ossification is usually only reported in long bones during development, longitudinal growth and during fracture repair, and in this chapter further possible explanations for this growth will be investigated.

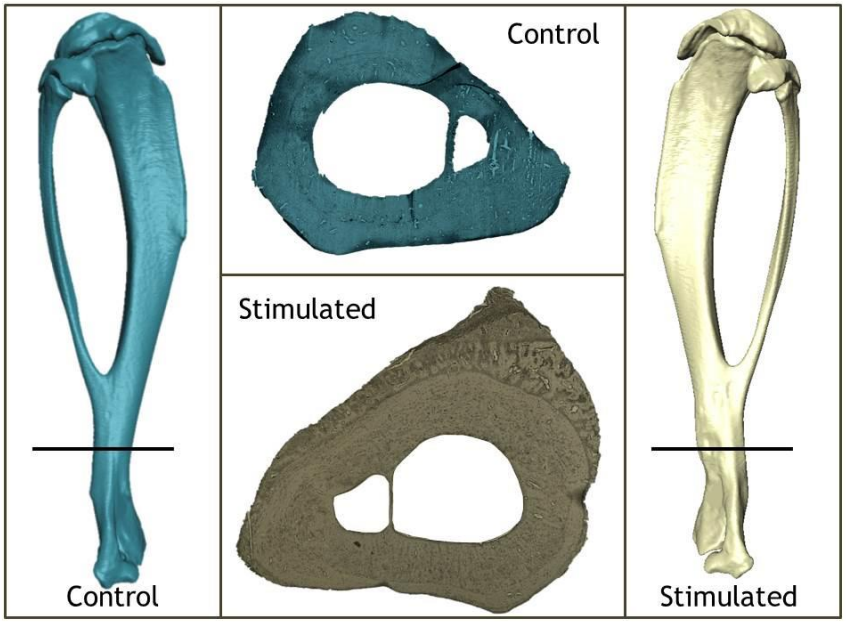

Figure 6.2 Control and experimental tibiae at both the macro and microscopic levels. The stimulated tibia-fibula complex (cream) showed a highly localised region of increased cortical thickness compared with the contra-lateral control tibia-fibula complex (turquoise), which can be clearly demonstrated by histological cross section (inset), taken at the level indicated by black line on the tibia-fibular complex.

The magnitude of loading associated with tibialis anterior contraction were substantially below those considered as a threshold for bone deposition (less than 10N as opposed to 40N, Turner et al. 1994). Therefore it does not appear to be the magnitude of load per se which is resulting in bone deposition. Rather the bone response is being provoked by the repetitive nature of the loading regime, which allows the bone 29 second rest periods between each load (under 10N). The insertion of rest periods into a loading regime has been found to be highly osteogenic in loading protocols using large loads (Robling et al. 2001), but ineffective at enhancing an osteogenic response to very small frequent loads (Xie et al. 2006). The use of implantable electronic stimulators allowed the investigation of far more frequent loads than are possible with an external loading rig, as animals do not require anaesthetic for each loading session. However a load applied every 30 seconds is far less frequent than loads applied by oscillatory loading. The loading regime utilised in this thesis is therefore an interesting previously unstudied middle ground for looking at the relationship between how frequently a load is applied against its magnitude in determining an osteogenic response (see section 1.5). The

resultant robust bone growth may imply that a continuum exists between the loading modalities, and that the bone is in some way responding to the aggregate load, in terms of magnitude and frequency. The possibility that bone responds to an aggregate of magnitude and frequency has interesting implications for the mechanosensory mechanisms within bone (see section 6.4). Furthermore the results in Chapter 4 indicate that bone may be responding by initiating endochondral ossification, a process which is often regarded as only active during the initial formation of long bone's and is only then reactivated in fracture repair. The manner in which bone responds to differing mechanical stimuli is often discretised into separate responses, for example, as discussed in the introduction bone modelling and remodelling share many common elements, and the different end result may be a factor of the prevailing mechanical environment (compression, shear, intermittent etc.) as opposed to the initial stimuli (discrete fracture, micro-cracks, habitual loading etc.).

Following assessment of musculoskeletal morphology the computational model used in Chapter 4 was developed for more comprehensive biomechanical analyses. The third major component of the thesis investigated the effect of skeletal form, and material properties upon biomechanical function. Dynamic finite element analysis was used to model the tibia-fibular complex in the contra-lateral control limb, and in the stimulated limb. To investigate the effects of the adapted muscle forces and the region of nascent bone, additional models incorporating these aspects were created. In total 8 models were created, 4 with the geometry of the control bone, 4 with the geometry of the adapted bone. Within each of these groups 2 had the control muscle force and 2 the adapted muscle force. These groups were further divided into a model with homogenous bone material properties, and ones with a region of nascent bone in the antero-distal region. Dynamic analyses were used to allow for an estimation of relative strain rates and magnitudes.

A region of nascent bone increased effective strain, and decreased effective stress magnitude within the antero-distal region of the tibia, compared with mature bone in both adapted and control geometries. Loading often results a surface bound layer of lowly mineralised bone deposition, similar to the nascent bone region modelled in the control geometry. These results would therefore suggest that initially bone formation exacerbates effective strain magnitude. This provokes the question, if a high strain event results in bone deposition, and this further increases local effective strain, then where does the cycle end? Whilst the models in Chapter 5 do not test this question directly, it can be seen that when a nascent region is as large as the

region found on the adapted tibia then both effective stress and strain are significantly reduced within this region. Implying that there is a tipping point at which bone mass becomes more influential than bone material properties in determining effective strain.

The muscular adaptation documented in Chapter 4 reduces strain and stress relative to the control muscle forces. Therefore, if the reduction in muscle force precedes the region of nascent bone formation then strains may only be decreased from the original values, highlighting the importance of considering the interactions between musculoskeletal tissues when considering adaptive responses. In this case it appears that bone and muscle worked in synergy to reduce both muscular energy expenditure and skeletal stress (see section 5.4).

Within the control model, with control muscle forces and no nascent region of bone, the average effective strain within the antero-distal region of the tibia was only 695με. This value differs from that of Chapter 4, as dynamic analyses were used in Chapter 5, whist a quasi-static analysis was used in Chapter 4. Strains were therefore still far below the level of strain considered sufficient to provoke bone growth (Turner et al. 1994) or osteocyte activation (You 2000). However, the computational simulation modelled the loads imposed by muscle stimulation, and the static load of body weight. In reality during ambulation reaction forces from the ground would be imposed on the tibia, and body weight will be spread across 2 or 3 limbs, not 4. Ambulatory loads, and additional muscular forces may then coincide with the stimulation induced contraction, increasing the effective strain values within the antero-distal region of the tibia. Therefore there will be times when the strain will exceed 695με. Yet such a substantial and consistent bone growth as documented across animals in Chapter 4 implies the tibia is responding to more than chance occurring high strain events. It should be taken into account that this is a model, not a measurement, and the extent to which natural variation of material properties influences the strain values reported was captured in a sensitivity analysis. The results of the sensitivity analysis showed that variation of material properties of the cortical bone had substantial effects upon the strains across the bone. Despite the substantial variation in strain magnitudes the highest effective strain in the antero-distal region were still below the strain values reported to provoke an osteogenic response.

The discussions in previous chapters have emphasised the importance of the presented work for studying mechanoadaptive responses of the skeleton. This

chapter puts the results within the wider context of musculoskeletal biology, as well as considering avenues for the development of the techniques and results presented here.

6.2 What is the bone response to electrical stimulation?

Within Chapter 4 a tibia from a stimulated limb was sectioned and investigated microscopically. This highlighted a number of interesting cellular characteristics including a clear region of bone growth. The new bone appeared somewhat separate from the established cortex, with a clear boundary between the two (Fig.6.3). Within the region of new bone there was very little collagen organisation and clear primary osteon formation. Between primary osteons were clusters of chondrocytes. Peripherally the periosteum appears to be proliferating and contributing to the new bone. This response is unusual in many ways, in particular is the presence of cartilage cells in a region which is not a growth plate.

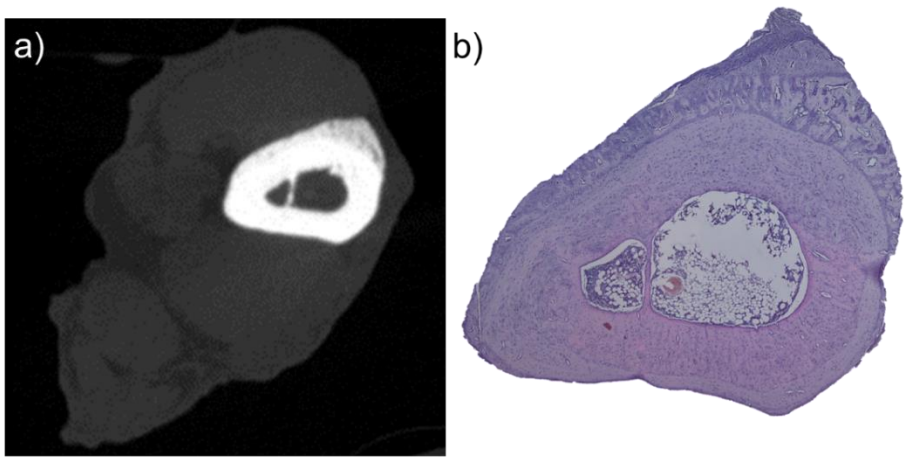

Figure 6.3 A section through the region of the tibia showing robust bone growth in microCT data and histologically. The new region of bone is clearly distinguishable on both a) the microCT data and b) the histology (stained with H and E).

The inclusion of cartilage within the region of bone growth is surprising. As introduced in section 1.1, long bones form from a cartilage precursor which is gradually replaced by bone. Cartilage is then only retained within growth plates to enable continued longitudinal growth. The results in Chapter 4 demonstrate that composite cartilage/bone tissues can form distinct from the growth plate. However

these experiments were conducted in growing rats, with active growth plates. It is therefore possible that the endochondral process observed here is due to the immaturity of the bone, and if the same experiment was carried out in a mature human tibia, a different response would be observed. Whilst long bones are thought to lose their ability to grow by endochondral ossification upon closure of their growth plates, they retain the ability to form bone via endochondral ossification in the event of fracture (see section 1.2.3). Therefore it would appear that bone never truly loses endochondral potential. Indeed as cartilage proliferation and hypertrophy is possible at a far faster rate than the time-consuming surface-bound process of bone apposition this would explain how such a large region of bone (necessitating over 10 µm of transverse bone growth a day) was created in such a short period of time. Similar islands of cartilage have been found in mature rat bone (Shipov et al. 2013). These islands were attributed to a lack of bone turnover in rats, resulting in cartilage from the initial cartilage precursor being retained. Endochondral ossification is extensively documented within the growth plates of bone, allowing longitudinal growth. During this process chondrocytes pass through a series of phases; rest, proliferation, hypertrophy and calcification, this is a highly ordered process with cells aligned longitudinally into rows (Fig.6.4). This sort of highly structured arrangement is clearly not present in the region of bone growth presented in Chapter 4, but may have been at earlier time points during the bone's growth. Furthermore if this region of bone were created as a cartilage precursor and was subsequently invaded with cortical blood vessels, then cartilage would be expected to be located in the periphery of the new bone, but it is not, it is central (Fig.6.5).

Chondrocytes within bone are not always part of a transitional tissue. Chondrocytes can exist within bone as chondroid bone, a calcified tissue which has elements of both bone and cartilage. Chondroid bone can exist as either a transient tissue between fibrous precursors and bone, such as in distraction osteogenesis (Yasui et al. 1997) or as a permanent tissue. The formation of chondroid bone differs from endochondral ossification as it does not involve invasion by blood vessels (Yasui et al. 1997). In this respect the process documented here more closely resembles an endochondral process, as there is clear blood vessel invasion of the cartilaginous region (Fig.4.21).

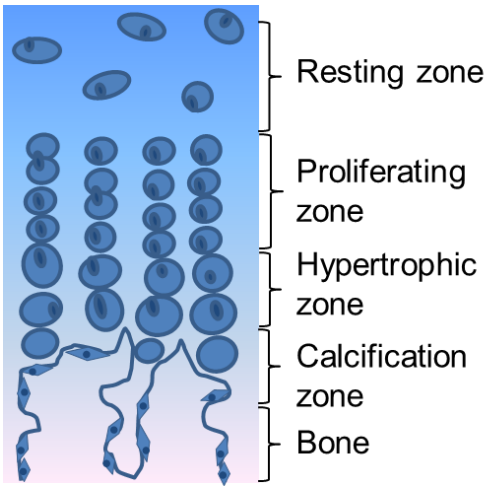

Figure 6.4 A diagram of the different cellular zones within a growth plate. Chondrocytes are initially resting, and then proliferate, this occurs in columns, producing the characteristic order to the growth plate. Following proliferation chondrocytes hypertrophy, and then calcify. The calcified chondrocytes are replaced by bone cells. Figure modified from Staines et al (2013).

The region of new bone is not homogenous and appears to have different regions within it (Fig.6.5). Peripherally the periosteum appears to proliferating, which cannot be seen on the control bone (Fig.4.15). At points the cells of the periosteum appear to be spilling into pockets of bone tissue (Fig.4.19), indicating that the peripheral region of new bone has been created by an intramembranous process. Medial to this is a region containing the clusters of cartilage, invading blood vessels, and primary osteon formation. This layered structure may indicate that initially the stimulus for bone growth was so large that it provoked growth by an endochondral process, however as the muscle contractions continued, the initial strain stimulus (see FEA results, section 4.3.2) was diminished, by the increased bone, but not removed so a slower process of direct bone formation took over.

The region of new bone growth appears separated from the existing bone, with a clear boundary between the two. The clear boundary is similar to a resting line, which are thought to be created by changes in the rate of bone formation (Skedros et al, 2005), and a rapid initiation of bone growth could have resulted in a boundary such as this, the new bone is continuous with the established cortex, as can be seen at the macroscopic level (Fig.6.6) and microscopically, by the presence of blood vessels passing between the two regions (Fig.6.7).

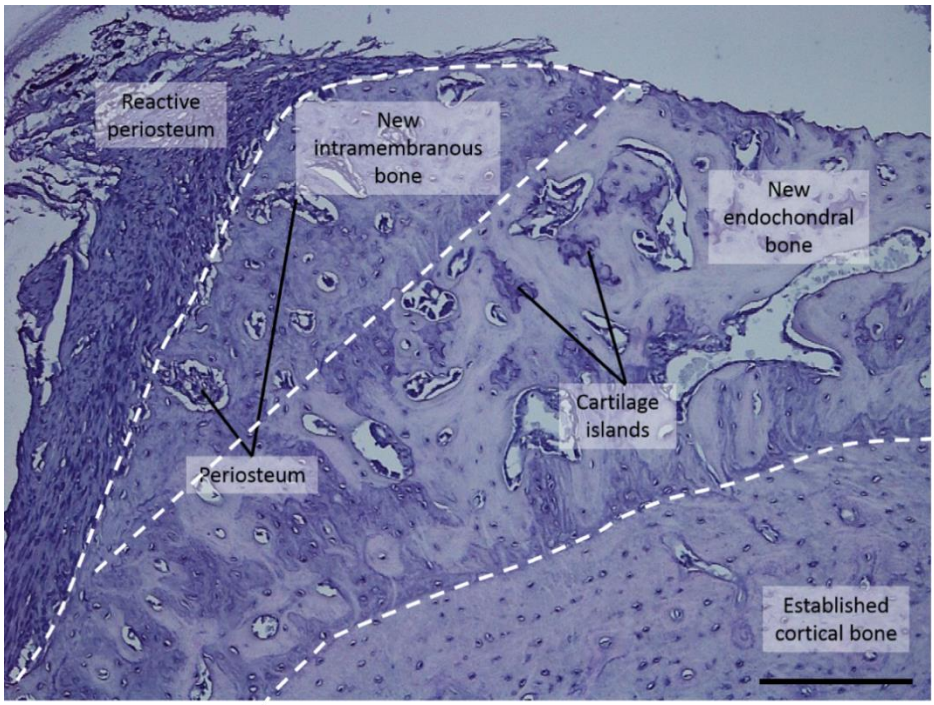

Figure 6.5 The four regions within the experimental bone. A histological section of the experimental bone, highlighting the region of new bone. The new region of bone shows chondrocytes and is being invaded by blood vessels, implying endochondral ossification. More peripheral bone does not appear to have any regions of cartilage, and contains pockets of the reactive periosteum, implying direct ossification. Stained with H and E, scale bar represents 200µm.

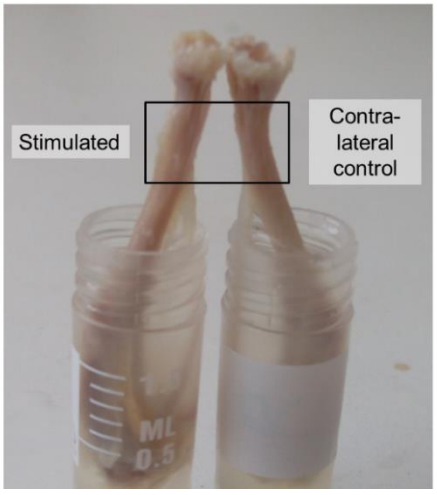

Figure 6.6 The stimulated and contra-lateral control tibiae, the region of new bone is visible. The tibia of the stimulated and contralateral control limbs, before they were sectioned for histology. Highlighted is the region of the tibia showing growth. It can be seen that the region of bone growth is continuous with the tibia, but less opaque than the established cortical bone.

The region of new bone growth has a disorganised structure compared with the established bone, which can be easily observed on the microCT data, light microscopy and polarised light microscopy (Fig.4.16-17). This response appears different from previously observed bone growth in response to loading, which is typically lamellar or woven. These two responses are often divided up and treated as separate responses (McBride and Silva, 2012; Turner et al, 1994). Lamellar bone is highly organised, and relatively slow to form (maximal rate of deposition 3.5±1.1µm per day), it is typically seen in growth and in response to low loads. Lamellar bone growth is therefore often deemed an advantageous or functional response (McBride and Silva, 2012). Woven bone is characterised by poor organisation, low mineral density and high cellularity and is often associated with damage (McBride and Silva, 2012). Woven bone is often seen alongside fracture, but it is unclear as to whether it is indicative of damage. For example, Sugiyama et al regard woven bone as a response to bone being required at a faster rate than can be achieved by lamellar deposition (Sugiyama et al, 2012). This would often be the cases in pathology, but need not always be the case.

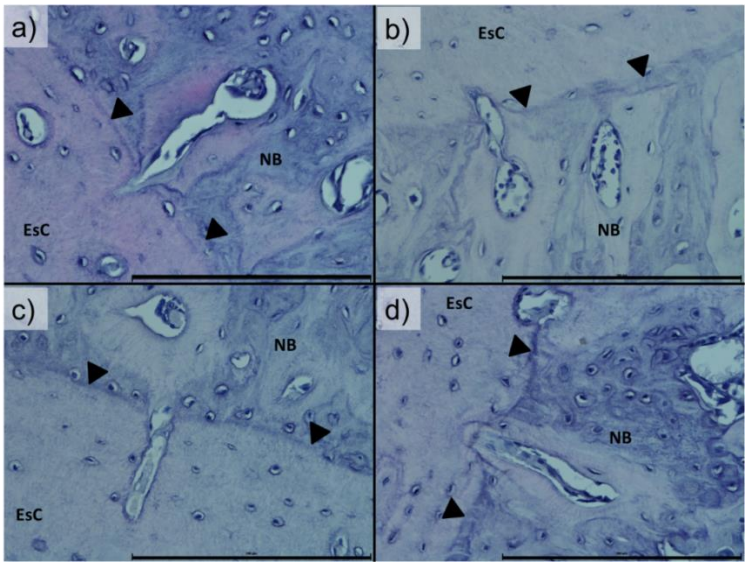

Figure 6.7 Histology of blood vessels traversing the boundary between cortical bone and new bone. a-d) Sections of the tibia in the stimulated limb. There is a clear boundary between the region of new bone and the established cortical bone, however there are points were blood vessels cross this boundary, implying they are continuous. EsC indicates established cortical bone, NB indicates new bone and arrows indicate the boundary between the two. Scale bars represent 200µm.

The histology of the tibia reveals that the new bone region is abruptly demarcated by a clear boundary. This boundary was probably a result of a rapid increase in bone production. A similar margin can be seen in Kidd et al (2010) who present histology of a rat tibia which has been subject to stress fractures (Fig.6.8). The region of new bone seen by Kidd et al is described as a region of woven bone, and has clearly identifiable stress fractures traversing the cortex, and clusters of cartilage were observed towards the exit point of the fracture, 2 weeks after fracture. This is interesting in the context of the results presented in Chapter 4, which shows very similar histology. However upon inspection the stress fractures are clearly evident in Kidd et al (Fig.6.8), but no fractures are identifiable in the histology presented here, furthermore Kidd et al do not show any periosteal proliferation, which is clearly present in Figure 6.5. The presence of cartilage cells within the region of woven bone is an interesting finding as post initial formation, bone is produced by osteoblasts. Therefore it is difficult to see where the cartilage has come from within their region of woven bone. It is possible that the authors did not find the presence of cartilage strange as fracture healing is often described as a recapitulation of development as it reinitiates endochondral and intramembranous processes (Ferguson et al, 1999).

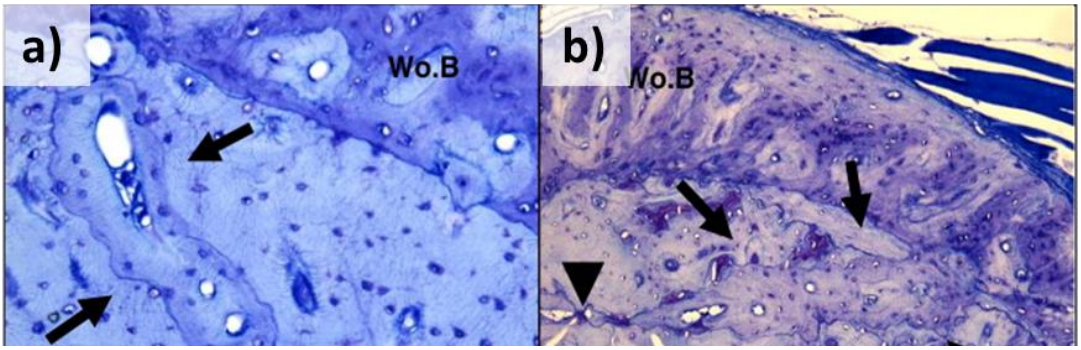

Figure 6.8 Histology of stress fracture healing. Histological sections of a rat tibia healing following stress fracture, Wo.B indicates woven bone and arrows indicate stress fractures. The fractures are evident from the cement line surrounding their region of repair. Between the established, damaged cortical bone and the woven bone response there is a clear boundary. a) six weeks post fracture, b) 10 weeks post fracture. Figure taken from Kidd et al, 2010.

There remains the possibility that the tibia sustained damage in the form of micro-cracks. As discussed in the introduction (see section 1. 2.3) micro-cracks within bone result in a reduced elastic modulus. Nanoindentation was used to assess the material properties within the antero-distal region of the stimulated and contra-lateral control tibiae. Within the stimulated bone the region of nascent bone was indented separately to the established cortical bone. The region of nascent bone showed a very low modulus (8.8±2.2 GPa), and the established cortex of the stimulated tibia showed a higher modulus (20±1.4 GPa) than the cortical bone of the contra-lateral control tibia (15±1.5 GPa). Taken together these results imply that the established cortical bone within the stimulated tibia is not micro-damaged (Burr et al. 1998) and that the region of nascent bone is therefore not a damage response to microcracking of the underlying established cortical bone. Alternatively, the lower modulus measured within the control tibia may imply that during the course of the stimulation period the tibia within the stimulated limb sustained micro-cracks, which provoked a remodelling response (Frost 1960) resulting in an increased modulus by the end of the stimulation period. In this way micro-crack accumulation can be seen as beneficial for the bone in the long-term. To establish if the rapid bone growth is in response to micro-cracking the tibia could be indented, or fushin stained at different time points throughout the stimulation period.

The histology in chapter 4 shows a periosteum which appears to be actively proliferating, and at points contributing to the region of new bone. The periosteum is a double layered structure surrounding bone. The outer layer is fibrous, whilst the inner layer is cellular, containing mesenchymal stem cells for bone growth and repair. Periosteal proliferation has been noted as a part of a woven bone response, alongside a marked increase in proliferation markers (McKenzie and Silva, 2011). Therefore the proliferating periosteum may be part of a woven bone response; however, the periosteum is highly sensitive and can also be provoked by surgical interference or direct pressure (Churches et al. 1980). In the stimulation model the surgical procedure is all performed proximal to the tibia, and therefore would not provoke a response in the tibial periosteum. Passing across the periosteum are tendons. Applying electrical stimulation to muscles increases the force being transmitted by tendons, which could have aggravated the periosteum. The tendon of tibialis anterior in particular, transverses the antero-distal region of the tibia (Fig.6.9) and could provoke the periosteum. However if the bone growth was a result of tendon rub upon the periosteum, it would be anticipated that bone growth would occur along the length of the tendon, which is not the case.

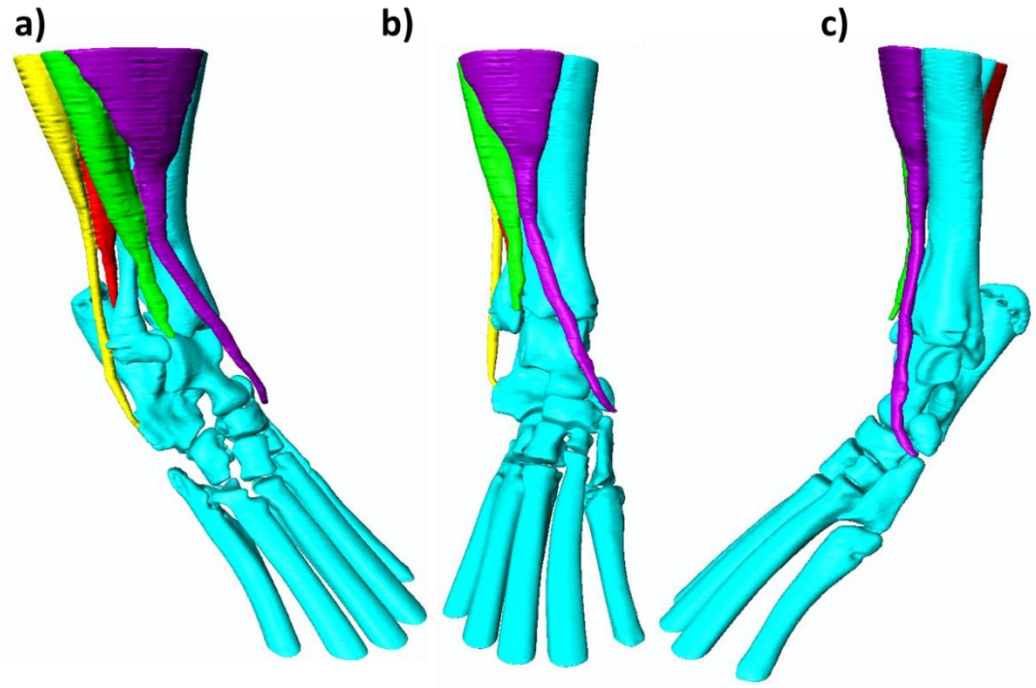

Figure 6.9 Three-dimensional reconstruction of a rat ankle joint, showing the course of the tendons of the stimulated muscles. Skeletal elements are reconstructed in turquoise. Tibialis anterior and its tendon are reconstructed in purple, Extensor digitorum longus in green, Peroneous longus in yellow and Peroneous brevis in red.

The extent to which this bony response differs from those previously reported is not clear as the exact stimulus applied to the tibia is difficult to determine. Applying an electrical current to the common peroneal nerve resulted in the contraction of the antero-lateral compartment of the leg. This occurred every 30 seconds for a period of 28 days. This provides the tibia with a load that is a physiological force, applied at a supra-physiological frequency, resulting in a stimulus which is closer to physiological loading than some of the more established bone loading models, yet still quite distinct from the ambulatory loads the animal would impose itself.

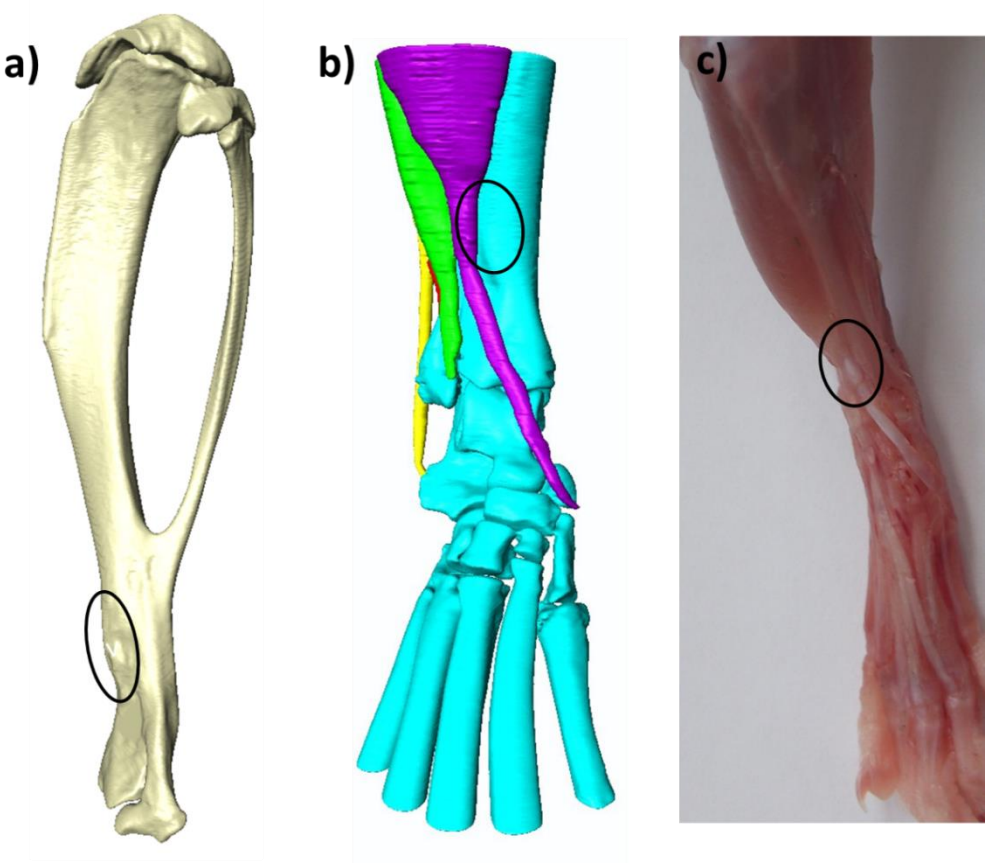

Figure 6.10 Three-dimensional reconstructions of a rat tibia and tibialis anterior compared with a dissected limb. a) A 3D reconstruction of a stimulated tibia, the region showing the robust bone growth is highlighted by the circle. b) A 3D reconstruction of I_2KI microCT data, showing the relationship of the region of bone growth to the tendons of the stimulated muscles. c) A dissection of a rat ankle, showing a small band of connective tissue crossing the tendon of tibialis anterior, close to the site of bone growth.

An electrical stimulus to the common peroneal nerve would increase not only innervation to the musculature, but also to the tibia itself. The influence of the nervous system upon muscle is, as discussed in section 1.11.2, profound. The effects of the nervous system upon bone are less clear, yet could be significant (see section 1.7). The skeleton has extensive innervation (Elefteriou 2005). However, neurectomy does not appear to affect bone formation (Hert et al. 1971). Furthermore, blockade of sympathetic nerves in particular had no effect upon bone formation (De Souza et al. 2005). It has therefore been concluded that the nervous system plays a modulating, not controlling influence upon bone remodelling. The method used here to load bone has the potential complication of increasing neural

innervation to both the muscle and the bone, possibly enhancing the bone formation stimulated by the mechanical forces demonstrated in section 5.3. An enhancing effect of neural modulation would explain why such a large region of bone formation resulted from a relatively low strain stimulus (see section 4.4). However, it is not clear how a bone-wide enhancement of sympathetic innervation would bring about regional responses in bone formation reported in Chapter 4, as previous studies show systemic effects (Kingery 2003). Indeed the inclusion of complete control animals into the analysis, which showed no differences from the contra-lateral control tibiae provides a degree of certainty that the stimulation was not provoking systemic effects upon the bone (see section 4.3).

An important function of the sympathetic nervous system is to regulate blood flow. Bone contains a vast network of blood vessels, the importance of this network for bone formation is rapidly gaining recognition (Le Noble and Le Noble 2014). Bone formation is clearly dependent upon a blood supply. This fact can be demonstrated in fracture repair, where the site can be either vascular or avascular. In avascular sites cartilage forms, and in vascular regions, bone forms (Wilson, 2002), demonstrating the dependence of mesenchymal stem cells upon their surrounding environment, for the direction of their differentiation. Woven bone formation has been found to be especially dependent upon angiogenesis (Tomlinson et al, 2014). Blood vessel growth is therefore clearly an important factor of the bone response documented in Chapter 4.

Bone receives the majority of its blood supply from vessels within its medullary cavity. Branches from these vessels pierce the endosteal surface and supply the cortex. The exception to this is at firm fascial attachments, where blood supply is instead from periosteal arteries (Wilson, 2002). This could be highly significant in the context of this bone response, as the region of growth is close to a band of connective tissue, and so the periosteal arteries may supply this region of cortex. This difference in blood supply could account for some of the characteristics seen histologically. For example, the stimulation increased forces acting on this region of the bone, provoking rapid bone growth. As the region of bone growth increased in size the periosteal arteries were unable to supply the entire region of bone, and vessels from the cortex had not yet reached the region, so cartilage formed instead. As blood vessels formed this cartilage was more slowly replaced by bone (Fig.6.11).

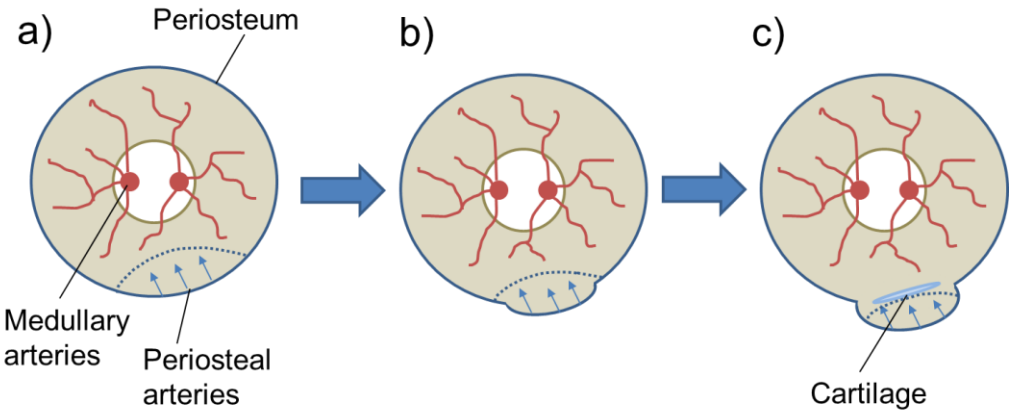

Figure 6.11 Potential blood vessel distribution during bone growth. Cortical bone receives its blood supply from medullary arteries (red lines) except at tendinous insertions, when blood is obtained from periosteal arteries instead (blue arrows). As the bone growth was so rapid and at a tendionous insertion it is possible that growth exceeded the rate of angiogenesis, resulting in a region which lacked blood vessels, and so cartilage formed instead. Figure modified from Wilson (2002).

It is clear, by the quantity of bone formed within the relatively short time-frame of 28 days, that the bone growth was rapid. The need for such a growth is not clear, as the forces applied and the resultant strains within the tibia are relatively low. It may be that these where enhanced by a fascial attachment at this point, resulting in a robust woven bone response. As bone growth outstripped angiogenesis cartilage formed instead of bone. If this were the case, it would be a response which is unique to the loading and anatomy of this model, and highlights the range of bone responses which can be employed as an adaptive response. It is unclear how many of the rats showed this bone response as only one was sectioned for histology, however the microCT data would imply that not all the tibiae had a large lowly mineralised region, yet they all showed cortical thickening. Taken together this may imply that the bone studied was showing a response which some of the other animals had shown, but that this region had subsequently mineralised. Therefore to get a clear idea of what is going on, a more comprehensive histological study would have to be undertaken, looking at the bone at several time points, to establish the time course which is associated with these cellular features.

6.3 Possible mechanisms behind observed bone growth

As outlined in section 1.6, the mechanisms behind bone responses to mechanical stimuli are not completely known. The widely held theory of mechanotransduction is that of interstitial fluid flow acting upon osteocytes to trigger a signalling response which acts upon osteoclasts and osteoblasts to bring about an appropriate response. The bone response documented in section 4.3.3 is substantial and rapid, especially in light of the relatively low-loads resulting from muscle stimulation (see section 5.3). Simulations of muscular loading resulted in a peak region of strain of 695με which is well below the threshold of bone activity (Frost 1987), and thus that of osteocyte activation. However, as covered in section 1.5, it has been found that bone responds to in a more continuous manner than originally proposed in the mechanostat model (Frost 1987). Therefore there is no critical strain threshold for bone activity to be activated (Sugiyama et al. 2012). This implies osteocytes, or indeed any such sensing mechanism, are not guided by thresholds, but instead respond to mechanical stimuli in a continuous manner. Therefore a cellular response could have been provoked by the strain stimulus in the model presented here. This is further reinforced by the fact that osteocytes have been found to regulate transcriptional activity in response to low-magnitude, high-frequency loading (Lau et al. 2010).

Osteocytes respond to mechanical forces by rapidly releasing signalling molecules NO, prostaglandin and Adenosine triphosphate (ATP) (Genetos et al. 2007). All three signalling molecules have a half-life of less than a minute (Nichols et al. 2012; Fitzpatrick et al. 1980; Bowler et al. 2001) with NO the shortest-lived with a half-life of less than 1 second (Nichols et al. 2012). Therefore these molecules are limited in their distribution, and convey local signals which rapidly degrade. However, if a low load (see section 5.3) caused a release of 10 units of signalling molecule, which had a half-life of 30 seconds, and every 30 seconds another equal load was applied, there would be 15 units, and at the subsequent loaf 17.5 and so on, resulting in a gradual accumulation of signalling molecules (Fig.6.12). This is an interesting concept in light of experiments to determine recovery periods for mechanosensitivity of rat tibiae (Robling et al. 2001). Robling et al investigated both short-term and long-term recovery responses of bone to cyclic loading. Short-term recovery experiments consisted of loads of 54N applied for 36 cycles, broken up by 0.5, 3.5, 7 or 14 seconds. Long-term recovery experiments applied 90 loads of 54N with rest periods of 0, 0.5, 1, 2, 4 or 8 hours. Both loading regimes resulted bone deformations in excess of 2000με, and thus were well into Frost's threshold of bone

formation (Frost 1987). Despite the lower load cycle in the short-term experiments the rate of bone formation did not differ significantly between the experiments. In each respective group 14 seconds and 8 hours showed maximal bone apposition of the tested rest periods, yet 14 seconds of rest between each load (36 cycles) appeared more osteogenic than 0.5 hours rest inserted between 4 bouts of loading (90 cycles). In light of the earlier discussion of a mechanism governed by signalling molecules, this may reflect that high loads resulted in large amounts of signalling molecule being released from sensory cells, which saturates the target binding sites, or exhausts cellular stores. A continued loading period can therefore provoke no further response. It has been found that pulsatile fluid flow increased NO release from osteocytes for 10 minutes, following this there was no further increase, indicating a limit point had been reached (Klein-Nulend et al. 1998). A rest period may allow for synthesis of additional signalling molecules and/or for the receptors of the effector cells to become available again (Fig. 6.12). The use of lower loads and rest periods may therefore avoid exhaustion of signalling molecule stores, or saturation of receptors, and so allow for a more continuous process of signalling, molecule synthesis, release and binding. This may be the mechanism behind the response observed in oscillatory loading. Oscillatory loading applies very low but frequent loads, resulting in strains in the order of 10με, yet as little as 15 minutes a day is capable of provoking robust bone growth, and shows no enhanced response with the insertion of rest periods (Xie et al. 2006). Therefore the strains created by oscillatory loading may be so small that there is no saturation in signalling response by 15 mins, and so a rest period does not provide recovery. Thus the continuous application of small loads could accumulate signalling molecules in a more continuous manner than bouts of very large loads.

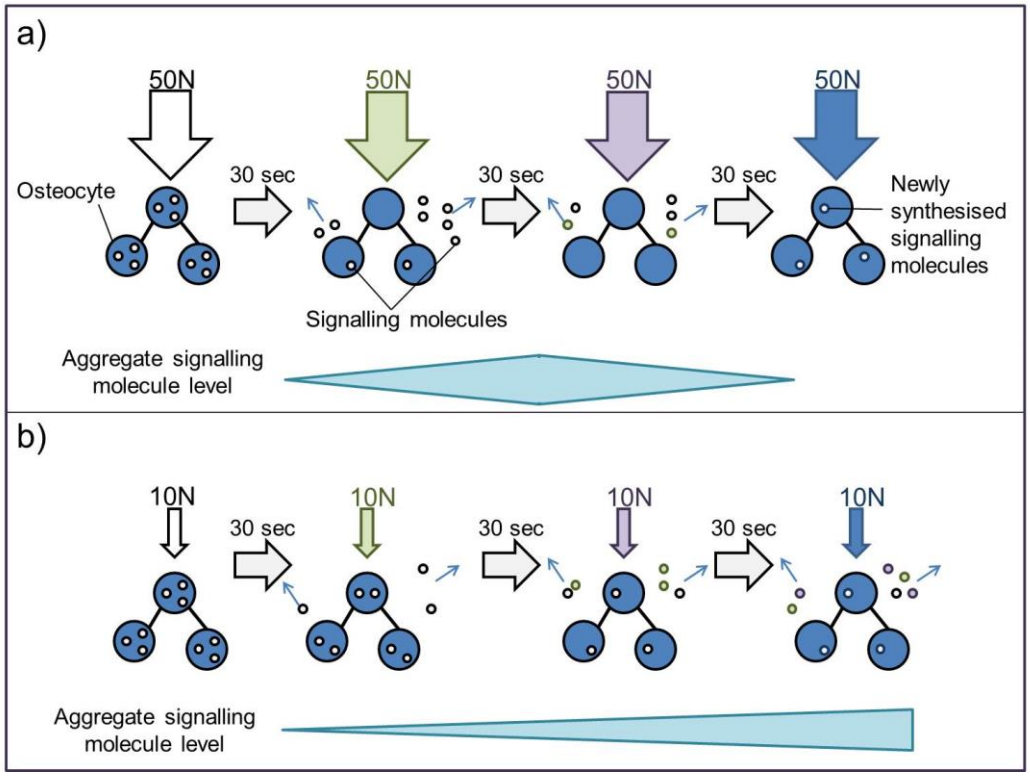

Figure 6.12 Diagrammatic representation of how lower loads could produce a higher signalling response than higher loads. a) The application of high loads causes a bone response which rapidly desensitises. This may be due to high loads causing a rapid and significant signalling response, which is depleted faster than it can be re-synthesised. b) Application of smaller loads may result in a more continuous signalling response, allowing for synthesis of signalling molecules during loading. The application of loads with short rest periods may also allow for an aggregation of signalling molecules.

One of the most rapid responses of bone cells to loading is the release of NO. NO is synthesised in cells via nitric oxide syntheses (NOS). Bone cells and blood vessel endothelium express endothelial nitric oxide synthase (eNOS)(Helfrich et al. 1997). ENOS is sensitive to shear stress, which in blood vessels causes NO release, acting back upon the vessel to relax the smooth muscle, cause vasodilation and reduced shear stress (Koller et al. 1994). In bone cells eNOS is also sensitive to shear stress (Helfrich et al. 1997) and eNOS knockout mice show low bone mass (Aguirre et al. 2001), low bone mineral density and mineral apposition rate (Armour et al. 2001). Low bone mass in eNOS knockout mice is attributed to defective osteoblasts (Aguirre et al. 2001). NO is not only released by bone and blood vessels but also by skeletal muscle in response to mechanical stimuli such as stretch, and is released in

reduced quantities in unloading (Tidball et al. 1998). In skeletal muscle the exact role of NO is not clear, but it potentially provides a mechanism for glucose transport to regions of skeletal muscle most in need (Balon and Nadler 1997). The shared release and responsiveness to NO could provide a linking signal between muscle and bone anabolism. The extent of the role that NO plays in governing the musculoskeletal response documented in Chapter 4 could be investigated by the implantation of miniature neuromuscular stimulators into eNOS knockout mice. However, is mentioned earlier, eNOS also plays a crucial role in regulating blood flow, and angiogenesis. Therefore the deficient bone seen in knockout eNOS mice could be a result of the vital interplay which exists between bone and blood supply (see section 6.5.3).

Another signalling molecule released by osteoclasts in response to loading is ATP (Hecht et al. 2013). ATP is an intracellular energy storage molecule, and also an extracellular signalling molecule (Schöfl et al. 1992). The exact downstream effects of ATP signalling are not entirely clear, but many, seemingly conflicting, roles have been attributed to ATP signalling including: inducing osteoblast proliferation (Nakamura et al. 2000), stimulating osteoclast formation and activity, whilst blocking osteoblast activity (Hoebertz et al. 2002), differentiation of MSCs (Ciciarello et al. 2013) and modulating systemic factors such as PTH (Bowler et al. 2001). ATP has also been implicated in triggering prostaglandin release in bone cells (Genetos et al. 2005).

Prostaglandin PGE_2 has an osteogenic effect upon bone, the nature of this pathway is not entirely clear, but it appears it may be regulated through activation of the Wnt pathway (Bonewald and Johnson 2008). Wnt signalling plays important roles in the differentiation of mesenchymal stem cells (MSCs). MSCs are capable of giving rise to osteoblasts and chondrocytes as well as a number of other cells types (Ling et al. 2009). Wnt signalling at low levels has been found to act upon MSCs and initiate differentiation along the osteoprogenitor lineage (cartilage). At high levels of Wnt signalling MSC differentiation switches instead to the osteogenic lineage (bone)(De Boer et al. 2004). This is especially interesting in light of the histology presented in Chapter 4, with the region of new bone appearing to show a region of endochondral ossification, and a more peripheral region of direct ossification (see section 4.4). Furthermore electrical muscle stimulation has been shown to affect a number of molecular pathways within bone marrow cells. Qin et al showed a highly significant decrease in sclorosin (Wnt inhibitor) and a corresponding increase in Wnt3a levels within bone marrow MSCs in response to one week of electrical stimulation of

hindlimb musculature in the rat (Qin et al. 2013). Although the pattern and duration of muscle stimulation used by Qin et al differs from that outlined in section 4.2.1, this is an interesting finding in the light of the aforementioned link between Wnt signalling and the bone and cartilage responses observed histologically.

The bone marrow is not the only pool of bone progenitor cells; the periosteum comprises an outer fibrous layer, and an inner cambial layer which is a source of osteoblasts and pre-osteoblastic cells. The cambial layer is therefore implicated in appositional bone growth. However, transplantation of the fibrous periosteum can result in endochondral bone growth (Ueno et al. 2001). This implies that the periosteum maintains the potential for growth via endochondral ossification when provided with the appropriate mechanical cues, or biochemical factors arising from mechanical cues. Wnt therefore presents an attractive possibility as the critical signalling molecule, which is increased in response to muscular stimulation. Initially, acting in conjunction with mechanical cues and stimulating chondrocyte formation. As Wnt levels continue to rise due to continued muscular contraction, there is a switching point and MSCs differentiate directly into osteoblasts instead (see section 5.4).

Wnt signalling also plays a crucial role in skeletal muscle development (Von Maltzahn et al. 2012), with Wnt3a increasing connective tissue in muscle (Brack et al. 2007). An increase in connective tissue is common in electrical muscle stimulation (Jarvis et al. 1996). Common signalling pathways between bone, muscle and connective tissue present a mechanism by which muscular loading could have more profound effects than gravitational loads (see section 1.8). These results therefore underline the importance of using muscular loading for investigating mechanoadaptive responses of the skeleton and future work using muscular loading present potential signalling pathways which could be manipulated therapeutically.

6.4 Combined strategy and future developments

The methods used within this thesis provide a powerful combination for current analysis of musculoskeletal form and function. As discussed previously electrical stimulation is not the only method of controlling muscular contraction. Optogenetics involves the insertion of a photo-sensitive ion channels and pumps into a target neuron, either by genetic modification of the animal before birth (Liske et al. 2013) or post-natally by the insertion of a genetically modified virus (Towne et al. 2013). The

photosensitive proteins are then expressed in neurons, and neuronal activity can be controlled with flashes of light. Optogenetics presents an interesting future development for assessing musculoskeletal mechanoadaptive responses (see section 2.1 and 6.6). Using an implantable neuromuscular stimulator it is possible to vary the frequency and duration of stimulation which the motor nerve receives, it cannot yet achieve the same graded response that is possible with optogenetics (Llewellyn et al. 2010). As an emerging technique, optogenetics are not presently developed to the stage where they can provide a simple method for loading bone (see section 2.1). However, in the future optogentics could be used to apply subtle variations in muscular activity to experimental animals, and as discussed in section 6.6, this has important clinical implications. The ability to precisely control skeletal muscle holds promise for establishing the extent which muscular forces determine skeletal morphology. For example, do muscular loads have a more profound effect upon bone morphology than external mechanical loads, due to a modulating factor, linking the activity of these tissues? Alternatively, is the rapid growth documented here primarily a result of the mechanical forces which are acting upon the bone, and the nature of muscular forces, lower force, but high frequency, are more osteogenic than high loads applied infrequently? This could have very important implications upon current understanding of the process of skeletal mechanotransduction. Furthermore, a system which allows for finely-tuned controlled muscular contraction could provide massive therapeutic benefits (see section 6.8).

The major limitation of iodine-enhanced microCT has been highlighted in Chapter 3 of this thesis. The stain causes rapid and substantial shrinkage in isolated pieces of soft-tissue. This limits its use in terms of absolute quantitative data, but can still be used for relative values of tissues in situ. I_2KI is only one of a spectrum of different contrast agents which can be used for microCT (see Pauwels et al. 2013 for review). At present it is the only contrast agent which has been found to provide sufficient contrast in large specimens such as entire skulls, but a variation upon I_2KI dissolved in PBFS could present a better option in the future. Recently iodine vapour has been used to stain tissue blocks embedded in polymethylmethacrylate and unfixed insects, for back-scattered electron scanning electron microscopy and microCT respectively (Boyde et al. 2014). Using vaporous, as opposed to aqueous iodine was deemed to result in less tissue shrinkage, though this was not quantified, and embedded tissue blocks had already undergone at least 20% shrinkage due to the embedding. Furthermore, the use of this technique for staining larger specimens,

such as entire rat limbs, was not commented upon, but this presents an interesting development for contrast-enhanced imaging.

In this thesis finite element analysis was used as a method for establishing the three-dimensional distribution of stress and strain throughout the rat tibia-fibular complex in response to loading. Currently such computational simulations provide the most precise method to do this. However, as mentioned in section 2.3.2 it is possible to measure strain directly with the use of digital volume correlation (DVC). However the error associated with DVC strain estimation is limited to a precision of 394με (Dall'Ara et al. 2014). Therefore a large proportion of the strain distributions investigated by the varying models in Chapter 5 would have been lost. This technique measures skeletal displacement in response to a given force, and so could also be used to calculate the elastic modulus of bone, and so remove the need for analysis via nanoindentation. The resolution and signal-to-noise ratio currently available with microCT can be substantially improved in synchrotron radiation-microCT. Synchrotron light is an electromagnetic radiation. To achieve a synchrotron beam, electrons are accelerated into a booster ring to increase their acceleration up to near the speed of light and then are transferred into a storage ring. Whilst in the storage ring magnetic fields are applied to the electrons to alter their velocity vector, until they produce the velocity of synchrotron light (Olubamiji et al. 2014). By using a synchrotron source for imaging it is possible to achieve resolutions of 0.55μm (Yue et al. 2010). At this resolution it is possible to see detail as fine as lacunae within bone. Therefore an imaging modality providing three-dimensional data at such a high resolution almost negates the need for histological sectioning. Currently the largest limiting factor for synchrotron imaging is that it is not widely accessible, and is very expensive. However, this was once the situation with microCT, and so it is plausible that one day synchrotron sources will replace microCT for imaging skeletal form in three-dimensions.

Whilst the methods used in this thesis addressed form and function, further information could be gained with the addition of positron emission tomography (PET). PET provides information upon the metabolic activity of tissues, via the uptake of radioactive isotopes by the tissues, whilst the resolution achieved clinically is of little use for small animal imaging, microPET can be used (Cherry et al. 1997). Whilst PET and microPET have been used extensively for the localisation of tumours, they can also provide information about bone turnover, and angiogenesis, for example in fracture healing (Hsu et al. 2007). Furthermore microPET data can be combined with microCT analysis, to provide clear localisation of metabolic activity to

skeletal regions (Silva et al. 2006). In light of the discussion in section 6.5.3, the metabolic activity within bone plays a vital role in the skeletal response elicited. The advantage to using an in vivo approach, such a microPET, is that serial imaging could provide information upon the time course of skeletal activity following initiation of loading.

The computational models presented in Chapter 5 test the biomechanical implications of different morphological and material differences. The ability to manipulate these parameters makes computational simulation a very powerful tool. Furthermore it brings ethical advantages by reducing the number of animals required for experiments. However, for a model to be meaningful it must be validated, ideally with experiments that closely match the simulation parameters, meaning simulations reduce, but do not remove the need for animal experimentation.

Finite element analysis provides a method for estimating the mechanical forces which are acting upon a structure. Simulations can also be extended to incorporate a bone response in accordance with the mechanical environment (Huiskes 2000; Tezuka et al. 2005). Whilst such models can provide interesting supportive evidence they have a major drawback, as they require the input data upon how the bone will respond. As discussed extensively throughout this thesis, the exact stimuli which bone responds to are unknown (see sections 1.3-1.6). A further complication is that models only simulate bone responses to mechanical forces, neglecting other influences such as the hormonal environment, or as discussed in section 6.3, the integration of musculoskeletal tissues. Therefore, until all the stimuli to which bone responds are established, a model will not be capable of completely replacing animal experimentation.

Therefore, whilst the methods used within this thesis present an exciting combination of methods currently available, they are likely to be replaced with future advancements, especially imaging. The techniques used here provided compelling evidence that the manner in which bone can respond to muscular loading can be substantial, rapid, and differs from the processes seen from loading with external loading devices.

6.5 Summary and future work

Musculoskeletal tissues are remarkably adaptable, a trait which has evolved, and resulted in a highly integrated system comprised of muscle, bone, tendon and cartilage. The evolution of a highly adaptive system has obvious advantages. A massive skeleton may decrease an animal's risk of trauma and disability through fracture, but limits the animals speed for catching prey or avoiding predators, and so it is clearly advantageous to be able to dynamically adjust the skeleton to more closely match the mechanical demands required of it. The ability of the musculoskeletal system for continual dynamic tuning to mechanical demands is clearly evidenced in Chapters 4 and 5 of this thesis. Chapters 4 and 5 present, for the first time, the profound effect of electrical muscular stimulation upon the form and function of the stimulated muscle, and the bone it loads. This is achieved with the use of a powerful combination of analytical techniques, including iodine-enhanced microCT. Despite the extensive shrinkage caused by this technique, documented in Chapter 3, substantial differences in muscular volume we detected between stimulated and control muscles.

The potent influence of muscular contraction in determining not only muscular but also skeletal form is not unexpected, as the tissues exist as a functional unit. Therefore pressures exist upon the system, not the individual parts. This can be demonstrated by the tight integration of muscular and skeletal form shown by the results presented in Chapter 4 and 5. The work imposed upon the musculoskeletal system here was highly repetitive, and provoked an endurance response in the stimulated muscle, which resulted in a smaller, slower muscle than in the contra-lateral control limb. The shift towards a muscle which produces less force in endurance training provides energy savings in two ways. Firstly it reduces the energy expenditure of the muscle in each contraction. Secondly a reduction in muscle force production reduces the strain stimulus within the adjacent bone, thus limiting the growth (and hence weight) of the bone which the muscle is moving. This idea is complementary to, but expands upon, the mechanostat hypothesis. The mechanostat hypothesis states that an increase in strain above habitual levels provokes bone growth, which subsequently reduces the strain, and stops bone activity. Conversely if bone strain drops below the normal range then bone resorption is activated, until bone strain is increased to habitual levels. This hypothesis neglects other tissues which are functionally linked with bone. For example, the results of Chapter 5 show that both the muscle adaptation and the bone adaptation documented in Chapter 4 contribute to a decrease in the strain

within the loaded bone. Furthermore the results of Chapter 5 challenge the mechanostat hypothesis, by suggesting that a small layer of lowly mineralised, newly deposited bone can act to exacerbate strain, not reduce it. This has interesting implications for understanding how bone responds to mechanical forces.

The way in which bone senses mechanical stimuli is not fully understood. Whilst osteocytes present the most likely mechanosensory cell, there are a number of examples which demonstrate that bone can undergo remodelling in their absence (Shahar and Dean 2013; Kwon et al. 2012). The putative mechanism for skeletal mechanosensation is that loading influences interstitial fluid flow within bone. As fluid flow reaches a threshold point osteocytes are stimulated to produce signalling molecules which coordinate the activity of osteoblasts and osteoclasts. It is often assumed that loading must reach a certain threshold of magnitude or rate to be osteogenic. The work here supports a growing body of evidence that small strains can be highly osteogenic if applied frequently (Judex and Rubin 2010). This implies that osteocytes, or any other sensory cell within bone is able to respond to all levels of loading, and does not require loads to exceed a threshold. Osteocytes respond to loading by releasing signalling molecules. Therefore a slow release of low levels of signalling molecules may accumulate, provoking a response similar to fewer larger loads. In this respect the model presented here represents an interesting method for investigating many of the questions which remain in musculoskeletal research. A key benefit being that it allows all components of the system to be tested at the same time, yet affords a greater degree of control than an exercise regime. This would be especially interesting model in which to test the adaptive potential of connective tissues and tendons, as their response to loading is a matter of conflicting opinion. However, the model itself throws up a large number of questions, especially with regard to the bone response. A great deal more could be established about the mechanisms behind the dramatic bone growth documented by analysing the bone at various time points throughout the stimulation period.

In summary the work of this thesis demonstrates the potential benefits of electrical muscular stimulation for investigating musculoskeletal relationships. The results presented here show a profound interaction of musculoskeletal tissues, which work in synergy to achieve maximal strength for minimal energy expenditure.

Bibliography

Adriaens, D., 2012. A qualitative comparison of 3D visualization in Xenopus laevis using a traditional method and a non-destructive method. Koninklijke belgische vereniging voor dierkunde koninklijk belgisch instituut voor natuurwetenschappen, 142(2), pp.101–113.

Agnew, W. McCreery, D., Yuen, T., Bullara, L., 1989. Histologic and physiologic evaluation of electrically stimulated peripheral nerve: Considerations for the selection of parameters. Annals of Biomedical Engineering, 17(1), pp.39–60.

Aguirre, J. Buttery, L., O'Shaughnessy, M., Afzal, F., Fernandez de Marticorena, I., Hukkanen, M., Huang, P., MacIntyre, I., Polak, J., 2001. Endothelial nitric oxide synthase gene-deficient mice demonstrate marked retardation in postnatal bone formation, reduced bone volume, and defects in osteoblast maturation and activity. The American journal of pathology, 158(1), pp.247–57.

Aguirre, J., Plotkin, L., Stewart, S., Weinstein, R., Parfitt, A., Manolagas, S., Bellido, T., 2006. Osteocyte apoptosis is induced by weightlessness in mice and precedes osteoclast recruitment and bone loss. Journal of bone and mineral research : the official journal of the American Society for Bone and Mineral Research, 21(4), pp.605–615.

Akhtar R, Daymond MR, Almer JD, Mummery PM. 2008. Load transfer in bovine plexiform bone determined by synchrotron x-ray diffraction. Journal of Materials Research 23:543-550.

Akhtar, R., Daymond, M., Almer, J., Mummery, P., 2008. Elastic strains in antler trabecular bone determined by synchrotron X-ray diffraction. Acta biomaterialia, 4(6), pp.1677–87.

Akhter MP, Cullen DM, Pedersen EA, Kimmel DB, Recker RR. 1998. Bone Response to In Vivo Mechanical Loading in Two Breeds of Mice. Calcified tissue international 63:442-449.

Akhter, M.P., Raab, D. M., Turner, C. H., Kimmel, D. B., Recker, R. R., 1992. Characterization of in vivo strain in the rat tibia during external application of a four-point bending load. Journal of Biomechanics, 25(10), pp.1241–1246.

Albright, J.A. and Skinner, H.C.W., 1987. Bone: structural organization and remodelling dynamics. The scientific basis of orthopaedics, 2, pp.161–198.

Alexander, R., 2003. Principles of animal locomotion, Princeton:Princton University Press.

Alexander, R. M., and Vernon, A. 1975. The dimensions of knee and ankle muscles and the forces they exert. Journal of Human Movement Studies, 1(1), 115–123.

Amin Yavari, S., van der Stok, J., Weinans, H., Zadpoor, A., 2013. Full-field strain measurement and fracture analysis of rat femora in compression test. Journal of Biomechanics, 46(7), pp.1282–1292.

Ammann, P., Badoud, I., Barraud, S., Dayer, R., Rizzoli, R., 2007. Strontium ranelate treatment improves trabecular and cortical intrinsic bone tissue quality, a determinant of bone strength. Journal of bone and mineral research : the official journal of the American Society for Bone and Mineral Research, 22(9), pp.1419–25.

Andersen, P. and Henriksson, J., 1977. Capillary supply of the quadriceps femoris muscle of man: adaptive response to exercise. The Journal of physiology, 270(3), pp.677–690. Available at: http://jp.physoc.org/content/270/3/677.abstract.

Aoyagi, H., Iwasaki, S. and Nakamura, K., 2013. Three-dimensional observation of mouse tongue muscles using micro-computed tomography. Odontology, pp.1–8. Available at: http://dx.doi.org/10.1007/s10266-013-0131-4.

Arampatzis, A., Peper, A., Bierbaum, S., Albracht, K., 2010. Plasticity of human Achilles tendon mechanical and morphological properties in response to cyclic strain. Journal of biomechanics, 43(16), pp.3073–9.

Arborgh, B., Bell, P., Brunk, U., Collins, V., 1976. The osmotic effect of glutaraldehyde during fixation. A transmission electron microscopy, scanning electron microscopy and cytochemical study. Journal of Ultrastructure Research, 56(3), pp.339–350.

Armour, K.E., Armour, K. J., Gallagher, M. E., Gödecke, A., Helfrich, M. H., Reid, D. M., Ralston, S. H., 2001. Defective bone formation and anabolic response to exogenous estrogen in mice with targeted disruption of endothelial nitric oxide synthase. Endocrinology, 142(2), pp.760–766.

Armstrong, R.B. and Phelps, R.O., 1984. Muscle fiber type composition of the rat hindlimb. American Journal of Anatomy, 171(3), pp.259–272. Available at: http://dx.doi.org/10.1002/aja.1001710303.

Ashman, R.B., Cowin, S.C., Van Buskirk, W.C., Rice, J.C., 1984. A continuous wave technique for the measurement of the elastic properties of cortical bone. Journal of Biomechanics, 17(5), pp.349–361.

Ashman, R.B., and Rho, J., 1988. Elastic modulus of trabecular bone material. Journal of Biomechanics, 21(3), pp.177–181.

Aslanidi, O., Nikolaidou, T., Zhao, J., Smaill, B., Gilbert, S., Jarvis, J., Stephenson, R., Hancox, J., Boyett, M., Zhang, H., 2012. Application of Micro-Computed Tomography with Iodine Staining to Cardiac Imaging, Segmentation and Computational Model Development. Medical Imaging, IEEE Transactions on, PP(99), p.1.

Athanasiou, K.A., Rosenwasser, M., Buckwalter, J., Malinin, T., Mow, V., 1991. Interspecies comparisons of in situ intrinsic mechanical properties of distal femoral cartilage. Journal of Orthopaedic Research, 9(3), pp.330–340.

Babault, N., Cometti, G., Bernardin, M., Pousson, M., Chatard, J., 2007. Effects of electromyostimulation training on muscle strength and power of elite rugby players. The Journal of Strength and Conditioning Research, 21(2), pp.431–437.

Bacallao, R., Sohrab, S. and Phillips, C., 2006. Guiding principles of specimen preservation for confocal fluorescence microscopy. Handbook of biological confocal microscopy, pp.368–380.

Bach-Gansmo, F., Irvine, S., Brüel, A., Thomsen, J., Birkedal, H., 2013. Calcified cartilage islands in rat cortical bone. Calcified tissue international, 92(4), pp.330–8.

Badea, C. T., Drangova, M., Holdsworth, D. W., & Johnson, G. A. 2008. In vivo small-animal imaging using micro-CT and digital subtraction angiography.Physics in medicine and biology, 53(19), R319.

Balon, T.W. and Nadler, J.L., 1997. Evidence that nitric oxide increases glucose transport in skeletal muscle. Journal of applied physiology (Bethesda, Md. : 1985), 82(1), pp.359–363.

Baverstock, H., Jeffery, N.S. and Cobb, S.N., 2013. The morphology of the mouse masticatory musculature. Journal of Anatomy, 223(1), pp.46–60. Available at: http://dx.doi.org/10.1111/joa.12059.

Bakker, A.D. and Klein-Nulend, J., 2010. Mechanisms of osteocyte mechanotransduction. Clinical Reviews in Bone and Mineral Metabolism, 8(4), pp.163–169.

Baldwin, K.M. and Haddad, F., 2001. Plasticity in skeletal, cardiac, and smooth muscle. Invited review: effects of different activity and inactivity paradigms on myosin heavy chain gene expression in striated muscle. J Appl Physiol, 90(1), pp.346–357.

Barak, M.M., Lieberman, D.E. and Hublin, J.-J., 2011. A Wolff in sheep's clothing: Trabecular bone adaptation in response to changes in joint loading orientation. Bone, 49(6), pp.1141–1151.

Barnett, C.H., 1954. The structure and functions of fibrocartilages within vertebrate joints. Journal of Anatomy, 88(Pt 3), p.363.

Bar-Shavit, Z., 2007. The osteoclast: A multinucleated, hematopoietic-origin, bone-resorbing osteoimmune cell. Journal of cellular biochemistry, 102(5), pp.1130–1139. Available at: http://dx.doi.org/10.1002/jcb.21553.

Bentolila, V., Boyce, T., Fyhrie, D., Drumb, R., Skerry, T., Schaffler, M., 1998. Intracortical remodelling in adult rat long bones after fatigue loading. Bone, 23(3), pp.275–281.

Bergquist, A.J., Clair, J.M. and Collins, D.F., 2011. Motor unit recruitment when neuromuscular electrical stimulation is applied over a nerve trunk compared with a muscle belly: triceps surae. Journal of applied physiology (Bethesda, Md. : 1985), 110(3), pp.627–637.

Berquist, T.H., 2012. MRI of the Musculoskeletal System, Lippincott Williams and Wilkins.

Bertram, J.E.A. and Biewener, A.A., 1988. Bone curvature: Sacrificing strength for load predictability? Journal of Theoretical Biology, 131(1), pp.75–92. Available at: http://www.sciencedirect.com/science/article/pii/S002251938880122X.

Bertram, J.E.A. and Swartz, S.M., 1991. The “Law of bone transformation”: A case of crying Wolff? Biological Reviews, 66(3), pp.245–273. Available at: http://dx.doi.org/10.1111/j.1469-185X.1991.tb01142.x.

Bewick, G. and Banks, R., 2014. Mechanotransduction in the muscle spindle. Pflügers Archiv - European Journal of Physiology, pp.1–16. Available at: http://dx.doi.org/10.1007/s00424-014-1536-9.

Biewener, A.A. and Roberts, T.J., 2000. Muscle and tendon contributions to force, work, and elastic energy savings: a comparative perspective. Exercise and sport sciences reviews, 28(3), pp.99–107.

Blemker, S.S., Pinsky, P.M. and Delp, S.L., 2005. A 3D model of muscle reveals the causes of nonuniform strains in the biceps brachii. Journal of Biomechanics, 38(4), pp.657–665.

Blitz, E., Viukov, S., Sharir, A., Shwartz, Y., Galloway, J., Pryce, B., Johnson, R., Tabin, C., Schweitzer, R., Zelzer, E., 2009. Bone Ridge Patterning during Musculoskeletal Assembly Is Mediated through SCX Regulation of Bmp4 at the Tendon-Skeleton Junction. Developmental Cell, 17(6), pp.861–873.

Bodine, S.C. Roy, R. Meadows, D., Zernicke, R., Sacks, R., Fournier, M., Edgerton, V., 1982. Architectural, histochemical, and contractile characteristics of a unique biarticular muscle: the cat semitendinosus. Journal of neurophysiology, 48(1), pp.192–201.

De Boer, J., Wang, H.J. and Van Blitterswijk, C., 2004. Effects of Wnt signaling on proliferation and differentiation of human mesenchymal stem cells. Tissue engineering, 10(3-4), pp.393–401.

Bonewald, L.F. and Johnson, M.L., 2008. Osteocytes, mechanosensing and Wnt signaling. Bone, 42(4), pp.606–615.

Bolshakov, A., Oliver, W. C., & Pharr, G. M. 1996. Influences of stress on the measurement of mechanical properties using nanoindentation: Part II. Finite element simulations. Journal of Materials Research, 11(03), 760-768.

Booth, F.W. and Kelso, J.R., 1973. Cytochrome oxidase of skeletal muscle: adaptive response to chronic disuse. Canadian journal of physiology and pharmacology, 51(9), pp.679–681.

Bottinelli, R., Canepari, M., Reggiani, C., Stienen, G., 1994. Myofibrillar ATPase activity during isometric contraction and isomyosin composition in rat single skinned muscle fibres. The Journal of physiology, 481(Pt 3), pp.663–675.

Bouxsein, M.L., Boyd, S., Christiansen, B., Guldberg, R., Jepsen, K., Müller, R., 2010. Guidelines for assessment of bone microstructure in rodents using micro–computed tomography. Journal of Bone and Mineral Research, 25(7), pp.1468–1486.

Bowler, W.B., Tattersall, J.A., Hussein, R., Dixon, C., Cobbold, P., Gallagher, J.A., 1998. Release of ATP by osteoblasts: modulation by fluid shear forces. Bone, 22(3).

Bowler, W. Buckley, K.A., Gartland, A., Hipskind, R.A., Bilbe, G., Gallagher, J.A., 2001. Extracellular nucleotide signaling: a mechanism for integrating local and systemic responses in the activation of bone remodelling. Bone, 28(5), pp.507–512.

Boyde, A., 2003. The real response of bone to exercise. Journal of Anatomy, 203(2), pp.173–189.

Boyde, A., 2012. Staining plastic blocks with triiodide to image cells and soft tissues in backscattered electron SEM of skeletal and dental tissues. European Cells and Materials, 24.

Boyde, A., McCorkell, F.A., Taylor, G.K., Bomphrey, R.J., Doube, M., 2014. Iodine vapor staining for atomic number contrast in backscattered electron and X-ray imaging. Microscopy Research and Technique.

Boyde, A. and Franc, F., 1981. Freeze-drying shrinkage of glutaraldehyde fixed liver. Journal of Microscopy, 122(1), pp.75–86.

Boyde, A. and Maconnachie, E., 1981. Morphological correlations with dimensional change during SEM specimen preparation. Scanning electron microscopy, 4, p.27.

Boyde, A. and Maconnachie, E., 1983. Not quite critical point drying. The Science of Biological Specimen Preparation for Microscopy and Microanalysis. Scanning Electron Microscopy Inc., Chicago, pp.71–75.

Boyde, A. and Maconnachie, E., 1980. Treatment with lithium salts reduces ethanol dehydration shrinkage of glutaraldehyde fixed tissue. Histochemistry, 66(2), pp.181–187. Available at: http://dx.doi.org/10.1007/BF00494644.

Brack, A.S. Conboy, M., Roy, S., Lee, M., Kuo, C., Keller, C., Rando, T., 2007. Increased Wnt signaling during aging alters muscle stem cell fate and increases fibrosis. Science (New York, N.Y.), 317(5839), pp.807–810.

Brandan, E., & Inestrosa, N. C., 1987. Isolation of the heparan sulfate proteoglycans from the extracellular matrix of rat skeletal muscle. Journal of neurobiology, 18(3), 271-282.

Braun, T. and Gautel, M., 2011. Transcriptional mechanisms regulating skeletal muscle differentiation, growth and homeostasis. Nat Rev Mol Cell Biol, 12(6), pp.349–361. Available at: http://dx.doi.org/10.1038/nrm3118.

Brooke, M.H. and Kaiser, K.K., 1970. Muscle fiber types: How many and what kind? Archives of neurology, 23(4), pp.369–379.

Brown, J.M., Henriksson, J. and Salmons, S., 1989. Restoration of fast muscle characteristics following cessation of chronic stimulation: physiological, histochemical and metabolic changes during slow-to-fast transformation. Proceedings of the Royal Society of London. Series B, Containing papers of a Biological character. Royal Society (Great Britain), 235(1281), pp.321–346.

Brüel, A., Olsen, J., Birkedal, H.,Risager, M., Andreassen, T., Raffalt, A., Andersen, J., Thomsen, J., 2011. Strontium Is Incorporated into the Fracture Callus but Does Not Influence the Mechanical Strength of Healing Rat Fractures. Calcified tissue international. 88(2), pp. 142-152.

Buie, H.R. and Boyd, S.K., 2010. Reduced bone mass accrual in swim-trained prepubertal mice. Med Sci Sports Exerc, 42(10), pp.1834–1842.

Buller, A.J., Eccles, J.C. and Eccles, R.M., 1960. Interactions between motoneurones and muscles in respect of the characteristic speeds of their responses. The Journal of physiology, 150(2), p.417.

Burkhart, T.A., Andrews, D.M. and Dunning, C.E., 2013. Finite element modeling mesh quality, energy balance and validation methods: A review with recommendations associated with the modeling of bone tissue. Journal of Biomechanics, 46(9), pp.1477–1488.

Burr, D.B., Milgrom, C., Fyhrie, D., Forwood, M., Nyska, M., Finestone, A., Hoshaw, S., Saiag, E., Simkin, A., 1996. In vivo measurement of human tibial strains during vigorous activity. Bone, 18(5), pp.405–410.

Burr, D.B., Turner, C., Naick, P., Forwood, M., Ambrosius, W., Sayeed H., Pidaparti, R., 1998. Does microdamage accumulation affect the mechanical properties of bone? Journal of Biomechanics, 31(4), pp.337–345.

Busa, B., Miller, L., Rubin, C., Qin, Y., Judex, S., 2005. Rapid Establishment of Chemical and Mechanical Properties during Lamellar Bone Formation. Calcified tissue international, 77(6), pp.386–394.

Bushby, A.J., Ferguson, V.L. and Boyde, A., 2004. Nanoindentation of bone: Comparison of specimens tested in liquid and embedded in polymethylmethacrylate. Journal of Materials Research, 19(01), pp.249–259.

Cancel, M., Grimard, G., Thuillard-Crisinel, D., Moldovan, F., & Villemure, I. 2009. Effects of in vivo static compressive loading on aggrecan and type II and X collagens in the rat growth plate extracellular matrix. Bone, 44(2), 306-315.

Carroll, C.C., Whitt, J. A., Peterson, A., Gump, B. S., Tedeschi, J., Broderick, T. L., 2012. Influence of acetaminophen consumption and exercise on Achilles tendon structural properties in male Wistar rats. AJP: Regulatory, Integrative and Comparative Physiology, 302(8), pp.R990–R995.

Changoor, A., Nelea, M., Méthot, S., Tran-Khanh, N., Chevrier, A., Restrepo, A., ... & Buschmann, M. D. (2011). Structural characteristics of the collagen network in human normal, degraded and repair articular cartilages observed in polarized light and scanning electron microscopies. Osteoarthritis and Cartilage, 19(12), 1458-1468.

Chen, J.-H., Liu, C., You, L., and Simmons, C. A., 2010. Boning up on Wolff's Law: mechanical regulation of the cells that make and maintain bone. Journal of Biomechanics, 43(1), 108–18. doi:10.1016/j.jbiomech.2009.09.016

Cherry, S.R., Shao, Y., Silverman, R.W., Meadors, K., Siegel, S., Chatziioannou, A., Young, J.W., Jones, W. F., Moyers, J.C., Newport, D., Boutefnouchet, A., Farquhar, T.H., Andreaco, M., Paulus, M.J., Binkley, D.M., Nutt, R., Phelps, M.E., Meadorsl, K., Siegell, S., Chatziioannoul, A., Boutefnouchetl, A., Farquharl, T.H., Phelpsl, M., 1997. MicroPET: a high resolution PET scanner for imaging small animals. IEEE Transactions on Nuclear Science, 44(3), pp.1161–1166.

Churches, A.E., Howlett, C.R. and Ward, G.W., 1980. Bone reaction to surgical drilling and pinning. Journal of Biomechanics, 13(3), pp.203–209.

Ciciarello, M., Zini, R., Rossi, L., Salvestrini, V., Ferrari, D., Manfredini, R., Lemoli, R., 2013. Extracellular purines promote the differentiation of human bone marrow-derived mesenchymal stem cells to the osteogenic and adipogenic lineages. Stem cells and development, 22(7), pp.1097–111.

Clifton, K.B., Yan, J., Mecholsky, J., Reep, R., 2008. Material properties of manatee rib bone. Journal of Zoology, 274(2), pp.150–159.

Cooke, R., 1997. Actomyosin interaction in striated muscle. Physiological Reviews, 77(3), pp.671–697.

Courant, R., 1943. Variational methods for the solution of problems of equilibrium and vibrations. Bull. Amer. Math. Soc, 49(1), pp.1–23.

Cox, P.G., Fagan, M., Rayfield, E., Jeffery, N., 2011. Finite element modelling of squirrel, guinea pig and rat skulls: using geometric morphometrics to assess sensitivity. Journal of Anatomy, 219(6), pp.696–709.

Cox, P.G., Rayfield, E., Fagan, M., Herrel, A., Pataky, T., Jeffery, N., 2012. Functional Evolution of the Feeding System in Rodents. PLoS ONE, 7(4), p.e36299. Available at: http://dx.doi.org/10.1371/journal.pone.0036299.

Cox, P.G. and Faulkes, C.G., 2014. Digital dissection of the masticatory muscles of the naked mole-rat, Heterocephalus glaber (Mammalia, Rodentia). PeerJ, PubMed 250.

Cox, P.G. and Jeffery, N., 2011. Reviewing the Morphology of the Jaw-Closing Musculature in Squirrels, Rats, and Guinea Pigs with Contrast-Enhanced MicroCt. The Anatomical Record: Advances in Integrative Anatomy and Evolutionary Biology, 294(6), pp.915–928. Available at: http://dx.doi.org/10.1002/ar.21381.

Csapo, R., Maganaris, C., Seynnes, O., Narici, M., 2010. On muscle, tendon and high heels. The Journal of Experimental Biology, 213(15), pp.2582–2588.

Currey, J.D., 1979. Mechanical properties of bone tissues with greatly differing functions. Journal of Biomechanics, 12(4), pp.313–319

Currey, J.D., 1988. The effect of porosity and mineral content on the Young's modulus of elasticity of compact bone. Journal of Biomechanics, 21(2), pp.131–139. Available at: http://www.sciencedirect.com/science/article/pii/0021929088900061.

Currey, J.D., 2003. The many adaptations of bone. Journal of Biomechanics, 36(10), pp.1487–1495. Available at: http://www.sciencedirect.com/science/article/pii/S0021929003001246.

Curtis, N., Jones, M. E., Evans, S. E., Shi, J., O'Higgins, P., & Fagan, M. J. (2010). Predicting muscle activation patterns from motion and anatomy: modelling the skull of Sphenodon (Diapsida: Rhynchocephalia). Journal of the Royal Society Interface, 7(42), 153-160.

Dall'Ara, E., Barber, D. and Viceconti, M., 2014. About the inevitable compromise between spatial resolution and accuracy of strain measurement for bone tissue: A 3D zero-strain study. Journal of Biomechanics. Available at: http://www.sciencedirect.com/science/article/pii/.

Dalle Carbonare, L., Valenti, M., Bertoldo, F., Zanatta, M., Zenari, S., Realdi, G., Lo Cascio, V., Giannini, S., 2005. Bone microarchitecture evaluated by histomorphometry. Micron (Oxford, England : 1993), 36(7-8), pp.609–16.

Dechow, P.C. and Hylander, W.L., 2000. Elastic properties and masticatory bone stress in the macaque mandible. American journal of physical anthropology, 112(4), pp.553–74.

Degenhardt, K., Wright, A., Horng, D., Padmanabhan, A., Epstein, J., 2010. Rapid 3D Phenotyping of Cardiovascular Development in Mouse Embryos by Micro-CT

With Iodine Staining / CLINICAL PERSPECTIVE. Circulation: Cardiovascular Imaging, 3(3), pp.314–322. Available at: http://circimaging.ahajournals.org/content/3/3/314.abstract.

Dempster, D.W., Compston, J., Drezner, M., Glorieux, F., Kanis, J., Malluche, H., Meunier, P., Ott, S., Recker, R., Parfitt, A., 2013. Standardized nomenclature, symbols, and units for bone histomorphometry: A 2012 update of the report of the ASBMR Histomorphometry Nomenclature Committee. Journal of Bone and Mineral Research, 28(1), pp.2–17.

Descamps, E., Sochacka, A., De Kegel, B., Van Loo, D., Van Hoorebeke, L., Adriaens, D., 2014. Soft tissue discrimination with contrast agents using micro-CT scanning. Belgian journal of zoology, 144(1), pp.20–40.

Dillon, J.P., Waring-Green, V., Taylor, A., Wilson, P., Birch, M., Gartland, A., Gallagher, J., 2012. Primary human osteoblast cultures. In Bone Research Protocols. Springer, pp. 3–18.

Donnelly, E., 2011. Methods for assessing bone quality: A review. In Clinical Orthopaedics and Related Research. pp. 2128–2138.

Donnelly E, Boskey AL, Baker SP, van der Meulen MCH. 2010. Effects of tissue age on bone tissue material composition and nanomechanical properties in the rat cortex. Journal of Biomedical Materials Research Part A 92A:1048-1056.

Doube M, Kłosowski MM, Arganda-Carreras I, Cordelières FP, Dougherty RP, Jackson JS, Schmid B, Hutchinson JR, Shefelbine SJ. 2010. BoneJ: Free and extensible bone image analysis in ImageJ. Bone 47:1076-1079.

Douglass, J.K. and Wcislo, W.T., 2010. An inexpensive and portable microvolumeter for rapid evaluation of biological samples. BioTechniques, 49(2), p.566.

Doweidar, M.H., Calvo, B., Alfaro, I., Groenenboom, P., Doblaré, M., 2010. A comparison of implicit and explicit natural element methods in large strains problems: Application to soft biological tissues modeling. Computer Methods in Applied Mechanics and Engineering, 199(25-28), pp.1691–1700.

Drachman, D.B. and Sokoloff, L., 1966. The role of movement in embryonic joint development. Developmental Biology, 14(3), pp.401–420.

Dudley, G.A., Castro, M. J., Rogers, S., Apple, D. F., 1999. A simple means of increasing muscle size after spinal cord injury: A pilot study. European Journal of Applied Physiology and Occupational Physiology, 80(4), pp.394–396.

Duncan, C.P. and Shim, S.S., 1977. J. Edouard Samson Address: the autonomic nerve supply of bone. An experimental study of the intraosseous adrenergic nervi vasorum in the rabbit. The Journal of bone and joint surgery. British volume, 59(3), pp.323–330.

During, D., Ziegler, A., Thompson, C., Ziegler, A., Faber, C., Muller, J., Scharff, C., Elemans, C., 2013. The songbird syrinx morphome: a three-dimensional, high-resolution, interactive morphological map of the zebra finch vocal organ. BMC Biology, 11(1), p.1. Available at: http://www.biomedcentral.com/1741-7007/11/1.

Ebenstein, D.M. and Pruitt, L.A., 2006. Nanoindentation of biological materials. Nano Today, 1(3), pp.26–33.

Eckstein, F., Faber, S., Mühlbauer, R., Hohe, J., Englmeier, K-H., Reiser, M., Putz, R., 2002. Functional adaptation of human joints to mechanical stimuli. Osteoarthritis and cartilage / OARS, Osteoarthritis Research Society, 10(1), pp.44–50.

Einhorn, T., 1992. Bone strength: The bottom line. Calcified tissue international, 51(5), pp.333–339. Available at: http://dx.doi.org/10.1007/BF00316875.

Eisenberg, B.R., Brown, J.M.C. and Salmons, S., 1984. Restoration of fast muscle characteristics following cessation of chronic stimulation - The ultrastructure of slow-to-fast transformation. Cell and Tissue Research, 238(2), pp.221–230.

Elefteriou, F., Ahn, J., Takeda, S., Starbuck, M., Yang, X., Liu, X., Kondo, H., Richards, W., Bannon, T., Noda, M., Clement, K., Vaisse, C., Karsenty, G., 2005. Leptin regulation of bone resorption by the sympathetic nervous system and CART. Nature, 434(7032), pp.514–520.

Elefteriou, F., Campbell, P. and Ma, Y., 2014. Control of bone remodeling by the peripheral sympathetic nervous system. Calcified Tissue International, 94(1), pp.140–151.

Elkasrawy, M.N. and Hamrick, M.W., 2010. Myostatin (GDF-8) as a key factor linking muscle mass and bone structure. J Musculoskelet Neuronal Interact, 10(1), pp.56–63.

Elliott, J.C. and Dover, S.D., 1982. X-ray microtomography. Journal of Microscopy, 126(2), pp.211–213. Available at: http://dx.doi.org/10.1111/j.1365-2818.1982.tb00376.x.

Ellman, R., Grasso, D., Vliet, M., Brooks, D., Spatz, J., Conlon, C., Bouxsein, M., 2014. Combined Effects of Botulinum Toxin Injection and Hind Limb Unloading on Bone and Muscle. Calcified tissue international, 94(3), pp.327–337.

Ellman, R., Spatz, J., Cloutier, A., Palme, R., Christiansen, B., Bouxsein, M., 2013. Partial reductions in mechanical loading yield proportional changes in bone density, bone architecture, and muscle mass. Journal of Bone and Mineral Research, 28(4), pp.875–885.

Erdemir A SS. 2010. Open Knee: A Three-Dimensional Finite Element Representation of the Knee Joint, . User's Guide Version 1.0.0.

Erdemir, A., Guess, T. M., Halloran, J., Tadepalli, S. C., & Morrison, T. M. (2012). Considerations for reporting finite element analysis studies in biomechanics. Journal of biomechanics, 45(4), 625-633.

Evans, J.H. and Barbenel, J.C., 1975. Structural and Mechanical Properties of Tendon related to Function. Equine Veterinary Journal, 7(1), pp.1–8. Available at: http://dx.doi.org/10.1111/j.2042-3306.1975.tb03221.x

Fang, T.-H., Weng, C.-I. and Chang, J.-G., 2003. Molecular dynamics analysis of temperature effects on nanoindentation measurement. Materials Science and Engineering: A, 357(1-2), pp.7–12.

Ferguson, A.S., Stone, H., Roessmann, U., Burke, M., Tisdale, E., Mortimer, J., 1989. Muscle plasticity: comparison of a 30, Hz burst with IO-Hz continuous stimulation.

Ferguson, C., Eytan A., Theodore M., and Helms J., 1999 "Does adult fracture repair recapitulate embryonic skeletal formation?." Mechanisms of development 87, no. 1: 57-66.

Fitzpatrick, F.A., Aguirre, R., Pike, J., Lincoln, F., 1980. The stability of 13,14-dihydro-15 keto-PGE2. Prostaglandins, 19(6), pp.917–931.

Fajardo, R. J., Cory, E., Patel, N. D., Nazarian, A., Laib, A., Manoharan, R. K., & Bouxsein, M. L. 2009. Specimen size and porosity can introduce error into μCT-based tissue mineral density measurements. Bone, 44(1), 176-184.

Forwood, M.R. and Turner, C.H., 1995. Skeletal adaptations to mechanical usage: results from tibial loading studies in rats. Bone, 17(4 Suppl), p.197S–205S.

Forwood, M.R., Owan, I., Takano, Y., Turner, C. H., 1996. Increased bone formation in rat tibiae after a single short period of dynamic loading in vivo. American Journal of Physiology - Endocrinology and Metabolism, 270(3), pp.E419–E423.

Frankel, V.H. and Nordin, M., 2001. Biomechanics of bone. Basic biomechanics of the musculoskeletal system, 3, pp.26–59.

Frost, H.M., 1960. Presence of microscopic cracks in vivo in bone. Henry Ford Hosp Med Bull, 8(2), p.35.

Frost, H.M., 1987. Bone “mass” and the “mechanostat”: A proposal. The Anatomical Record, 219(1), pp.1–9. Available at: http://dx.doi.org/10.1002/ar.1092190104.

Frost, H.M., 2003. Bone’s mechanostat: A 2003 update. The Anatomical Record Part A: Discoveries in Molecular, Cellular, and Evolutionary Biology, 275A(2), pp.1081–1101. Available at: http://dx.doi.org/10.1002/ar.a.10119.

Frost, H.M., 1997. On our age-related bone loss: insights from a new paradigm. Journal of Bone and Mineral Research, 12(10), pp.1539–1546.

Garner, S.C. and Anderson, J.J.B., 2011. 4 Skeletal Tissues and Mineralization. Diet, Nutrients, and Bone Health, p.33.

Gefen A, Dilmoney B. 2007. Mechanics of the normal woman's breast. Technology and Health Care 15:259-271.

Genetos, D.C., Geist, D., Liu, D., Donahue, H., Duncan, R., 2005. Fluid shear-induced ATP secretion mediates prostaglandin release in MC3T3-E1 osteoblasts. Journal of bone and mineral research : the official journal of the American Society for Bone and Mineral Research, 20(1), pp.41–49.

Genetos, D.C., Kephart, C., Zhang, Y., Yellowley, C., Donahue, H., 2007. Oscillating fluid flow activation of gap junction hemichannels induces ATP release from MLO-Y4 osteocytes. Journal of Cellular Physiology, 212(1), pp.207–214.

Gerhard, F.A., Webster, D., van Lenthe, G. H., Müller, R., 2009. In silico biology of bone modelling and remodelling: adaptation. Philosophical Transactions of the Royal Society A: Mathematical, Physical and Engineering Sciences, 367(1895), pp.2011–2030. Available at: http://rsta.royalsocietypublishing.org/content/367/1895/2011.abstract.

Gerrits, H.L., Hopman, M., Sargeant, A., Jones, D., De Haan, A., 2002. Effects of training on contractile properties of paralyzed quadriceps muscle. Muscle and Nerve, 25(4), pp.559–567.

Gignac, P.M. and Kley, N.J., 2014. Iodine-enhanced micro-CT imaging: Methodological refinements for the study of the soft-tissue anatomy of post-embryonic vertebrates. Journal of Experimental Zoology Part B: Molecular and Developmental Evolution, p.n/a–n/a. Available at: http://dx.doi.org/10.1002/jez.b.22561.

Gillard, F., Boardman, R., Mavrogordato, M., Hollis, D., Sinclair, I., Pierron, F., Browne, M., 2014. The application of digital volume correlation (DVC) to study the microstructural behaviour of trabecular bone during compression. Journal of the mechanical behavior of biomedical materials, 29, pp.480–99.

Goldspink, D.F., Cox, V., Smith, S., Eaves, L., Osbaldeston, N., Lee, D., Mantle, D., 1995. Muscle growth in response to mechanical stimuli. American Journal of Physiology-Endocrinology And Metabolism, 31(2), p.E288.

Gollnick PD, King DW. 1969. Effect of exercise and training on mitochondria of rat skeletal muscle. American Journal of Physiology--Legacy Content 216:1502-1509.

Gorgey, A.S. and Dudley, G.A., 2007. Skeletal muscle atrophy and increased intramuscular fat after incomplete spinal cord injury. Spinal Cord, 45(4), pp.304–309.

Gourion-Arsiquaud S, Burket JC, Havill LM, DiCarlo E, Doty SB, Mendelsohn R, van der Meulen MCH, Boskey AL. 2009. Spatial Variation in Osteonal Bone Properties

Relative to Tissue and Animal Age. Journal of Bone and Mineral Research 24:1271-1281.

Green, D.J., Richmond, B.G. and Miran, S.L., 2012. Mouse shoulder morphology responds to locomotor activity and the kinematic differences of climbing and running. Journal of Experimental Zoology Part B: Molecular and Developmental Evolution, 318(8), pp.621–638.

Greene, E.U., 1963. Anatomy of the Rat. , XXVII.

Green H.J., Klug G.A., Reichmann H., Seedorf U., Wiehrer W., Pette D. 1984. Exercise-induced fibre type transitions with regard to myosin, parvalbumin, and sarcoplasmic reticulum in muscles of the rat. Pflugers Arch 400:432-438.

Gröning, F., Fagan, M. and O'Higgins, P., 2012. Modeling the Human Mandible Under Masticatory Loads: Which Input Variables are Important? The Anatomical Record: Advances in Integrative Anatomy and Evolutionary Biology, 295(5), pp.853–863. Available at: http://dx.doi.org/10.1002/ar.22455.

Gros, M., 1846. La disposition des nerfs des os. Bull Soc Anat Paris, 21, pp.369–372.

Gross TS, Srinivasan S, Liu CC, Clemens TL, Bain SD. 2002. Noninvasive Loading of the Murine Tibia: An In Vivo Model for the Study of Mechanotransduction. Journal of Bone and Mineral Research 17:493-501.

Gruner, J.A., Altman, J. and Spivack, N., 1980. Effects of arrested cerebellar development on locomotion in the rat. Experimental Brain Research, 40(4), pp.361–373. Available at: http://dx.doi.org/10.1007/BF00236145.

Guidoni, G., Swain, M. and Jäger, I., 2010. Nanoindentation of wet and dry compact bone: Influence of environment and indenter tip geometry on the indentation modulus. Philosophical Magazine, 90(5), pp.553–565.

Guo, X.E. and Goldstein, S. a, 2000. Vertebral trabecular bone microscopic tissue elastic modulus and hardness do not change in ovariectomized rats. Journal of orthopaedic research : official publication of the Orthopaedic Research Society, 18(2), pp.333–6.

Gusnard, D. and Kirschner, R.H., 1977. Cell and organelle shrinkage during preparation for scanning electron microscopy: effects of fixation, dehydration and

critical point drying. Journal of Microscopy, 110(1), pp.51–57. Available at: http://dx.doi.org/10.1111/j.1365-2818.1977.tb00012.x.

Guth, L., & Samaha, F. J. 1970. Procedure for the histochemical demonstration of actomyosin ATPase. Experimental neurology, 28(2), 365-367.

Hadjidakis, D.J. and Androulakis, I.I., 2006. Bone Remodeling. Annals of the New York Academy of Sciences, 1092(1), pp.385–396. Available at: http://dx.doi.org/10.1196/annals.1365.035.

Haibo, N., Castro, S.J., Stephenson, R.S., Jarvis, J.C., Lowe, T., Hart, G., Boyett, M.R., Zhang, H., 2013. Extracting myofibre orientation from micro-CT images: An optimisation study. Computing in Cardiology Conference (CinC), p.823,826.

Haj, A.J., Minter, S., Rawlinson, S., Suswillo, R., Lanyon, L. E.,1990. Cellular responses to mechanical loading in vitro. Journal of Bone and Mineral Research, 5(9), pp.923–932.

Hall, B.K., 2005. Bones and cartilage: developmental and evolutionary skeletal biology, Academic Press.

Ham, A. W. 1974. Histology (7th edn).

Hamann N, Kohler T, Müller R, Brüggemann G-P, Niehoff A. 2012. The effect of level and downhill running on cortical and trabecular bone in growing rats. Calcified tissue international 90:429-437.

Hammer, O., Harper, D.A.T. and Ryan, P.D., 2001. PAST: Palaeontological Statistics software package for eduction and data analysis. Palaeontologica Electronica, 4(1), p.9.

Han, X., Lin G., Fuyou W., Qingsheng Z., and Liu Y., 2014 "Contribution of PTHrP to mechanical strain-induced fibrochondrogenic differentiation in entheses of Achilles tendon of miniature pigs." Journal of biomechanics 47, no. 10: 2406-2414.

Hansen, P., Aagaard, P., Kjaer, M., Larsson, B., Magnusson, S P., 2003. Effect of habitual running on human Achilles tendon load-deformation properties and cross-sectional area. Journal of applied Physiology, 95 (6), pp 2375-2380.

Hautier, L., Lebrun, R. and Cox, P.G., 2012. Patterns of covariation in the masticatory apparatus of hystricognathous rodents: Implications for evolution and diversification. Journal of Morphology. Available at: http://dx.doi.org/10.1002/jmor.20061.

Hay, G., Hughes, D., 1983. First-Year Physics for Radiographers third edit., Bailliere Tindall.

Hecht, E., Liedert, A., Ignatius, A., Mizaikoff, B., Kranz, C., 2013. Local detection of mechanically induced ATP release from bone cells with ATP microbiosensors. Biosensors and Bioelectronics, 44(1), pp.27–33.

Helfrich, M.H., Evans, D. E., Grabowski, P. S., Pollock, J., Ohshima, H., Ralston, S. H., 1997. Expression of nitric oxide synthase isoforms in bone and bone cell cultures. Journal of bone and mineral research : the official journal of the American Society for Bone and Mineral Research, 12(7), pp.1108–1115.

Hengsberger, S., Kulik, A. and Zysset, P., 2002. Nanoindentation discriminates the elastic properties of individual human bone lamellae under dry and physiological conditions. Bone, 30(1), pp.178–184.

Henneman, E., Somjen, G., and Carpenter, D. O. (1965). Functional significance of cell size in spinal motoneurons. Journal of neurophysiology, 28, 560–580.

Hennig, R. and Lomo, T., 1985. Firing patterns of motor units in normal rats. Nature, 314(6007), pp.164–166. Available at: http://dx.doi.org/10.1038/314164a0.

Herman, B.C., Cardoso, L., Majeska, R. J., Jepsen, K., Schaffler, M. B., 2010. Activation of bone remodeling after fatigue: differential response to linear microcracks and diffuse damage. Bone, 47(4), pp.766–772.

Hert, J., Sklenska, A. and Liskova, M., 1971. Effect of intermittent stress on the rabbit tibia after resection of the peripheral nerves. Folia morphologica, XIX, pp.378–387.

Himeno-Ando, A., Izumi, Y., Yamaguchi, A., Iimura, T., 2012. Structural differences in the osteocyte network between the calvaria and long bone revealed by three-dimensional fluorescence morphometry, possibly reflecting distinct mechano-adaptations and sensitivities. Biochemical and Biophysical Research Communications, 417(2), pp.765–770.

Hirose, S., Li, M., Kojima, T., de Freitas, P., Ubaidus, S., Oda, K., Saito, C., Amizuka, N., 2007. A histological assessment on the distribution of the osteocytic lacunar canalicular system using silver staining. Journal of Bone and Mineral Metabolism, 25(6), pp.374–382.

Hoebertz, A., Mahendran, S., Burnstock, G., Arnett, T., 2002. ATP and UTP at low concentrations strongly inhibit bone formation by osteoblasts: A novel role for the P2Y2 receptor in bone remodeling. Journal of Cellular Biochemistry, 86(3), pp.413–419.

Hohmann, E.L., Elde, R., Rysavy, J. A., Einzig, S., Gebhard, R. L., 1986. Innervation of periosteum and bone by sympathetic vasoactive intestinal peptide-containing nerve fibers. Science (New York, N.Y.), 232(4752), pp.868–871.

Holdsworth, D. W., & Thornton, M. M. (2002). Micro-CT in small animal and specimen imaging. Trends in Biotechnology, 20(8), S34-S39.

Holliday, C.M., Tsai, H. P., Skiljan, R. J., George, I. D., Pathan, S., 2013. A 3D Interactive Model and Atlas of the Jaw Musculature of Alligator mississippiensis. PLoS ONE, 8(6).

Hopwood, D., 1982. Fixation and fixatives. In A. Stevens and J. D. Bancroft, eds. Theory and Practice of Histological Techniques. New York: Churchill Livingstone, pp. 20–40.

Hosokawa, A., 1997. Ultrasonic wave propagation in bovine cancellous bone. The Journal of the Acoustical Society of America, 101(1), p.558.

Hsieh, J. 2009, November. Computed tomography: principles, design, artifacts, and recent advances. Bellingham, WA: SPIE.

Hsu, W.K., Feeley, B. T., Krenek, L., Stout, D. B., Chatziioannou, A. F., Lieberman, J. R. 2007. The use of 18F-fluoride and 18F-FDG PET scans to assess fracture healing in a rat femur model. European Journal of Nuclear Medicine and Molecular Imaging, 34(8), pp.1291–1301.

Huddleston, A.L., Rockwell, D., Kulund, D. N., Harrison, R., 1980. BOne mass in lifetime tennis athletes. JAMA, 244(10), pp.1107–1109. Available at: http://dx.doi.org/10.1001/jama.1980.03310100025022.

Hughes, J.M. and Petit, M.A., 2010. Biological underpinnings of Frost's mechanostat thresholds: the important role of osteocytes. J Musculoskelet Neuronal Interact, 10(2), pp.128–135.

Huiskes, R., 2000. If bone is the answer, then what is the question? Journal of Anatomy, 197(2), pp.145–156. Available at: http://dx.doi.org/10.1046/j.1469-7580.2000.19720145.x.

Hung, C.T., Allen, F. D., Pollack, S. R., Brighton, C. T., 1996. Intracellular Ca2+ stores and extracellular Ca2+ are required in the real-time Ca2+ response of bone cells experiencing fluid flow. Journal of Biomechanics, 29(11), pp.1411–1417.

Jämsä T, Rho J-Y, Fan Z, MacKay CA, Marks Jr SC, Tuukkanen J. 2002. Mechanical properties in long bones of rat osteopetrotic mutations. Journal of Biomechanics 35:161-165.

Jang, Y. C., and Van Remmen, H. 2011. Age-associated alterations of the neuromuscular junction. Experimental Gerontology, 46(2-3), 193–8. doi:10.1016/j.exger.2010.08.029

Jaramillo Isaza, S., Mazeran, P-E., El Kirat, K., Ho Ba Tho, M-C., 2014. Time-dependent mechanical properties of rat femoral cortical bone by nanoindentation: An age-related study. Journal of Materials Research, 29(10), pp.1135–1143.

Jaremko, J.L., Maciejewski, C. M., Cheng, R. W. T., Ronsky, J. L., Thompson, R. B., Lambert, R. G. W., Dhillon, S. S., 2007. Accuracy and reliability of MRI vs. laboratory measurements in an ex vivo porcine model of arthritic cartilage loss. Journal of magnetic resonance imaging : JMRI, 26(4), pp.992–1000.

Jarvis JC. 1993. Power production and working capacity of rabbit tibialis anterior muscles after chronic electrical stimulation at 10 Hz. The Journal of physiology 470:157-169.

Jarvis, J., C., Mokrusch, T., Kwende, M., Sutherland, H., Salmons, S., 1996, Fast-to-slow transformation in stimulated rat muscle. Muscle and Nerve, 19 (11). pp 1469-1475.

Jarvis, J.C. and Salmons, S., 2001. The application and technology of implantable neuromuscular stimulators: an introduction and overview. Medical Engineering and Physics, 23(1), pp.3–7. Available at: http://www.sciencedirect.com/science/article/pii/S1350453301000054.

Jarvis, J.C. and Stephenson, R., 2013. Studying the microanatomy of the heart in three dimensions: a practical update. Frontiers in pediatrics, 1(October), p.26. Available at: http://www.pubmedcentral.nih.gov/articlerender.fcgi?artid=3864221andtool=pmcentrezandrendertype=abstract.

Jeffery, N.S., Stephenson, R. S., Gallagher, J. A., Jarvis, J. C., Cox, P. G., 2011. Micro-computed tomography with iodine staining resolves the arrangement of muscle fibres. Journal of Biomechanics, 44(1), pp.189–192.

Jones, M.E.H., Werneburg, I., Curtis, N., Penrose, R., O'Higgins, P., Fagan, M. J., Evans, S. E., 2012. The Head and Neck Anatomy of Sea Turtles (Cryptodira: Chelonioidea) and Skull Shape in Testudines. PLoS ONE, 7(11).

Joseph, D., Gu, W. Y., Mao, X. G., Lai, W. M., & Mow, V. C. True density of normal and enzymatically treated bovine articular cartilage, Transact. Orthop. Res. Soc. 24 (1999) 642

Jowsey, J., 1966. Studies of Haversian systems in man and some animals. Journal of Anatomy, 100 (Pt 4), p.857.

Judex, S., Lei, X., Han, D., Rubin, C., 2007. Low-magnitude mechanical signals that stimulate bone formation in the ovariectomized rat are dependent on the applied frequency but not on the strain magnitude. Journal of Biomechanics, 40(6), pp.1333–1339

Judex, S. and Carlson, K.J., 2009. Is bone's response to mechanical signals dominated by gravitational loading. Med Sci Sports Exerc, 41(11), pp.2037–2043.

Judex, S. and Rubin, C.T., 2010. Is bone formation induced by high-frequency mechanical signals modulated by muscle activity? Journal of musculoskeletal and neuronal interactions, 10(1), p.3.

Kamioka, H., Honjo, T. and Takano-Yamamoto, T., 2001. A three-dimensional distribution of osteocyte processes revealed by the combination of confocal laser scanning microscopy and differential interference contrast microscopy. Bone, 28(2), pp.145–149.

Kannus, P., Haapasalo, H., Sankelo, M., Sievanen, H., Pasanen, M., Heinonen, A., Oja, P., Vuori, I., 1995. Effect of starting age of physical activity on bone mass in the dominant arm of tennis and squash players. Annals of internal medicine, 123(1).

Karsenty, G., and Wagner, E. F. 2002. Reaching a genetic and molecular understanding of skeletal development. Developmental Cell.

Kember N.F. 1960. Cell division in endochondral ossification: A Study of Cell Proliferation in Rat Bones by the Method of Tritiated Thymidine Autoradiography. Journal of Bone and Joint Surgery, British Volume 42-B:824-839.

Kidd, L. J., Stephens, A. S., Kuliwaba, J. S., Fazzalari, N. L., Wu, A. C. K., & Forwood, M. R. 2010. Temporal pattern of gene expression and histology of stress fracture healing. Bone, 46(2), 369-378.

Kilborn, S.H., Trudel, G. and Uhthoff, H., 2002. Review of Growth Plate Closure Compared with Age at Sexual Maturity and Lifespan in Laboratory Animals. Journal of the American Association for Laboratory Animal Science, 41(5), pp.21–26.

Kim, J.H., Manuelidis, E. E., Glenn, W. W., Fukuda, Y., Cole, D. S., Hogan, J. F., 1983. Light and electron microscopic studies of phrenic nerves after long-term electrical stimulation. Journal of neurosurgery, 58(1), pp.84–91.

Kingery, W., 2003. A substance P receptor (NK1) antagonist enhances the widespread osteoporotic effects of sciatic nerve section. Bone, 33(6), pp.927–936.

Kjaer, M., 2004. Role of extracellular matrix in adaptation of tendon and skeletal muscle to mechanical loading. Physiological reviews, 84(2), pp.649–698.

Kjaer, M. and Magnusson, S.P., 2008. Mechanical adaptation and tissue remodeling. Collagen. Springer, pp. 249–267.

Klein-Nulend, J., Semeins, C. M., Ajubi, N. E., Nijweide, P. J., Burger, E. H., 1995. Pulsating Fluid Flow Increases Nitric Oxide (NO) Synthesis by Osteocytes but Not Periosteal Fibroblasts - Correlation with Prostaglandin Upregulation. Biochemical and Biophysical Research Communications, 217(2), pp.640–648.

Klein-Nulend, J., Helfrich, M. H., Sterck, J. G., MacPherson, H., Joldersma, M., Ralston, S. H., Semeins, C. M., Burger, E. H., 1998. Nitric oxide response to shear stress by human bone cell cultures is endothelial nitric oxide synthase dependent. Biochemical and biophysical research communications, 250(1), pp.108–14.

Klein-Nulend, J., Bakker, A. D., Bacabac, R. G., Vatsa, A., Weinbaum, S., 2012. Mechanosensation and transduction in osteocytes. Bone. 54 (2) pp, 182-190.

Klingenberg CP. 2011. MorphoJ: an integrated software package for geometric morphometrics. Molecular Ecology Resources 11:353-357.

Knudson, C.B. and Knudson, W., 2001. Cartilage proteoglycans. Seminars in cell and developmental biology, 12(2), pp.69–78.

Knupp, P.M., 2001. Algebraic Mesh Quality Metrics. SIAM Journal on Scientific Computing, 23(1), pp.193–218.

Kobayashi, T. and Kronenberg, H., 2014. Overview of Skeletal Development. In M. J. Hilton, ed. Skeletal Development and Repair. Humana Press, pp. 3–12. Available at: http://dx.doi.org/10.1007/978-1-62703-989-5_1.

Kohrt, W.M., Barry, D.W. and Schwartz, R.S., 2009. Muscle forces or gravity: what predominates mechanical loading on bone? Medicine and science in sports and exercise, 41(11), p.2050.

Koller, A., Sun, D., Huang, A., Kaley, G., 1994. Corelease of nitric oxide and prostaglandins mediates flow-dependent dilation of rat gracilis muscle arterioles. The American journal of physiology, 267(1 Pt 2), pp.H326–H332.

Kotha, S.P., Hsieh, Y. F., Strigel, R. M., Müller, R., Silva, M. J., 2004. Experimental and finite element analysis of the rat ulnar loading model—correlations between strain and bone formation following fatigue loading. Journal of Biomechanics, 37(4), pp.541–548.

Kronenberg, H.M., 2003. Developmental regulation of the growth plate. Nature, 423(6937), pp.332–336.

Kupczik, K., Dobson, C. A., Fagan, M. J., Crompton, R. H., Oxnard, C. E., & O'Higgins, P. 2007. Assessing mechanical function of the zygomatic region in macaques: validation and sensitivity testing of finite element models. Journal of Anatomy, 210(1), 41-53.

Kwon, R.Y., Meays, D. R., Tang, W. J., Frangos, J. A., 2010. Microfluidic enhancement of intramedullary pressure increases interstitial fluid flow and inhibits bone loss in hindlimb suspended mice. Journal of Bone and Mineral Research, 25(8), pp.1798–1807.

Kwon, R.Y., Meays, D. R., Meilan, A. S., Jones, J., Miramontes, R., Kardos, N., Yeh, J-C., Frangos, J., 2012. Skeletal Adaptation to Intramedullary Pressure-Induced Interstitial Fluid Flow Is Enhanced in Mice Subjected to Targeted Osteocyte Ablation. PLoS ONE, 7(3), p.e33336.

Laib, A., Barou, O., Vico, L., Lafage-Proust, M. H., Alexandre, C., Rügsegger, P., 2000. 3D micro-computed tomography of trabecular and cortical bone architecture with application to a rat model of immobilisation osteoporosis. Medical and Biological Engineering and Computing, 38(3), pp.326–332.

Lanyon, L.E., Hampson, W. G. J., Goodship, A. E., Shah, J. S., 1975. Bone deformation recorded in vivo from strain gauges attached to the human tibial shaft. Acta Orthopaedica, 46(2), pp.256–268.

Lanyon, L.E., 1987. Functional strain in bone tissue as an objective, and controlling stimulus for adaptive bone remodelling. Journal of Biomechanics, 20(11–12), pp.1083–1093.

Lanyon LE, Goodship AE, Pye CJ, MacFie JH. 1982. Mechanically adaptive bone remodelling. Journal of Biomechanics 15:141-154.

Lanyon, L.E. and Rubin, C.T., 1984. Static vs dynamic loads as an influence on bone remodelling. Journal of Biomechanics, 17(12), pp.897–905.

Lanyon, L.E. and Smith, R.N., 1969. Measurements of bone strain in the walking animal. Research in veterinary science, 10(1), pp.93–94.

Lau, E., Al-Dujaili, S., Guenther, A., Liu, D., Wang, L., You, L., 2010. Effect of low-magnitude, high-frequency vibration on osteocytes in the regulation of osteoclasts. Bone, 46(6), pp.1508–1515.

Lautenschlager, S., Bright, J.A. and Rayfield, E.J., 2014. Digital dissection - using contrast-enhanced computed tomography scanning to elucidate hard- and soft-tissue anatomy in the Common Buzzard Buteo buteo. Journal of Anatomy, 224(4), pp.412–431.

LeBlanc, A., Schneider, V., Shackelford, L., West, S., Oganov, V., Bakulin, A., Voronin, L., 2000. Bone mineral and lean tissue loss after long duration space flight. J Musculoskelet Neuronal Interact, 1(2), pp.157–160.

LeBlanc, A., Shackelford, L. and Schneider, V., 1998. Future Human Bone Research in Space. Bone, 22(5, Supplement 1), p.113S–116S.

LeBrasseur, N.K., Walsh, K. and Arany, Z., 2010. Metabolic benefits of resistance training and fast glycolytic skeletal muscle. American Journal of Physiology - Endocrinology and Metabolism, 300(1), pp.E3–E10. Available at: http://ajpendo.physiology.org/ajpendo/300/1/E3.full.pdf.

Lecker, D.N., Kumari, S. and Khan, A., 1997. Iodine binding capacity and iodine binding energy of glycogen. Journal of Polymer Science Part a-Polymer Chemistry, 35(8), pp.1409–1412. Available at: <Go to ISI>://A1997WU85300009.

Lee, D.-J., Ko, W.-S. and Cho, B.-J., 2012. The Effects of Exercise Participation on Bone Mineral Density and Bone Mineral Content in Swimmers. Journal of Physical Therapy Science, 24(11), pp.1137–1139.

Lee, K.-L., Sobieraj, M., Baldassarri, M., Gupta, N., Pinisetty, D., Janal, M. N., Tovar, N., Coelho, P. G., 2013. The effects of loading conditions and specimen environment on the nanomechanical response of canine cortical bone. Materials science and engineering. C, Materials for biological applications, 33(8), pp.4582–6.

Lee, V.W.K., De Kretser, D. M., Hudson, B., Wang, C., 1975. Variations in serum FSH, LH and testosterone levels in males rats from birth to sexual maturity. Journal of Reproduction and Fertility, 42(1), pp.121–126.

Lelovas, P.P., Xanthos, T. T., Thoma, S. E., Lyritis, G. P., Dontas, I. A., 2008. The laboratory rat as an animal model for osteoporosis research. Comparative medicine, 58(5), p.424.

Lerner, U.H., 2002. Neuropeptidergic regulation of bone resorption and bone formation. Journal of musculoskeletal and neuronal interactions, 2(5), pp.440–447.

Lewis, G. and Nyman, J.S., 2008. The use of nanoindentation for characterizing the properties of mineralized hard tissues: State-of-the art review. Journal of Biomedical Materials Research - Part B Applied Biomaterials, 87(1), pp.286–301.

Lexell, J., Jarvis, J., Downham, D., Salmons, S., 1992. Quantitative morphology of stimulation-induced damage in rabbit fast-twitch skeletal muscles. Cell and Tissue Research, 269(2), pp.195–204.

Li, X. and Bhushan, B., 2002. A review of nanoindentation continuous stiffness measurement technique and its applications. Materials Characterization, 48(1), pp.11–36.

Lieber, R., Fride´n, J., 2000. Functional and clinical significance of skeletal muscle architecture. Muscle and Nerve, 23, pp.1647–1666.

Lieber, R.L., 2002. Skeletal muscle structure, function, and plasticity, Wolters Kluwer Health.

Lieber, R.L. and Ward, S.R., 2011. Skeletal muscle design to meet functional demands. Philosophical Transactions of the Royal Society B: Biological Sciences, 366(1570), pp.1466–1476.

Ling, L., Nurcombe, V. and Cool, S.M., 2009. Wnt signaling controls the fate of mesenchymal stem cells. Gene, 433(1–2), pp.1–7.

Liske, H., Towne, C., Anikeeva, P., Zhao, S., Feng, G., Deisseroth, K., Delp, S., 2013. Optical inhibition of motor nerve and muscle activity in vivo. Muscle and nerve, 47(6), pp.916–21.

Llewellyn, M.E., Thompson, K. R., Deisseroth, K., Delp, S., 2010. Orderly recruitment of motor units under optical control in vivo. Nat Med, 16(10), pp.1161–1165.

Logan, D., 2011. A first course in the finite element method, Cengage Learning.

Lohmander, S. and Hjerpe, A., 1975. Proteoglycans of mineralizing rib and epiphyseal cartilage. Biochimica et Biophysica Acta (BBA) - General Subjects, 404(1), pp.93–109.

Maas, H., Baan, G.C. and Huijing, P.A., 2001. Intermuscular interaction via myofascial force transmission: effects of tibialis anterior and extensor hallucis longus length on force transmission from rat extensor digitorum longus muscle. Journal of Biomechanics, 34(7), pp.927–940.

Maas SA, Ellis BJ, Ateshian GA, Weiss JA. 2012. FEBio: finite elements for biomechanics. Journal of biomechanical engineering 134.

Maas, S., A. and Weiss, J., A., 2007. FEBio Theory Manual., p.http://mrl.sci.utah.edu/software/febio.

Macho, G.A., Shimizu, D., Jiang, Y., Spears, I. R., 2005. Australopithecus anamensis: A finite-element approach to studying the functional adaptations of extinct hominins. In Anatomical Record - Part A Discoveries in Molecular, Cellular, and Evolutionary Biology. pp. 310–318.

Mackie, E.J., Ahmed, Y. A., Tatarczuch, L., Chen, K. S., Mirams, M., 2008. Endochondral ossification: How cartilage is converted into bone in the developing skeleton. The International Journal of Biochemistry and Cell Biology, 40(1), pp.46–62.

Mackie, E.J., Tatarczuch, L. and Mirams, M., 2011. The skeleton: a multi-functional complex organ. The growth plate chondrocyte and endochondral ossification. Journal of Endocrinology, 211(2), pp.109–121.

Magnusson, S.P. and Kjaer, M., 2003. Region-specific differences in Achilles tendon cross-sectional area in runners and non-runners. European Journal of Applied Physiology, 90(5-6), pp.549–553.

Mahns, D.A., Ivanusic, J. J., Sahai, V., Rowe, M. J., 2006. An intact peripheral nerve preparation for monitoring the activity of single, periosteal afferent nerve fibres. Journal of Neuroscience Methods, 156(1-2), pp.140–144.

Maier, A., Gambke, B. and Pette, D., 1986. Degeneration-regeneration as a mechanism contributing to the fast to slow conversion of chronically stimulated fast-twitch rabbit muscle. Cell and Tissue Research, 244(3), pp.635–643.

Von Maltzahn, J., Chang, N. C., Bentzinger, C. F., Rudnicki, M. A., 2012. Wnt signaling in myogenesis. Trends in Cell Biology.

Manske, S.L., Boyd, S.K. and Zernicke, R.F., 2010. Muscle and bone follow similar temporal patterns of recovery from muscle-induced disuse due to botulinum toxin injection. Bone, 46(1), pp.24–31.

Marieb, E. N., and Hoehn, K. (2007). Human anatomy and physiology. Pearson Education.

Marsell, R. and Einhorn, T.A., 2011. The biology of fracture healing. Injury, 42(6), pp.551–555.

Martin, E.A., Ritman, E.L. and Turner, R.T., 2003. Time course of epiphyseal growth plate fusion in rat tibiae. Bone, 32(3), pp.261–267.

Martin, R.B., 2002. Size, structure and gender: lessons about fracture risk. Journal of Musculoskeletal and Neuronal Interactions, 2(3), pp.209–211.

Martinez, M.D., Schmid, G. J., McKenzie, J. A., Ornitz, D. M., Silva, M. J., 2010. Healing of non-displaced fractures produced by fatigue loading of the mouse ulna. Bone, 46(6), pp.1604–1612.

McBride, S.H. and Silva, M.J., 2012. Adaptive and Injury Response of Bone to Mechanical Loading. BoneKEy osteovision, 1.

McNeal, D.R. and Bowman, B.R., 1985. Selective activation of muscles using peripheral nerve electrodes. Medical and biological engineering and computing, 23(3), pp.249–253.

Mendez, J., Keys, A., Anderson, J. T., Grande, F., 1960. Density of fat and bone mineral of the mammalian body. Metabolism, 9, pp.472–477.
Merzin M. 2008. Applying stereological method in radiology. Volume measurement. Bachelor's thesis University of Tartu.

Metscher, B.D., 2009. MicroCT for developmental biology: A versatile tool for high-contrast 3D imaging at histological resolutions. Dev Dyn, 238, pp.632 – 40.

Van der Meulen PhD, M.C.H., Yang, X. and Bostrom, M.P.G., 2009. The effects of loading on cancellous bone in the rabbit. Clinical Orthopaedics and Related Research®, 467(8), pp.2000–2006.

Michna, H., 1984. Morphometric analysis of loading-induced changes in collagen-fibril populations in young tendons. Cell and Tissue Research, 236(2), pp.465–470.

Mizutani, R. and Suzuki, Y., 2012. X-ray microtomography in biology. Micron, 43(2-3), pp.104–115.

Moazen, M., Curtis, N., O'Higgins, P., Jones, M. E. H., Evans, S. E., Fagan, M. J., 2009. Assessment of the role of sutures in a lizard skull: a computer modelling study. Proceedings of the Royal Society B: Biological Sciences, 276(1654), pp.39–46.

Morey-Holton, E., Globus, R. K., Kaplansky, A., Durnova, G., 2005. The hindlimb unloading rat model: literature overview, technique update and comparison with space flight data. Advances in space biology and medicine, 10, pp.7–40.

Mosley, J.R. and Lanyon, L.E., 1998. Strain rate as a controlling influence on adaptive modeling in response to dynamic loading of the ulna in growing male rats. Bone, 23(4), pp.313–318.

Nagira, K., Hagino, H., Kameyama, Y., Teshima, R., 2013. Effects of minodronate on cortical bone response to mechanical loading in rats. Bone, 53(1), pp.277–283.

Nakamura, E., Uezono, Y., Narusawa, K., Shibuya, I., Oishi, Y., Tanaka, M., Yanagihara, N., Nakamura, T., Izumi, F., 2000. ATP activates DNA synthesis by acting on P2X receptors in human osteoblast-like MG-63 cells. American journal of physiology. Cell physiology, 279(2), pp.C510–C519.

Nakashima, T., Hayashi, M., Fukunaga, T., Kurata, K., Oh-hora, M., Feng, J. Q., Bonewald, L. F., Kodama, T., Wutz, A., Wagner, E. F., 2011. Evidence for osteocyte regulation of bone homeostasis through RANKL expression. Nature medicine, 17(10), pp.1231–1234.

Naveiras, O., Nardi, V., Wenzel, P. L., Hauschka, P. V., Fahey, F., Daley, G. Q., 2009. Bone-marrow adipocytes as negative regulators of the haematopoietic microenvironment. Nature, 460(7252), pp.259–263.

Nazarian, A., Hermannsson, B. J., Muller, J., zurakowski, D., Snyder, B. D., 2009. Effects of tissue preservation on murine bone mechanical properties. Journal of biomechanics, 42(1), pp.82–6.

Nichols, S.P., Storm, W. L., Koh, A., Schoenfisch, M. H., 2012. Local delivery of nitric oxide: targeted delivery of therapeutics to bone and connective tissues. Advanced drug delivery reviews, 64(12), pp.1177–88.

Nishimune, H., Numata, T., Chen, J., Aoki, Y., Wang, Y., Starr, M. P., Stanford, J. A. 2012. Active Zone Protein Bassoon Co-Localizes with Presynaptic Calcium Channel, Modifies Channel Function, and Recovers from Aging Related Loss by Exercise. PLoS ONE, 7(6), e38029. doi:10.1371/journal.pone.0038029

Le Noble, F. and le Noble, J., 2014. Bone Biology: Vessels of Rejuvenation. Nature, 507, pp.7–8.

O'Hare, L.M.S., Cox, P. G., Jeffery, N., Singer, E. R., 2012. Finite element analysis of stress in the equine proximal phalanx. Equine Veterinary Journal.

Ohman, C., Dall'Ara, E., Baleani, M., Van Sint Jan, S., Viceconti, M., 2008. The effects of embalming using a 4% formalin solution on the compressive mechanical properties of human cortical bone. Clinical biomechanics (Bristol, Avon), 23(10), pp.1294–8.

Olubamiji, A.D., Izadifar, Z. and Chen, D., 2014. Synchrotron imaging techniques for bone and cartilage tissue engineering: potentials, current trends, and future directions. Tissue Eng Part B Rev.

Ozcivici E, Luu YK, Adler B, Qin Y-X, Rubin J, Judex S, Rubin CT. 2010. Mechanical signals as anabolic agents in bone. Nature Reviews Rheumatology 6:50-59.

Panagiotopoulou, O., 1976. A Procedure for Differential Staining of Cartilage and Bone in Whole Formalin-Fixed Vertebrates. Biotechnic and Histochemistry, 51(2), pp.131–134.

Pauwels, E., Van Loo, D., Cornillie, P., Brabant, L., Van Hoorebeke, L., 2013. An exploratory study of contrast agents for soft tissue visualization by means of high

resolution X-ray computed tomography imaging. Journal of Microscopy, 250(1), pp.21–31.

Pedersen, H.E., 1949. The ossicles of the semilunar cartilages of rodents. The Anatomical Record, 105(1), pp.1–9.

Peterson, J. and Dechow, P.C., 2003. Material properties of the human cranial vault and zygoma. The Anatomical Record Part A: Discoveries in Molecular, Cellular, and Evolutionary Biology, 274A(1), pp.785–797.

Pharr, G.M., 1998. Measurement of mechanical properties by ultra-low load indentation. Materials Science and Engineering: A, 253(1-2), pp.151–159.

Phelps, J.B., Hubbard, G. B., Wang, X., Agrawal, C. M., 2000. Microstructural heterogeneity and the fracture toughness of bone. Journal of Biomedical Materials Research, 51(4), pp.735–741.

Pitsillides, A.A., 2006. Early effects of embryonic movement: “a shot out of the dark.” Journal of Anatomy, 208(4), pp.417–431.

Pitsillides, A.A., Rawlinson, S. C., Suswillo, R. F., Bourrin, S., Zaman, G., Lanyon, L E., 1995. Mechanical strain-induced NO production by bone cells: a possible role in adaptive bone (re)modeling? The FASEB Journal, 9(15), pp.1614–1622.

Plate, J.F. et al., 2013. Normal aging alters in vivo passive biomechanical response of the rat gastrocnemius-Achilles muscle-tendon unit. Journal of biomechanics, 46(3), pp.450–5.

Poliachik, S.L. et al., 2010. Transient muscle paralysis disrupts bone homeostasis by rapid degradation of bone morphology. Bone, 46(1), pp.18–23.

Poulet B., Hamilton R.W., Shefelbine S., Pitsillides A.A. 2011. Characterizing a novel and adjustable non-invasive murine joint loading model. Arthritis and Rheumatism 63:137-147.

Powell, P.L., Roy, R. R., Kanim, P., Bello, M. A., Edgerton, V R., 1984. Predictability of skeletal muscle tension from architectural determinations in guinea pig hindlimbs. Journal of Applied Physiology, 57(6), pp.1715–1721.

Pullen A. 1977. The distribution and relative sizes of three histochemical fibre types in the rat tibialis anterior muscle. Journal of Anatomy 123:1.

Purslow, P.P., 2010. Muscle fascia and force transmission. Journal of Bodywork and Movement Therapies, 14(4), pp.411–417.

Qin, W., Sun, L., Cao, J., Peng, Y., Collier, L., Wu, Y., Creasey, G., Li, J., Qin, Y., Jarvis, J. 2013. The central nervous system (CNS)-independent anti-bone-resorptive activity of muscle contraction and the underlying molecular and cellular signatures. Journal of Biological Chemistry. 288 (19) pp 13511-13521.

Qin, Y.-X. and Lam, H., 2009. Intramedullary pressure and matrix strain induced by oscillatory skeletal muscle stimulation and its potential in adaptation. Journal of biomechanics, 42(2), pp.140–5.

Qin, Y.-X., Rubin, C.T. and McLeod, K.J., 1998. Nonlinear dependence of loading intensity and cycle number in the maintenance of bone mass and morphology. Journal of Orthopaedic Research, 16(4), pp.482–489.

Radak, Z., Chung, H.Y. and Goto, S., 2008. Systemic adaptation to oxidative challenge induced by regular exercise. Free radical biology and medicine, 44(2), pp.153–9.

Radhakrishnan P, Lewis N, Mao J. 2004. Zone-Specific Micromechanical Properties of the Extracellular Matrices of Growth Plate Cartilage. Annals of Biomedical Engineering 32:284-291.

Rajaram, A. and Ramanathan, N., 1982. Tensile properties of antler bone. Calcified tissue international, 34(1), pp.301–305.

Ramos, A. and Simões, J.A., 2006. Tetrahedral versus hexahedral finite elements in numerical modelling of the proximal femur. Medical engineering and physics, 28(9), pp.916–24.

Ranvier, L., 1874. De quelques faits relatifs à l'histologie et à la physiologie des muscles striés. Arch. Physiol. Norm. Pathol, 1(5).

Ranvier, L., 1873. Propriétés et structures différentes des muscles rouges et des muscles blancs, chez les Lapins et chez les Raies. CR Acad Sci Paris, 77, pp.1030–1034.

Rath Bonivtch, A., Bonewald, L.F. and Nicolella, D.P., 2007. Tissue strain amplification at the osteocyte lacuna: A microstructural finite element analysis. Journal of Biomechanics, 40(10), pp.2199–2206.

Rauner, M., Stein, N. and Hofbauer, L.C., 2012. Basics of Bone Biology. In P. Pietschmann, ed. Principles of Osteoimmunology. Springer Vienna, pp. 1–26. Available at: http://dx.doi.org/10.1007/978-3-7091-0520-7_1.

Rayfield, E.J., 2007. Finite Element Analysis and Understanding the Biomechanics and Evolution of Living and Fossil Organisms. Annual Review of Earth and Planetary Sciences, 35(1), pp.541–576.

Reddy, G.K., 2004. Cross-Linking in Collagen by Nonenzymatic Glycation Increases the Matrix Stiffness in Rabbit Achilles Tendon. Experimental diabesity research, 5(2), pp.143–153.

Reichmann, H., Hoppeler, H., Mathieu-Costello, O., von Bergen, F., Pette, D., 1985. Biochemical and ultrastructural changes of skeletal muscle mitochondria after chronic electrical stimulation in rabbits. Archiv European Journal of Physiology, 404(1), pp.1–9.

Resnicow, D.I., Deacon, J. C., Warrick, H. M., Spudich, J. A., Leinwand, L. A., 2010. Functional diversity among a family of human skeletal muscle myosin motors. Proceedings of the National Academy of Sciences, 107(3), pp.1053–1058.

Rho, J.-Y., Kuhn-Spearing, L. and Zioupos, P., 1998. Mechanical properties and the hierarchical structure of bone. Medical Engineering and Physics, 20(2), pp.92–102.

Rho, J.-Y. and Pharr, G.M., 1999. Effects of drying on the mechanical properties of bovine femur measured by nanoindentation. Journal of Materials Science: Materials in Medicine, 10(8), pp.485–488.

Rho J-Y, Tsui TY, Pharr GM. 1997. Elastic properties of human cortical and trabecular lamellar bone measured by nanoindentation. Biomaterials 18:1325-1330.

Richmond, B.G., Wright, B. W., Grosse, I., Dechow, P. C., Ross, C. F., Spencer, M. A., Strait, D. S., 2005. Finite element analysis in functional morphology. The Anatomical Record Part A: Discoveries in Molecular, Cellular, and Evolutionary Biology, 283A(2), pp.259–274.

Riggs, C.M., Vaughan, L.C., Evans, G. P., Lanyon, L. E., Boyde, A., 1993. Mechanical implications of collagen fibre orientation in cortical bone of the equine radius. Anatomy and Embryology, 187(3), pp.239–248.
Riggs, C.M., Lanyon, L.E. and Boyde, A., 1993. Functional associations between collagen fibre orientation and locomotor strain direction in cortical bone of the equine radius. Anatomy and Embryology, 187(3), pp.231–238.

Rittweger, J. and Ferretti, J.-L., 2014. Imaging Mechanical Muscle–Bone Relationships: How to See the Invisible. Clinical Reviews in Bone and Mineral Metabolism, 12(2), pp.66–76.

Robling, A.G., Niziolek, P. J., Baldridge, L. A., Condon, K. W., Allen, M. R., Alam, I., Mantila, S. M., Gluhak-Heinrich, J., Bellido, T. M., Harris, S. E.,
Turner, C. H., 2008. Mechanical Stimulation of Bone in Vivo Reduces Osteocyte Expression of Sost/Sclerostin. Journal of Biological Chemistry, 283(9), pp.5866–5875.

Robling, A.G., Burr, D.B. and Turner, C.H., 2000. Partitioning a Daily Mechanical Stimulus into Discrete Loading Bouts Improves the Osteogenic Response to Loading. Journal of Bone and Mineral Research, 15(8), pp.1596–1602.

Robling, A.G., Burr, D.B., Turner, C.H., 2001a. Recovery periods restore mechanosensitivity to dynamically loaded bone. Journal of Experimental Biology 204:3389-3399.

Robling, A., Duijvelaar, K.M., Geevers, J.V., Ohashi, N., Turner, C.H., 2001b. Modulation of appositional and longitudinal bone growth in the rat ulna by applied static and dynamic force. Bone, 29(2), pp.105–113.

Rodríguez, J.I., Garcia-Alix, A., Palacios, J., Paniagua, R., 1988. Changes in the long bones due to fetal immobility caused by neuromuscular disease. A radiographic and histological study. The Journal of bone and joint surgery. American volume, 70(7), p.1052.

Rosager, S., Aagaard, P., Dyhre-Poulsen, P., Neergaard, K., Kjaer, M., Magnusson, S. P., 2002. Load-displacement properties of the human triceps surae aponeurosis and tendon in runners and non-runners. Scandinavian journal of medicine and science in sports, 12(2), pp.90–98.

Roux W. 1912. Anpassungslehre, Histomechanik und Histochemie. Virchows Archiv für pathologische Anatomie und Physiologie und für klinische Medizin 209:168-209.

Ruan, J.S., Khalil, T. and King, A.I., 1994. Dynamic response of the human head to impact by three-dimensional finite element analysis. Journal of biomechanical engineering, 116(1), pp.44–50.

Rubin, C.T. and Lanyon, L.E., 1984. Regulation of bone formation by applied dynamic loads C. T. Rubin and L. E. Lanyon, eds., Available at: http://jbjs.org/jbjsam/66/3/397.full.pdf.

Rubin, C., Turner, S.A., Bain, S., Mallinckrodt, C., McLeod, K., 2001. Anabolism: Low mechanical signals strengthen long bones. Nature, 412(6847), pp.603–604.

Rubin, C.T. and Lanyon, L.E., 1982. Limb mechanics as a function of speed and gait: a study of functional strains in the radius and tibia of horse and dog. Journal of Experimental Biology, 101(1), pp.187–211.

Rubinstein, N., 1978. Use of type-specific antimyosins to demonstrate the transformation of individual fibers in chronically stimulated rabbit fast muscles. The Journal of Cell Biology, 79(1), pp.252–261.

Ruff, C., Holt, B. and Trinkaus, E., 2006. Who's afraid of the big bad Wolff?:"Wolff's law" and bone functional adaptation. American Journal of Physical Anthropology, 129(4), pp.484–498.

Russold, M. and Jarvis, J.C., 2007. Implantable stimulator featuring multiple programs, adjustable stimulation amplitude and bi-directional communication for implantation in mice. Medical and Biological Engineering and Computing, 45(7), pp.695–699.

Sakai, D., Kii, I., Nakagawa, K., Matsumoto, H. N., Takahashi, M., Yoshida, S., Hosoya, T., Takakuda, K., Kudo, A., 2011. Remodeling of actin cytoskeleton in mouse periosteal cells under mechanical loading induces periosteal cell proliferation during bone formation. PLoS ONE, 6(9), p.e24847.

Salmons, S., 2009. Adaptive change in electrically stimulated muscle: a framework for the design of clinical protocols. Muscle and Nerve, 40(6), pp.918–935.

Salmons, S. and Sreter, F.A., 1976. Significance of impulse activity in the transformation of skeletal muscle type. Nature, 263, pp.30–34.

Sample, S.J., Behan, M., Smith, L., Oldenhoff, W. E., Markel, M. D., Kalscheur, V. L., Hao, Z., Miletic, V., Muir, P., 2008. Functional adaptation to loading of a single bone is neuronally regulated and involves multiple bones. Journal of Bone and Mineral Research, 23(9), pp.1372–1381.

Schiaffino, S. and Reggiani, C., 2011. Fiber Types in Mammalian Skeletal Muscles. Physiological Reviews, 91(4), pp.1447–1531.

Schmidt, E., Parsons, T., Jamniczky, H., Gitelman, J., Trpkov, C., Boughner, J., Logan, C.C., Sensen, C., Hallgrimsson, B., 2010. Micro-computed tomography-based phenotypic approaches in embryology: procedural artifacts on assessments of embryonic craniofacial growth and development. BMC Developmental Biology, 10(1), p.18.

Schmitz, N., Laverty, S., Kraus, V. B., Aigner, T., 2010. Basic methods in histopathology of joint tissues. Osteoarthritis and Cartilage, 18(SUPPL. 3).
Schindeler, A. et al., 2008. Bone remodeling during fracture repair: The cellular picture. Seminars in Cell and Developmental Biology, 19(5), pp.459–466.

Schneider CA, Rasband WS, Eliceiri KW. 2012. NIH Image to ImageJ: 25 years of image analysis. Nat Methods 9:671-675.

Schoenau, E., 2005. From mechanostat theory to development of the“ Functional Muscle-Bone-Unit.” Journal of Musculoskeletal and Neuronal Interactions, 5(3), p.232.

Schöfl, C., Cuthbertson, K. S., Walsh, C. A.,Mayne, C., Cobbold, P., von zur Mühlen, A., Hesch, R. D., Gallagher, J. A., 1992. Evidence for P2-purinoceptors on human osteoblast-like cells. Journal of bone and mineral research : the official journal of the American Society for Bone and Mineral Research, 7(5), pp.485–491.

Schulte, F.A., Wagner, K., Stolz, L., Hubner, C., Riebel, T., Komen, W., Braun, T., Tobin, J., Lee, S. 2013. Local Mechanical Stimuli Regulate Bone Formation and Resorption in Mice at the Tissue Level. PLoS ONE, 8(4), p.e62172.

Seeram, E. 1996. 3-D imaging: basic concepts for radiologic technologists.Radiologic technology, 69(2), 127-44.

Sengle, G., Tufa, S. F., Sakai, L. Y., Zulliger, M. A., Keene, D. R., 2013. A correlative method for imaging identical regions of samples by micro-CT, light microscopy, and electron microscopy: imaging adipose tissue in a model system. The journal of histochemistry and cytochemistry : official journal of the Histochemistry Society, 61(4), pp.263–71.

Seppet, E., Orlova, E., Seene, T., Gellerich, F. N., 2013. Adaptation of Cardiac and Skeletal Muscle Mitochondria to Endurance Training: Implications for Cardiac Protection. In Cardiac Adaptations. Springer, pp. 375–402.

Seref-Ferlengez, Z., Basta-Pljakic, J., Kennedy, O. D., Philemon, C. J., and Schaffler, M. B. 2014. Structural and Mechanical Repair of Diffuse Damage in Cortical Bone in vivo. Journal of Bone and Mineral Research (accepted) DOI: 10.1002/jbmr.2309.

Shahar, R. and Dean, M.N., 2013. The enigmas of bone without osteocytes. BoneKEy Rep, 2. Available at: http://dx.doi.org/10.1038/bonekey.2013.77.

Shapiro F. 2008. Bone development and its relation to fracture repair. The role of mesenchymal osteoblasts and surface osteoblasts. Eur Cell Mater 15:53-76.

Sharafi, B. and Blemker, S.S., 2010. A micromechanical model of skeletal muscle to explore the effects of fiber and fascicle geometry. Journal of Biomechanics, 43(16), pp.3207–3213.

Sharir, A., Stern, T., Rot, C., Shahar, R., Zelzer, E., 2011. Muscle force regulates bone shaping for optimal load-bearing capacity during embryogenesis. Development (Cambridge, England), 138(15), pp.3247–3259.

Sheng, Z., Dai, R-C., Wang, P., Yao, X-F., Feng, X-P., Fang, L-N., Fan, H-J., Wu, X-P., Liao, E-Y., 2006. Nanomechanical properties of vertebral trabeculae in ovariectomized rats. Zhonghua yi xue za zhi, 86(8), pp.515–9.

Shipov, A., Zaslansky, P., Riesemeier, H., Segev, G., Atkins, A., Shahar, R., 2013. Unremodeled endochondral bone is a major architectural component of the cortical

bone of the rat (Rattus norvegicus). Journal of Structural Biology, 183(2), pp.132–140.

Sibole S, Bennetts, C., Borotikar, B., Maas, S., van den Bogert, A. J., Weiss, J. A. and Erdemir, A. 2010. Open knee: a 3D finite element representation of the knee joint. 34th Annual Meeting of the American Society of Biomechanics August 18-21.

Silva, M.J., Uthgenannt, B.A., Rutlin, J.R., Wohl, G. R., Lewis, J. S., Welch, M.J., 2006. In vivo skeletal imaging of 18F-fluoride with positron emission tomography reveals damage- and time-dependent responses to fatigue loading in the rat ulna. Bone, 39(2), pp.229–36

Skedros, J. G., Holmes, J. L., Vajda, E. G., & Bloebaum, R. D. 2005. Cement lines of secondary osteons in human bone are not mineral- deficient: New data in a historical perspective. The Anatomical Record Part A: Discoveries in Molecular, Cellular, and Evolutionary Biology, 286(1), 781-803.

Skerry, T.M., 2006. One mechanostat or many? Modifications of the site-specific response of bone to mechanical loading by nature and nurture. Journal of Musculoskeletal and Neuronal Interactions, 6(2), p.122.

Somerville, J.M., Aspden, R. M., Armour, K. E., Armour, K. J., Reid, D. M., 2004. Growth of C57BL/6 mice and the material and mechanical properties of cortical bone from the tibia. Calcified tissue international, 74(5), pp.469–75.

De Souza, R.L. and Saxon, L., 2012. In Vivo Mechanical Loading. In Bone Research Protocols. Springer, pp. 621–636.

De Souza, R.L., Pitsillides, A. A., Lanyon, L. E., Skerry, T. M., Chenu, C., 2005a. Sympathetic nervous system does not mediate the load-induced cortical new bone formation. Journal of bone and mineral research : the official journal of the American Society for Bone and Mineral Research, 20(12), pp.2159–2168.

De Souza, R.L., Matsuura, M., Eckstein, F., Rawlinson, S. C. F., Lanyon, L. E., Pitsillides, A. A., 2005b. Non-invasive axial loading of mouse tibiae increases cortical bone formation and modifies trabecular organization: A new model to study cortical and cancellous compartments in a single loaded element. Bone, 37(6), pp.810–818.

Spoor, F., Jeffery, N. and Zonneveld, F., 2000. Using diagnostic radiology in human evolutionary studies. Journal of anatomy, 197 (Pt 1, pp.61–76.

Spudich, J.A., Huxley, H.E. and Finch, J.T., 1972. Regulation of skeletal muscle contraction: II. Structural studies of the interaction of the tropomyosin-troponin complex with actin. Journal of molecular biology, 72(3), pp.619–632.

Staines, K.A., Pollard, A.S., McGonnell, I. M., Farquharson, C., Pitsillides, A. A., 2013. Cartilage to bone transitions in health and disease. Journal of Endocrinology, 219(1), pp.R1–R12.

Stauber, M. and Müller, R., 2008. Micro-Computed Tomography: A Method for the Non-Destructive Evaluation of the Three-Dimensional Structure of Biological Specimens Osteoporosis. In J. J. Westendorf, ed. Humana Press, pp. 273–292.

Stephenson, R.S., Boyett, M.R., Hart, G., Nikolaidou, T., Cai, X., Corno, A. F., Alphonso, N., Jeffery, N., Jarvis, J. C., 2012. Contrast Enhanced Micro-Computed Tomography Resolves the 3-Dimensional Morphology of the Cardiac Conduction System in Mammalian Hearts. PLoS ONE, 7(4), p.e35299.

Stern-Perry, M., Gefen, A., Shabshin, N., Epstein, Y., 2011. Experimentally tested computer modeling of stress fractures in rats. Journal of Applied Physiology, 110(4), pp.909–916.

Stewart, L.K., Flynn, M. G., Campbell, W.W., Craig, B. A., Robinson, J. P., Timmerman, K.L., McFarlin, B.K., Coen, P.M., Talbert, E., 2007. The influence of exercise training on inflammatory cytokines and C-reactive protein. Medicine and Science in Sports and Exercise, 39(10), pp.1714–1719.

Strait DS, Wang Q, Dechow PC, Ross CF, Richmond BG, Spencer MA, Patel BA. 2005. Modeling elastic properties in finite-element analysis: How much precision is needed to produce an accurate model? The Anatomical Record Part A: Discoveries in Molecular, Cellular, and Evolutionary Biology 283A:275-287.

Sugawara, Y., Kamioka, H., Ishihara, Y., Fujisawa, N., Kawanabe, N., Yamashiro, T., 2013. The early mouse 3D osteocyte network in the presence and absence of mechanical loading. Bone, 52(1), pp.189–196.

Sugiyama, T., Meakin, L.B., Browne, W. J., Galea, G.L., Price, J. S., Lanyon, L.E., 2012. Bones' adaptive response to mechanical loading is essentially linear between

the low strains associated with disuse and the high strains associated with the lamellar/woven bone transition. Journal of Bone and Mineral Research, 27(8), pp.1784–1793.

Sugiyama, T., Price, J.S. and Lanyon, L.E., 2010. Functional adaptation to mechanical loading in both cortical and cancellous bone is controlled locally and is confined to the loaded bones. Bone, 46(2), pp.314–321.

Sun, L., Fan, Y-B., Li, D-Y., Zhao, F., Xie, T., Yang, X., Gu, Z-T., 2009. Evaluation of the mechanical properties of rat bone under simulated microgravity using nanoindentation. Acta Biomaterialia, 5(9), pp.3506–3511.

Sutherland, H., Jarvis, J.C., Kwende, M. M. N., Gilroy, S.J., Salmons, S., 1998. The dose-related response of rabbit fast muscle to long-term low-frequency stimulation. Muscle and Nerve, 21(12), pp.1632–1646.

Sztefek, P., Vanleene, M., Olsson, R., Collinson, R., Shefelbine, S., 2010. Using digital image correlation to determine bone surface strains during loading and after adaptation of the mouse tibia. Journal of Biomechanics, 43(4), pp.599–605.

Tahara, R. and Larsson, H.C.E., 2013. Quantitative analysis of microscopic X-ray computed tomography imaging: Japanese quail embryonic soft tissues with iodine staining. Journal of Anatomy, 223(3), pp.297–310.

Tatsumi, S., Amizuka, N., Li, M., Ishii, K., Kohno, K., Ito, M., Takeshita, S., Ikeda, K., 2006. Targeted ablation of osteocytes in transgenic mice. J Bone Miner Res, 21(suppl 1), p.S18.

Taylor, A.M., Preston, A. J., Paulk, N. K., Sutherland, H., Keenan, C. M., Wilson, P., Wlodarski, B., Grompe, M., Ranganath, L. R., Gallagher, J. A., Jarvis, J. C., 2012. Ochronosis in a murine model of alkaptonuria is synonymous to that in the human condition. Osteoarthritis and Cartilage, 20(8), pp.880–886.

Tezuka, K.I., Wada, Y., Takahashi, A., Kikuchi, M., 2005. Computer-simulated bone architecture in a simple bone-remodeling model based on a reaction-diffusion system. Journal of Bone and Mineral Metabolism, 23(1), pp.1–7.

Tidball, J.G., Lavergne, E., Lau, K. S., Spencer, M. J., Stull, J. T., Wehling, M., 1998. Mechanical loading regulates NOS expression and activity in developing and adult skeletal muscle. The American journal of physiology, 275(1 Pt 1), pp.C260–C266.

Tomlinson, R. E., Schmieder, A. H., Quirk, J. D., Lanza, G. M., & Silva, M. J. 2014. Antagonizing the αvβ3 Integrin Inhibits Angiogenesis and Impairs Woven but Not Lamellar Bone Formation Induced by Mechanical Loading.Journal of Bone and Mineral Research, 29(9), 1970-1980.

Torcasio A, Zhang X, Duyck J, van Lenthe GH. 2012. 3D characterization of bone strains in the rat tibia loading model. Biomech Model Mechanobiol 11:403-410.

Torrance, A.G., Mosley, J. R., Suswillo, R. F.L., Lanyon, L. E., 1994. Noninvasive loading of the rat ulna in vivo induces a strain-related modeling response uncomplicated by trauma or periostal pressure. Calcified tissue international, 54(3), pp.241–247.

Towne, C., Montgomery, K. L., Iyer, S.M., Deisseroth, K., Delp, S. L., 2013. Optogenetic Control of Targeted Peripheral Axons in Freely Moving Animals. PLoS ONE, 8(8).

Trotter, J. A., & Purslow, P. P., 1992. Functional morphology of the endomysium in series fibered muscles. Journal of morphology, 212(2), 109-122.

Trudel, G., Kilborn, S.H. and Uhthoff, H.K., 2001. Bone growth increases the knee flexion contracture angle: A study using rats. Archives of Physical Medicine and Rehabilitation, 82(5), pp.583–588.

Tsui, B.C.H., Bhargava, R. and Chan, V., 2007. Atlas of ultrasound-and nerve stimulation-guided regional anesthesia, Springer.

Tunell GL, Hart MN. 1977. Simultaneous determination of skeletal muscle fiber, types I, IIA, and IIB by histochemistry. Archives of neurology 34:171.

Turner, C.H., 1998. Three rules for bone adaptation to mechanical stimuli. Bone, 23(5), pp.399–407.

Turner, C.H., 2002. Biomechanics of Bone: Determinants of Skeletal Fragility and Bone Quality. Osteoporosis International, 13(2), pp.97–104.

Turner, C.H., 2006. Bone strength: Current concepts. In Annals of the New York Academy of Sciences. pp. 429–446.

Turner, C.H., Rho, J., Takano, Y., Tsui, T. Y., Pharr, G. M., 1999. The elastic properties of trabecular and cortical bone tissues are similar: results from two microscopic measurement techniques. Journal of Biomechanics, 32(4), pp.437–441.

Turner CH, Burr DB. 1993. Basic biomechanical measurements of bone: a tutorial. Bone 14:595-608.

Turner C.H., Forwood M.R., Rho J.Y., Yoshikawa T. 1994. Mechanical loading thresholds for lamellar and woven bone formation. Journal of Bone and Mineral Research 9:87-97.

Tuukkanen, J., Wallmark, B., Jalovaara, P., Takala, T., Sjögren, S., Väänänen, K., 1991. Changes induced in growing rat bone by immobilization and remobilization. Bone, 12(2), pp.113–118.

Ueno, T., Kagawa, T., Mizukawa, N., Nakamura, H., Sugahara, T., Yamamoto, T., 2001. Cellular origin of endochondral ossification from grafted periosteum. Anatomical Record, 264(4), pp.348–357.

Ulrich, D., van Rietbergen, B., Weinans, H., Rüegsegger, P.,1998. Finite element analysis of trabecular bone structure: a comparison of image-based meshing techniques. Journal of Biomechanics, 31(12), pp.1187–1192.

Umemura, Y., Ishiko, T., Yamauchi, T., Kurono, M., Mashiko, S., 1997. Five jumps per day increase bone mass and breaking force in rats. Journal of Bone and Mineral Research, 12(9), pp.1480–1485.

Urlando, A. and Hawkins, D., 2007. Achilles tendon adaptation during strength training in young adults. Medicine and Science in Sports and Exercise, 39(7), pp.1147–1152.

Vatsa, A., Mizuno, D., Smit, T. H., Schmidt, C.F., MacKintosh, F. C., Klein-Nulend, J., 2008. Osteocyte morphology in fibula and calvaria — Is there a role for mechanosensing? Bone, 43(3), pp.452–458.

Velleman, S. G. 1999. The role of the extracellular matrix in skeletal muscle development. Poultry science, 78(5), 778-784.

Vicente-Manzanares, M., Ma, X., Adelstein, R. S., and Horwitz, A. R. 2009. Non-muscle myosin II takes centre stage in cell adhesion and migration. Nat Rev Mol Cell Biol, 10(11), 778–790.

Vickerton, P., Jarvis, J. C., Gallagher, J. A., Akhtar, R., Sutherland, H., Jeffery, N., 2014. Morphological and histological adaptation of muscle and bone to loading induced by repetitive activation of muscle. Proceedings of the Royal Society B: Biological Sciences, 281(1788).

Wagner, E.B., Granzella, N. P., Saito, H., Newman, D. J., Young, L.R., Bouxsein, M. L., 2010. Partial weight suspension: a novel murine model for investigating adaptation to reduced musculoskeletal loading. Journal of Applied Physiology, 109(2), pp.350–357.

Wang, M., VanHouten, J.N., Nasiri, A. R., Tommasini, S. M., Broadus, A., 2014. Periosteal PTHrP regulates cortical bone modeling during linear growth in mice. Journal of Anatomy, 225(1), pp.71–82.

Warner, S.E., Sanford, D. A., Becker, B.A., Bain, S. D., Srinivasan, S., Gross, T. S., 2006. Botox induced muscle paralysis rapidly degrades bone. Bone, 38(2), pp.257–264.

Weisbecker, V., 2012. Distortion in formalin-fixed brains: using geometric morphometrics to quantify the worst-case scenario in mice. Brain Structure and Function, 217(2), pp.677–685. Available at: http://dx.doi.org/10.1007/s00429-011-0366-1.

Weninger, W.J., Geyer, S. H., Mohun, T. J., Rasskin-Gutman, D., Matsui, T., Ribeiro, I., Costa L., Izpisua-Belmonte, J. C., Muller, G. B., 2006. High-resolution episcopic microscopy: a rapid technique for high detailed 3D analysis of gene

activity in the context of tissue architecture and morphology. Anat Embryol (Berl), 211, pp.213 – 21.

Westerblad, H., Bruton, J.D. and Katz, A., 2010. Skeletal muscle: Energy metabolism, fiber types, fatigue and adaptability. Experimental Cell Research, 316(18), pp.3093–3099.

Whiting, W.C. and Rugg, S., 2006. Dynatomy: dynamic human anatomy, Human Kinetics 1.

Wick, M.R., 2012. Histochemistry as a tool in morphological analysis: a historical review. Annals of Diagnostic Pathology, 16(1), pp.71–78.

Wicks, K.L. and Hood, D.A., 1991. Mitochondrial adaptations in denervated muscle: relationship to muscle performance. American Journal of Physiology-Cell Physiology, 260(4), pp.C841–C850.

Wigston, D. J., 1989. Remodeling of neuromuscular junctions in adult mouse soleus. The Journal of Neuroscience, 9(2), 639–647.

Wiley, D.F., Amenta, N., Alcantara, D. A., Ghosh, D., Kil, Y. J., Delson, E., Harcourt-Smith, W., Rohlf, F. J., St John, K., Hamann, B., 2005. Evolutionary morphing. In Visualization, 2005. VIS 05. IEEE. pp. 431–438.

Williams, P.E. and Goldspink, G., 1978. Changes in sarcomere length and physiological properties in immobilized muscle. Journal of Anatomy, 127(Pt 3), p.459.

Wilson, J. W., 2002. Blood supply to developing, mature and healing bone. Bone in clinical orthopaedics, 40-45.

Wolff J. 1892. Das gesetz der transformation der knochen. DMW-Deutsche Medizinische Wochenschrift 19:1222-1224.

Wolfram, U., Wilke, H.-J. and Zysset, P.K., 2010. Transverse isotropic elastic properties of vertebral trabecular bone matrix measured using microindentation under dry conditions (effects of age, gender, and vertebral level). Journal of Mechanics in Medicine and Biology, 10(01), pp.139–150.

Wolfram, U., Wilke, H.-J. and Zysset, P.K., 2010. Rehydration of vertebral trabecular bone: Influences on its anisotropy, its stiffness and the indentation work with a view to age, gender and vertebral level. Bone, 46(2), pp.348–354.

Wu, B., Zhang, C., Chen, B., Zhang, L., Dai, R., Wu, X., Jiang, Y., Liao, E., 2013. Self-Repair of Rat Cortical Bone Microdamage after Fatigue Loading In Vivo. International Journal of Endocrinology, 2013, p.8.

Xie, L., Jacobson, J. M., Choi, E. S., Busa, B., Donahue, L. R., Miller, L. M., Rubin, C. T., Judex, S., 2006. Low-level mechanical vibrations can influence bone resorption and bone formation in the growing skeleton. Bone, 39(5), pp.1059–1066.

Yang, L., Zhang, P., Liu, S., Samala, P., Su, M., Yokota, H., 2007. Measurement of Strain Distributions in Mouse Femora with 3D-Digital Speckle Pattern Interferometry. Optics and lasers in engineering, 45(8), pp.843–851.

Yang, J., Pham, S.M. and Crabbe, D.L., 2014. Effects of oestrogen deficiency on rat mandibular and tibial microarchitecture.

Yasui, N., Sato, M., Ochi, T., Kimura, T., Kawahata, H., Kitamura, Y., Nomura, S., 1997. Three modes of ossification during distraction osteogenesis in the rat. The Journal of bone and joint surgery. British volume, 79(5), pp.824–830.

You, J., Yellowley, C. E., Donahue, H. J., Zhang, Y., Chen, Q., Jacobs, C. R., 2000. Substrate deformation levels associated with routine physical activity are less stimulatory to bone cells relative to loading-induced oscillatory fluid flow. Journal of biomechanical engineering, 122(4), pp.387–393.

Young, J.Z., 1935. Osmotic pressure of fixing solutions. Nature, 135, pp.823–824.

Yue, S., Lee, P. D., Poologasundarampillai, G., Yao, Z., Rockett, P., Devlin, A.H., Mitchell, C. A., Konerding, M.A., Jones, J. R., 2010. Synchrotron X-ray microtomography for assessment of bone tissue scaffolds. In Journal of Materials Science: Materials in Medicine. pp. 847–853.

Zannoni, C., Mantovani, R. and Viceconti, M., 1999. Material properties assignment to finite element models of bone structures: a new method. Medical Engineering and Physics, 20(10), pp.735–740.

Zaslansky, P., Riesemeier, H., Segev, G., Atkins, A., Shahar, R., 2013. Unremodeled endochondral bone is a major architectural component of the cortical bone of the rat (Rattus norvegicus). Journal of Structural Biology.

Zelditch, M.L., 2004. Geometric morphometrics for biologists: a primer.

Zelzer, E., McLean, W., Ng, Y-S., Fukai, N., Reginato, A. M., Lovejoy, S., D'Amore, P. A., Olsen, B. R., 2002. Skeletal defects in VEGF120/120 mice reveal multiple roles for VEGF in skeletogenesis. Development, 129(8), pp.1893–1904.

Zhang, C. and Gao, Y., Effects of Aging on the Lateral Transmission of Force in Rat Skeletal Muscle. Journal of Biomechanics, 47 (5) pp, 944-948.

Zhou, J., Koike, Y., Uhthoff, H.K., Trudel, G., 2007. Quantitative histology and ultrastructure fail to explain weakness of immobilized rabbit Achilles' tendons. Archives of physical medicine and rehabilitation, 88(9), pp.1177–84.

Zhou, S., Cui, Z. and Urban, J.P.G., 2004. Factors influencing the oxygen concentration gradient from the synovial surface of articular cartilage to the cartilage-bone interface: a modeling study. Arthritis and rheumatism, 50(12), pp.3915–24.

Zhu, J., Ma, H. T., Zhao, X., Ren, R., Xing, X., Griffth, J. F., Leung, P-C., 2013. Finite element analysis of trabecular bone with bone marrow fat. In 2013 IEEE International Conference of IEEE Region 10 (TENCON 2013). IEEE, pp. 1–4.

Zioupos, P., Currey, J.D. and Casinos, A., 2000. Exploring the Effects of Hypermineralisation in Bone Tissue by Using an Extreme Biological Example. Connective Tissue Research, 41(3), pp.229–248.

Appendices

Appendix 1: Microvolumeter data

Ball-bearing volume measured with microvolumeter compared with calculated volumes.

Ball-bearing diameter/mm	6	7	8	9	9.53
Volume measured (ml)	0.11	0.175	0.275	0.38	0.44
	0.12	0.165	0.27	0.37	0.45
	0.12	0.18	0.275	0.39	0.455
	0.12	0.18	0.28	0.39	0.46
	0.11	0.17	0.275	0.37	0.45
Average	0.116	0.174	0.275	0.38	0.451
Actual Volume (ml)	0.113	0.179	0.268	0.381	0.453
Difference (ml)	0.003	0.005	0.007	0.001	0.002

Appendix 2: Histology solutions and protocols

Slide subbing protocol

- 400ml distilled H_2O
- 0.8g type B bovine gelatine
- 0.08g Chromic Potassium Sulphate

Method

Dissolve gelatine in H_2O on hotplate at approximately 40°C. Add the chromic potassium sulphate and mix until dissolved. Do not exceed 50°C. Use the solution the same day. Rinse slides with absolute ethanol, and dry for 5 minutes. Coat the slides in subbing solution and leave to dry on a rack. Leave slides to dry overnight.

Haematoxylin and Eosin staining protocol

Stock Solutions

- Ehrlich's Haematoxylin (ripened)
- Eosin (1%)
- Hydrochloric acid conc. (HCl)
- 70% Ethanol (70ml EtOH + 30ml dH_20)

Working solutions

- 1% Acid Alcohol
- 1ml HCl into 99ml 70% EtOH

Method

Dewax paraffin sections in xylene (x2; 3-5 min) and hydrate through graded alcohols to water (1 min each). Place slides in haematoxylin solution (2-3 mins). Wash in running warm tap water (3 min) and then very quickly dip in 1% acid to remove excess haematoxylin (15 s). Follow this with a vigorous wash in running tap water (5 min). Place the slides in Eosin solution (1-2 min). Rinse the slides in running tap water until water runs clear, and then dehydrate the slides through ascending alcohols (50%, 70%, 100%, 100%; 2 min each). Clear the slides in xylene (2x 3 min each) and mount with DPX.

NADH dehydrogenase staining protocol

Solutions

Tetrazolium solution

0.2 M	Tris buffer, pH 7.4	100ml
1mg/ml	Nitroblue tetrazolium	100mg

(TRIS buffer: 6.61g TRIZMA HCl to 0.97g TRIZMA base in 250ml distilled water)

Method

Add NADH to the defrosted tetrazolium solution (1mg/ml). Pipette solution onto thawed sections (can circle with silicone pen) and incubate at 37^{o}C for 30 min. Dehydrate through ascending grades of alcohol to xylene and mount in DPX.

Tunnel & Hart Stain for fibre type determination staining protocol

Solutions

Pre-incubating solution (100mls)

0.7508g (0.1M) Glycine

1.0g (1%) $CaCl_2$ (anhydrous)

10ml (3.7%) Formaldehyde (fresh) Sigma F-1635 pH to 7.0

ATP incubation solution (100mls)

0.37g (50mM) KCl

0.152g (2.7mM) ATP

6.7ml (100mM) 1.5M Sigma buffer

1.8mls (18mM) 1M $CaCl_2$ pH to 9.4

SIGMA BUFFER (1.5M stock) Aldrich A6,518-2

ALKALI WASH (100mM sigma buffer)

33.3 mls of 1.5M STOCK to 500 mls pH to 9.4

Tris rinse solution (1 litre)

12.1g (100mM) TRIS

1.998g (18mM) $CaCl_2$ (anhydrous)

Stir overnight then pH next day pH to 7.8

Calcium wash (1% $CaCl_2$) 10g (anhydrous) in 1000mls

Cobalt chloride (2%): 2.48g in 100 mls

Ammonium sulphide (1%): 1 ml in 100 mls

Method

Switch on water bath 37oc and thaw slides for 20 mins. In this time make up pre-incubating and ATP solutions. Incubate thawed sections for 7.5 mins in pre-incubation solution. Rinse 5x in distilled water, and then rinse 2 x 1min in TRIS rinse buffer. Incubate the slides in ATP solution for 50 min at 37°C, and agitate occasionally throughout this time.

Following incubation rinse slides three times for 30s in 1% CaCl2 , and then immerse slides for 3 min in CoCl2 solution. Rinse slides in distilled water, followed by alkali was 4 times for 30 seconds. Then immerse slides for 3 min in 1% Ammonium sulphide solution, and then wash in running tap water, followed by distilled water. Drain slides, dehydrate with ascending alcohols and mount with DPX.

Safranin-O staining protocol

Solutions

- Ehrlich's Haematoxylin (ripened)
- 70% Ethanol (70ml EtOH + 30ml dH_20)
- 1ml HCl into 99ml 70% EtOH (1% acid alcohol)

- Xylene
- Fast green (0.01%)
- Sarfranin O (0.1%)

Method

Dewax the slides by emersion in xylene for 5 minutes, repeat with a second container of xylene and hydrate through graded alcohols to water (1 min each). Place slides in haematoxylin solution (2-3 mins). Wash in running warm tap water (3 min) and then very quickly dip in 1% acid to remove excess haematoxylin (15 s). Rinse slides in running tap water for 5 mins. Immerse slides in 0.01% Fast green for 3 mins, and follow with 1% acetic acid for 30 seconds, then 0.1% safranin O for 30 mins. Immerse slides in running tap water and dehydrate the slides through ascending alcohols (50%, 70%, 100%, 100%; 2 min each). Clear the slides in xylene (2x 3 min each) and mount with DPX.

Appendix 3: Bone and muscle measurements following electrical muscle stimulation

Stimulated tibialis anterior muscle							
muscle fibre type	muscle fibre area (μm^2)	muscle fibre type	muscle fibre area (μm^2)	muscle fibre type	muscle fibre area (μm^2)	muscle fibre type	muscle fibre area (μm^2)
1	257.075	1	255.625	1	161.325	1	206.1
1	250.25	1	240.275	1	249.925	1	116.6
1	337.725	1	216.2	1	189.75	1	172.1
1	278.825	1	293.85	1	150.675	1	147.3
1	369.475	1	250.225	1	157.675	1	134
1	310.3	1	425.425	2a	258.125	1	148
1	321.8	1	284.825	2a	201.125	1	195.6
1	246.9	1	240.875	2a	317.775	1	208.1
1	276.425	1	190.125	2a	217.6	1	168.6
1	215.2	1	380.75	2a	288.775	1	173.7
1	177.825	1	281.575	2a	261.175	1	173.7
1	246.525	1	162.725	2a	348.125	1	76.9
1	243.8	1	218.325	2a	316.9	1	133.4
1	311.325	1	250.65	2a	276.95	1	138.7
1	428.925	1	178.35	2a	299.5	1	229.7
1	230.7	1	248.175	2a	284.275	1	220.7
1	217.4	1	279.8	2a	224.125	1	138.2
1	249.3	1	379.725	2a	318	1	216.4
1	191.95	1	179.1	2a	203	2a	228
1	212.625	1	321.3	2a	342.5	2a	343.3
1	243.825	1	149.525	2a	279.425	2a	308.5
1	244	1	369.975	2a	264.15	2a	361.2
1	302.475	1	495.75	2a	293.05	2a	303.6
1	248.025	1	298.2	2a	191.575	2a	321.6
1	405.675	1	343.925	2a	309.875	2a	302.2
1	283.675	1	335.025	2a	271.75	2a	268.5
1	217.075	1	294.225	2a	437.825	2a	344.2
1	235.65	1	388.9	2a	298.925	2a	340.3
1	270.775	1	220.95	2a	294.925	2a	326.3
1	418.3	1	334.775	2a	148.3	2a	245.9
1	192.125	1	249.075	2a	234.45	2a	337
1	198	2a	363.025	2a	246.425	2a	170.8
1	219.825	2a	167.8	2a	167.95	2a	330.8
1	416.425	2a	270.775	2a	270.125	2a	256.5
1	335.25	2a	332.85	2a	270.85	2a	240.9
1	273.325	2a	174.1	2a	286.85	2a	321.5

1	393.3	2a	391.5	2a	279.325	2a	317.9
1	326.425	2a	207.95	2a	313.3	2a	330.8
1	312.75	2a	218.775	2a	368.2	2a	296.2
1	274.575	2a	283.25	2a	226.45	2a	264.5
1	341.25	2a	109.65	2a	363.075	2a	314.5
1	233.825	2a	225.2	2a	220.175	2a	384.8
1	370.225	2a	332.6	2a	379.575	2a	235.6
1	282	2a	324.625	2a	456.3	2a	271.4
1	308.925	2a	279.125	2a	401.025	2a	389.5
1	311.675	2a	206.15	2a	198.75	2a	494.7
2a	340.45	2a	173	2a	278.625	2a	366.3
2a	257.4	2a	176.2	2a	430.975	2a	216.6
2a	359.1	2a	179.775	2a	326.625	2a	259.7
2a	210.725	2a	156.475	2a	290.2	2a	199.6
2a	204.675	2a	255.05	2a	351.9	2a	427.3
2a	218.35	2a	95.9	2a	349.65	2a	302.9
2a	332.75	2a	268.075	2a	320.05	2a	180.3
2a	379.95	2a	178.975	2a	366.6	2a	322.1
2a	212.1	2a	269.3	2a	377.625	2a	250.9
2a	131.375	2a	396.075	2a	248.725	2a	346.6
2a	401	2a	382.95	2a	297.4	2a	319.1
2a	402.45	2a	338.325	2a	256	2a	356
2a	189.9	2a	276.675	2a	258.9	2a	237.6
2a	147.425	2a	189.575	2a	309.575	2a	315.3
2a	377.775	2a	175.875	2a	241.625	2a	261.4
2a	257.625	2a	387.25	2a	400.625	2a	211.8
2a	278.875	2a	314.85	2a	289.175	2a	272.2
2a	175.875	2a	360	2a	311.85	2a	489.9
2a	329.425	2a	374.95	2a	367.475	2a	331.4
2a	394.6	2a	328.25	2a	339.225	2a	235.5
2a	178.025	2a	250.875	2a	323.325	2a	328.1
2a	136.875	2a	332.25	2a	345.975	2a	401.6
2a	385.65	2a	311.3	2a	386.1	2a	332.4
2a	359.625	2a	338.65	2a	257.95	2a	163.2
2a	506.1	2a	266.225	2a	343.625	2a	284
2a	388	2a	282.9	2a	273.975	2a	459.6
2a	298.55	2a	390.325	2a	353.7	2a	303
2a	385.275	2a	402.75	2a	287.4	2a	348.9
2a	264.975	2a	385.5	2a	231	2a	214
2a	339.775	2a	288.45	2a	168.925	2a	285.5
2a	367.85	2a	268.3	2a	391.35	2a	266.1
2a	408.3	2a	304.6	2a	373.35	2a	466.3
2a	372.475	2a	391.675	2a	235.75	2a	342.5

2a	404.45	2a	267.825	2a	251.2	2a	271.4
2a	350.425	2a	318.8	2a	351.525	2a	316.3
2a	350.525	2a	98.35	2a	299.875	2a	170.6
2a	251.55	2a	315.275	2a	279.7	2a	303.1
2a	325.7	2a	240.525	2a	310.45	2a	272.6
2a	273.675	2a	277.6	2a	272.55	2a	267.2
2a	238.575	2a	340.625	2a	354.975	2a	248
2a	317.075	2a	290.7	2a	351.45	2a	281.8
2a	373.55	2a	348	2a	273.7	2a	329.3
2a	429.075	2a	357.05	2a	333.55	2a	246.5
2a	398.975	2a	345.075	2a	245.475	2a	265.5
2a	223.4	2a	285.575	2a	287.3	2a	231
2a	382.575	2a	308.775	2a	178.75	2a	497.9
2a	289.8	2a	344.9	2a	397.525	2a	338.7
2a	231.75	2a	401.7	2a	240.975	2a	221.1
2a	321.95	2a	270.875	2a	316.075	2a	429.7
2a	320.475	2a	332.175	2a	234.725	2a	266.8
2a	245.625	2a	188.15	2a	190.35	2a	266.8
2a	290.625	2a	405.2	2a	312	2a	283.4
2a	182.55	2a	343.5	2a	244.9	2a	252.3
2a	239.725	2a	396.3	2a	175.725	2a	277.1
2a	192.525	2a	384.375	2a	339.45	2a	358.2
2a	168.375	2a	161.775	2a	257.925	2a	341.4
2a	310.425	2a	240.825	2a	269.1	2a	264.4
2a	385.5	2a	318.525	2a	172.35	2a	316.7
2a	178.3	2a	183.5	2a	248.95	2a	350.9
2a	336.125	2a	416	2a	239.325	2a	351.8
2a	251.1	2a	300.725	2a	339.15	2a	207
2a	230.825	2a	261.825	2a	254.825	2a	405.5
2a	265.775	2a	307.025	2a	169.65	2a	238.3
2a	142.375	2a	203.725	2a	236.45	2a	393.7
2a	320.1	2a	275.45	2a	294	2a	314.6
2a	247.65	2a	120.275	2a	305.875	2a	483.1
2a	306.075	2a	314.225	2a	305.875	2a	309.2
2a	305.825	2a	252.25	2a	250.8	2a	275
2a	428.625	2a	263.5	2a	302.65	2a	373.1
2a	345.45	2a	303.8	2a	304.875	2a	245.9
2a	374.05	2a	274.5	2a	240.75	2a	349.6
2a	128.45	2a	254.325	2a	330.05	2a	292.7
2a	494.475	2a	419.7	2a	264.674	2a	298.1
2a	397.6	2a	251.525	2a	307.425	2a	300.7
2a	201.225	2a	182.175	2a	265.3	2a	375.5
2b	457.6	2a	328.425	2a	289.425	2a	359.4

2b	392.25	2a	325.425	2a	276.9	2a	305
2b	405.275	2a	196.85	2a	242.55	2a	274.1
2b	428.575	2a	300.825	2b	261.75	2a	292.5
2b	395.6	2a	182.75	2b	216.7	2a	273.8
2b	364.725	2a	417.85	2b	250.35	2a	310.8
2b	238.7	2a	318.325	2b	258.075	2a	377.3
2b	325.3	2a	218.85	2b	234.15	2b	229.7
2b	379.55	2a	330.925	2b	324.575	2b	135.2
2b	332.425	2a	163.7	2b	250.475	2b	182.8
2b	382.625	2a	202.15	2b	304.6	2b	191.5
2b	482.05	2b	283.3	2b	293.425	2b	210
2b	353.575	2b	276.375	2b	191.025	2b	353.8
2b	386.15	2b	309.225	2b	187.675	2b	314.3
2b	374.95	2b	296.575	2b	197.325	2b	214.7
2b	219.4	2b	231.45	2b	291.325	2b	214.7
2b	429.15	2b	341.325	2b	196.675	2b	387.8
2b	415.525	2b	255.05	2b	292.65	2b	267.9
2b	371.2	2b	168.925	2b	286.225	2b	328.2
2b	397.5	2b	102.125	2b	261.15	2b	383
2b	361.8	2b	275.725	2b	294.5	2b	241
2b	400.825	2b	268.725	2b	241.925	2b	300.4
2b	236.6	2b	279.225	2b	350.275	2b	168.8
2b	356.7	2b	338	2b	232.9	2b	182.9
2b	294.75	2b	268.175	2b	312.6	2b	249.9
2b	287.2	2b	308.6	2b	121.95	2b	247.4
2b	360.7	2b	334.425	2b	150.85	2b	514.9
2b	434.2	2b	305.325	2b	277.2	2b	191.6
2b	378.75	2b	303.075	2b	256.1	2b	199.1
2b	279.825	2b	250.65	2b	154.05	2b	244.6
2b	405.45	2b	333.35	2b	301.65	2b	227.1
2b	273.625	2b	435.9	2b	136.15	2b	157.4
2b	337.775	2b	307.2	2b	170.375	2b	318.7
2b	396.725	2b	311.35	2b	150.75	2b	181.7
2b	388.125	2b	220.525	2b	203.8	2b	280.4
2b	325.475	2b	291.225	2b	173.55	2b	274.2
2b	335.575	2b	324.375	2b	260.65	2b	343
2b	371.55	2b	265.55	2b	291.6	2b	170.9
2b	385.275	2b	260.15	2b	233.325	2b	221.9
2b	454.35	2b	282.675	2b	179.2	2b	326.6
2b	359.925	2b	315.375	2b	162.5	2b	292.2
2b	374.475	2b	276.9	2b	188.425	2b	201.2
2b	194.1	2b	253.95	2b	156.725	2b	249.9
2b	176.425	2b	316.275	2b	215.225	2b	279.4

2b	312.6	2b	343.35	2b	275.325	2b	209.6
2b	366.15	2b	238.025	2b	258.4	2b	170.4
2b	330.45	2b	338.1	2b	226.95	2b	152.9
2b	270.55	2b	417.25	2b	280.45	2b	286.4
2b	333.6	2b	234.225	2b	220.2	2b	319.2
2b	298.575	2b	306.95	2b	252.75	2b	241.5
2b	311.925	2b	239.25	2b	216.725	2b	267.6
2b	408.55	2b	249.525	2b	202.725	2b	191.1
2b	439.225	2b	298.4	2b	151.075	2b	272.2
2b	317.625	2b	315.425	2b	231.35	2b	328.8
2b	456.7	2b	196.5	2b	247.05	2b	271.1
2b	41.575	2b	298.125	2b	183.15	2b	261.1
2b	48.3	2b	265.175	2b	160	2b	235.6
2b	315.925	2b	217.2	2b	165	2b	314.2
2b	322.05	2b	264.575	2b	283.575	2b	238
2b	325.225	2b	233.925	2b	226.35	2b	162.2
2b	451.95	2b	293.375	2b	275.725	2b	349
2b	191.2	2b	311.75	2b	178.4	2b	273.2
2b	388.15	2b	232.7	2b	199.875	2b	410.5
2b	467.925	2b	315.8	2b	209.375	2b	367.6
2b	370.275	2b	407.475	2b	179.1	2b	236.3
2b	341.425	2b	271.65	2b	331.275	2b	240.3
2b	428.8	2b	273.025	2b	176.1	2b	241.3
2b	423.75	2b	349.55	2b	368.4	2b	203.9
2b	343.825	2b	343.25	2b	189.725	2b	151.9
2b	161.625	2b	271.45	2b	201.025	2b	258.9
2b	362.175	2b	348.925	2b	162.1	2b	168.8
2b	300.775	2b	323.75	2b	311.75	2b	279
2b	304.85	2b	222.025	2b	233.55	2b	245.4
2b	412.725	2b	330.475	2b	220.525	2b	202.5
2b	329.05	2b	275.125	2b	135.3	2b	310.6
2b	438.9	2b	290.875	2b	195.075	2b	296.5
2b	412.1	2b	366.8	2b	340.8	2b	248.6
2b	269.775	2b	280.375	2b	231.625	2b	254.2
2b	442.05	2b	326.325	2b	262.575	2b	216.8
2b	375.05	2b	312.975	2b	128.325	2b	216.8

Contra-lateral control tibialis anterior muscle							
muscle fibre type	**muscle fibre area (μm^2)**	**muscle fibre type**	**muscle fibre area (μm^2)**	**muscle fibre type**	**muscle fibre area (μm^2)**	**muscle fibre type**	**muscle fibre area (μm^2)**
1	249.325	1	214.275	1	144.525	1	134.075
1	145.875	1	133.675	1	189.125	1	179.525
1	272.5	1	158	1	132.725	1	186.525
1	213.525	1	158.9	1	235.775	1	167.225
1	168.225	1	128.225	1	237.65	1	93.275
1	183.475	1	196.1	1	132.475	2a	377.475
1	175.5	1	205.275	1	162.6	2a	315.85
1	240.825	1	222.075	1	211.625	2a	289.875
2a	279.75	1	171.925	1	136.625	2a	294.45
2a	260.025	1	163.05	1	233.65	2a	287.925
2a	280.875	1	159.675	1	194.175	2a	238.55
2a	320.275	1	181.7	1	253.9	2a	251.4
2a	273.425	1	186.525	1	262.85	2a	203.55
2a	165.425	1	275.225	1	321.45	2a	339.025
2a	316.1	1	182.6	1	270.45	2a	392.35
2a	251.3	1	169.275	1	220.5	2a	334.475
2a	115.525	1	267.425	1	142.25	2a	228.925
2a	272.45	1	148.35	1	254.7	2a	238.575
2a	267.225	1	214.125	1	136.05	2a	375.675
2a	181.55	1	194.7	1	143.2	2a	341.775
2a	213.55	1	235.5	1	164.575	2a	287.35
2a	243.85	1	202.275	2a	267.7	2a	247.75
2a	242.525	1	261.7	2a	369.05	2a	284.375
2a	204.075	2a	232.7	2a	256.45	2a	291.525
2a	169.525	2a	197.65	2a	165.65	2a	193.575
2a	180.575	2a	280.35	2a	203.925	2a	182.55
2a	176.4	2a	243.1	2a	161.65	2a	359.4
2a	194.7	2a	265.525	2a	283.925	2a	257.425
2a	224.175	2a	255.6	2a	183.7	2a	263.325
2a	206.875	2a	191.075	2a	254.075	2a	293.375
2a	184.275	2a	209.125	2a	216.925	2a	179.8
2a	186.975	2a	293.8	2a	180.325	2a	286.35
2a	217.4	2a	159.25	2a	214.025	2a	392.325
2a	137.775	2a	189.6	2a	252.525	2a	266.7
2a	156.35	2a	256.5	2a	247.575	2a	204.325
2a	203.4	2a	250.325	2a	251.025	2a	349.8
2a	225.925	2a	370.7	2a	222.875	2a	343.45
2a	428.25	2a	260.25	2a	211.075	2a	283.8
2a	214.8	2a	254.3	2a	163.775	2a	396.025

2a	116.3	2a	168.075	2a	122.675	2a	396.025
2a	161.25	2a	332.725	2a	214.3	2a	221.75
2a	203.85	2a	332.725	2a	139.275	2a	295.125
2a	82.925	2a	323.45	2a	312.6	2a	259.575
2a	281.125	2a	158.225	2a	145.65	2a	253.125
2a	201.45	2a	255.725	2a	266.55	2a	308.95
2a	126.075	2a	309.55	2a	270.375	2a	203.6
2a	141	2a	474.475	2a	283.725	2a	253.5
2a	237.5	2a	346.575	2a	104.525	2a	187.65
2a	125.475	2a	257.5	2a	210.225	2a	350.45
2a	404.325	2a	184	2a	279.775	2a	335.35
2a	273.55	2a	385.7	2a	266.025	2a	221.95
2a	158.35	2a	402.675	2a	214.6	2a	245.05
2a	234.3	2a	337.35	2a	303.825	2a	278.025
2a	130.2	2a	286.425	2a	291.025	2a	369.025
2a	193.975	2a	243.7	2a	221.4	2a	283.5
2a	250.95	2a	206.675	2a	295.575	2a	246.325
2a	311.15	2a	190.575	2a	243.925	2a	248.4
2a	415.825	2a	200.55	2a	168.45	2a	286.625
2a	463.325	2a	343.975	2a	107.1	2a	246.9
2a	101.3	2a	197.925	2a	304.975	2a	217.125
2a	314.675	2a	254.025	2a	258.6	2a	407.5
2a	136.575	2a	243.6	2a	201.15	2a	269.775
2a	213.35	2a	248.7	2a	245.775	2a	270.825
2a	144.525	2a	318.125	2a	229.95	2a	226.95
2a	194.925	2a	235.2	2a	193.275	2a	282.475
2a	181.7	2a	180.825	2a	284.625	2a	233.35
2a	127.8	2a	274.15	2a	312.15	2a	235.6
2a	255.825	2a	220.275	2a	210.9	2a	202.125
2a	149.7	2a	315.225	2a	330.3	2a	242.475
2a	231.4	2a	447.7	2a	181.95	2a	317.35
2a	202.5	2a	336.15	2a	95.925	2a	372.7
2a	235.25	2a	141.725	2a	178.65	2a	364.125
2a	282.8	2a	399.375	2a	264.55	2a	271.075
2a	273.6	2a	177.25	2a	367.2	2a	263.85
2a	167.175	2a	454.05	2a	263.525	2a	261.375
2a	195.9	2a	232.4	2a	334.05	2a	281.025
2a	139.425	2a	251.1	2a	205.875	2a	338.85
2a	241.2	2a	207.3	2a	299.475	2a	340.1
2a	200	2a	232.575	2a	243.6	2a	214.525
2a	264.975	2a	132.55	2a	266.075	2a	157.825
2a	312.825	2a	332.775	2a	357.525	2a	266.8
2a	126.35	2a	301.075	2a	270.4	2a	217.125

2a	211.625	2a	358.875	2a	194.4	2a	208.575
2a	236.85	2a	205.575	2a	245.025	2a	167.025
2a	177.325	2a	279.325	2a	262.575	2a	286.475
2a	329.175	2a	277.975	2a	232.05	2a	92.625
2a	288.4	2a	430.425	2a	278.925	2a	267.525
2a	315.725	2a	241.425	2a	268.7	2a	242
2a	202.55	2a	183.075	2a	235.125	2a	254.25
2a	140.725	2a	346.55	2a	269.725	2a	132.225
2b	384.425	2a	428.55	2a	92.025	2a	180.125
2b	413.5	2a	328.625	2a	214.325	2a	155.1
2b	386.4	2a	317.475	2a	262.8	2a	257.625
2b	388.15	2a	408.5	2a	189.825	2a	141.375
2b	266.725	2a	257.525	2a	207.425	2a	333.325
2b	419.275	2a	245.725	2a	354.825	2a	174.7
2b	465.9	2a	202.425	2a	156.075	2a	199.075
2b	306.65	2a	260.7	2a	256.975	2a	152.85
2b	371.875	2a	314.125	2a	268.3	2a	190.5
2b	281.275	2a	221.4	2a	209.8	2b	246.525
2b	308.575	2a	354.325	2a	281.7	2b	208.925
2b	282.825	2a	369.375	2a	329.625	2b	89.1
2b	351.175	2a	319	2a	198.025	2b	281.325
2b	351.575	2a	233.8	2a	213.15	2b	181.85
2b	466.825	2a	191.825	2a	341.325	2b	217.35
2b	499.025	2a	313.2	2a	201.45	2b	134.325
2b	122.375	2a	156	2a	298.95	2b	184.125
2b	321.475	2a	182.95	2a	286.275	2b	221.55
2b	172.225	2a	342.375	2a	177.525	2b	324.225
2b	239.575	2a	233.7	2a	296.875	2b	130.125
2b	331.3	2a	408.6	2a	262.125	2b	303.15
2b	389.925	2a	295.05	2b	259.15	2b	191.975
2b	380.625	2a	379.525	2b	291.35	2b	255.075
2b	164.35	2a	240.7	2b	267.125	2b	167.725
2b	408.35	2a	199.5	2b	247.825	2b	167.325
2b	300.925	2a	409	2b	222.175	2b	145.475
2b	260.575	2a	221.725	2b	278.7	2b	241.35
2b	452.525	2a	192.15	2b	304.425	2b	310.825
2b	507	2b	126.475	2b	263.275	2b	235.95
2b	203.475	2b	294.45	2b	219.575	2b	249.725
2b	410.925	2b	459.55	2b	179.725	2b	167.775
2b	350.625	2b	282.5	2b	232.675	2b	326.925
2b	316.525	2b	470.35	2b	353.775	2b	149.9
2b	281.5	2b	428.8	2b	219.6	2b	266.725
2b	330.9	2b	352.1	2b	348.725	2b	152.675

2b	391.2	2b	344.25	2b	146.025	2b	209.925
2b	455.775	2b	361.225	2b	346.975	2b	252.15
2b	364.55	2b	396.525	2b	296.225	2b	151.5
2b	364.55	2b	433.4	2b	234.65	2b	275.425
2b	295.725	2b	357.925	2b	228.55	2b	146.325
2b	405.75	2b	304.05	2b	223.175	2b	383.125
2b	237.175	2b	376.975	2b	276.1	2b	403.5
2b	487.2	2b	239.05	2b	312.75	2b	255.525
2b	576.525	2b	383.025	2b	222.325	2b	197.25
2b	398.9	2b	179.15	2b	279.95	2b	228.025
2b	335.625	2b	427.55	2b	260.85	2b	306.3
2b	305.925	2b	484.825	2b	307.45	2b	266.75
2b	514.05	2b	162.6	2b	220.575	2b	228.15
2b	328.875	2b	383.2	2b	184.125	2b	151.625
2b	196.175	2b	270.6	2b	275.525	2b	223.2
2b	222.3	2b	466.8	2b	248.4	2b	272.2
2b	345.075	2b	416.725	2b	284.1	2b	281.6
2b	248.625	2b	430.325	2b	342.875	2b	317.175
2b	318.175	2b	253.575	2b	266.95	2b	193.7
2b	417.75	2b	319.575	2b	261.625	2b	183
2b	304.725	2b	416.1	2b	319.2	2b	167.6
2b	288.55	2b	160.8	2b	259.275	2b	247.6
2b	336.3	2b	432.025	2b	348.9	2b	196.2
2b	480.05	2b	175.5	2b	273.675	2b	251
2b	372.25	2b	437.2	2b	343.275	2b	207
2b	272.925	2b	447.15	2b	328.35	2b	232.9
2b	336.9	2b	396	2b	316.5	2b	212.425
2b	383.3	2b	142.725	2b	292.4	2b	295.975
2b	244.9	2b	475.725	2b	224.525	2b	231.15
2b	232.6	2b	353.325	2b	290.475	2b	226.75
2b	375.125	2b	449.925	2b	180.4	2b	285.15
2b	330.625	2b	371.1	2b	285.675	2b	282.4
2b	591.525	2b	308.025	2b	255.45	2b	336.05
2b	350.65	2b	450.25	2b	340.3	2b	156.9
2b	340.8	2b	318.9	2b	277.125	2b	163.55
2b	558.925	2b	517.8	2b	190.275	2b	193.775
2b	318.8	2b	414.65	2b	449.85	2b	259.2
2b	307.05	2b	463.375	2b	436.675	2b	176.1
2b	344.3	2b	172.9	2b	257.625	2b	189.075
2b	338.45	2b	466.15	2b	302.7	2b	257.575
2b	404.7	2b	357.45	2b	341.4	2b	207.775
2b	282.275	2b	444.575	2b	228.4	2b	330.6
2b	232.45	2b	408.7	2b	350.325	2b	328.775

2b	298.95	2b	455.175	2b	200.525	2b	278.125
2b	310.125	2b	394.2	2b	395.4	2b	243.75
2b	343.05	2b	203.025	2b	321.75	2b	250.6
2b	409.35	2b	343.5	2b	366	2b	252
2b	394.3	2b	356.4	2b	369.9	2b	255.45
2b	400.125	2b	484.15	2b	341.025	2b	148.475
2b	321.4	2b	448.2	2b	301.525	2b	418.575
2b	499.875	2b	366.7	2b	320.4	2b	207.975
2b	251.575	2b	374.325	2b	304.575	2b	304.925
2b	265.05	2b	177	2b	360.125	2b	257.95
2b	393.5	2b	410.025	2b	284.975	2b	337.35
2b	210.075	2b	354.6	2b	395.35	2b	226.05
2b	428.7	2b	449.6	2b	351.15	2b	189.775
2b	432.75	2b	388.15	2b	326.85	2b	367.875
2b	488.025	2b	325.25	2b	343.5	2b	310.8
2b	563.05	2b	390.225	2b	132.45	2b	409.275
2b	324.45	2b	365.95	2b	363.075	2b	240.825
2b	410.975	2b	438.725	2b	174.025	2b	231.15
2b	390.625	2b	226.425	2b	279.975	2b	320.95
2b	424.125	2b	276.05	2b	331.725	2b	456.75
2b	397.5	2b	370.9	2b	290.675	2b	175.55
2b	248.475	2b	357.55	2b	153.225	2b	306
2b	477.9	2b	483.825	2b	291.675	2b	446.575
2b	273	2b	498.175	2b	277.275	2b	371.8
2b	408.675	2b	416.55	2b	180.375	2b	288.85
2b	349.625	2b	327.55	2b	332.95	2b	401.05
2b	343.25	2b	375.925	2b	329.6	2b	305.775
2b	270.15	2b	442.275	2b	279.725	2b	385.65
2b	395.5	2b	188.7	2b	320.55	2b	367.6
2b	448.775	2b	319.5	2b	371.475	2b	260.425
2b	591.375	2b	446.1	2b	255.3	2b	415.35
2b	295.025	2b	479.125	2b	349.45	2b	467.175
2b	341.125	2b	489.325	2b	349.45	2b	467.175

Cortical thickness, bone and muscle volumes

					Cortical thickness (mm)										Antero-distal region	
ID	Limb (R/L)	Stimulated (No, Yes)	TA volume (mm^3)	EDL volume (mm^3)	1	2	3	4	5	6	7	8	9	10	bone volume (mm^3)	bone area (mm^2)
rat1	L	yes	61.19	14.09	1.13	0.46	0.96	0.81	0.49	0.76	1.05	1.46	1.11	0.71	24.16	7.46
	R	no	83.03	20.08	1.08	0.56	0.86	0.95	0.75	0.80	0.82	0.76	0.69	0.68	16.58	5.12
rat2	L	yes	63.49	18.13	0.84	0.52	0.54	0.73	0.57	0.77	0.90	0.98	0.93	0.85		
	R	no	83.38	22.33	0.97	0.53	0.66	0.68	0.67	0.75	0.98	0.93	0.73	0.66		
rat3	L	yes	54.77	14.15	0.87	0.35	0.50	0.71	0.70	0.74	0.73	0.90	1.07	0.83	19.93	5.80
	R	no	81.54	18.01	0.88	0.36	0.57	0.78	0.79	0.85	0.79	0.83	0.74	0.71	16.03	4.84
rat4	L	yes	59.70	14.91	0.82	0.36	0.55	0.49	0.62	0.73	0.69	0.89	1.16	0.66	19.98	5.93
	R	no	69.39	16.60	0.87	0.38	0.40	0.53	0.60	0.72	0.78	0.78	0.60	0.60	15.73	4.61
rat5	L	yes	86.12	18.35	0.82	0.49	0.56	0.41	0.69	0.79	0.97	1.04	0.86	0.68		
	R	no	81.44	18.78	1.07	0.44	0.34	0.66	0.57	0.82	0.98	0.96	0.78	0.70		
rat6	L	yes	63.01	17.71	0.93	0.39	0.59	0.46	0.62	0.78	0.71	0.94	1.00	0.69		

	R	**no**	**83.25**	**21.33**	**1.08**	**0.38**	**0.60**	**0.36**	**0.78**	**0.79**	**0.78**	**0.82**	**0.68**	**0.77**		
rat7	**L**	**no**	**74.07**	**16.83**	**0.72**	**0.49**	**0.57**	**0.47**	**0.60**	**0.78**	**0.82**	**0.89**	**0.71**	**0.59**	**21.67**	**6.25**
	R	**no**	**76.12**	**17.44**	**0.98**	**0.47**	**0.61**	**0.45**	**0.57**	**0.80**	**0.86**	**0.93**	**0.73**	**0.68**	**17.47**	**5.22**
rat8	**L**	**no**	**88.71**	**20.66**	**0.99**	**0.38**	**0.53**	**0.43**	**0.74**	**0.81**	**0.79**	**0.97**	**0.73**	**0.69**		
	R	**no**	**92.40**	**20.68**	**0.93**	**0.35**	**0.60**	**0.43**	**0.75**	**0.76**	**0.87**	**0.86**	**0.80**	**0.78**		
rat9	**L**	**no**	**89.14**	**20.27**	**0.89**	**0.49**	**0.49**	**0.51**	**1.02**	**0.79**	**1.01**	**1.12**	**0.86**	**0.76**		
	R	**no**	**91.72**	**21.24**	**0.94**	**0.48**	**0.50**	**0.51**	**0.87**	**0.91**	**0.96**	**1.04**	**0.87**	**0.75**		

Bone mineral density values

	Left								Right						
	Site	pixel value 1	pixel value 2	pixel value 3	pixel value 4	pixel value 5	average	BMD (HPa conc.)	pixel value 1	pixel value 2	pixel value 3	pixel value 4	pixel value 5	average	BMD (HPa conc.)
Rat 1	1	78.6	80.3	82.6	84.3	86.1	82.4	413.8	74.2	76.3	78.7	81.4	84.1	78.9	385.5
	2	127.7	129.3	130.1	130.2	130.9	129.6	803.5	130.6	130.6	131.2	131.9	131.8	131.2	816.6
	3	127.0	125.5	124.7	124.8	125.0	125.4	768.5	127.9	124.6	120.4	118.3	117.3	121.7	738.0
	4	114.3	114.6	116.0	115.3	112.7	114.6	679.4	131.6	127.8	125.6	127.7	128.5	128.3	792.0
	5	160.0	159.4	158.7	157.6	157.1	158.6	1041.8	162.8	162.2	162.0	161.9	161.2	162.0	1070.4
	6	164.7	163.1	164.9	163.6	165.9	164.5	1090.6	168.7	168.1	172.1	172.2	171.9	170.6	1141.2
	7	159.9	159.8	159.2	158.7	158.3	159.2	1046.8	175.6	174.7	173.7	173.0	172.2	173.8	1167.8
	8	143.0	141.5	140.5	139.8	138.2	140.6	893.7	175.7	175.7	175.3	174.1	175.4	175.2	1179.5
	9	147.6	148.2	146.9	143.4	142.9	145.8	936.6	172.0	171.0	170.7	171.3	170.5	171.1	1145.4
	10	158.5	158.3	158.2	158.3	158.2	158.3	1039.7	161.5	160.1	158.1	160.9	160.1	160.1	1055.0
Rat	1	85.3	86.3	87.6	89.0	90.1	87.7	457.6	77.5	75.8	74.6	73.0	71.7	74.5	349.0

2	**2**	**135.5**	**136.0**	**136.7**	**136.5**	**134.6**	**135.9**	**854.8**	**140.9**	**140.6**	**140.3**	**139.5**	**138.7**	**140.0**	**889.0**
	3	**145.7**	**144.0**	**144.3**	**145.1**	**145.5**	**144.9**	**929.4**	**144.0**	**145.4**	**146.2**	**146.6**	**146.5**	**145.7**	**936.2**
	4	**135.5**	**136.9**	**138.8**	**140.7**	**140.9**	**138.6**	**877.1**	**152.2**	**151.7**	**150.1**	**148.9**	**148.6**	**150.3**	**973.6**
	5	**164.1**	**165.0**	**166.0**	**166.4**	**166.1**	**165.5**	**1099.2**	**172.4**	**171.6**	**170.2**	**168.3**	**171.1**	**170.7**	**1142.2**
	6	**172.4**	**172.3**	**171.4**	**170.1**	**168.6**	**170.9**	**1144.1**	**171.9**	**170.1**	**173.4**	**172.1**	**170.5**	**171.6**	**1149.5**
	7	**169.8**	**168.6**	**167.6**	**166.5**	**165.2**	**167.5**	**1116.0**	**177.0**	**175.5**	**174.8**	**173.9**	**172.2**	**174.7**	**1174.7**
	8	**176.3**	**175.6**	**174.6**	**174.1**	**173.6**	**174.8**	**1176.2**	**178.9**	**177.7**	**176.7**	**176.5**	**175.9**	**177.1**	**1195.1**
	9	**166.7**	**166.3**	**165.0**	**163.4**	**162.1**	**164.7**	**1092.2**	**167.9**	**168.5**	**167.8**	**166.6**	**169.4**	**168.0**	**1119.9**
	10	**152.6**	**152.4**	**152.4**	**150.9**	**147.8**	**151.2**	**981.2**	**161.9**	**161.5**	**161.0**	**160.2**	**159.7**	**160.9**	**1060.9**
Rat 3	**1**	**81.0**	**84.2**	**86.9**	**89.7**	**92.0**	**86.8**	**450.0**	**81.6**	**78.9**	**75.9**	**73.2**	**71.9**	**76.3**	**363.6**
	2	**124.0**	**125.7**	**127.5**	**129.1**	**130.7**	**127.4**	**784.8**	**128.4**	**128.1**	**127.6**	**128.4**	**129.1**	**128.3**	**792.7**
	3	**145.6**	**146.1**	**147.7**	**149.6**	**150.3**	**147.9**	**953.8**	**144.5**	**144.4**	**143.7**	**143.7**	**144.0**	**144.1**	**922.5**
	4	**128.8**	**129.8**	**129.6**	**138.2**	**138.3**	**132.9**	**830.7**	**121.8**	**122.6**	**122.1**	**120.8**	**119.7**	**121.4**	**735.3**
	5	**160.6**	**159.4**	**158.7**	**158.0**	**156.4**	**158.6**	**1042.3**	**159.2**	**158.3**	**156.9**	**155.3**	**154.1**	**156.7**	**1026.9**
	6	**173.8**	**173.3**	**172.0**	**169.7**	**175.9**	**173.0**	**1160.7**	**167.8**	**166.5**	**165.0**	**163.6**	**166.3**	**165.9**	**1102.0**

	7	176.4	175.2	173.5	180.4	180.1	177.2	1195.2	171.4	170.3	169.0	166.9	171.0	169.8	1134.2
	8	178.5	177.6	176.2	174.4	172.1	175.8	1183.9	174.6	174.1	172.9	173.9	173.2	173.7	1167.0
	9	165.7	163.8	162.2	160.1	157.8	161.9	1069.5	172.6	172.3	172.2	171.5	170.9	171.9	1151.8
	10	158.0	156.3	153.9	149.9	147.0	153.0	996.2	160.2	158.6	157.0	154.7	156.7	157.4	1032.8
Rat 4	1	82.9	84.0	85.0	78.3	74.5	80.9	402.0	83.4	80.0	76.1	71.8	67.2	75.7	358.6
	2	126.1	126.1	127.3	129.5	131.3	128.1	790.4	136.3	136.9	137.2	137.0	138.1	137.1	864.9
	3	147.4	148.8	149.8	150.1	150.1	149.2	965.0	142.1	142.7	143.6	144.8	146.0	143.8	920.5
	4	135.0	134.4	133.1	131.7	130.9	133.0	831.4	134.9	131.8	130.3	131.9	134.3	132.7	828.3
	5	160.3	158.5	157.4	157.0	156.6	157.9	1036.8	168.7	168.4	167.8	167.5	166.7	167.8	1118.1
	6	173.9	173.6	173.0	172.0	170.6	172.6	1157.7	174.7	174.2	172.9	171.4	170.1	172.6	1158.0
	7	175.2	174.4	174.2	174.0	173.3	174.2	1171.1	177.0	177.0	177.0	176.4	175.9	176.6	1191.0
	8	160.6	159.7	158.4	157.1	155.5	158.3	1039.4	181.3	181.2	180.4	179.4	179.3	180.3	1221.5
	9	113.1	112.8	114.9	114.3	113.0	113.6	671.4	173.4	173.1	172.6	172.1	172.0	172.6	1158.0
	10	162.4	162.7	162.8	162.4	162.3	162.5	1074.5	160.6	159.2	157.5	161.0	160.3	159.7	1051.2
Rat	1	63.1	65.5	67.7	70.0	73.0	67.9	294.2	66.6	70.3	73.1	75.8	78.4	72.8	335.2

5	**2**	**134.4**	**134.8**	**134.6**	**134.6**	**134.5**	**134.6**	**844.2**	**132.2**	**132.1**	**132.5**	**133.3**	**133.1**	**132.6**	**828.3**
	3	**147.8**	**147.9**	**148.3**	**147.3**	**145.4**	**147.4**	**949.6**	**153.6**	**153.0**	**153.0**	**152.7**	**152.2**	**152.9**	**995.2**
	4	**140.0**	**139.6**	**139.3**	**139.3**	**139.9**	**139.6**	**885.8**	**133.8**	**134.0**	**133.6**	**133.3**	**132.6**	**133.5**	**834.9**
	5	**158.4**	**157.0**	**154.4**	**151.5**	**157.3**	**155.7**	**1018.3**	**160.3**	**159.6**	**158.3**	**162.2**	**161.4**	**160.4**	**1056.9**
	6	**170.8**	**170.0**	**169.4**	**168.6**	**167.3**	**169.2**	**1129.8**	**171.2**	**171.2**	**170.9**	**170.9**	**171.4**	**171.1**	**1145.4**
	7	**173.9**	**173.0**	**172.6**	**172.1**	**171.2**	**172.6**	**1157.4**	**173.3**	**173.2**	**172.8**	**172.0**	**171.4**	**172.5**	**1157.2**
	8	**170.8**	**170.7**	**169.9**	**169.3**	**169.3**	**170.0**	**1136.1**	**175.5**	**175.5**	**175.1**	**174.8**	**174.6**	**175.1**	**1178.2**
	9	**171.8**	**171.1**	**170.3**	**169.4**	**168.7**	**170.2**	**1138.1**	**173.4**	**173.1**	**173.1**	**172.8**	**172.5**	**173.0**	**1160.9**
	10	**163.4**	**162.7**	**162.3**	**162.2**	**161.5**	**162.4**	**1073.9**	**157.7**	**154.4**	**157.5**	**155.3**	**152.0**	**155.4**	**1015.9**
Rat 6	**1**	**78.8**	**77.9**	**82**	**81**	**81**	**80.14**	**400.1**	**66.7**	**69.4**	**71.6**	**74.0**	**76.4**	**71.4**	**324.8**
	2	**74.6**	**78.0**	**81.2**	**84.3**	**87.5**	**81.1**	**403.4**	**66.7**	**69.1**	**71.7**	**74.1**	**76.3**	**71.6**	**324.8**
	3	**137.3**	**138.1**	**138.4**	**138.3**	**138.3**	**138.1**	**873.0**	**138.8**	**137.8**	**138.0**	**138.9**	**138.9**	**138.5**	**876.3**
	4	**149.3**	**151.1**	**151.7**	**151.8**	**152.3**	**151.2**	**981.5**	**158.2**	**158.0**	**157.1**	**156.9**	**156.8**	**157.4**	**1032.4**
	5	**139.7**	**139.3**	**138.8**	**138.4**	**138.2**	**138.9**	**879.6**	**139.1**	**138.7**	**138.2**	**138.8**	**141.3**	**139.2**	**882.6**
	6	**168.0**	**167.5**	**166.9**	**165.8**	**168.6**	**167.3**	**1114.4**	**166.4**	**165.4**	**162.8**	**166.7**	**167.0**	**165.7**	**1100.4**

	7	**174.3**	**173.8**	**173.5**	**172.3**	**173.9**	**173.5**	**1165.4**	**172.5**	**171.5**	**170.1**	**169.4**	**170.0**	**170.7**	**1142.0**
	8	**174.8**	**174.4**	**173.9**	**173.3**	**172.6**	**173.8**	**1167.5**	**176.4**	**175.1**	**174.2**	**178.2**	**177.2**	**176.2**	**1187.5**
	9	**171.5**	**170.1**	**169.1**	**168.1**	**166.8**	**169.1**	**1129.0**	**176.1**	**175.7**	**175.8**	**174.8**	**173.4**	**175.2**	**1178.9**
	10	**161.2**	**160.6**	**160.0**	**159.1**	**158.7**	**159.9**	**1053.1**	**171.8**	**171.5**	**170.8**	**170.9**	**171.4**	**171.3**	**1146.9**

Appendix 4: Literature review of material properties and structural densities for FEA models

Dehydrated bone material properties

Material	Bone	Species	Age (weeks)	Elastic modulus (GPa)	Number of individuals	average *number of individuals	Dehydrated (D) / hydrated (H)	Paper
Cortical bone (inner cortical)	tibia	rat	10	28.80	8	230.4	D	Busa, B., et al., 2005
Cortical bone (endosteal approximately 10-14 days old)	tibia	rat	10	27.70	8	221.6	D	Busa, B., et al., 2006
Cortical bone (periosteal approximately 10-14 days old)	tibia	rat	10	27.60	8	220.8	D	Busa, B., et al., 2007
Cortical bone	Tibia	rat	12	15.00	1	15	D	Vickerton et al, 2014
Cortical bone	Tibia	rat	12	20.00	1	20	D	Vickerton et al, 2015
cortical bone	femur	rat	14	34.20	1	34.2	no information	Bach-Gansmo,

(cartilage islands)							**available**	**F., et al., 2013**
cortical bone (surrounding bone)	**femur**	**rat**	**14**	**27.10**	**1**	**27.1**	**no information available**	**Bach-Gansmo, F., et al., 2014**
cortical bone	**tibia**	**rat**	**15**	**23.00**	**21**	**483**	**no information available**	**Brüel, A., et al., 2011**
cortical bone	**femur**	**rat**	**16**	**40.70**	**5**	**203.5**	**D**	**Jaramillo Isaza, S., 2014**
Cortical bone (lamellar region)	**femur**	**rat**	**32**	**27.80**	**10**	**278**	**D**	**Shipov, A., et al., 2013**
Cortical bone (disorganised region)	**femur**	**rat**	**32**	**30.10**	**10**	**301**	**D**	**Shipov, A., et al., 2014**
Cortical bone (mineralised cartilage islands)	**femur**	**rat**	**32**	**33.40**	**10**	**334**	**D**	**Shipov, A., et al., 2015**
cortical bone	**femur**	**rat**	**36**	**35.90**	**5**	**179.5**	**D**	**Jaramillo Isaza, S., et al., 2014**
cortical bone	**femur**	**rat**	**52**	**39.80**	**5**	**199**	**D**	**Jaramillo Isaza, S., et al., 2015**

cortical bone	**femur**	**rat**	**78**	**38.40**	**5**	**192**	**D**	**Jaramillo Isaza, S., et al., 2016**
cortical bone	**femur**	**rat**	**104**	**34.60**	**5**	**173**	**D**	**Jaramillo Isaza, S., et al., 2017**
Cortical bone	**femur**	**rat**	**10 (bone 5-70 days)**	**30.00**	**4**	**120**	**no information available**	**Donnelly et al, 2009,**
			Average (GPa)	**30.24**	**Weighted average (GPa)**	**29.93**		
			SD	**6.91**				
			plus SD wet	**24.67**				
			minus SD wet	**15.49**				

Trabecular bone

Material	Bone	Species	Age (weeks)	Elastic modulus (GPa)	Number of individuals	average *number of individuals	Dehydrated (D) / hydrated (H)	Paper
Trabecular bone	lumbar vertebrae	rat	104 weeks	19.35	12	232.20	D	Ammann et al, 2007
Trabecular bone	lumbar vertebrae	rat	37 weeks	16.10	1	16.10	no information avaliable	Guo et al 2000
Trabecular bone	femur	rat	8 weeks	10.66	6	63.96	D	Sun et al 2009
Trabecular bone	vertebrea	rat	10 months	22.03	10	220.30	no information avaliable	Sheng et al 2006
			Dry average	17.04	Weighted dry average	18.36		
			sd	4.89				
			plus SD wet	4.70				

	minus SD wet	**2.60**	

Difference between hydrated and dehydrated bone

Dehydrated bone						
Material	**Bone**	**Species**	**Age**	**Elastic modulus (GPa)**	**Number of individuals**	**Paper**
Cortical bone	**lumbar vertebrae**	**rat**	**104 weeks**	**20.18**	**12**	**Ammann et al, 2007**
Cortical bone	**femur**	**homo sapien**	**adult**	**21.33**	**1**	**Hengsberger, et al, 2002**
Cortical bone	**metacarpal**	**horse**	**2yrs**	**19.40**	**1**	**Bushby et al, 2004**
Cortical bone	**femur**	**bovine**	**1.5yrs**	**32.00**	**1**	**Guidoni et al, 2010**
Cortical bone	**femur**	**canine**	**n/a**	**26.98**	**3**	**Lee et al, 2013**
Trabecular bone	**lumbar vertebrae**	**rat**	**104 weeks**	**19.35**	**12**	**Ammann et al, 2007**
Trabecular bone	**antler**	**cervid**	**adult**	**10.90**	**1**	**Akhtar et al, 2008**
Cortical bone	**femur**	**bovine**	**adult**	**27.50**	**1**	**Rho and Pharr, 1999**
Cortical bone	**femur**	**homo sapien**	**adult**	**26.80**	**4**	**Wolfram et al, 2010**

Trabecular bone	**vertebrea**	**homo sapien**	**adult**	**12.00**	**104**	**Wolfram et al, 2010**

Hydrated bone								
Material	**Bone**	**Species**	**Age**	**Elastic modulus (GPa)**	**Number of individuals**	**Paper**	**Difference in modulus (GPa)**	**Percentage difference**
Cortical bone	**lumbar vertebrae**	**rat**	**104 weeks**	**12.92**	**12**	**Ammann et al, 2007**	**7.26**	**35.98**
Cortical bone	**femur**	**homo sapien**	**adult**	**12.95**	**1**	**Hengsberger, et al, 2002**	**8.38**	**39.29**
Cortical bone	**metacarpal**	**horse**	**2yrs**	**11.70**	**1**	**Bushby et al, 2004**	**7.70**	**39.69**
Cortical bone	**femur**	**bovine**	**1.5yrs**	**23.00**	**1**	**Guidoni et al, 2010**	**9.00**	**28.13**
Cortical bone	**femur**	**canine**	**n/a**	**13.41**	**3**	**Lee et al, 2013**	**13.57**	**50.30**
Trabecular bone	**lumbar vertebrae**	**rat**	**104 week**	**12.37**	**12**	**Ammann et al, 2007**	**6.98**	**36.07**

			s					
Trabecular bone	antler	cervid	adult	5.40	1	Akhtar et al, 2008	5.50	50.46
Cortical bone	femur	bovine	adult	25.10	1	Rho and Pharr, 1999	2.40	8.73
Cortical bone	femur	homo sapien	adult	20.80	4	Wolfram et al, 2010	6.00	22.39
Trabecular bone	vertebrea	homo sapien	adult	9.00	104	Wolfram et al, 2010	3.00	25.00
						Average	6.98	33.60

Structural densities

Tissue	bone	Species	Structural density (kg/m³)	number	Paper
Cortical bone	antler	cervid	1860	10	Rajaram et al 1982
Cortical bone	femur	bovine	1940	10	Rajaram et al 1983
Cortical bone	parietal	homo sapien	1810	14	Petersonet al 2003

Cortical bone	**frontal**	**homo sapien**	**1780**	**9**	**Petersonet al 2004**
Cortical bone	**occipital**	**homo sapien**	**1860**	**5**	**Petersonet al 2005**
Cortical bone	**temporal**	**homo sapien**	**1870**	**4**	**Petersonet al 2006**
Cortical bone	**zygomatic**	**homo sapien**	**1680**	**4**	**Petersonet al 2007**
Cortical bone	**mandible**	**rhesus monkey**	**2000**	**1**	**Dechow et al 2000**
Cortical bone	**femur**	**olive baboon**	**2060**	**18**	**Phelps et al 2000**
Cortical bone	**femur**	**homo sapien**	**2040**	**39**	**Currey et al 1979**
Cortical bone	**tibia**	**murine**	**1950**	**37**	**Somerville et al 2004**
Cortical bone	**rib**	**florida mantee**	**2150**	**1**	**Clifton et al 2008**
		Average	**1916.67**		
		Weighted average	**1946.05**		
Trabecular bone	**femur**	**human**	**1770**	**3**	**Ashman & Rho 1988**
Trabecular bone	**femur**	**bovine**	**1739**	**1**	**Ashman & Rho 1989**

		Average	1754.50		
		Weighted average	1762.25		
		Apparent density	569.21		
Bone marrow	femur	bovine	930	2	Hosokawa & Otani, 1997
Bone marrow		canid	903	1	Mendez et al 1960
		Average	916.50		
		Weighted average	921.00		
Articular cartilage	knee	bovine	1050	45	Joseph et al 1999
Articular cartilage	patella	rorcine	1150	27	Jaremko et al 2007
Articular cartilage	rib	cavia	1548	1	Lohmander & Hjerpe 1975
Epiphyseal cartilage	tibia	canid	1554	2	Lohmander & Hjerpe 1975

Articular cartilage	**metacarpophalangeal joint**	**bovine**	**1110**	**9**	**Zhou et al 2004**
		Average	**1282.40**		
		Weighted average	**1106.50**		

Appendix 5: nodal data from FEA models

Effective Strain (με)							
model a	**model b**	**model c**	**model d**	**model e**	**model f**	**model g**	**model h**
681.7	540.0	648.0	514.0	519.3	413.4	470.4	374.6
727.8	578.3	675.2	537.8	537.2	425.4	516.1	409.9
673.3	535.2	633.8	503.4	467.0	371.3	454.1	362.1
684.2	546.2	625.6	496.3	537.7	427.5	547.3	433.6
657.2	524.0	741.2	590.7	485.8	383.9	536.4	426.0
698.9	556.3	771.7	612.7	409.4	325.1	482.6	382.6
697.8	554.4	798.4	633.3	502.8	400.6	571.9	455.7
713.8	565.3	787.6	624.5	507.1	400.8	656.9	519.9
681.9	541.7	702.6	558.7	394.1	311.4	467.9	372.6
711.7	566.0	779.3	616.2	409.7	326.0	515.5	409.5
724.0	575.3	783.8	620.1	436.0	346.7	567.3	449.1
709.6	566.2	776.0	615.5	502.2	399.2	670.5	533.9
697.0	555.6	756.1	599.8	389.1	308.0	536.8	425.0
685.3	544.4	742.4	589.2	392.2	310.3	529.6	419.0
685.2	545.1	784.1	621.7	329.2	262.0	402.3	317.9
729.7	581.2	777.5	617.2	342.5	272.6	484.0	384.6
694.6	552.0	817.2	648.3	313.9	250.0	424.4	336.5
707.8	563.4	777.1	617.2	333.8	266.8	472.3	375.9
710.1	563.7	757.2	601.9	342.8	273.2	477.1	377.2
717.8	570.3	758.6	602.4	287.1	227.8	414.8	328.1
712.6	566.1	776.3	615.4	279.4	222.7	356.9	283.2
721.3	574.0	842.4	668.8	303.2	240.1	429.9	341.1
684.7	546.1	802.7	637.7	334.2	264.1	472.1	376.2
649.3	515.9	726.6	577.4	289.0	228.8	424.7	336.4
730.3	578.2	789.2	626.8	308.7	244.9	421.1	333.5
753.8	598.0	786.5	622.7	286.2	225.9	338.3	268.2
696.0	554.4	747.9	593.7	294.0	230.9	441.8	348.9
695.0	552.4	756.5	599.6	303.6	242.1	384.5	305.6
668.7	531.5	730.2	579.0	285.4	227.6	351.8	280.0
692.5	551.7	753.9	598.2	302.4	240.0	418.8	331.8
711.9	563.2	778.7	616.7	278.4	223.5	420.8	334.4
660.0	524.9	732.7	581.3	291.6	231.6	428.1	340.4
691.5	548.2	763.3	604.7	286.6	226.9	389.9	309.6
703.1	556.8	789.8	626.8	250.9	198.8	316.4	249.9
672.3	532.0	747.0	593.0	283.9	225.7	409.2	324.0
665.8	528.6	731.9	582.6	264.3	208.9	360.8	284.6

678.7	539.5	744.5	591.3	282.9	223.3	418.6	332.9
679.5	537.9	747.3	593.7	286.2	226.3	413.8	327.0
675.5	536.7	738.1	588.3	269.1	214.7	387.9	306.4
649.3	516.1	662.8	524.4	307.4	241.5	449.4	359.5

Effective Stress (Pa)							
model a	**model b**	**model c**	**model d**	**model e**	**model f**	**model g**	**model h**
10406836	8272534	9892436	7858457	7927609	6294485	7197201	5714342
11145427	8859782	10310691	8190823	8206277	6515035	5908991	4691181
10286166	8178802	9681143	7692828	7153160	5680173	4699440	3731784
10409219	8274181	9583801	7612909	8224937	6528843	5455502	4330629
10061882	7998208	7525178	5977997	7395732	5872447	4185785	3323592
10674487	8486618	6486412	5153633	6255245	4968682	5241282	4162846
10642126	8458085	5995636	4762171	7688011	6102809	2558064	2030450
10890805	8658137	7240319	5752187	7727924	6133383	2946730	2338584
10423134	8289878	8176817	6499138	6013380	4776565	4619346	3668583
10871951	8642333	7564908	6009418	6279599	4985355	2313220	1836240
11055249	8786532	3513711	2790832	6651601	5278286	2547131	2021125
10860084	8634564	6987770	5552121	7676225	6090296	3016496	2393206
10652813	8469564	6122805	4864810	5952056	4723906	2405660	1909026
10455344	8313806	6620893	5261301	5988656	4754074	2372230	1882827
10482785	8336314	6378803	5069431	5017960	3987144	4327853	3437692
11164888	8873986	6705865	5326490	5246882	4160852	2177480	1726648
10624901	8447650	7230531	5745215	4796983	3810133	3932136	3121978
10824983	8605467	7481617	5943794	5108689	4052155	2125671	1685899
10833296	8612282	7175592	5700904	5233841	4153984	2140095	1698195
10961662	8711009	7049807	5598762	4374835	3467642	1859023	1473458
10869347	8639415	7976259	6335785	4274707	3396926	3709329	2946184
11021129	8757487	6625271	5261093	4633039	3673524	1929776	1529933
10463873	8317638	8165161	6486329	5110770	4055786	2124662	1685719
9913334	7875540	8296388	6586810	4412686	3497114	1904851	1509531
11122320	8838680	5224090	4148771	4701319	3728598	1891585	1499919
11470701	9113692	3527812	2800948	4342952	3450071	2806824	2228667
10617295	8436597	5363091	4258722	4459722	3532725	1969722	1560319
10618317	8435994	6840161	5430877	4646812	3687315	1723686	1367298
10208388	8108398	7147131	5673305	4367185	3466938	3868076	3069486
10581588	8406058	6179234	4905718	4619861	3664499	1882698	1493004
10853259	8622066	3488953	2769933	4290111	3405174	3210582	2547342
10098991	8025193	7289847	5789161	4457761	3533400	1923190	1524136
10549812	8379863	5339356	4238445	4374841	3470281	1751475	1388885
10760798	8547340	3552409	2819809	3812204	3028112	3672457	2915497

10264404	8151607	5035542	3996433	4320803	3426939	1838344	1457584
10170615	8080149	7735410	6141454	4038327	3205439	3106154	2464322
10356827	8227616	5913233	4694400	4313015	3418716	1883798	1492867
10363493	8235041	5532940	4393625	4362096	3458685	1855612	1470896
10306946	8186367	5499739	4365265	4113686	3263978	1742047	1381629
9937389	7893633	5287556	4197313	4701565	3726392	2029434	1608161

Effective strain (με) output from region of interest when the material properties of the trabecular bone, cortical bone and cartilage were altered.

Effective strain (με)											
model 1						**model 6**					
trabecular		**cortical**		**cartilage**		**trabecular**		**cortical**		**cartilage**	
minus	plus	minus	plus	minus	plus	minus	plus	minus	plus	minus	plus
684	675	906	531	649	707	414	412	548	321	393	429
737	727	974	570	692	758	429	425	565	334	402	444
676	671	894	525	643	696	374	370	492	290	352	387
683	680	908	532	648	707	428	427	569	333	406	444
659	659	876	513	627	682	386	384	512	299	363	398
700	698	927	546	666	722	327	324	433	254	308	338
696	697	926	545	666	723	398	398	534	312	379	413
715	712	946	557	682	739	402	401	532	313	381	417
684	681	904	534	652	703	313	312	416	243	296	324
712	713	943	555	681	736	326	326	433	252	308	339
723	726	960	563	691	747	345	344	460	268	327	359
713	710	942	557	681	736	399	399	529	309	380	414
698	698	924	545	666	721	309	310	412	241	294	321
686	685	906	535	654	708	310	311	414	243	296	321
687	685	907	536	657	709	262	260	347	202	247	270
731	731	969	571	699	755	272	273	362	212	258	282
695	695	922	543	665	718	250	249	333	194	236	259
709	709	940	553	677	732	265	265	354	207	250	275
709	709	940	554	678	732	272	271	363	211	256	283
718	718	952	560	687	741	227	228	304	177	216	237
712	713	944	557	681	734	222	223	297	173	210	232
721	722	958	564	691	746	241	241	320	187	228	249
686	687	907	536	657	706	265	266	353	206	253	276
648	649	861	508	622	670	228	229	306	177	218	239
727	729	965	569	696	751	242	244	325	190	231	255
750	751	996	586	719	774	226	225	300	175	213	236
693	696	920	541	665	716	232	230	309	181	220	238
695	696	922	544	666	720	241	240	323	187	227	252
667	668	886	522	641	690	228	226	305	178	212	237
693	693	920	541	665	714	241	240	320	187	227	250
711	711	940	558	679	735	222	225	299	172	208	234

662	661	876	518	633	684	230	231	308	178	219	241
690	692	917	540	661	713	227	225	303	175	215	237
703	704	937	549	675	724	199	197	265	154	186	206
672	672	894	525	645	693	224	225	300	172	210	234
665	666	884	521	638	687	209	209	280	162	197	220
678	679	900	529	650	700	224	224	298	173	212	233
678	680	901	530	650	700	227	227	304	175	214	237
677	677	894	529	646	698	215	215	286	166	200	221
649	651	863	509	622	671	242	244	327	189	231	254

Effective stress (Pa) model 1					
trabecular		**cortical**		**cartilage**	
minus	plus	minus	plus	minus	plus
10463369	10380588	10777509	10094711	9891138	10801663
11204628	11117686	11540471	10811628	10594271	11565874
10321762	10268813	10636411	9984297	9798783	10648819
10436018	10396429	10783889	10094826	9914581	10787856
10075064	10055114	10422198	9758750	9594833	10417707
10699792	10661924	11040913	10360816	10179136	11044802
10646394	10639429	11031278	10317667	10152175	11018976
10908735	10881586	11264207	10571463	10393457	11262271
10444783	10412055	10753487	10130259	9957147	10756806
10879900	10867377	11250547	10550442	10380773	11241239
11054835	11054557	11451391	10723180	10557251	11435168
10877020	10851287	11223808	10546010	10370169	11221588
10663737	10646886	11007804	10346124	10179247	11001188
10468007	10448605	10794820	10158232	9992814	10790313
10493769	10476982	10817188	10187015	10022479	10811273
11162960	11165010	11550141	10837727	10674584	11531760
10631077	10621330	10973835	10321242	10159157	10963453
10828843	10822429	11189113	10511862	10348719	11176296
10834100	10832290	11193576	10521072	10360185	11178069
10953387	10964682	11348180	10637823	10483808	11325026
10865786	10870411	11236118	10554510	10397950	11216315
11013037	11024279	11403832	10699351	10546791	11379080
10461187	10464669	10811231	10163423	10012641	10792426
9902561	9917787	10261587	9627330	9498155	10236115
11116466	11124570	11501983	10798644	10641543	11478360
11463643	11473487	11868327	11135399	10975920	11842035
10611586	10619570	10977733	10311129	10163838	10954242
10610589	10621422	10986524	10311081	10167423	10961318

10200761	10211521	10564089	9916451	9783232	10538377
10574110	10584621	10948697	10276327	10134357	10923073
10846609	10855950	11228478	10538822	10390862	11202558
10093965	10101011	10438225	9808516	9667522	10415953
10543142	10552525	10916456	10246175	10105449	10890538
10754906	10763174	11134347	10449741	10304311	11108144
10258256	10266904	10623083	9971587	9838122	10597192
10165670	10172619	10516539	9877925	9738265	10492755
10352190	10358687	10710887	10056071	9912131	10686343
10358746	10365386	10713461	10061184	9913402	10690125
10302021	10308936	10663061	10010395	9871709	10637827
9933142	9939101	10277424	9648915	9511385	10253255

Effective stress (Pa) model 6					
trabecular		**cortical**		**cartilage**	
minus	plus	minus	plus	minus	plus
6330908	6277358	6522066	6100609	5962410	6549704
6546197	6500268	6752217	6313281	6175062	6776248
5705697	5668219	5881687	5506900	5388155	5901206
6542001	6522266	6772896	6322117	6196147	6784651
5888289	5864916	6084073	5690362	5574472	6096989
4978922	4963810	5144374	4815245	4718758	5153324
6108875	6099651	6332381	5906647	5791616	6338746
6136710	6131476	6366173	5935677	5822754	6370489
4781636	4774070	4952053	4622556	4529673	4957482
4987023	4984383	5175764	4820841	4726353	5178552
5277323	5278499	5482907	5104249	5008135	5483593
6088651	6090745	6327969	5889679	5780135	6328350
4722806	4724242	4908031	4565962	4478196	4908521
4753995	4753934	4938690	4594493	4504231	4940122
3990428	3985536	4134869	3855683	3776252	4138911
4155575	4163127	4328580	4020285	3947677	4325410
3810744	3809767	3957302	3680277	3604708	3959160
4048117	4053890	4215984	3913504	3840201	4213755
4152022	4154776	4319838	4010835	3931648	4319518
3461931	3470165	3611923	3347745	3287581	3607983
3398323	3396233	3527983	3279256	3208940	3530470
3668541	3675710	3823517	3547733	3483000	3820282
4053332	4056816	4219272	3915006	3837782	4218465
3491539	3499593	3641949	3377067	3316866	3637903
3724457	3730423	3883897	3596600	3526806	3881380
3449999	3450064	3590009	3325088	3252165	3591323
3527260	3535189	3679262	3412493	3352955	3674816

3684377	3688607	3844757	3550696	3475709	3843456
3465161	3467697	3610940	3340789	3269978	3610671
3660697	3666181	3822540	3528815	3455886	3820378
3402889	3406169	3552451	3276105	3204075	3551728
3529242	3535257	3684901	3405822	3339096	3681904
3467147	3471661	3620189	3341249	3271196	3618471
3026731	3028682	3159930	2910190	2842284	3160226
3423756	3428344	3576825	3298159	3228404	3574975
3203270	3206371	3347286	3080712	3010689	3346653
3415618	3420096	3563209	3296787	3232054	3560878
3455776	3459970	3610533	3328809	3258491	3608621
3261586	3265008	3410656	3136097	3064997	3409635
3723186	3727822	3890778	3586930	3512197	3888350

Strain gauge validation values

	1st principal strain FEA (με)	**Strain gauge values (με)**
	156	120
	169	123
	151	115
	154	124
	151	
	158	
	145	
	147	
	95	
	159	
	125	
	114	
	150	
	142	
	82	
	105	
	65	
	65	
	129	
	16	
	90	
	111	
	58	
	116	
	111	
average	**118.4722**	**120.5**